Intermittent chaos in
Hamiltonian dynamical systems

Dissertation

vorgelegt von
Eduardo Goldani Altmann
geboren am 08.11.1979 in São Paulo (Brasilien)

Januar 2007

Die Dissertation kann wie folgt zitiert werden:

urn:nbn:de:hbz:468-20070152
[http://nbn-resolving.de/urn/resolver.pl?urn=urn%3Anbn%3Ade%3Ahbz%3A468-20070152]

Abstract

The topic of this Thesis is the statistical characterization of chaotic trajectories in Hamiltonian dynamical systems. Such systems usually show coexistence of regions of chaotic and regular (periodic or quasi-periodic) motion in the phase space. When chaotic trajectories approach the regular regions they *stick* to their border inducing long periods of almost regular motion. This intermittent behavior determines the main dynamical properties of the system (e.g., transport and decay of correlations); it is quantified through the power-law statistics of regular periods $P(T) \propto T^{-\gamma-1}$. The fundamental problem is how to quantitatively relate the intermittency of the chaotic dynamics to the distribution and stability properties of the regular regions of the phase space (e.g., periodic orbits, KAM islands, and *cantori*). Different classes of Hamiltonian systems are investigated through numerical simulations and phenomenological models. The exponent $\gamma = 2$ is derived for the *stickiness* close to one-parameter families of marginally unstable periodic orbits. This theory applies to: chaotic billiards with parallel walls (e.g., Sinai and stadium billiards), circular-like billiards (e.g., annular and mushroom billiards), and piecewise-linear area-preserving maps. Such systems have sharply-divided phase space, i.e., a simple curve defines the border between the regions of regular and chaotic motion. Generic perturbations lead to the usual hierarchical phase space, where it is observed that the stickiness is enhanced ($\gamma < 2$). The addition of white noise has two effects on $P(T)$: it enhances ($\gamma \approx 0.5$) the probability for intermediate times T by placing trajectories inside the regular regions; and it introduces an exponential cutoff at larger times T. Similar results are shown to appear for N weakly coupled area-preserving maps. In this case an additional asymptotic power-law decay of $P(T)$ is observed as a consequence of the stickiness to high-dimensional KAM *tori*. Numerical results indicate that the exponent γ of this decay increases with N. This suggests a novel explanation for the onset of strong chaos in high-dimensional Hamiltonian systems. The different regimes of decay of $P(T)$ impact on the transport properties leading to a anomalous or normal diffusion. In the last case a nontrivial dependence of the asymptotic diffusion coefficient on the noise intensity or coupling strength is observed. Applications to physically relevant problems are discussed, such as, the transport of passive tracers in two-dimensional incompressible fluids and the decay of correlation in systems with time scale separation. Altogether, the different results lead to a new unified interpretation of the chaotic dynamics in Hamiltonian systems and raise the phenomenon of stickiness to a fundamental status.

Additional keywords: Hamiltonian dynamics, long-term correlation, anomalous diffusion, Poincaré recurrence time, symplectic maps.

Zusammenfassung

Diese Dissertation beschäftigt sich mit der statistischen Charakterisierung von chaotischen Trajektorien in Hamiltonschen dynamischen Systemen. Im Phasenraum solcher Systeme koexistieren typischerweise Gebiete mit regulärer (periodischer oder quasi-periodischer) und chaotischer Dynamik. Chaotische Trajektorien, die in die Nähe regulärer Gebiete geraten, verweilen nahe ihrer Grenzen und beschreiben eine quasi-reguläre Dynamik für eine begrenzte Zeitperiode. Das Verweilen oder "Kleben" der Trajektorie in der Nähe regulärer Gebiete wird als *Stickiness* (engl. Klebrigkeit) bezeichnet. Solches intermittierendes Verhalten bestimmt die wichtigsten dynamischen Eigenschaften des Systems (z.B. die Transporteigenschaften und den Zerfall der Korrelation); es wird quantifiziert durch das Potenzgesetz in der Statistik von Verweilenzeiten $P(T) \propto T^{-\gamma-1}$. Das zentrale Problem ist es, den Zusammenhang zwischen der Intermittenz der chaotischen Dynamik und der Verteilung und den Stabilitäteigenschaften von regulären Gebieten im Phasenraum (periodische Bahnen, KAM Inseln und *Cantori*) zu bestimmen. Verschiedene Systeme werden durch ein einziges Verfahren analysiert, das auf numerischen Simulationen und phänomenologischen Modellen basiert. Für den Fall von Systemen mit Ein-Parameter-Familien von marginal-instabilen periodischen Bahnen wird der Exponent $\gamma = 2$ analytisch berechnet. Diese Theorie beschreibt chaotische Billards mit parallelen Wänden (z.B. Sinai und Stadion Billards), Kreis-Billards (z.B. ringförmige und Pilz-Billiards), und stückweise lineare zweidimensionale Abbildungen. In solchen Systemen besteht die Grenze zwischen Regionen regulärer und chaotischer Bewegung im Phasenraum aus einer einfachen Kurve (einfach getrennter Phasenraum). Generische Störungen dieses Falls führen zu dem typischen hierarchischen Phasenraum, in dem die *Stickiness* stärker ist als im einfachen getrennten Phasenraum ($\gamma < 2$). Zusätzliches weißes Rauschen hat zwei Auswirkungen auf $P(T)$: mittlere Verweilenzeiten T werden wahrscheinlicher ($\gamma \approx 0.5$), da die Trajektorien in die regulären Gebiete eintreten; für größere T zerfällt $P(T)$ exponentiell. Ähnliche Ergebnisse wurden in einem Modell von N gekoppelten zweidimensionalen Abbildungen gefunden. Ein zusätzliches asymptotisches Potenzgesetz existiert in diesem Fall wegen der *Stickiness* an hochdimensionalen KAM-*tori*. Numerische Simulationen zeigen dass der Exponent γ dieses Gesetzes mit N wächst. Dies bietet eine neue Erklärung für das Auftreten von starkem Chaos in hochdimensionalen Hamiltonschen Systemen. Das Verhalten von $P(T)$ in den verschiedenen Bereichen führt entweder zu anomaler oder normaler Diffusion und prägt im letzeren Fall eine nichttriviale Abhängigkeit des asymptotischen Diffusionskoeffizienten von der Rauschintensität oder von der Kopplungsstärke. Anwendungen auf physikalisch relevante Probleme werden diskutiert; u.a. die Dispersion von passivem Teilchen in zweidimensionalen nicht-komprimierbaren Flüssigkeiten und der Zerfall von Korrelation in Systemen mit verschiedenen Zeitskalen. Zusammengenommen stützen alle Ergebnisse dieser Arbeit eine neuartige Interpretation der chaotischen Hamiltonschen Dynamik, in der die *Stickiness* eine zentrale Rolle spielt.

Titel der Dissertation: Intermittierendes Chaos in Hamiltonschen dynamischen Systemen
Zusätzliche Schlüsselwörter: Hamiltonsche Dynamik, Langzeitkorrelation, Poincaré Wiederkehrzeit, symplektische Abbildung.

Resumo

O tema desta Tese é a caracterização estatística de trajetórias caóticas em sistemas dinâmicos Hamiltoneanos. Tais sistemas apresentam tipicamente coexistência de regiões de dinâmica caótica e regular (periódica ou quasi-periódica) no espaço de fases. Ao se aproximarem de regiões regulares, as trajetórias caóticas *grudam* (prendem-se) a sua borda apresentando longos períodos de movimento aproximadamente regular. Este comportamento intermitente determina as principais propriedades dinâmicas do sistema (e.g., transporte e decaimento de correlações); ele é quantificado através do decaimento algébrico da distribuição de períodos regulares $P(T) \propto T^{-\gamma-1}$. O problema fundamental é relacionar quantitativamente a intermitência das trajetórias caóticas à distribuição e às propriedades de estabilidade das regiões regulares do espaço de fases (órbitas periódicas, ilhas KAM e *cantori*). Diversas classes de sistemas Hamiltoneanos são investigados através de simulações numéricas e modelos fenomenológicos. O expoente $\gamma = 2$ é obtido para o *grudamento* (termo em inglês: *stickiness*) próximo a familias de órbitas marginalmente instáveis parametrizáveis. Esta teoria aplica-se a: bilhares caóticos com paredes paralelas (e.g., bilhar de Sinai e do estádio), bilhares com componentes circulares (e.g., bilhares anulares e em forma de cogumelo) e mapas bidimensionais lineares por partes. Estes sistemas apresentam espaço de fases onde regiões regulares e caóticas são divididas por curvas simples. Perturbações genéricas aplicadas a estes sistemas levam ao caso típico de espaço de fases hierárquico, onde o grudamento das trajetórias é intensificado ($\gamma < 2$). A adição de ruído branco tem dois efeitos sobre $P(T)$: tempos T intermediários tornam-se mais prováveis ($\gamma \approx 0.5$) devido a trajetórias que penetram nas regiões regulares; para tempos T longos, transição para decaimento exponencial (*cutoff*). Resultados similares são obtidos em um sistema de N mapas bidimensionais fracamente acoplados. Neste caso um decaimento algébrico assintótico é adicionalmente observado, como consequência do grudamento a toros KAM. Experimentos numéricos indicam que o expoente assintótico γ deste decaimento cresce com N, o que sugere uma nova explicação para o surgimento de caos forte em sistemas Hamiltoneanos de alta dimensão. Os diferentes regimes de decaimento de $P(T)$ afetam as propriedades de transporte podendo levar a difusão anômala ou normal. No último caso, é observada uma dependência não trivial do coeficiente de difusão assintótico com a intensidade do ruído ou do acoplamento. Aplicações a problemas relevantes de Física são discutidos, tais como o transporte de marcadores passivos em fluidos bidimensionais incompressiveis e o decaimento de correlações em sistemas com separação de escalas temporais. Considerando os resultados em conjunto, emerge uma interpretação nova e unificada da dinâmica caótica em sistemas Hamiltoneanos onde a propriedade de grudamento desempenha um papel fundamental.

Título da tese: Caos intermitente em sistemas dinâmicos Hamiltoneanos.

Outras palavras chaves: dinâmica Hamiltoneana, correlação de longo alcance, difusão anômala, tempo de retorno de Poincaré, mapas simpléticos.

Abbreviations, acronyms, and most used variables:

KAM Kolmogorov-Arnold-Moser, usually used to refer to their theory of dealing with problems of small denominator.

MUPOs marginally unstable periodic orbits, that appear as one-parameter families in contact with the chaotic component.

RTD recurrence time distribution $P(T)$.

RTS recurrence time statistics $\rho(\tau)$ which is the cumulative version of the RTD $P(T)$.

RW random walk.

PDF probability density function.

ν anomalous transport exponent for the growth of the mean squaredD displacement.

D_ν anomalous transport coefficient (generalized diffusion coefficient).

D_A asymptotic value of the usual diffusion coefficient.

D_m molecular diffusion coefficient.

γ exponent of the power-law decay of the RTS $\rho(\tau)$.

T recurrence time.

$P(T)$ recurrence time distribution (RTD).

$\rho(\tau)$ recurrence time statistics (RTS).

ξ intensity of the noise perturbation or of the coupling strength.

q, η integer numbers corresponding to the period and winding number of a periodic orbit in a circular billiard or, correspondingly, the order and density of a star polygon.

Additionally, the following standard abbreviations were used in the text:
Sec. for Section, Chap. for Chapter, Eq. for Equation, and Fig. for Figure.

In the caption of the figures:

- (Color online) indicates that color helps the interpretation of the figure but that black and white prints are understandable.

- (Color) indicates that color is essential for the understanding of the figure.

Contents

Chapter 1

Introduction

> The present PhD Thesis is a theoretical and numerical study of a particular effect of chaotic trajectories in Hamiltonian systems, namely, the stickiness near regions of regular motion. This introductory chapter motivates the importance of both Hamiltonian systems and stickiness phenomenon to physics.

There are good reasons to ask about the relevance of studying classical Hamiltonian systems. From a dynamical-systems perspective Hamiltonian systems are very particular. In general, a set of $2N$ differential equations $\dot{\boldsymbol{x}} = \boldsymbol{F}(\boldsymbol{x}, t)$ requires the specification of all the components of the vector function $\boldsymbol{F}(\boldsymbol{x}, t)$ while Hamiltonian systems are uniquely defined by a single scalar function: the Hamiltonian $H(\boldsymbol{p}, \boldsymbol{q}, t)$ [Ott02][1]. From the perspective of physical **models** (also biological, economical, etc.) Hamiltonian systems are also exceptional. The reason is that natural systems are never completely isolated and/or include inherent sources of dissipation/creation of energy. Considering additionally that the dynamics in Hamiltonian systems is fundamentally different from the one in dissipative systems, one sees that a justification in general terms for a theoretical study in this field is necessary. A short answer to the previous objections is that virtually all fundamental physical **theories** are Hamiltonian once the usual atomistic/mechanistic viewpoint is assumed, i.e., once the dynamics of particles, fields, and classical or quantum objects is described. Assuming this point of view, dissipation and noise perturbations arise from the **Hamiltonian** interaction to many degrees of freedom which are usually replaced by effective dissipative and stochastic terms in the models. It is remarkable that such an interpretation of reality, manifested in well-known experiments, played an important role in two key moments of science's history: a major conceptual development that led to the rupture with the Aristotelic theories and to the birth of classical mechanics was the isolation of the role of friction in mechanical systems made by Galileo Galilei (1564-1642); similarly, an important contribution to the atomistic interpretation of matter and to the birth of modern physics was the statistical interpretation of Brownian motion given by Albert Einstein (1879-1955).

From the previous considerations it should be no surprise that important questions of physics rely on properties of Hamiltonian dynamics. The most prominent ones are those related to the foundations of statistical mechanics. Other important basic issues which are presently under investigation refer to wave and quantum mechanical systems that are classically chaotic. In such cases semi-classical methods based on the classical properties of Hamiltonian systems have shown to be extremely powerful. Despite the restrictions mentioned in the previous paragraph, there are still several relevant specific examples where classical Hamiltonian dynamics applies, such as, e.g., astronomical objects (rockets, asteroids, planets, and galaxies), incompressible

---

[1] More generally, Hamiltonian systems are symplectic, what implies important restrictions to the solutions (see Sec. 2.1.1).

fluids, and magnetic field lines (in devices for plasma confinement or in accelerator beams). Despite the relevance and the long time these problems have already been studied, some basic properties of classical Hamiltonian systems are still not yet understood.

One of the main distinctions in deterministic dynamics is between regular (periodic and quasi-periodic) and irregular (chaotic) motion. In Hamiltonian systems this distinction is particularly important. Well-known examples of periodic trajectories are Kepler's ellipses (in the two-body problem) and the oscillation of a simple pendulum. Quasi-periodic motion appears in higher-dimensional systems as a linear composition of two periodic motions with incommensurable periods. Quasi-periodic trajectories never perfectly close themselves but build up a torus in the phase space $(\boldsymbol{p}, \boldsymbol{q})$. They are more generic than periodic trajectories in the same sense in which irrational numbers are more generic than rational numbers. The existence of chaotic motion was first glimpsed by Henry Poincaré (1854-1912) at the end of the XIX century while working on the (restricted) three-body problem [Poi92]. Among his astonishing findings, two of them indicated that trajectories beyond the regular ones exist: (i) the non-convergence of series corresponding to quasi-periodic solutions, due to the problem of small denominators; (ii) the existence of homoclinic orbits, as a result of Poincaré's new geometrical approach to the problem [BG96]. Chaotic trajectories combine (long-term) unpredictability and determinism by showing sensitivity to initial conditions: close by trajectories diverge exponentially fast in time from each other (i.e., at least one Lyapunov exponent is positive). An everynight example of chaos is the orbit of Hyperion – one of the moons of Saturn [WPM84].

The establishment of chaotic motion as a general property of nonlinear dynamical systems took place only in the 1970's, partially due to computer simulations. Doubtless, the possibility of performing reliable numerical simulations had a great impact on nonlinear dynamics. However, important developments happened also between the pioneering works of Poincaré and the invention of computers. It is also not completely correct to say that the investigations on dynamics happened apart from the major physical theories of the early XX century (quantum mechanics and relativity), as indicated by Einstein's remarks about the relevance of non-integrability in quantum systems [Sto05]. fundamental results in nonlinear dynamics were achieved as the two Poincaré's insights mentioned above were further developed: The structural stability of integrable systems was proved at the beginning of the second half of the XX century as a result of the so-called KAM theory, named after the methods used by Kolmogorov, Arnold, and Moser to deal with the problem of small denominators (see Sec. 2.1.2); The existence of chaos can be proved by the homoclinic (or heteroclinic) intersection of manifolds of periodic orbits using the Melnikov method (see Sec. 2.1.3). However, so far the existence of non-negligible chaotic regions (with positive measure in the phase space) have been proven to exist only in a few (non-generic) systems, such as fully hyperbolic systems (Anosov systems, cat map, baker map) [Ott02], Sinai and stadium billiards (see Sec. 4.1), and piecewise-linear maps (see Sec. 5.1). Many properties of the chaotic motion (e.g., entropies and Lyapunov exponents) can be analytically calculated or estimated through periodic orbits [Dor99]. The extension of these mathematical methods to the more realistic class of non-hyperbolic systems is a field of intense research. The difficulty of proving or quantifying analytically the existence of chaos in realistic systems does not extend to numerical simulations and experiments, where chaos is regularly observed. This is well illustrated by the problem of existence of chaos in nonlinear area-preserving maps (e.g., in the standard map[2]): despite the mathematical difficulties of proving it, numerical simulations show convincing results that chaotic trajectories fill large portions of the phase space when non-linearity is increased [LL83, Ott02]. The intricate interplay between results achieved using formal and numerical methods is one central element in the modern investigation of nonlinear

---

[2] The standard map, also called (Taylor-Greene-)Chirikov map, is a paradigmatic area-preserving map defined in Eq. (2.14) below that will be used throughout this Thesis. See also Refs. [LL83, Ott02, Zas91].

dynamics, and contributes to make this such a fascinating field. In this Thesis profit is taken from the combination of mathematical results, numerical simulations, and qualitative models, what provides a much richer understanding of Hamiltonian chaotic dynamics.

The distinction between regular and chaotic **motion** emphasized above does not apply to **systems**, since both kinds of motion can coexist for different initial conditions of the same system. Indeed, it is nowadays widely accepted that typical Hamiltonian systems are neither completely regular (integrable) [SM70] nor completely chaotic, but rather show the coexistence of both kinds of motion in independent invariant components of the phase space. How does the chaotic dynamics in a Hamiltonian system with such a *mixed phase space* look like? Since chaotic and regular trajectories are separated in the phase space one could expect that chaotic trajectories would behave **inside** its component like those of strongly chaotic (hyperbolic) systems mentioned above. However, numerical simulations show that one remarkable difference occurs when chaotic trajectories approach the border of a region of regular motion: they spend a long time close to the *regular island* before visiting again other parts of the *chaotic sea*. In other words, such trajectories *stick* to the islands. Such phenomenon is called *stickiness* and is the main subject of this Thesis. It is important to note that due to ergodicity of the chaotic component[3] on average a trajectory does not spend more time near islands than in any other region of equal volume of the same chaotic component of the phase space. However, ergodicity does not provide any information about the **order** in which the trajectory visits the phase space. The stickiness effect is thus characterized by the long **successive** time it spends near a sticky region. During this time trajectories perform almost periodic motion in contrast to the stronger chaotic motion when away of islands. Hamiltonian chaotic trajectories show thus *intermittency* between periods of regular motion and irregular bursts sharing thus similarities with other important physical systems such as turbulent flows and one-dimensional intermittent maps. Generally speaking, the stickiness is defined by an asymptotic algebraic distribution of the regular periods.

The phenomenological description presented above interprets the Hamiltonian chaotic dynamics as an intermittent process where the stickiness phenomenon has a fundamental status. Such interpretation is supported and expanded by the results of this Thesis. The investigation of this phenomenon is thus justified on purely theoretical grounds. Not surprisingly, stickiness has a strong influence on all quantifications of chaotic dynamics such as Lyapunov exponents, decay of correlations, and transport properties. Relevant effects of stickiness are thus expected to appear as often as Hamiltonian chaos itself, and include virtually all previously mentioned areas of physics. As a straightforward application one can mention the chaotic scattering problems in both macroscopic (e.g., fluids and astronomical objects) or microscopic (e.g., atoms and electrons) systems: the trajectories that survive for a long time in the scattering region are those stuck to regions of regular motion. Stickiness also impacts on other microscopic measurements and quantum mechanical properties (see Sec. 2.2.2). Additionally, stickiness has drastic influence on the violation of strong chaotic properties which are assumed in both fundamental theories and calculation procedures (see Sec. 7.1). For instance, the long-term correlations due to stickiness may lead to anomalous transport, i.e., nonlinear growth of the mean squared displacement of an ensemble of trajectories (see Sec. 6.2). This effect has been numerically studied in different Hamiltonian systems and experimentally observed in a fluid experiment [SWS93] (see Sec. 6.3).

Since the first direct numerical observations of stickiness during the 1970's [Con71] and early 1980's [Kar83, CS84], different models and theories addressing specifically the problem of stickiness in generic two-dimensional maps have been developed [MO85, CS99, Zas02a] (Sec. 2.2).

---

[3]It is assumed here that the Hamiltonian system is closed and that the chaotic component where the referred trajectory is initiated has positive hyper-volume of the phase space (Liouville measure).

The *stickiness problem* can be stated as follows: how the dynamical properties of the chaotic trajectories are related to the properties of the invariant non-chaotic sets of the phase space? Or in other words, how the relaxation towards equilibrium in one chaotic component of the phase space depends on the properties of different regular components in its vicinity? Different conflicting claims of universality without convincing numerical verifications emphasize the difficulty of this problem, which is related to the complex phase-space configuration of the maps. This Thesis studies the phenomenon of stickiness of chaotic trajectories in Hamiltonian systems in different classes of systems with an increasing level of complexity. It starts from the simplest case of zero measure sets in ergodic systems (Chap. 4), passes through systems with sharply-divided and hierarchical phase spaces (Chap. 5), and finally explores noise perturbed (Chap. 6) and high-dimensional systems (Chap. 7). Considering the results as a whole, the Hamiltonian chaotic dynamics is seen from a novel perspective. Intermittency due to the stickiness close to regular components is not restricted to the case of hierarchical area-preserving maps but appears as a generic phenomenon of nonlinear Hamiltonian systems.

About this thesis

The present Thesis is a result of the studies performed at the Max Planck Institute for the Physics of Complex systems in Dresden (Germany) between April 2004 and December 2006 under the supervision of Prof. Dr. Holger Kantz. It has been supported through a DAAD (Germany) / CAPES (Brazil) project with a CAPES fellowship (project number BEX1073/03). Part of the scientific results contained in this Thesis are published in Refs. [AK05, AMK05, AMK06, AK07], which are cited in the corresponding sections of the Thesis[4]. A more detailed introduction to the topics of this Thesis is provided in Chap. 2 and Sec. 3.1, while starting from Sec. 3.2 mainly original results are presented.

The description of the contents of the chapters follows. The general motivation and detailed contents of each chapter can be found in its first paragraph. The basic results of Hamiltonian systems and a brief survey of the literature are presented in Chap. 2. In Chap. 3 the statistical method used to quantify the stickiness phenomenon is introduced: the statistics of Poincaré recurrence times. Its relation to correlation functions and to the power spectrum is discussed and compared to the recurrence time analysis in long-range correlated time series. The study of Hamiltonian systems starts in Chap. 4 with the simple case of stickiness to one-parameter families of marginally unstable periodic orbits, in which case the stickiness exponent $\gamma = 2$ is deduced. It is shown that circular-like billiards (e.g., mushroom and annular billiards) typically have an infinite number of such families. In Chap. 5 it is shown that the previous results explain more generally the stickiness in systems with sharply-divided phase space. The transition to the generic hierarchical phase space is discussed and illustrated. The effect of additive noise perturbations to the stickiness, and consequently to the transport properties, is discussed in detail in Chap. 6. The problem of stickiness in higher-dimensional systems is approached in Chap. 7 by systematically studying the influence of the dimensionality in a paradigmatic model of coupled two-dimensional maps. A summary of the main conclusions, an outlook, and a list of open questions appear in Chap. 8. Appendix A reviews the continued-fraction representation of real numbers and basic results of number theory. Appendix B presents some ideas on how to couple symplectic maps with time scale separation and provides a relevant application of the stickiness results of Chaps. 6 and 7.

---

[4]Further publications by the author during the PhD period *not* included in this thesis are [AHK06, ACP06, HAHK07].

Chapter 2

Dynamics in Hamiltonian systems

Basic and fundamental results on Hamiltonian systems are revised. Section 2.1 describes the basic structures and invariant sets of the phase space, which are nowadays well understood. Section 2.2 addresses the more difficult problem of the dynamics in such a phase space. In particular, the behavior of chaotic trajectories and the basic models of stickiness are discussed

2.1 Invariant components of the phase space

2.1.1 Basic notions and properties of Hamiltonian systems

A *Hamiltonian system* with N *degrees of freedom* is a dynamical system defined by a scalar function $H(\boldsymbol{p}, \boldsymbol{q},t)$ – the *Hamiltonian* – of $2N$ pairs of conjugate variables (q_i, p_i), which define the phase space Γ. The dynamics is defined through

$$\begin{aligned} \dot{\boldsymbol{p}} &= -\partial H/\partial \boldsymbol{q}, \\ \dot{\boldsymbol{q}} &= \partial H/\partial \boldsymbol{p}, \end{aligned} \tag{2.1}$$

where the dot indicates derivative with respect to time d/dt. Time discrete systems (maps) $(\boldsymbol{p}, \boldsymbol{q}) \mapsto (\boldsymbol{p}', \boldsymbol{q}')$ can be defined in a similar way through the generating function $F(\boldsymbol{q}', \boldsymbol{p})$ and the (implicit) relations

$$\boldsymbol{q} = \frac{\partial F}{\partial \boldsymbol{p}} \ \text{ and } \ \boldsymbol{p}' = \frac{\partial F}{\partial \boldsymbol{q}'} \tag{2.2}$$

From a broader perspective, Hamiltonian systems are *symplectic* dynamical systems meaning that not only the macroscopic volume of the phase space is preserved (the Liouville theorem) but also microscopic areas. For a map $(\boldsymbol{p}', \boldsymbol{q}') = \boldsymbol{M}_N(\boldsymbol{p}, \boldsymbol{q})$, the symplectic condition is written explicitly as [Ott02]

$$\boldsymbol{S}_N = \left(\frac{\partial \boldsymbol{M}_N}{\partial \boldsymbol{x}} \right)^{\dagger} \boldsymbol{S}_N \left(\frac{\partial \boldsymbol{M}_N}{\partial \boldsymbol{x}} \right). \tag{2.3}$$

where $\left(\frac{\partial \boldsymbol{M}_N}{\partial \boldsymbol{x}} \right)_{i,j} = \left(\frac{\partial M_j}{\partial x_i} \right)$ is the Jacobian matrix, $\boldsymbol{x} = (q_1, ..., q_N, p_1, ..., p_N)$, $\dagger$ indicates transposition, and

$$\boldsymbol{S}_N = \left(\begin{array}{cc} \boldsymbol{0}_N & -\boldsymbol{I}_N \\ \boldsymbol{I}_N & \boldsymbol{0}_N \end{array} \right), \tag{2.4}$$

is the symplectic matrix, which is composed by identity matrices $\boldsymbol{I}_N$ and null matrices $\boldsymbol{0}_N$ of order N. Particular properties of Hamiltonian systems follow from its symplectic character, e.g., non-existence of attractors (due to volume conservation), for each Lyapunov exponent there is

one with opposite sign, and if λ is an eigenvalues of the Jacobian matrix $\lambda, 1/\lambda, \lambda^*, 1/\lambda^*$ also are. This last condition is specially restrictive in the case of two-dimensional (area-preserving) maps ($N = 1$): eigenvalues calculated at periodic orbits lie either in the imaginary circle $|\lambda_{1,2}| = 1$ being thus stable (elliptic) or on the real axis $\lambda_1 < 1 < \lambda_2$ being thus unstable (hyperbolic or hyperbolic with reflection). The border case $\lambda_1 = \lambda_2 = 1$ is marginally stable (parabolic).

Invariant measure: The quantification of sets in the phase space is done mathematically rigorously defining a measure μ of the phase space which is a non-negative and countably-additive function defined in a bounded region R [Ott02, dA92, CFS82]. For a map $x \mapsto M(x)$ a measure is called *invariant* under the map if $\mu(E) = \mu(M^{-1}(E))$ for any measurable set $E \in R$. Similarly, a measure is invariant under a flow φ^t if $\mu(\varphi^t(E)) = \mu(E)$ for all times t. The measure $\mu(R)$ is called *ergodic* if it can **not** be written as the composition of different invariant measures. In this case the temporal average of some function of the phase space variables $\bar{f}(\boldsymbol{I}, \boldsymbol{\theta})$ of a single typical trajectory equals the ensemble averages $\langle f(\boldsymbol{I}, \boldsymbol{\theta}) \rangle$ along the invariant measure

$$\bar{f}(\boldsymbol{I}, \boldsymbol{\theta}) = \lim_{t^* \to \infty} \frac{1}{t^*} \int_0^{t^*} f(\boldsymbol{I_0}(t), \boldsymbol{\theta_0}(t)) dt = \int_R f(\boldsymbol{I}, \boldsymbol{\theta}) d\mu = \langle f(\boldsymbol{I}, \boldsymbol{\theta}) \rangle. \tag{2.5}$$

For closed Hamiltonian systems (where the phase space coordinates remain bounded) the natural invariant measure is given by the volume of the phase space the Liouville measure which is denoted by Γ. Hereafter Γ(phase space) $= 1$ is assumed. A **system** is called ergodic if the Liouville measure over the full phase space is ergodic. As will be argued below, this is not the case of typical Hamiltonian systems where the phase space can be decomposed into different invariant components with positive measure. Numerical simulations strongly indicate that a single chaotic trajectories typically fills regions of positive phase-space volume meaning that the Liouville measure is ergodic in the chaotic component of the phase-space. For the quasi-periodic trajectories, an ergodic measure can be defined as a delta function of Γ.[1] It is straightforward to apply most of the results of this Thesis to open systems (e.g., scattering problems), i.e., systems where the phase-space coordinates are unbounded. However, in this case the mathematical treatment is more cumbersome since one cannot speak about invariant components.

Invariant of motion: A function $F(\boldsymbol{p}, \boldsymbol{q}, t)$ is an invariant (constant) of motion if

$$\frac{dF}{dt} = 0 = \frac{\partial F}{\partial \boldsymbol{p}} \frac{\partial \boldsymbol{p}}{\partial t} + \frac{\partial F}{\partial \boldsymbol{q}} \frac{\partial \boldsymbol{q}}{\partial t} + \frac{\partial F}{\partial t} = \frac{\partial F}{\partial \boldsymbol{q}} \frac{\partial H}{\partial \boldsymbol{q}} - \frac{\partial F}{\partial \boldsymbol{p}} \frac{\partial H}{\partial \boldsymbol{p}} + \frac{\partial F}{\partial t} =: \{F, H\} + \frac{\partial F}{\partial t},$$

where the last equality defines the *Poisson bracket* $\{., .\}$. In the usual case when H is independent of t, F is an invariant of motion if and only if $\{F, H\} = 0$.

The existence of invariants of motion reduces the effective dimension of the dynamics, e.g., if there are M invariants of motion the dynamics occurs in a $2N - M$-dimensional manifold. The effective dimension of the system can be explicitly reduced if a canonical transformation of variables $(\boldsymbol{p}, \boldsymbol{q}) \mapsto (\boldsymbol{I}, \boldsymbol{\theta})$ is found. $(\boldsymbol{I}, \boldsymbol{\theta})$ are called action-angle variables. Such transformations preserve the Hamiltonian character of the system and are also defined through the generating function $S(\boldsymbol{I}, \boldsymbol{q}, t)$, where Eq. (2.2) apply, and the Hamiltonian is written as

$$H(\boldsymbol{I}, \boldsymbol{\theta}, t) = H(\boldsymbol{p}, \boldsymbol{q}, t) + \frac{\partial S}{\partial t} \tag{2.6}$$

Integrable system: A Hamiltonian system is called (completely) integrable if the two following properties hold [Ott02]: (i) it has N invariants of motion independent of each other, i.e., F_i cannot be written as a function of the F_j, for any $j \neq i$; (ii) the N invariants of motion

---

[1]In a $2N$-dimensional phase space the invariant tori have usually dimension N (see Sec. 7.2.2). The integral over all δ-functions has a positive Liouville measure corresponding to the area of the island.

are in involution: $\{F_i, F_j\} = 0$ for each i, j. In this case the Liouville-Arnold theorem (see, e.g., [dA92]) guarantees that a canonical transformation $S(\boldsymbol{I}, \boldsymbol{q}, t)$ exists such that Eq. (2.6) is written as $H(\boldsymbol{I}, \boldsymbol{\theta}, t) = H(\boldsymbol{I})$. Using (2.1), this leads to the following equations of motion

$$\begin{aligned}\boldsymbol{I} &= \text{const.}\\ \boldsymbol{\theta} &= \boldsymbol{\omega}(\boldsymbol{I})t.\end{aligned} \tag{2.7}$$

The frequencies $\boldsymbol{\omega} = \{\omega_1, ..., \omega_N\}$ are usually irrationally conjugated, Eq. (2.7) describes a quasi-periodic motion on a torus of dimension N (a circle for $N = 1$, a usual torus for $N = 2$, etc.). In appropriate coordinates the motion of completely integrable systems is thus trivial. The (nontrivial) task in this case is to find the N invariants of motion and the appropriate canonical transformation. The class of integrable systems include, e.g., one-dimensional systems, 2-particle systems subjugated to a central force, harmonic oscillators, and rotation of rigid bodies.

2.1.2   The fundamental problem of classical mechanics and the KAM solution

Once the case of integrable systems is clarified, one natural step is to look at *near-integrable* systems

$$H(\boldsymbol{I}, \boldsymbol{\theta}) = H_0(\boldsymbol{I}) + \varepsilon H_1(\boldsymbol{I}, \boldsymbol{\theta}), \tag{2.8}$$

where ε is a small perturbation parameter. Poincaré called this *the fundamental problem of mechanics* [Poi92, BG96]. A first guess would be that solutions of the near-integrable system (2.8) resemble those of an integrable one (2.7) meaning that integrable systems are structurally stable. This turns out to be true for the majority of the solutions, which is the most prominent result of the KAM theory discussed in this section.

Formally, the assumption of structurally stability of integrable systems means that small perturbations do not change the integrable character of the Hamiltonian. In this case there exist a transformation of variables $S(\boldsymbol{J}, \boldsymbol{\theta})$ where Eqs. (2.2) and (2.6) apply so that in the new variables $(\boldsymbol{J}, \boldsymbol{\phi})$ the system has again the trivial dynamics of Eq. (2.7). In accordance to Eq. (2.8), the problem is approached perturbatively and the desired transformation is written as

$$S(\boldsymbol{J}, \boldsymbol{\theta}) = \boldsymbol{J}.\boldsymbol{\theta} + \varepsilon S_1(\boldsymbol{J}, \boldsymbol{\theta}) + O(\varepsilon^2). \tag{2.9}$$

Assuming that H_1 is periodic in the angles $\boldsymbol{\theta}$, H_1 and S_1 are expanded in Fourier series

$$\begin{aligned}S_1(\boldsymbol{J}, \boldsymbol{\theta}) &= \sum_{\boldsymbol{m}} S_{1m}(\boldsymbol{J}) \exp(i\boldsymbol{m}.\boldsymbol{\theta}),\\ H_1(\boldsymbol{J}, \boldsymbol{\phi}) &= \sum_{\boldsymbol{m}} H_{1m}(\boldsymbol{J}) \exp(i\boldsymbol{m}.\boldsymbol{\phi}).\end{aligned} \tag{2.10}$$

Introducing the relations above in Eq. (2.6) one arrives after straightforward calculations [dA92, Ott02] at

$$H(\boldsymbol{J}, \boldsymbol{\phi}) = H_0(\boldsymbol{J}) + \varepsilon\left[H_1(\boldsymbol{J}, \boldsymbol{\phi}) + \boldsymbol{w}(\boldsymbol{J}).\frac{\partial S_1(\boldsymbol{J}, \boldsymbol{\phi})}{\partial \boldsymbol{\phi}}\right] + O(\varepsilon^2). \tag{2.11}$$

If the system is integrable, Eq. (2.11) depends only on $\boldsymbol{J}$, i.e, the terms depending on $\boldsymbol{\phi}$ must vanish for all orders ε. Using the Fourier expansions (2.10) the first order in ε in Eq. (2.11) vanishes if

$$S_1(\boldsymbol{J}, \boldsymbol{\theta}) = i \sum_{\boldsymbol{m} \neq 0} \frac{H_{1\boldsymbol{m}}(\boldsymbol{J}, \boldsymbol{\theta})}{\boldsymbol{m}.\boldsymbol{w}} \exp(i\boldsymbol{m}.\boldsymbol{\phi}) \tag{2.12}$$

The convergence of the series (2.12) depends crucially on the denominator $\boldsymbol{m}.\boldsymbol{w}$: recall that $\boldsymbol{m}$ is a vector of integer numbers which assumes all possible combinations upon summation and $\boldsymbol{w} = \frac{\partial H_0(\boldsymbol{J})}{\partial \boldsymbol{J}}$ is the vector of frequencies of the unperturbed tori. It is obvious that for rationally conjugated frequencies (periodic orbits) the denominator vanishes (e.g., for $N = 2$

and $w_1/w_2 = p/q$, this happens for $m_1 = q$ and $m_2 = -p$) while for irrational frequencies it assumes arbitrarily small values increasing $|\boldsymbol{m}|$. This illustrates the problem of small denominators for the convergence of series, what was perhaps the fundamental problem of Henri Poincaré. In the case of Eq. (2.12) it is possible to proceed. Assuming that H_1 is an analytic function, the terms $H_{1\boldsymbol{m}}$ decay with $|\boldsymbol{m}|$ exponentially $H_{1\boldsymbol{m}} \sim \exp(-\lambda|\boldsymbol{m}|)$. For all irrational frequencies for which $\boldsymbol{m}.\boldsymbol{w}$ decays slower than exponentially the series (2.12) converges. In Appendix A some basic results of number theory and continued fractional representation of irrational numbers are reviewed. One finds that almost all (except zero measure sets) frequencies satisfy the Diophantine condition [Eq. (A.2)] and fulfill thus the convergence conditions of Eq. (2.12).

It remains, however, to be shown that this procedure works for the higher-order correction terms in Eq. (2.11). Put differently, one has to show that the series (2.9) is *not* a non-convergent asymptotic series. For this purpose more refined methods are needed, that are provided by the so called Kolmogorov-Arnold-Moser (KAM) theory. In general terms, the KAM method is applied at each iteration to the results of the previous iteration providing a convergence of order ε^{2n-1} after n iterations, in contrast to ε^n obtained by repeating the method sketched above. A faster convergence in each iteration is desired in order to guarantee that the stripe of convergence of the series, which is reduced after each iteration of the procedure, does not vanish in the limit $n \to \infty$ [dA92, AA89]. The KAM procedure can be seen as an extension of the Newton method of finding roots of functions [AA89]. More than a remarkable theorem, the KAM methods build a powerful tool to deal with small denominators in the investigation of structural stability of quasi-periodic motion. It applies not only to Hamiltonian systems (discussed here) but also to volume-preserving and reversible systems (see [Sev98, Sev03] and references therein)[2]. The main novelty of this method is that instead of searching for solutions for a particular initial condition, or trying to classify the geometry of the possible trajectories, in the KAM theory one concentrates in the structural stability of the quasi-periodic tori. Without giving further details, the results achieved through such a procedure are stated next.

Let us define (in general words) the concept of KAM stability [Sev03]: a Hamiltonian H_0 is considered *KAM stable* if for any sufficiently small perturbation H_1, the perturbed system (2.8) presents quasiperiodic invariant n-tori close to the unperturbed tori, and the measure of these tori goes to one when the perturbation goes to zero.

Systems that can be proved to be KAM stable have to satisfy mainly two hypothesis: (h-i) smoothness of the Hamiltonian H and (h-ii) non-degeneracy of the frequencies. This fact was proved for analytic H and systems satisfying either one of the following two nondegeneracy conditions:

$$\det \frac{\partial \boldsymbol{w}}{\partial \boldsymbol{I}} \neq 0, \text{ or } \det \left| \begin{array}{cc} \frac{\partial \boldsymbol{w}}{\partial \boldsymbol{I}} & \boldsymbol{w} \\ \boldsymbol{w} & 0 \end{array} \right| \neq 0. \tag{2.13}$$

The first condition is the usual twist condition while the second is restricted to a given energy shell[3]. Necessary and sufficient nondegeneracy conditions were recently discovered for analytic perturbations [Sev03]. The condition of analyticity can be relaxed to C^r systems (r-times continuously differentiable systems) provided $r > 2N$. In the case of area-preserving maps the optimal condition is $r = 3$ [Mei92, SM70]. The KAM theory is constructive, leading in some cases to system-specific estimations of values ε^* such that for any $\varepsilon < \varepsilon^*$ the system is KAM

---

[2]It is interesting to note that a picture of the phase space similar to the Hamiltonian one is found in dissipative time-reversible systems [RQ92, ACP06] and conservative non-Hamiltonian systems, which are ignored in this Thesis. One expects that similar stickiness phenomena take place on these systems.

[3]Non-degeneracy conditions are in some sense natural if one thinks that the frequencies increase (non-linearly) and independent from each other with the momentum. Nevertheless, generically one can expect that they are violated *locally* [ACP06, dCNGM96]. One important completely degenerate system is the harmonic oscillator, which is thus no-where KAM stable.

stable. The proof of KAM stability of analytical twist Hamiltonian systems mentioned above is also known as the KAM theorem.

2.1.3   Broken tori and chaotic components

For a broad class of near-integrable systems the KAM theory establishes that almost all tori survive small perturbations. However, all tori build as the union of periodic of same period are destroyed for arbitrarily small perturbation, i.e., one-parameter periodic orbits in Hamiltonian systems are generically not structurally stable. This poses the question of what happens to the remaining set of tori and for increasing perturbations. General answers to the previous question in arbitrary dimensions are rare, and the further description is restricted to the special case of twist area-preserving maps (continuous-time autonomous system with $N = 2$) for which the review [Mei92] provides a comprehensive summary of the known results. The twist condition (2.13) in this case states simply that the rotation number ($f = \omega_1/\omega_2$) is a monotonous increasing (or decreasing) function of the action I.

Additionally, for arbitrarily small perturbations there are resonances for all rational rotation numbers $f = p/q$, as discussed after Eq. (2.12). In the integrable case different initial conditions lead to different periodic orbits p/q. The union of all periodic orbits p/q cover the torus. For these orbits, the eigenvalues of the stability matrix are degenerate $\lambda_{1,2} = 1$ [properties of λ are mentioned after Eq. (2.3)]. Most of these orbits disappear for arbitrarily small perturbations, and only an even number of them (usually two) survive: half of the orbits are saddle points $\lambda_i \in \mathbb{R}$ and half of the orbits are elliptic $|\lambda_i| = 1$, in agreement with the Poincaré-Birkhoff theorem [dA92, Ott02]. A qualitative discussion of the picture around these points provide insights into the complex picture of Hamiltonian systems [Poi92]:

(i) Elliptic points (the resonances) are stable and thus nearby initial conditions create trajectories that circulate it in a quasi-periodic motion that build a more complicated torus (libration). Indeed, close to an elliptic point the picture is the same as in the near-integrable system described by Eq. (2.8). It is clear that this picture repeats in finer and finer scales leading to a hierarchical picture. Elliptic points may lose stability through bifurcation.

(ii) Hyperbolic points have a stable and an unstable direction: the set of all points that under forward (backward) iterations tend to the saddle point is called stable (unstable) manifold [Ott02] . Poincaré observed that the stable and unstable manifold of the same (different) orbit may intersect leading to homoclinic (heteroclinic) orbits [Poi92]. Homoclinic points are mapped again onto homoclinic points, showing that the manifolds intersect in an infinite number of points. In some cases, the existence of such intersections can be proved through Melnikov's method [dA92]. Transversal intersections lead to the existence of horseshoes (stretching and folding), the basic mechanism of chaos [dA92]. The picture is however much more complicated than the hyperbolic horseshoes (baker map) since embedded in the area of homoclinic intersections there are manifold tangencies and further elliptic points.

Invariant KAM-tori with irrational frequencies may be destroyed if they violate the Diophantine condition (A.2) or if the perturbation strength ε is increased. Despite the non-existence of the KAM-tori with a given rotation number f, it is shown that for twist area-preserving maps, quasi-periodic orbits of all frequencies exist [Mei92]: these quasi-periodic orbits do not build a smooth connected torus anymore but are confined to a fractal subset of the phase space, i.e, a cantor set [Mei92, Ott02]. These orbits can be seen as the survival of the KAM-tori and are called "cantorus". In the next section it will be argued that the chaotic dynamics is strongly influenced by the low flux through *cantori*.

2.1.4   A qualitative picture

Finally, the general picture of the phase-space of near-integrable Hamiltonian systems is presented, and it is argued to be valid in a much broader class of systems. The KAM theory shows that quasi-periodic trajectories are structurally stable and one expects it to cover regions of positive measure of the phase space $\mu(tori) > 0$. For the case of chaotic trajectories it is usually difficult to have rigorous results about its measure. On the other hand, there is overwhelming numerical evidence that an increase of the non-linear perturbations induces an increase of the chaotic region increases that has also positive measure. One says that such a system has *mixed phase space*. When the most irrational tori is broken [see Eq. (A.4)] chaotic trajectories assume any value of the action I and the KAM tori are restricted to resonances. One usually calls these resonances *regular islands* embedded in a *chaotic sea*. Typically both have positive measure. Consider now the border between the chaotic component and the regular island. For each island this is a well defined torus, which is called *boundary circle*, but around it the whole picture of near-integrable system is again observed: an infinite hierarchical sequence of islands-around-islands surrounded by cantori.

Even though many of the above statements are usually proved only in very special systems, this scenario is easily illustrated numerically in a large variety of systems. Here the standard map (also called Chirikov map) is used since it describes very generally the phase space around one resonance [LL83]. It is defined as

$$
\begin{aligned}
p_{n+1} &= p_n + K\sin(2\pi q_n) \quad &\mod 1, \\
q_{n+1} &= q_n + p_{n+1} \quad &\mod 1.
\end{aligned}
\tag{2.14}
$$

The parameter K plays the role of the perturbation strength ε of Sec. 2.1.2. Without loss of generality the control parameter $K = 0.45$ was used. Figure 2.1(a) shows the iteration of different initial condition of the map (2.14) where one dot was plotted at each point of the trajectory. A caricature of the picture with the notation used is given in Fig. 2.1(b). Many trajectories spread irregularly through the phase space building a single dotted region, the chaotic sea. Close to the center the trajectories regularly circle a central elliptic point, composing the *main island* (order 1). Around this island one *secondary* island chain of period 4 is seen (order 2). Further secondary resonances (order 2) are observed closer to the boundary circle, as shown in the inset (period 15 winding number 4). Close to the secondary islands additional island chains are observed (order 3), and so on.

Finally some qualitative arguments for the generality of such picture are collected and the alternative structures that may be present in the phase space discussed. First of all, one should mention that it has been proved that completely integrable systems are exceptional systems among the analytic Hamiltonian systems [SM70]. Even if one can say that hyperbolic systems (completely chaotic) are structurally stable, building thus "open sets" in the space of Hamiltonian systems, it is clear that the conditions for hyperbolicity are very restrictive and usually not fulfilled by typical Hamiltonian systems. Another way of looking at the near-integrable scenario is that one can define approximated local invariants of motion around one elliptic periodic orbit associated to the invariant tori. Far away from the periodic orbit this approximation becomes worse. This can be associated to a greater strength of the perturbation ε in Eq. (2.8). The size of the islands is not particularly important for our purposes since the stickiness phenomenon studied below occurs exactly at its border, where the near integrable results are valid as argued above. If on the one hand it seems clear that Hamiltonian systems (specially low-dimensional ones) have generically mixed phase space, on the other hand the properties of the regular islands and invariant tori may vary. Apart from the regular structures described above (also called KAM-islands or resonant-islands) a whole zoo of other structures may exist in the phase
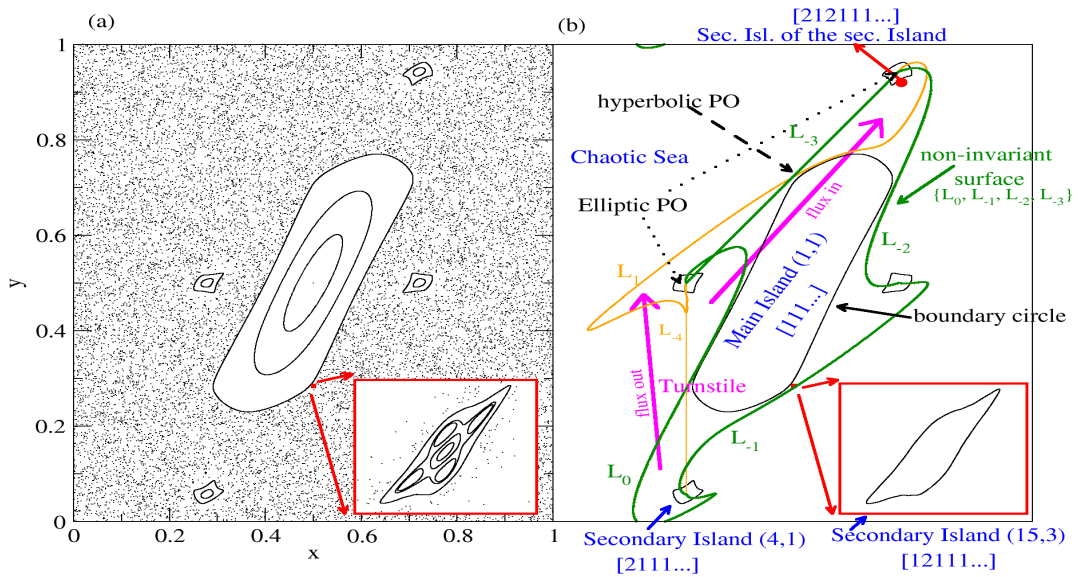
Figure 2.1: (Color online) (a) Phase space of a representative example of an Hamiltonian system with mixed phase space, the standard map (2.14) with $K = 0.45$. Inset shows an amplification close to the island. (b) Sketch of part (a) with the labels of the different structures of each structure. In parenthesis (q, n) the period and winding number of the island and in brackets its possible position in the Markov-tree model discussed in Sec. (2.2.3).

space. The violation of the twist condition (2.13) may lead to a different topological structure (locally) around the shearless torus [HH84, dCNGM96, dCNGM97] and to systems like the web-map [Zas91] that may have all tori broken for any small perturbation. The KAM theory also fails completely when the system cannot be written in a near-integrable form (as in Sec. 2.1.2) giving rise to phenomena like the nets and web tori emphasized in chapters 7 and 8 of Ref. [Zas05]. Additionally, there exist the so-called tangle islands, islands that appear inside the lobes created by the stable and unstable manifold of an hyperbolic point between two intersections. These islands may also appear hierarchically distributed in the phase space, as emphasized in Ref. [RKZ99], where the classification of different kinds of islands was proposed. These structures may coexist in the phase space and typically have different "sticky" properties [Zas02b].

In summary, near-integrable Hamiltonian systems have regions of chaotic motion – created through the heteroclinic intersection of manifolds – and regions of quasi-periodic motion – KAM tori similar to the integrable one and KAM islands. These regions coexist and build a mixed phase space, i.e., they exist for the same control parameter for different initial conditions. The hierarchical picture of near-integrable systems is expected to appear in generic Hamiltonian systems with mixed phase space near the border of regular regions and is the relevant scenario for stickiness. Nevertheless, islands with different properties may exist (or even coexist) in the phase-space.

2.2   Dynamics in the phase space

2.2.1   Basic properties

So far the phase space of Hamiltonian systems has been described: the invariant structures and their structural stability. This section focus on the dynamics of individual trajectories inside such a phase space. Nothing special is observed for the regular trajectories since quasi-periodic and periodic trajectories are conjugated to a simple rotation and are thus described by Eq. (2.7) [Ott02]. More interesting behavior is observed in the chaotic component where stickiness will be emphasized and related to the different properties of regular islands discussed in Sec. 2.1.4. For simplicity, again only closed Hamiltonian systems will be treated.

Perhaps the most basic and useful property of regular and chaotic Hamiltonian trajectories is their **recurrent** status. This is formally stated by the Poincaré recurrence theorem [Ott02, CFS82] that says that in a bounded Hamiltonian systems, given a set I of positive Liouville measure $\Gamma(I) > 0$, almost all trajectories $w \in I$ (except sets with zero Liouville measure) there exists a time T such that $M_T w \in I$, i.e., the trajectory returns to the vicinity of its initial condition. This property is further explored in the next Chapter and will be extensively used throughout this Thesis.

Specific properties of chaotic trajectories can be obtained analytically, e.g., for hyperbolic systems. In such systems all periodic orbits are hyperbolic (no elliptic point or KAM-tori exist) and the stable and unstable manifolds of such orbits cross transversally and completely split the phase space. For such systems many mathematical results have proved that there are **Lyapunov exponents** (exponential separation of close by trajectories), systems are **ergodic**, the **strong mixing property** is valid (bunch of initial conditions spread uniformly in the phase space), **correlation** decays exponentially, and there exists a complete symbolic dynamics (see Refs. [LL83, Dor99, Ott02] and references therein). Examples of such systems are the cat map, the baker map, and flows in geodesics with everywhere negative curvature. However, as argued in Sec. 2.1.4, the typical Hamiltonian systems are not hyperbolic but poses a mixed phase space. In this case, there is usually no proof of such mathematical results even though many similarities are expected for the dynamics restricted to the chaotic invariant component. Perhaps the key property of chaotic trajectories in such systems, absent in the case of hyperbolic systems, is the **stickiness phenomenon** discussed in the following section.

2.2.2   Stickiness

The previously discussed stickiness phenomenon is pictorially illustrated in Fig. 2.2 where one sees that the distance of a chaotic trajectory to the border of a regular island alternates between irregular fast oscillations at large distances and long periods of regular behavior at small distances. The distribution of events which became stuck for a time T, $P(T)$, is the fundamental measure of stickiness. Chapter 3 discusses carefully the different distributions used to measure this effect and defines formally stickiness as their slow decay. By now, it is sufficient to consider that the distribution of the laminar phases behaves for large T roughly as a power-law

$$P(T) \sim T^{-\gamma-1} \tag{2.15}$$

Figure 2.2b shows one numerically obtained example of such distribution plotted in log-log scale where scalings like in (2.15) appear as straight lines. It is clear that despite the overall power-law decay strong oscillations occur. For visualization purposes instead of $P(T)$ the integrated distribution $\rho(T > \tau) \sim \tau^{-\gamma}$ is plotted, i.e., the probability distribution of having one stickiness event with time T greater than τ. During the sticking time the trajectory performs an almost regular motion what motivates the analogy to intermittent systems. One intuitive idea about
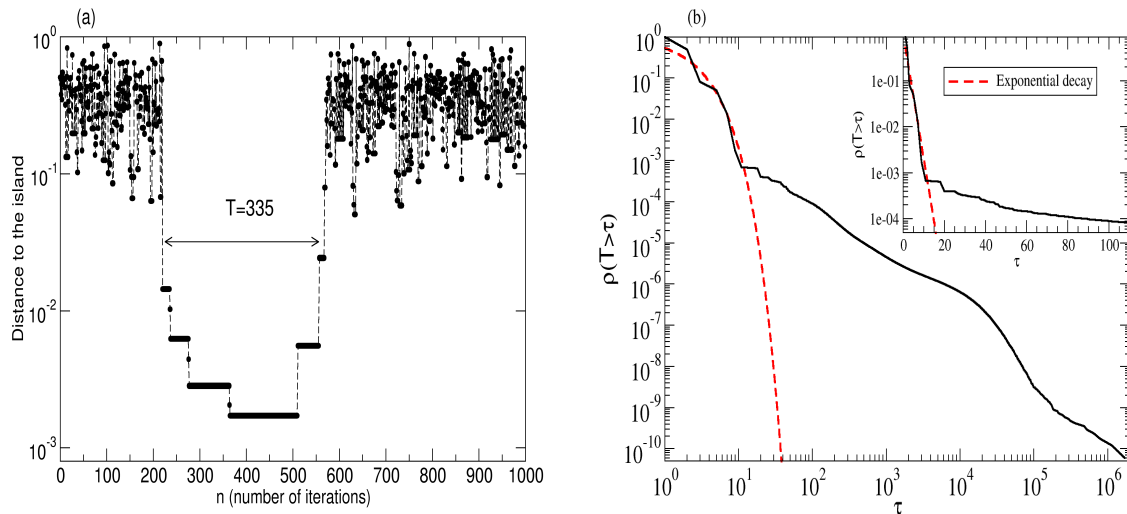
Figure 2.2: Illustration of the stickiness phenomenon that leads to an intermittent behavior of the chaotic trajectories. (a) The distance of one chaotic trajectory to the border of the regular island is plotted as a function of time for the area-preserving map discussed in Sec. 5.1. One stickiness event of size $T = 335$ is emphasized; and (b) the distribution of the sticking times T greater than τ (see Sec. 3.1.2) for the standard map (2.14) with $K = 0.52$ and 10^{11} iterations of a single trajectory. The main plot is in log-log scale while the inset is in linear-log scale, emphasizing the short-time exponential followed by a power-law like decay for long times.

the reasons for the stickiness is that the instability of chaotic trajectories (e.g., the local diffusion coefficient or the finite-time Lyapunov exponent) must approach *continuously* zero when approaching the boundary circle y_0 from outside: $D \sim (y - y_0)^\delta$. This idea will be further developed in Sec. (4.2) for a particular case.

Sometimes stickiness does not appear as a fundamental property on its own, but is studied in the context of transport properties in general [Wig91]. Another approach was to define properties of weak-mixing [Zas05] or pseudo-ergodicity [Zas02b] to deal with systems displaying stickiness. A description through fractional Fokker-Planck equation was also proposed for what was called *Strange Kinetics* [SZK93, Zas02a]. In this Thesis the perspective of stickiness as a fundamental property of individual chaotic trajectories is assumed. The main reason for this choice is that it preserves the intuitive aspect of the phenomenon. This is similar as describing chaos as Lyapunov instability of individual trajectories instead of speaking about properties of invariant sets. Moreover, pure ergodic theoretical arguments may be misleading since even zero measure sets (e.g., cantori and MUPOs) in contact with the chaotic component have strongly influence on the dynamics. Based on the topological properties of the phase space discussed in the previous section, different theories described below attempt to describe quantitatively the stickiness. A short chronological review of the main results is given next. The discussion is restricted to area-preserving maps (Hamiltonian flows with one and a half or two degrees of freedom) of the cylinder $T(x, y) \to (x, y)$ (x periodic) satisfying the twist condition (2.13). The higher-dimensional case will be investigated explicitly in Chap. 7, where the few references dealing with it will be mentioned.

The phenomenon denoted stickiness [Kar83, CS84] in this Thesis appears in the literature under different names such as: clinging [KG87a], dynamical trapping [Zas05, Zas02a], and stag-

nant motion [Aiz89]. Perhaps the first evidence of stickiness was obtained by Contopoulos in Ref. [Con71] where an astronomical model with mixed phase space was investigated numerically and the following situation was described near the boundary of the regular region:

> *"Orbits near this boundary may have many points on an empirically defined smooth curve on the surface of section. However, if we continue calculating points of intersection, we may see deviations from this curve, and these deviations very soon become important; ...It seems that as we approach the empirical boundary between the two regions, the number of points that do not deviate from an empirically defined curve increases abruptly, going presumably to infinity."*

But it was only more than ten years later that this phenomenon was explicitly explored in the inspiring Refs. [Kar83, CS84]. Stickiness was immediately accepted as a fundamental property of Hamiltonian systems and different works during the 1980's addressed this point and its consequence to fundamental properties of the system (Lyapunov exponents [KG87a], long-term correlations [CS84], and spectrum [GZR87]). Since then many different applications and consequences of stickiness were investigated. The onset of anomalous transport is perhaps the most prominent one [Kar83, ISM00, ZT91, ZK94], what will be discussed carefully in Sec. 6.2. Direct experimental observations of stickiness and anomalous transport were performed in fluid dynamics [SWS93, SWS94]. Stickiness manifests itself also in the survival probability of a quantum system up to the Heisenberg time [CMS99]. Microscopic and quantum manifestations of stickiness include both closed systems (e.g., the statistics of eigenstates [KHSW00]) and open systems [LBOG92, CGM00, HKL00]. Stickiness was used to explain the observed magnetoresistence of 2D anti-dot arrays [FGK92] and to predict fractal conductance fluctuations in cavities [Ket96], later observed experimentally [Nar96, SKG$^+$98]. In all these cases important observable quantities are related to the stickiness and the exponent γ appearing in Eq. (2.15) plays an important role. A deeper understanding of stickiness and a theory for the exponent γ are thus highly desirable.

2.2.3   Flux through cantori and the Markov-tree model

The first idea to build a theory of stickiness was to use the at that time recently discovered cantori to define partial barriers to the transport of trajectories. By calculating the flux through a single cantorus and by using the scaling properties of the cantori close to the islands one arrives at the Markov-tree model of stickiness [MO85, MO86]. Following Refs. [Mei92, MO86], where more details can be found, the main ideas of this model are sketched below and illustrate the main components of the problem of stickiness in the hierarchical phase space.

Flux is the area (volume) per unit of time that crosses from one side of a non-invariant surface in phase space to another. Initially the calculation of the flux through a surface passing through a sequence of periodic orbits is calculated. It is known from the Poincaré-Birkhoff theorem that there are at least two families of periodic orbits for each frequency m/n: the hyperbolic (minimax) and the one which were born as elliptic (minimizing). The following procedure, illustrated in Fig. 2.1b, defines a (non-invariant) surface and estimates the flux through it: join with an arbitrary curve $\mathfrak{L}_{\mathbf{o}}$ two successive minimizing orbits passing through the middle minimax orbit; the union of the $n-1$ past iterations of this curve define a surface; the first iteration $\mathfrak{L}_{\mathbf{1}}$ intersects this surface in (at least) the three periodic orbits, defining two regions of equal area in a kind of figure-of-eight (the so-called turnstile); this areas are, by construction, mapped inside and outside the surface each iteration, defining thus the flux $\mathfrak{F}$. It can be shown that the flux, irrespective of the curve $\mathfrak{L}$ chosen above, can be obtained directly from the Hamiltonian [or from

the definition of the symplectic map as in Eq. (2.2)] as the difference in action W between the minimax and minimizing orbit:

$$\mathfrak{F} = \Delta W_{(m,n)} = W_{(m,n)}(minimizing) - W_{(m,n)}(minimax). \qquad (2.16)$$

One can obtain the flux through cantori by similar reasoning. For practical calculation, the quasi-periodic cantorus is approached by a sequence of periodic orbits m_j/n_j. This approach is optimal (closer for each j) through the use of continued fraction expansions (see Appendix A). The flux through an invariant circle is obviously zero, and it can be proved that it is a continuous function on the irrationals, i.e., the flux on the cantori close to the invariant torus decrease to zero when approaching it. It turns out that the flux through the cantori with most irrational frequencies correspond to local minima of the flux. This occurs when the frequencies belong to the noble numbers (see Appendix A).

Markov-tree model

The noble cantori are thus used to define "Markov states" close to the invariant tori with frequency ν_0. The bigger resonances close to the last torus are given by the convergents (rational approximations) of the frequency of the last torus. Due to the twist condition [see Eq. (2.13)], the frequencies are ordered in the phase space increasing (or decreasing) monotonously with the distance to the torus. The area between two consecutive noble cantori are chosen to define one state. This procedure leads to a countable infinite sequence of states. In each state there is typically one additional secondary island (at the resonance used to define the state), for which the procedure described above is repeated. Starting from the chaotic sea, an arbitrary exit region away from islands, the following labeling procedure is adopted: each state reached through a step approaching the principal resonance receives a number $\sigma_i = 1$ (different *level*) while each state approaching a secondary island receives the number $\sigma_i = 2$ (different *class*). All states can thus be labeled as

$$S = [\sigma_1, \sigma_2, ..., \sigma_N],$$

where $\sigma_i = 1$ or $\sigma_i = 2$. A sketch of this labeling is illustrated in Fig. 2.1(b) where the labels appear in brackets [...]. Note that the islands (actually their border) are reached only after an infinite sequence of states which end with $[1, 1, 1, 1..]$. The "order" of the island chain referred in Sec. 2.1.4 correspond to the number of "$\sigma_i = 2$" (minus 1) it has. Note also that this division of the phase space in states is complete, i.e., all chaotic components of the phase space belong to some state.

An important assumption of this model is that the time the trajectory spends inside one state is large compared to the mixing time inside it. The dynamics is thus assumed to be Markovian *between* states, i.e., transitions between states occur with a given probability $p_{S \to S'}$ independent of the past. In addition only transitions between neighboring states are allowed. In this case, the picture of the sticky motion of the trajectory close to the island correspond to a random-walk in a binary tree: at each state the trajectory may step to the next state approaching the main island or may step into the state related to the secondary island, or may step back. The corresponding transition probabilities are given by

$$p_{S \to S'} = \Delta W_{S,S'}/A_S,$$

where $\Delta W_{S,S'}$, given by (2.16) is the flux through the cantorus in the border between states S and S', and A_S is the total area of state S. Denote DS the state just above S. It is important to know how the probabilities of stepping to a new class (index 1) or level (index 2) depend on the areas and times associated to each state. The self-similar characteristics of the above

picture motivates the use of results from renormalization theory to determine these scalings asymptotically, which can be resumed in the following scaling factors

$$\epsilon_1 = \frac{w_1}{a_1} = \frac{\Delta W_{S,S1}/\Delta W_{DS,S}}{A_{S1}/A_S} \text{ and } \epsilon_2 = \frac{w_2}{a_2} = \frac{\Delta W_{S,S1}/\Delta W_{DS,S}}{A_{S2}/A_S}$$

The factors ϵ correspond to time scales (e.g., time to encircle some chain of islands) and the factors a corresponds to the scaling of area (e.g., the area between noble cantori or of chain of islands). The results for the case of noble frequencies are especially simple due to its simple continued fraction expansion. It is also reasonable to apply this result in our problem since the boundary circle are usually not far from noble. The estimation of the scaling factors of the class scaling follow from similar procedures, but are less precise due to the lack of reasoning for the universality of the "island-around-island" structure.

The final step is to solve the problem of the survival probability $\rho(t)$ of a random walker in such a tree, which is given by an integral equation in the continuous time approximation [$\rho(t)$ is directly related to the measured $\rho(T)$ in Eq. (2.15)]. Taking its Laplace transformation, the asymptotic time dependence of the survival probability is given by its singularity with smallest real part. Since an exponential decay is not expected neither in the case of stickiness nor for a random walk in an infinite tree, one assumes that this singularity is indeed a branch point which yields a power-law with exponent $\rho(t) \sim t^{-\gamma} f(ln(t))$. The value of γ is finally given by solving

$$w_1 \epsilon_1^{-\gamma} + w_2 \epsilon_2^{-\gamma} = 1, \tag{2.17}$$

that would have more terms of similar forms in the case of trees with more branches (e.g., different chains of secondary island at each level). Inserting the values of the scaling factors w_i, ϵ_i obtained through renormalization theory one obtains the value of $\gamma = 1.96$. This exponent is smaller than the exponent $\gamma = 3.05$ one gets by considering only the level scaling (chain model) [HCM85], but still higher than most of the numerical simulations. However, the comparison with numerical data has to be done very carefully in order to determine if for the times obtained the trajectory already explored the Markov tree sufficiently deep so that the results of normalization theory apply. Further difficulties are the log-periodicities that have a strong effect for small times.

The Markov-tree model, an improvement of the chain models, remains perhaps the most refined and solid model of stickiness. Further refinements can be incorporated, like the existence of other chains of secondary islands at each state, or the existence of other types of sticky islands and structures, provided it is known how they scale in the phase space. Some noteworthy simplifications are related to the Markov assumption *within* each state and the "believe" in the existence of universal renormalization results in the phase space of Hamiltonian systems. Further criticism appear in Chap. 5 of Ref. [Wig91] where, e.g., it is argued that the turnstiles of one state may penetrate further states. At the end of the next section one generalization of the Markov-tree that incorporates many of this criticisms and shows promising results will be discussed [CK].

2.2.4   Universality of the exponent γ and the stickiness problem

The 20 years old Markov-Tree model remains one of the deepest models of stickiness providing a framework where different effects can be included. Through the 1990's, the stickiness picture was changed by the exploration of different scenarios and by different associations to statistical physics. For instance, the previous results on anomalous transport [Kar83, GZR87] were related to continuous time random walks and Lévy flights [SZK93, Zas02a, ZK94, KSZ96]. Furthermore,

the consequences of the slow relaxation on the statistical mechanical approach to thermodynamics was explored in Ref. [Zas99]. A general approach to the problem is substantially motivated by the studies of G.M. Zaslavsky and collaborators, summarized in Refs. [Zas02a, Zas05]. In these works one finds, besides a novel fractional kinetic description of transport, the study of stickiness in a rich variety of systems, not restricted to the Hamiltonian picture described above. Some of the structures in the phase space are mentioned at the end of Sec. 2.1.4 and lead to different trapping phenomena proposed in Ref. [Zas02b].

Regarding the stickiness exponent γ, the picture that arises from the different works mentioned above contrast with the claims of universality drawn by Chirikov and Shepelyansky [CS99]. In this paper a simple renormalization approach for the level scaling is used to predict an universal exponent $\gamma \approx 3$. In this context one should mention the very instructive papers [WHK02a, WHK02b] that show numerically the limitation of the models considered in Ref. [CS99] and in Ref. [Zas02a] even for the particular parameters considered in these works, i.e., at the breakdown of the last torus and when self-similar islands-around-islands are observed and, respectively. Interestingly, the authors of Refs.[WHK02a] demonstrate that neither level scaling (approaching the main islands) nor class scaling (approaching other secondary islands) *alone* are enough to describe the stickiness process restating thus some of the key ideas of the Markov-tree model. What is observed numerically for the distribution of laminar phases (2.15)? As illustrated in Fig. 2.2b, the existence of a "power-law like" behavior is ubiquitous but different oscillations are usually observed what makes a fit of γ over more than two decades unfeasible. Despite the claims of universality of γ and the deduction of values of γ in particular cases, no convincing universal behavior was observed numerically for individual systems (see next paragraph for some promising recent results). The few estimations of the times for which the universal exponent should be visible [Mur91, CS99] are usually quite large for any practical purpose. This leads to a more pragmatic point of view where finite time behaviors are considered on its own. In this spirit, an effective model was derived in Ref. [MdMGK05] and questions related to the finite-time behavior addressed in Ref. [Zas05]. This provides another argument in favor of discrete models (like the chain and tree models). If by one hand they have to have *infinite* number of states accumulating at the boundary circle, in order to describe systems which are continuous in space, on the other hand they may take into account the finite time oscillations observed numerically [MdMGK05, AMK06]. From the perspective of the discrete-state models, power-laws are seen as sums of an infinite number of exponentials (analogously, a branch point singularity can be thought to be built by an infinite number of poles).

A very recent (unpublished) work by Cristadoro and Ketzmerick [CK] provides convincing numerical and theoretical results indicating that an universal asymptotic exponent indeed exists for the systems with hierarchical phase-space. The idea was to generalize the Markov tree picture described above to a kind of stochastic tree, in the sense that the transition probabilities do not follow precise scalings but are randomly taken from fixed (unknown) distributions. The number of states that contribute for the stickiness at a given time increases with time and one expects that some self-averaging takes place. This was indeed observed by the authors of [CK] in the stochastic model. In order to verify their results in real Hamiltonian systems the following equivalence was proposed: the distribution of sticking times in individual systems for very long times is equivalent to the average distribution of sticking times over different generic systems. The reason for this analogy is that in both cases the distribution of sticking times is obtained as an average over many different states of the phase space. In this way a statistically significant result can be numerically obtained and the oscillations typically observed (as in Fig. 2.2b) are reduced. This is illustrated in Fig. 2.3, where simulations of 100 different standard maps (2.14) with an additional control parameter are shown. Each curve shows wild oscillations, as expected by the arguments above. However, the average over all maps displays
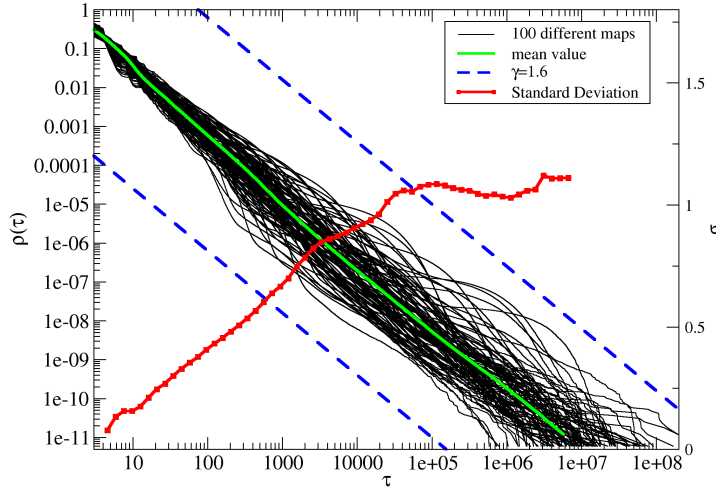
Figure 2.3: (Color online) Sticking time distribution $\rho(\tau)$ for 100 different standard maps (2.14) with a constant $K^\dagger$ added to the y equation: $K \in [0.5, 0.6], K^\dagger \in [0, 0.2]$. The central green (gray) curve is the average [for fixed $\rho(\tau)$] over all curves, and the red curve (axis on the right) corresponds to the standard deviation of the curves (for fixed $\rho(\tau)$ projected to the x-axis). The further parameters are equivalent to those of Fig. 6.1b below.

a very robust power-law decay. Moreover, the standard deviation around this mean increases for small times and seems to stabilizes for larger times, indicating that the deviations from the power-law behavior are bounded oscillations and not due to different power-law exponents. The scaling exponent obtained for the fitting is $\gamma = 1.60 \pm 0.05$ and is thus expected to be universal also for each individual system for sufficiently long time. These results are in agreement with similar simulations performed by Cristadoro and Ketzmerick in different area-preserving maps where the exponent was estimated to be $\gamma = 1.57$.

From the very first studies of stickiness the aim was to determine the existence of an universal exponent for the stickiness in area-preserving maps. Considering the different numerical experiments mentioned above as well as the different structures that may be present in the phase space (mentioned at the end of Sec. 2.1.4) one cannot even be sure whether a well defined power-law arises for long times. Inspired in Ref. [WHK02a], a re-stating of the problem in a general terms could be:

The **stickiness problem** *is to determine how the properties of the different structures in the phase space (Sec. 2.1) are connected to the dynamical properties of chaotic trajectories (Sec. 2.2), considering specifically their effect on the distribution (2.15).*

This is a fundamental question of Hamiltonian dynamics, for which this Thesis provides answers in specific but relevant cases.

Chapter 3

Recurrences

One of the fundamental properties of Hamiltonian systems is the recurrent character of trajectories in the phase space, as stated by the Poincaré recurrence theorem. In this chapter it is shown how the statistics of recurrence times can be used to characterize the stickiness phenomenon and how it is related to other important measures, e.g., decay of correlations and survival probabilities (Sec. 3.1). Additionally, this statistical tool is applied to time series and analogies to the case of Poincaré recurrences are explored (Sec. 3.2). In the case of long-term correlated time series, the numerical simulations suggest stretched exponential distribution shedding new light about the meaning of the power-law tails obtained in Hamiltonian systems.

3.1   Poincaré recurrence time

3.1.1   Origins and connection to stickiness

A recurrence in an Hamiltonian systems refers to the return of a trajectory to the vicinity of its initial condition in the pase space. The Poincaré Recurrence Theorem, stated in Sec. 2.2.1, ensures that in closed Hamiltonian systems this happens for almost all trajectories[1]. Poincaré actually used the recurrence property as a stability criterion, which he claims to be due to Siméon D. Poisson (1781-1840) [BG96], and interpreted his theorem as a proof of stability.

Poincaré's result became well known to the physics community due to the work of Ernst Zermello (1871-1953), who used it to criticize the (at that time newly born) statistical mechanical description of thermodynamics [Kac59, Zas99]. The arguments of the so-called "Zermello paradox" are fairly simple: if a thermodynamical system is described through the statistical properties of particles submitted to some potential one is dealing with a Hamiltonian system; according to the recurrence theorem, an infinite number of recurrences to the initial condition should be observed; since a recurrence in the phase space implies a recurrence of all possible observables, one has to expect returns of the value of the entropy to its initial state; this is in disagreement with the (empirically determined) second law of thermodynamics that states that the entropy increases monotonically in time. Boltzmann's solution of this apparent paradox contains no correction to this chain of arguments. However, he argued that the probability of a Poincaré recurrence is very small in such a high-dimensional system and that the second law of thermodynamics should be interpreted probabilistically. More concretely, he showed that the mean recurrence time of a typical thermodynamical system is many times larger than the age of the universe [Leb99]. The explicit calculation of the recurrence time represents an important

---

[1]Except trajectories that build zero measure sets, like, e.g., the stable and unstable manifolds of periodic orbits.

conceptual progress from Poisson's stability interpretation of recurrence. As it will be clear below, a further step is enough to quantify stickiness in an elegant way: to consider instead of the mean recurrence time, the statistics of recurrence times [CS84].

The connection to stickiness becomes evident considering the following procedure to determine the recurrence time in the $2N$-dimensional phase space Ω. Define a recurrence region $I \in E$ inside the chaotic component $E \in \Omega$, i.e., away of sticky regions. Consider $\mu(I)$ the invariant measure of the recurrence region [by convention $\mu(E) = 1$]. Start a *single* initial condition inside I and consider the time T between the exit and the first return to I. According to Poincaré recurrence theorem such a recurrence generally occurs and the procedure can be repeated, leading to an sequence of recurrence times $\{T_1, T_2, ..., T_M\}$, where M increases indefinitely with the observation time. The intuitive connection to stickiness is that a stuck trajectory will have longer T_i (consider Fig. 2.2a and a recurrence region far from the island). It is shown below that if the trajectory does not stick it returns exponentially fast and that in case of stickiness roughly algebraic distribution is observed. This shows that large recurrence times T are composed essentially by the time the trajectory remained stuck.

3.1.2 Recurrence time statistics

The recurrence time distribution $P(T)$ (RTD) is the distribution of the sequence $\{T_1, T_2, ..., T_M\}$, for $M \to \infty$. In continuous time $P(T)$ is a probability density function (PDF) and thus $P(T)dT$ is the probability of finding a recurrence time T_i between T_i and $T_i + dT_i$. There are two conditions that $P(T)$ satisfies: normalization

$$\int_0^\infty P(T)dT = 1, \tag{3.1}$$

and Kac's lemma [Kac47, Kac59]

$$\langle T \rangle = \int_0^\infty TP(T)dT = 1/\mu(I). \tag{3.2}$$

valid under the same hypotheses of the Poincaré recurrence theorem mentioned in Sec. 2.2.1 and $\mu(I)$ corresponds to the measure of the recurrence region. A small correction is needed in the case of small recurrence interval $\mu(I) \to 0$ and continuous time systems [Kac59], what is irrelevant in this Thesis. Indeed, mainly discrete time systems (maps or time series with finite sampling time) are used, in which case $T \in \mathbb{N}^*$ and integrals should be replaced by a sums in Eqs. (3.1)-(3.3). Kac's lemma [Eq. (3.2)] can be interpreted as an immediate consequence of ergodicity (or stationarity of a time series): the probability of finding a trajectory in the interval I is equal to the inverse of $\langle T \rangle$. This is similar to what is shown in Eq. (2.5), i.e., the trajectory spends on average equal times in equal volumes of the chaotic component of the phase space. It implies also that the mean recurrence time is uniquely defined by the measure of the recurrence region. Altogether, this shows that the stickiness phenomena is neither characterized by a longer time spend near the regular regions, nor by the mean recurrence time $\langle T \rangle$. Stickiness consists in a long **consecutive** time a trajectory spends near the islands and can be characterized by the tails of the RTD.

It is numerically convenient to use the distribution of the recurrence times greater than τ^*

$$\rho(\tau) \equiv \int_\tau^\infty P(T)dT, \tag{3.3}$$

also called cumulative recurrence time distribution or, hereafter, recurrence time statistics (RTS). It is a monotonous decreasing function of τ, starting at $\rho(0) = 1$ due to (3.1).

Examples of RTS

The RTS is calculated now for two simple processes in discrete time: (i) fixed return probability [Fel50, AdSC04] and (ii) simple random-walk [Fel50].

(i) Consider a random system that has a fixed recurrence probability μ at each time step, independent of time. After one recurrence, the probability of having $T - 1$ non-recurrences before one recurrence at time T is

$$P_R(T) = \mu(1 - \mu)^{T-1} = \frac{\mu}{1 - \mu} e^{T ln(1-\mu)},$$

which is a binomial distribution. In the limit of small probability μ this reduces to the Poisson distribution

$$P_R(T) = \mu e^{-\mu T} \Rightarrow \rho_R(\tau) = e^{-\mu \tau}, \tag{3.4}$$

and one sees from (3.2) that $\mu = \mu(I)$. Poisson distribution has been shown to describe the RTS [in the limit of $\mu(I) \to 0$] of strongly chaotic (hyperbolic) systems [HSV99, Hir93]. This shows that from the point of view of the RTS these systems are indistinguishable from a simple random process. For finite $\mu(I)$ some deviations of the exponential rate of the binomial distribution are observed due to periodic orbits of low-period [AdSC04, Alt04]. However, for our purposes the more relevant observation is that the RTS in this case also decays exponentially for large recurrence times.

(ii) Consider the usual random walk in one dimension with a fixed probability $p = 0.5$ of stepping to the left or to the right a step of size 1 after each time interval n. The probability that it will be again at the initial position (the origin) at time n is zero for n odd and for n even

$$p(2n) = \frac{2n!}{n!n!} 2^{-2n},$$

where the first term corresponds to the number of combinations $\mathfrak{p}$ having equal number of steps to the right and to the left and the second is (one over) the total number of steps. Using Stirlings formula $n! \sim \sqrt{2\pi} n^{n+0.5} e^{-n}$, one gets that for large times

$$p(2n) \sim \frac{1}{\sqrt{\pi n}},$$

where the symbol "$\sim$" means that asymptotically for large times the ratio of both sides of the equation tends to a constant. In order to calculate the recurrence one has to impose the condition that n is the *first* time that the trajectory comes back to the origin. This can be calculated using the ballot theorem [Fel50] that, in this particular case, says that the number of path that do not cross the origin scales as $\mathfrak{p}/n$. [2] Taking this into account and writing $n = T$, coherently with the previous notation one gets that the RTS for large T can be written as

$$P(T) \sim T^{-1.5} \Rightarrow \rho(\tau) \sim \tau^{-0.5}. \tag{3.5}$$

The two examples described above lead to the two paradigmatic RTS observed in Hamiltonian systems: the exponential decay as in (3.4) and a power-law decay as in (3.5) which is more generally written as

$$P(T) \sim T^{-(\gamma+1)} \Rightarrow \rho(\tau) \sim \tau^{-\gamma}. \tag{3.6}$$

---

[2] Another way of taking the effect of first return into account is to consider it the time derivative of the probability of being at the origin: $P(2n) = p(2n) - p(2n - 2)$. This result is also deduced in chapter 3 of Ref. [Fel50] and can be interpreted as a particular case of the effect (i) discussed in Sec. 3.1.3. It is easy to see that it leads also to relation (3.5).

The exponent γ is the same used in Chap. 2, which was qualitatively defined in Eq. (2.15). A typical RTS of a sticky system will show an exponential decay for short times, related to the events that do not stick, followed by a power-law like decay for large times as shown in Fig. 2.2b.

Applying condition (3.2) to (3.6) leads to the restriction $\gamma > 1$. The random-walk model violates this condition ($\gamma = 0.5$) what means that it has a divergent mean recurrence time. Notice that the origin of the power-law in the random walk case is the existence of an infinite sequence of states where the probability of passing to each state is fixed. Whenever the random-walker is restricted to a finite domain an asymptotic exponential decay is observed after the regime (3.5). This mechanism to generate power-law RTS is the same of the Markov-chain and tree models of stickiness, discussed in Sec. 2.2.3. One important difference is that in those models the probability of stepping inside decays with the depth (algebraically) what leads to a greater power-law exponent which satisfies $\gamma > 1$. From this perspective the cantori discussed in Sec. 2.2.3 lead to stickiness because they allow to divide the phase space in an *infinite* sequence of states and only indirectly because they build partial barriers.

At this point a **definition of stickiness** can be provided. Based in the fundamental distinction between exponential and power-law decay of the RTS one would like to say that a system shows stickiness if the RTS, obtained through the recipes mentioned above, decays as a power-law [Eq. (3.6)]. A drawback in this definition is that in most numerical results a well defined power-law decay (more than two decades) is *not* observed. One would like to define stickiness as a "roughly power-law" decay of the RTS. This can be stated precisely through the following definition [Zas02a]:

> A system has the property of stickiness if all $m \geq m_0$ moments $\langle T^m \rangle$ of $P(T)$ diverge, for a fixed $m_0 \in \mathbb{R}$.

Condition (3.2) implies $m_0 > 1$. If asymptotically power-law distribution (3.6) is observed one gets $m_0 = \gamma - 1$, while no m_0 exists for asymptotical exponential decay of the RTS. For simplicity γ will be used hereafter as the quantifier of stickiness even if in some cases it would be formally correct to use m_0. Stickiness was defined here as a property of the Hamiltonian system, but one can also speak from different "sticky regions" in the phase space. For this purpose it is enough to be able to determine precisely the region of interest, i.e., define some encircling curve so that the escape from it (or recurrence to the outside) can be computed.

3.1.3 Relation to other PDFs

In the previous section the main properties of the RTS were presented and it was argued that it can be used to characterize stickiness. In this section this quantifier is carefully related to other measures and PDFs used in the literature. The main advantage of the RTS is that it is obtained from a single trajectory being thus independent of the choice of the ensemble of initial conditions. Additionally, no real arbitrariness related to the choice of the recurrence interval exists since, as discussed above, its main influence is in the definition of the exponent of the short time exponential decay [AdSC04]. In order to increase the power-law regime one usually needs a rapidly decaying exponential what suggests that the recurrence interval should be chosen as large as possible, provided it does not touch the sticky regions. The most important parameter in order to obtain a statistically significant RTS is the number of times the map was iterated (number of recurrences). For the results shown in this Thesis usually 10^{11} iterations of the different systems were performed[3]. The main drawback of the RTS is that it is not suited for open systems, where usually the survival probability of an ensemble of trajectories is used.

---

[3]Typically one day of computation time.

For long times stickiness leads to the same characteristic distribution obtained with different PDFs because only the phase-space structures close to the sticky region are relevant. In particular, the power-law tail of the RTS translates into power-law distributions of other PDFs like survival probabilities, decay rates, and distribution of trapping times. There are essentially two points one has to pay attention in order to compare the power-law exponent γ^* of a given PDF with γ of the RTS: (i) the kind of distribution measured: survival probability or escape rate; (ii) where the trajectories were initiated: touching or away from the sticky region. As argued below, in both cases a difference in the exponent of ± 1 is observed depending if, respectively, the first or second case is being used.

(i) The difference in the power-law exponent of $P(T)$ and $\rho(\tau)$ given in Eq. (3.6) is a direct consequence of the definition (3.3). More generally, this is always the case when some cumulative distribution is used. Another typical situation where this distinction appears is when an ensemble of trajectories is initiated inside a given region. In this case one may calculate the number of trajectories that stay at the region as a function of time – the survival probability $f(t) \sim t^{-\gamma^*}$ – or the rate the trajectories leave the region – the escape rate $df(t)/dt \sim t^{-(\gamma^*-1)}$.

(ii) The second aspect is where the trajectories were started. A difference of -1 in the exponent is observed when the trajectories are started touching the sticky region in comparison with the case of trajectories started away from it (as in the recurrence case). This very basic result is studied in Ref. [Pik92] where the first case is referred to be typical in transient chaos and the second in scattering problems. Different explanations also appear in Refs. [AHO04, CS99, Mei97]. An alternative deduction of this result is provided below (Appendix of Ref. [AMK06]).

Consider a uniform distribution of initial conditions in the neighborhood of a sticky region of the phase space (in the chaotic component touching the island) and consider the time it takes for the corresponding trajectories to escape to a pre-defined region away from the sticky region. The survival probability $S(\tau)$ is proportional to the measure $\mu(\tau)$ of the region of the phase space to which the trajectories stick for a time longer than τ. Due to ergodicity,

$$S(\tau) \propto \mu(\tau) = \frac{t_\tau}{t}, \tag{3.7}$$

where t_τ is the total time spent inside the sticky region and t is the total observation time used to calculate the recurrences. In this case the trajectories are initiated outside the sticky region and the RTS (3.3) is written as

$$\rho(\tau) = \frac{M_\tau}{M}, \tag{3.8}$$

where M_τ is the number of recurrences with time $T \geq \tau$ and M is the total number of recurrences observed in time t. Notice that both $S(\tau)$ and $\rho(\tau)$ are survival probabilities in order to avoid the effect (i) discussed above. The relation between the times in Eq. (3.7) and the number of recurrences in Eq. (3.8) is given by [CS99]

$$t \quad \sim M \langle T \rangle, \tag{3.9}$$

$$t_\tau \quad \sim M_\tau \, \tau, \tag{3.10}$$

where $\langle T \rangle$ is the average recurrence time. Altogether, this leads to

$$\rho(\tau) \sim \frac{S(\tau)}{\tau} \, , \tag{3.11}$$

and thus to a reduced exponent in the case of power-law decay of $\rho(\tau)$ and $S(\tau)$.

Summing up the two effects mentioned above, Table 3.1 presents the relation between the power-law exponent in the usual PDFs where stickiness plays an important role.

PDF	Distribution	Initial Conditions	Exponent
Recurrence Time Statistics (RTS)	$\rho(\tau)$	outside	γ
Recurrence time distribution	$P(T) = d\rho(\tau)/d\tau$	outside	$\gamma + 1$
Survival probability (transient chaos)	$S(t)$	inside	$\gamma - 1$
Escape rate (transient chaos)	$dS(t)/dt$	inside	γ
Survival probability (scattering)	$g(t)$	outside	γ
Escape rate (scattering)	$dg(t)/dt$	outside	$\gamma + 1$

Table 3.1: Relation between the power-law exponent of the RTS and of other PDFs directly related to the problem of stickiness.

Stickiness and power-law decay of the RTS lead also to a power-law decay of correlations since during the time the trajectory is stuck it performs essentially a quasi-periodic motion. If one considers a correlation function which is constant within a strip around the sticky region, the decay of the autocorrelation is simply proportional to the measure of the sticky region $\mu(\tau)$ defined in Eq. (3.7) and thus [CS84, CS99, Kar83]

$$\rho \sim \tau^{-\gamma} \Rightarrow C(\tau) \sim \tau^{-(\gamma-1)}. \tag{3.12}$$

This means that long-term correlation is obtained for $1 < \gamma < 2$, i.e., there is a non-normalizable distribution and no typical decorrelation time. In this case the spectrum shows also a power-law decay $S(w) \propto w^{-\beta}$ with $\beta = 1 - \gamma/2$ [GZR88].

In the next section the problem of recurrence in time series is considered. In some sense it departs from the main topic of the thesis and can be considered as a problem on its own, as in the original publication of these results [AK05]. However, the comparison of the RTS as a statistical tool with the Hamiltonian case is very fruitful for both fields. E.g., one sees that differently from the PDFs considered in Table 3.1, the correlation function may have different relations to the RTS than the one in Eq. (3.12). This will be clear from the discussion of the next section where it is shown that long-term correlated time series may have a RTS which is not power-law.

3.2   Recurrences in long-term correlated time series

3.2.1   Results from time series and comparison with Poincaré recurrences

Recurrence time analysis is a powerful tool to characterize temporal properties of well defined events [BEHK03, BEKH05]. It has been recently extensively performed in a rich variety of experimental time series: records of the climate, seismic activities, solar flares, spikes in neurons, turbulence in magnetic confined plasma and stock market indices (see Refs. [BEHK03, BEG$^+$03, AK05], and references therein). Calculated essentially in the same way, these analyses receive different names: waiting time distribution, interocurrence time statistics, distribution of interspike intervals, and distribution of laminar phases. They consist essentially to a recurrence in a one-dimensional system (see definition below).

The similarities of the the Poincaré RTS discussed in Sec. 3.1 (recurrence to the phase space) and the recurrence in time series used in the previously mentioned references is remarkable. Surprisingly, no systematic connection between the two recurrence approaches described above were made until now, as far as known by the author. The most evident way to establish this relationship is to define an observable $x = x(\vec{v})$, when $\vec{v}(t) \in \zeta$ is the trajectory in phase space of the Hamiltonian system. The recurrence volume $\mathcal{V}$ is mapped to an interval $I_{\mathcal{V}}$ on the real

axis by the observation function $x(\vec{v})$. However, the sequence of recurrence times of the series $x_n := x(\vec{v}(t = n\Delta t))$ with respect to $I_{\mathcal{V}}$ is generally *not* identical to the sequence of Poincaré recurrences of $\vec{v}(t)$ with respect of $\mathcal{V}$, since there is usually a large set $\bar{\mathcal{V}}$ which also maps to $I_{\mathcal{V}}$ due to the non-invertibility of $x(\vec{v})$. Moreover, generally $I_{\mathcal{V}}$ will be of the kind of $I(X_c, \delta)$ rather than $I_{ext}(q)$ [see Eqs (3.13) and (3.14) below]. However, as will be shown below, the analogy to Poincaré recurrences motivates issues related to the recurrence times of extreme events which will reveal fundamental insights into their properties. Two main results will be the lack of invariance of the RTS under change of the observable and the fact that long-term correlations are *not* fully characterized by the autocorrelation function.

3.2.2 Definition and basic results

Given a time series $\{x_n\}, n = 1, \ldots, M$, and having defined a recurrence interval I as a subset of the data range, then the ith recurrence time T_i is the time interval Δn between the ith and the $i+1$st visit of a time series point in I. Here again, the RTD is obtained as the distribution $P(T)$ of the sequence of recurrence times T_i. Evidently, the sequence of recurrence times generated this way depends sensitively on the choice of I, which in fact will be one prominent issue investigated below. While for the recurrence of *extreme events* the recurrence interval is defined by the points above a threshold [BEHK03]

$$I_{ext}(q) = [q, \infty[\, , \tag{3.13}$$

in a more general way it may be defined around a position X_c with a semi-width δ [AdSC04]

$$I(X_c, \delta) = [X_c - \delta, X_c + \delta] \, . \tag{3.14}$$

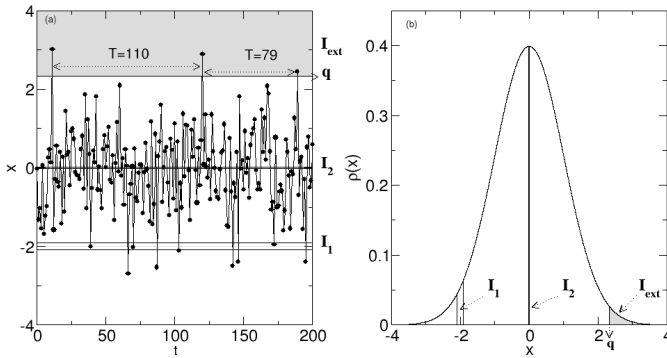Both kinds of intervals are illustrated in Fig. 3.1.

Figure 3.1: Gaussian distributed time series with recurrence intervals with measure $\mu(I) = 0.01$, what implies $\langle T \rangle = 100$. One extreme interval $I_{ext}(q = 2.3263) = [2.3263, \infty[$ and two recurrence intervals $I_1(-2, 0.0922) = [-1.9078, -2.0922]$, $I_2(0, 0.0125) = [-0.0125, 0.0125]$ illustrated in the (a) time series and (b) probability density function.

The mean recurrence time

$$\langle T \rangle \equiv \lim_{M_e \to \infty} \frac{1}{M_e} \sum_1^{M_e} T_i,$$

is a direct result of the choice of the recurrence interval as argued after Eq. (3.2). In the case of stationary time series, as illustrated in Fig. 3.1, an equivalent result to Kac's lemma is obtained from the normalized PDF $\rho(x)$,

$$\frac{\Delta t}{\langle T \rangle} = \mu(I) \equiv \int_{x \in I} \rho(x)dx, \tag{3.15}$$

where Δt is the sampling rate used to record the time series[4]. This is the most important constraint to the statistics of recurrence times. In the time series analysis this measure is estimated as the fraction of valid events (points inside the recurrence interval) $\mu(I) = M_{events}/M$. Intuitively, relation (3.15) states simply that the total observation time t is given by

$$t = M\Delta t = M_{events}\langle T \rangle.$$

Besides the RTD $P(T)$ the PDF $\rho(x)$ of the series of points itself is typically used to characterize the time series. The existence of such a PDF in time series is equivalent to the ergodicity condition in dynamical systems. Contrary to other time series analyses (as the detrended fluctuation analysis discussed below), the RTD is independent of the PDF. In particular, it is irrelevant whether the second moment of the PDF is finite. A time series with a well behaved (Gaussian) PDF can have either exponential or power-law RTD [5]. Reversely, a time series with fat tails in the PDF can lead to a RTD that might be Poisson or power-law [6]. The reason for this is simple: the RTD depends on the sequence of the time series points and changes under their temporal rearrangement, which does not change the PDF of the data. While the RTD is independent of the PDF of the series, the opposite happens to the mean recurrence time $\langle T \rangle$. Once the recurrence interval is defined, whether by relation (3.13), (3.14) or by any other possible definition, the PDF $\rho(x)$ provides $\langle T \rangle$ through relation (3.15).

These two trivial observations, i.e., independence of the RTD and dependence of $\langle T \rangle$ on the PDF, which are well known in the context of Poincaré recurrences, shed new light on previous results of time series analysis. In particular, previous reported results are reinterpreted and fitting constants specified. In what follows, these points are exemplified in the analysis of recurrence times between earthquakes and in the study of the stretched exponential distribution, previously used to describe linear long-term correlated data.

3.2.3 Applications to earthquakes and stretched exponential distribution

Earthquake results

One of the most important examples of the recurrence analysis is the study of the waiting time between earthquakes or avalanches in models exhibiting self-organized criticality (SOC). The idea of studying recurrences in SOC started with the first connections between SOC and earthquakes. More recently, the investigation of seismic catalogs of different regions of the globe indicate the existence of an universal distribution of recurrence times between big earthquakes [BCDS02, DG99], which may be roughly described as a power-law distribution

$$P(T) \propto T^{-\alpha}, \tag{3.16}$$

followed by a faster decay. Simple SOC models have a Poisson (exponential) distribution of recurrence times, what was used as argument against the use of SOC to model not only earthquakes but also (and originally) solar flares. However, non-Poissonian distributions are obtained in more sophisticated SOC models, what keeps open the debate over the use of SOC in these fields, with the RTD as one of its central ingredients (see Ref. [AK05] for references).

---

[4]When there is no such parameter, as in the series of earthquakes, the time scale is defined by the total number of events and the total recording time.

[5]Take for instance the analysis made in Sec. 3.2.3 which will give the desirable RTD if we choose $\zeta_c = 1$ or $\zeta_c \to 0$ respectively.

[6]These are obtained applying the transformation (3.25) below again to uncorrelated ($\zeta = 1$) or correlated ($\zeta = 0$) time series respectively.

Despite (or because of) the complexity of this field it has an important simplicity: the Gutenberg-Richter law

$$\rho(\mathfrak{M}) \propto e^{-b\,\ln(10)\mathfrak{M}} \, , \tag{3.17}$$

where A, b are constants and $\mathfrak{M}$ is the magnitude of the earthquake, which is proportional to the logarithm of the released energy. The constant b is almost the same for different parts of the world and the empirical law (3.17) is valid for $2 \leq \mathfrak{M} \lesssim 7.5$. From the perspective mentioned above this means that the PDF of the time series of seismic activity is given[7].

The mean recurrence time between earthquakes of a given magnitude $\mathfrak{M}$ is obtained inserting the PDF given by (3.17) in relation (3.15), and using the interval of the type (3.14) with $X_c = \mathfrak{M}$,

$$\langle T \rangle(\mathfrak{M}) = T_0 e^{b\,ln(10)\mathfrak{M}} \, , \tag{3.18}$$

where $T_0 \propto \frac{b\,ln(10)}{(1-e^{-b\,ln(10)\delta})}$. This relation is equivalent to the one obtained previously through a "mean-field approach". It was also noted the "remarkable" scaling of $\langle T \rangle(\mathfrak{M} \geq \mathfrak{M}_\mathfrak{c}) \propto 10^{b\mathfrak{M}_\mathfrak{c}}$, which is nothing else than a consequence of relation (3.15) when intervals of the type (3.13) are used with $q = \mathfrak{M}_\mathfrak{c}$.

So far, the relation between $\langle T \rangle$ and the PDF was used to show that the mean waiting time between earthquakes is directly related to the Gutenberg-Richter law, but has nothing to do with temporal correlations between earthquakes. On the other hand, the RTD obtained from earthquakes records [BCDS02, DG99] is an independent result that can be used as a test for the dynamical models of earthquakes. Recently, it was suggested that in SOC models the sequence of avalanches is uncorrelated and should thus be discarded (see [AMK06] for references). The solution of this debate is beyond the scope of this Thesis. Nevertheless, as a consequence of the unrelatedness of $\rho(x)$ and $P(T)$, shuffling data of whatever distribution randomly (as was done for the time series of seismic activity) trivially implies $P(T)$ of being exponential, also for finite recurrence intervals (see [AK05] for references).

Closed expression of the stretched exponential distribution

If time series data $\{x_n\}$ are exponentially (short range) correlated, the RTD is well known to be Poissonian (or Binomial) independent of the choice of I, as derived in Eq. (3.4). In the case of fully chaotic systems mentioned above correlations decay fast and the RTD is also Poisson. Hence, for systems with an exponential decay of correlations, details of defining recurrence times and further details of the system are irrelevant; instead there exists a unique RTD.

Many time series data have been found to be long-term correlated [BEG$^+$03, SK05, KZKB$^+$02]. Typically, this situation is characterized in the time series $\{x_n\}$ (assuming $\langle x_n \rangle = 0$) by the exponent $0 < \zeta_c < 1$ of the power-law decay of the autocorrelation function as a function of the time s

$$C_x(s) = \langle x_i x_{i+s} \rangle = \frac{1}{M-s} \sum_{i=1}^{M-s} x_i x_{i+s} \sim s^{-\zeta_c} \, . \tag{3.19}$$

In a recent paper [BEHK03], Bunde et al. analyzed the effect of long-term correlations on the return periods of extreme events, i.e., of recurrence times obtained using recurrence intervals of type (3.13). The main results of Refs. [BEHK03, BEKH05] for long-term correlated time series, that will be analyzed in detail below, can be summarized by the following three points. While

---

[7]This assumption is not completely precise since in order to use extreme intervals [defined by Eq. (3.13)] it is necessary to know the PDF in the limit $\mathfrak{M} \to \infty$. In the case of earthquakes it is well known, from general energy considerations, that a faster decay of the Gutenberg-Richter law is necessary asymptotically. In order to obtain a sufficient statistics in the analyses of experimental data, the choice of q in Eq. (3.13) is usually considerably smaller than 7.5 and the influence of the unknown asymptotic of the PDF becomes negligible.

the first was obtained considering statistical arguments, the two others were based on numerical simulations.

(i) The mean recurrence time is equal to the inverse of the fraction of extreme points in the series

$$\langle T \rangle = \frac{M_{total}}{M_{extreme}}.$$

(ii) The statistics of T follows a stretched exponential

$$\ln P(T) \propto -(T/\langle T \rangle)^{\zeta} \ , \tag{3.20}$$

where $\zeta = \zeta_c$ is identical to the correlation exponent in Eq. (3.19).

(iii) The series of recurrence times is long-term correlated with an exponent ζ_T close to ζ_c.

The three points mentioned above are re-interpreted now in the more general context of recurrence analysis presented in this Chapter. Statement *(i)* is the time series analogous of Kac's Lemma [Eqs. (3.2) and (3.15)] Concerning result *(ii)* suppose that the stretched exponential distribution

$$P_{\zeta}(T) = a e^{-(bT)^{\zeta}} \tag{3.21}$$

is valid for all recurrence times $T \in \ ]0, \infty[$. This is actually a stronger assumption than Eq. (3.20). As any RTD, Eq. (3.21) must satisfy the two conditions mentioned in Sec. 3.1.2: normalization (3.1) and the analogous of Kac's lemma (3.15) Imposing these two conditions to the distribution (3.21), it is possible to express the constants a and b as functions of ζ and $\mu(I)$. Further simplification is obtained performing the following transformation of variables $\mathfrak{T} = \frac{T}{<T>} = \mu(I)T$, i.e., counting the time in units of the mean recurrence time. The complete stretched exponential distribution for recurrence times is then written as

$$p_{\zeta}(\tau^*) = a_{\zeta} e^{-(b_{\zeta} \ \tau^*)^{\zeta}}, \ \text{with} \begin{cases} a_{\zeta} = & b_{\zeta} \ \frac{\zeta}{\Gamma(1/\zeta)}, \\ \\ b_{\zeta} = & \frac{(2^{1/\zeta})^2 \Gamma(\frac{2+\zeta}{2\zeta})}{2\sqrt{\pi}}, \end{cases} \tag{3.22}$$

and depends exclusively on the exponent ζ.

Equation (3.22) is illustrated in Fig. 3.2 for different values of ζ in two different ways. Graph (a) (log-log) shows that decreasing the value of ζ the distribution starts from the exponential (Poisson) case ($\zeta = 1$) and approaches a power-law ($\zeta \to 0$) with an exponent $\alpha = 1.5$. Graph (b) shows the distribution in the form that the stretched exponentials are seen as straight lines [BEHK03, BEG+03, SK05]. Generally, to obtain graph (b) from (a) one needs to divide the distribution $P(T)$ by the correct pre-factor $a = P(0)$, which is typically unknown. Distribution (3.22) shows the dependence of the pre-factor a on the exponent ζ when the stretched exponential $p_{\zeta}(\tau^*)$ is valid in the whole interval of times. For experimental or numerical data, where neither a nor ζ are known a priori, the relation between both is useful to correctly visualize and fit the RTD. In practice the numerical fitting of the exponent ζ is very sensitive and typically depends on the choice of the pre-factor a.

Numerical results for long-term correlated linear time series

The stretched exponential distribution (3.22) is compared now to the numerical results of the RTD obtained in long-term correlated time series. As in Ref. [BEHK03], the data were generated using the Fourier transform technique [PHSS92]: imposing a power-law decay on the Fourier spectrum
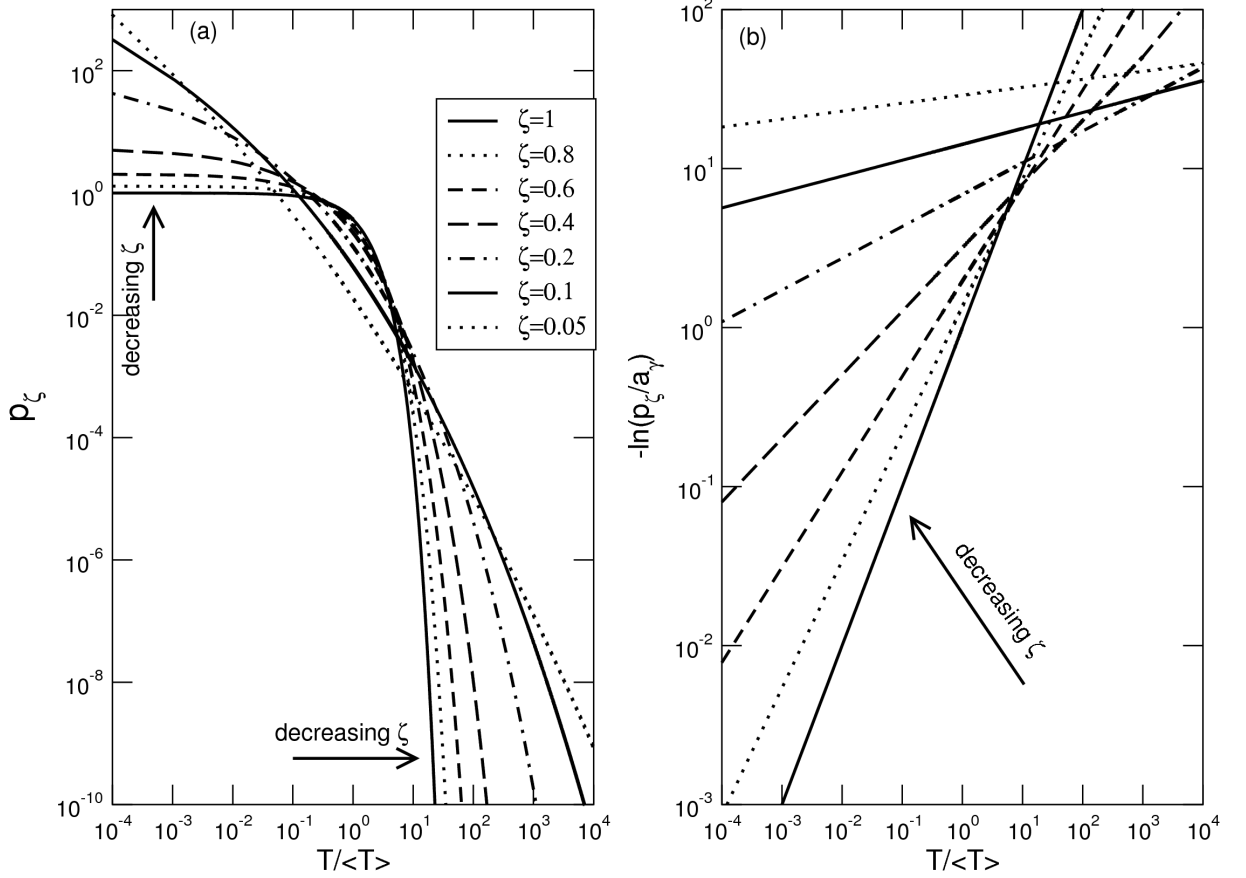
$$f_x(k) \propto k^{-\beta} \ , \tag{3.23}$$

Figure 3.2: The stretched exponential distribution (3.22) for different values of the exponent ζ.

with $0 < \beta < 0.5$ and choosing phase angles at random, one obtains through an inverse Fourier transform the long-term correlated time series in x with $\zeta_c = 1 - 2\beta$ in Eq. (3.19). The data are Gaussian distributed with $\langle x \rangle = 0, \sigma = 1$, and Eq. (3.15) was used to calculate the times $\mathfrak{T} = T/\langle T \rangle$.

Having specified the power spectrum or, correspondingly, the autocorrelation function for sequences of Gaussian random numbers means to have fixed all parameters of a linear stochastic process. Hence, in principle, the coefficients of an auto regressive [AR(r)] or moving average [MA(r)] process can be uniquely determined, where, due to the power-law nature of spectrum and autocorrelation function, the orders r of either of these models have to be infinite. Hence, the following results are valid for the class of *linear* long-term correlated processes [BEKH05]. In other words, higher order correlations for this class of processes follow trivially from the two-point correlations.

Figure 3.3 shows that the stretched exponential distribution (3.22) with $\zeta = \zeta_c$ describes considerably well the RTD, obtained using extreme intervals [Eq. (3.13)], of long-term correlated linear time series. The agreement is especially good for small values of ζ_c (long correlations) and $q \to \infty$ [which is equivalent to $\mu(I) \to 0$]. This result is a generalization of the result (*ii*) [BEHK03] since, using Eq. (3.22) and considering $\zeta = \zeta_c$, the comparison between the theoretical and numerical distributions has no free parameter and no fitting is made.

Furthermore, the results of Fig. 3.4 show that, for small $\mu(I)$, the distribution (3.22) is valid also for recurrence intervals in the inner part of the data range [centered at X_c and defined by Eq. (3.14)]. When $X_c \to \infty$, approaching the extreme interval, the value of ζ in Eq. (3.22)
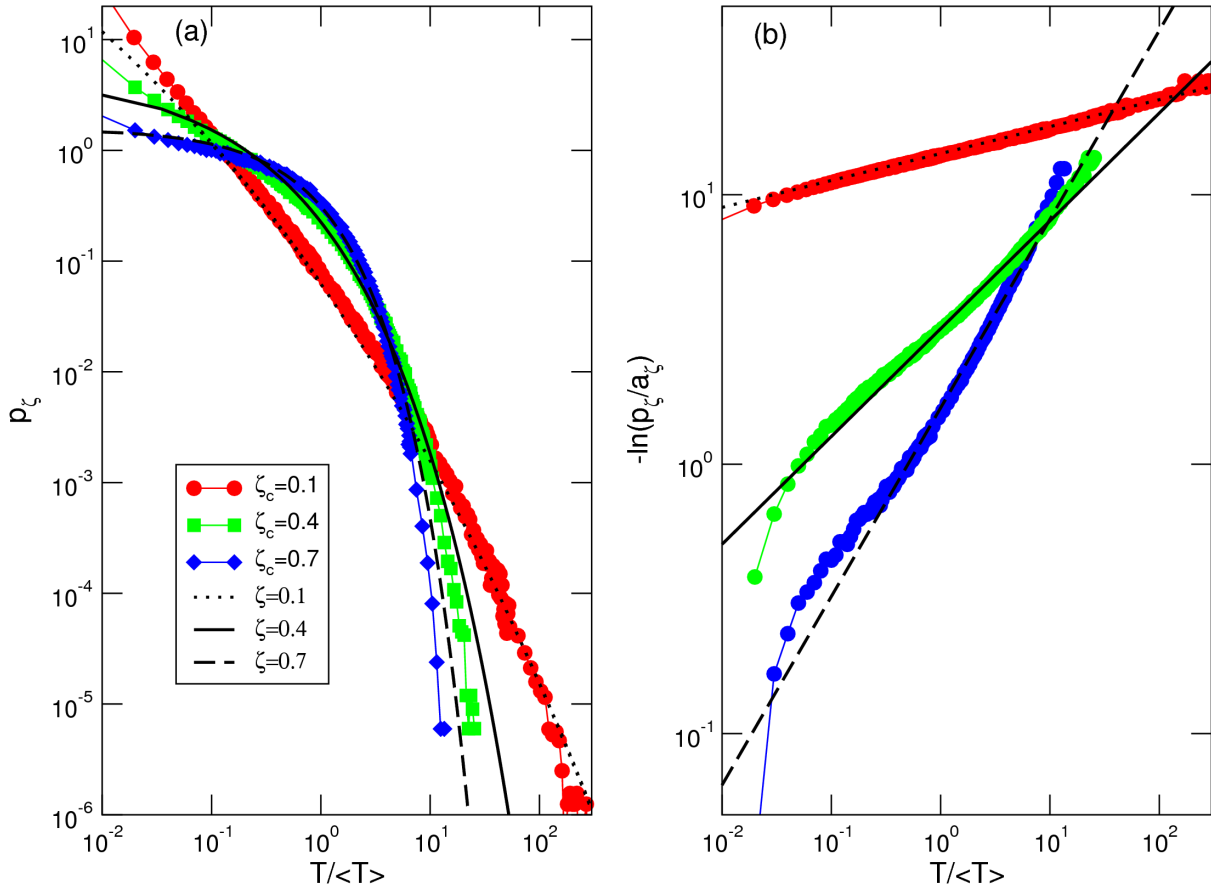
Figure 3.3: (Color online) RTD of long-term correlated linear time series with $M = 2^{25} \approx 3 \; 10^7$ points for different values of ζ_c (symbols). Lines are the stretched exponential distribution (3.22) with $\zeta = \zeta_c$. The recurrence interval is extreme with $\mu(I_{ext}) = 10^{-2}$.

approaches the value of the correlation exponent ζ_c. Decreasing the value of X_c towards the mean value of the PDF ($\langle x \rangle = 0$) results in an increase of ζ. This case was analyzed carefully in Fig. 3.4c, where the dependence of the RTD on the size of the recurrence interval $\mu(I)$ is shown. While for big intervals the stretched exponential seems not to hold, when $\mu(I) \to 0$ (the limit Poincaré was interested in) the distribution for $X_c = 0$ tends to the upper limit $\zeta = 1$, the Poisson distribution.

In summary, the RTD of long-term correlated linear time series with exponent ζ_c, in the limit of small interval $\mu(I) \to 0$, is described by the stretched exponential distribution Eq. (3.22) for all recurrence times T and for recurrence intervals of both types (3.13) and (3.14). The exponent ζ is a continuous and monotonically decreasing function of the center X_c of the recurrence interval, with the limits

$$\zeta = \begin{cases} \zeta_c & \text{when } X_c \to \infty \text{ (extreme)}, \\ 1 & \text{when } X_c = 0. \end{cases} \qquad (3.24)$$

This result has a simple interpretation in terms of the long-term correlations contained in the time series. Calculating the RTD to a specific interval measures the correlation between events inside this interval. In this sense, the results presented here suggest that the long-term correlations of the time series are concentrated in the extreme events (large fluctuations) and vanish for events near the mean value (small fluctuations). Relation (3.24) can then be interpreted as: approaching pure extreme events $[\mu(I) \to 0$ and $X_c \to \infty]$ the RTD shows the whole correlation and thus $\zeta = \zeta_c$. Approaching pure middle events $[\mu(I) \to 0$ and $X_c = 0]$ no correlation is
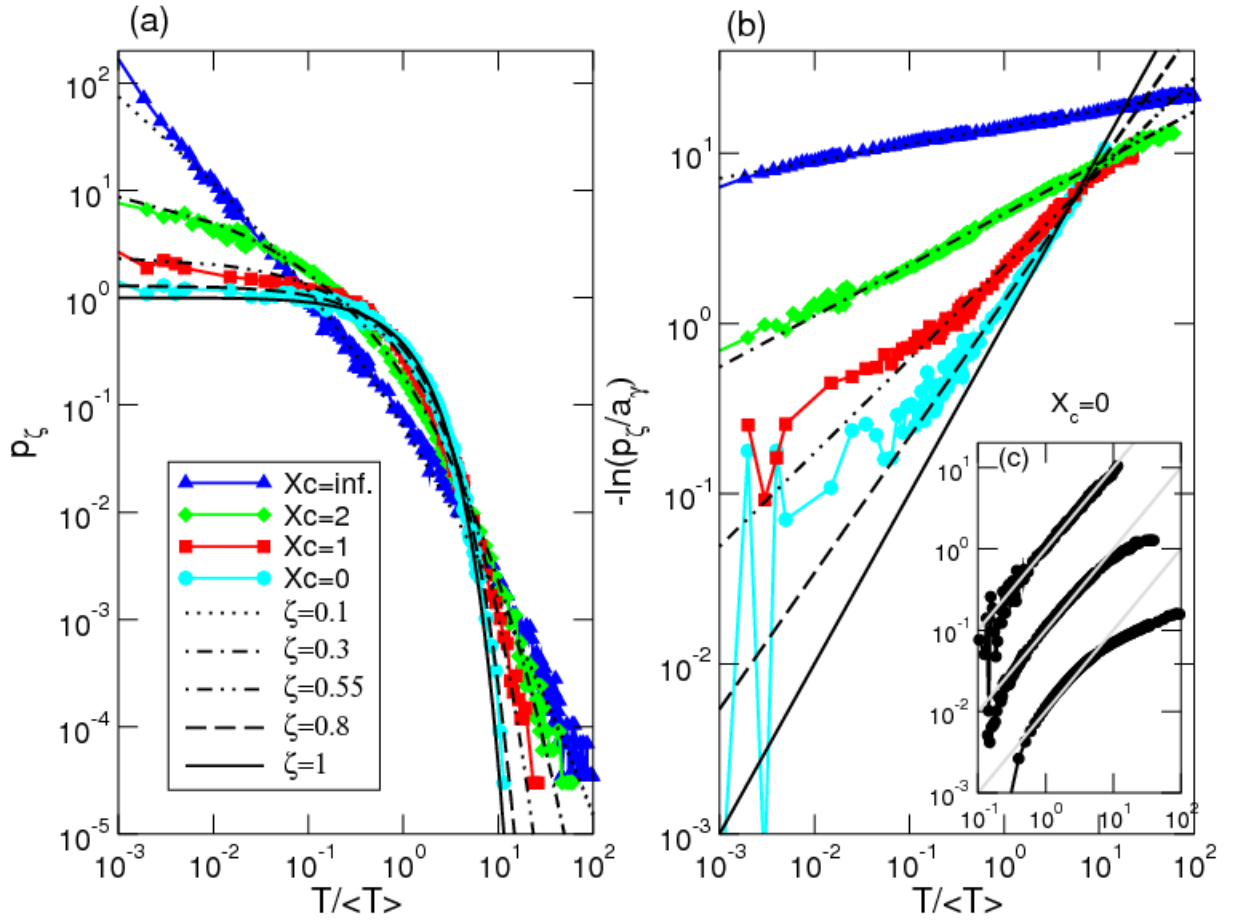
Figure 3.4: (Color online) RTD of long-term correlated linear time series with $\zeta_c = 0.1$ and different recurrence intervals [centered in X_c with measure $\mu(I) = 10^{-3}$]. The lines are stretched exponentials distributions and the symbols connected by lines are the numerical simulations. From (a) to (b) the values given by a_ζ of the best fitting of Eq. (3.22) in (a) are used. In (c) the case $X_c = 0$ for different values of $\mu(I)$, from bottom to top: $\mu(I) = 10^{-1}$ (shifted down by 10^2), $\mu(I) = 10^{-2}$ (shifted by 10) and $\mu(I) = 10^{-3}$ are analyzed. The gray lines are the Poissonian distribution [$\zeta = 1$ in Eq. (3.22)]. $a_{\zeta=1} = 1$ was used for all three cases.

detected and consequently the Poisson distribution ($\zeta = 1$) is recovered.

Change of observables

The link between recurrence times on time series and Poincaré recurrences motivates the issue of the change of observables. All of the empirical data exhibiting long-term correlations mentioned before represent systems which involve a huge number of degrees of freedom. Hence, there is a similarly huge arbitrariness in choosing a given observation function $x(\vec{v})$, and the natural question is what to expect when one changes this observation function.

For instance, the correlations in the weather can be studied through records of the daily maximum temperature or of the daily precipitation [BEG$^+$03]. For the first observable, long-term correlations for times larger than 10 days were found with an exponent $\zeta \approx 0.7$ for continental stations, independent of the location and of the climatic zone of the weather station. On the other hand, the series of precipitation, obtained in the same locations and for the same time windows, are not long-term correlated. A similar situation is observed in financial market data. While the fluctuation of prices are typically uncorrelated the volatility is long-term correlated (see [AK05] for references). This gives already a clue that correlations measured on a given time

series do in fact characterize the fluctuations of the given observable but do not characterize the underlying system in a more abstract way.

The aim now is to study the dependence of correlations and RTD on the chosen observable in more detail by comparing the properties of different observables. Generally, both observables x and y are functions of the $d-$dimensional phase space vectors $\vec{\zeta}$, and no simple function connecting x and y exists. Since the previous results were obtained from time series data without underlying multi-dimensional phase space, the analysis is restricted to a subclass of changes of observables, where in fact y is given by a nonlinear (potentially non-invertible) function of x. Hence, time series of different observables y as functions of the original long-term correlated time series of the variable x are constructed. Having in mind a recurrence interval defined through (X_c, δ) by relation (3.14), consider the following reversible transformation

$$y_n = \frac{1}{x_n - (X_c - \delta)}, \tag{3.25}$$

which is essentially the inverse of the original series $\{x_n\}$. If the x-series is Gaussian distributed as considered previously, the PDF of the new series $\{y_n\}$ is given by

$$\rho'(y) = \frac{1}{\sqrt{2\pi}} \frac{1}{y^2} e^{-\frac{1}{2}(1/y + (X_c - \delta))^2}, \tag{3.26}$$

which is illustrated in Fig. 3.5 for the case $X_c = 1, \delta = 0.0207$. In this figure it is also shown that the interval I_1, defined by the same (X_c, δ) in x, is transformed into an extreme interval in y. On the other hand, the extreme interval I_2 in x is transformed into a recurrence interval in the middle of the PDF of y. Since the sequence of recurrence times T obtained using the original intervals in the x-series is also obtained using the transformed intervals in the y-series, the RTD remains invariant under simultaneous transformation of variables and recurrence intervals. Therefore, the previous observation that the change of the recurrence interval in the x-series does not affect the functional form of the stretched exponential distribution (3.22), but does affect the exponent ζ, carries over to transformations of the form (3.25). For instance, the RTD of a series obtained from transformation (3.25) applied to a time series x with $\zeta_c = 0.1$, is well described by the stretched exponential distribution (3.22) with (see Fig. 3.4): $\zeta \approx 0.55$ for extreme interval (I_1 in Fig. 3.5b) and $\zeta = 0.1$ for central interval (I_2 in Fig. 3.5). This result holds for all reversible transformations.
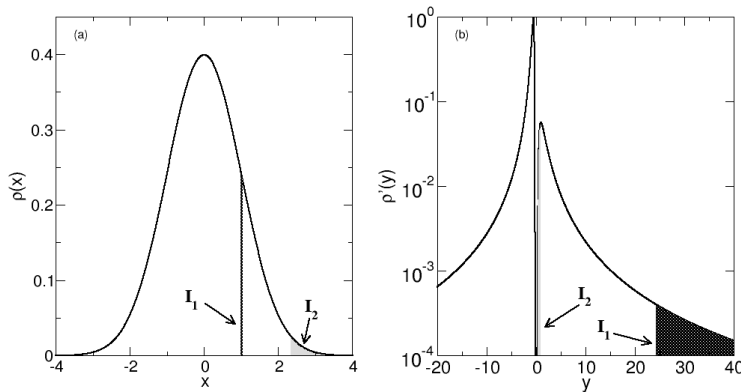

Figure 3.5: PDF of the series (a) of x (Gaussian) and (b) of y [Eq. (3.26) with $X_c = 1, \delta = 0.0207$]. The points inside the interval $I_1(X_c = 1, \delta = 0.0207)$ in x become extreme events in y. The opposite happens for the extreme interval $I_2 = I_{ext}(q = 2.3263)$.

An important fundamental question in this context is the behavior of the long-term correlations under transformations of variables. Whereas the normalized autocorrelation function

remains unchanged under shifts and rescalings of x, this is not the case under transformations like (3.25), where the transformed time series of y is not long-term correlated at all, despite the long-term correlations of the original x-series (see Fig. 3.6 where $h(2) \approx 0.5$). The y-series is characterized using the multi-fractal detrended fluctuation analysis [KZKB$^+$02], which is a much more powerful tool than the simple autocorrelation function, since for different values of the parameter q_{DFA} different scales of fluctuations are amplified. In order to distinguish between the multifractality due to long-term correlations and due to a broad PDF, the typical procedure is to shuffle the time series randomly, i.e., a new order of the M points of the original time series is chosen randomly. Since the shuffled series loses all its temporal correlations but retains the same PDF, the difference between the results of the two series (original and shuffled) is exclusively due to temporal correlations. In Fig. 3.6 the multi-fractal analysis (MF-DFA1 [KZKB$^+$02]) for the long-term correlated, Gaussian distributed, linear time series $\{x_n\}$ and for the transformed [through Eq. (3.25)] time series $\{y_n\}$ are shown. As expected, in the first case roughly a single generalized Hurst exponent $h(s)$ is obtained for all scales in the original ($h(s) = 1 - \zeta_c/2 = 0.95$) and shuffled ($h(s) = 0.5$) time series. Due to the broad tails present in Eq. (3.26), both the y-series and its shuffled version have multi-fractal spectrum, shown by the nontrivial dependence of $h(q_{DFA})$ on q_{DFA}. The difference between the two, which measures the effect of the temporal correlations, appears for small scales, where the generalized Hurst exponent of the shuffled series is smaller. This result is consistent with the interpretation made at the end of Sec. 3.2.3 that the correlations of the x-series is concentrated on the extreme events. Through transformation (3.25), the extreme events in x are mapped into very small fluctuations in y and the temporal correlations of $\{y_n\}$ are coherently noticeable for small values of q_{DFA}.
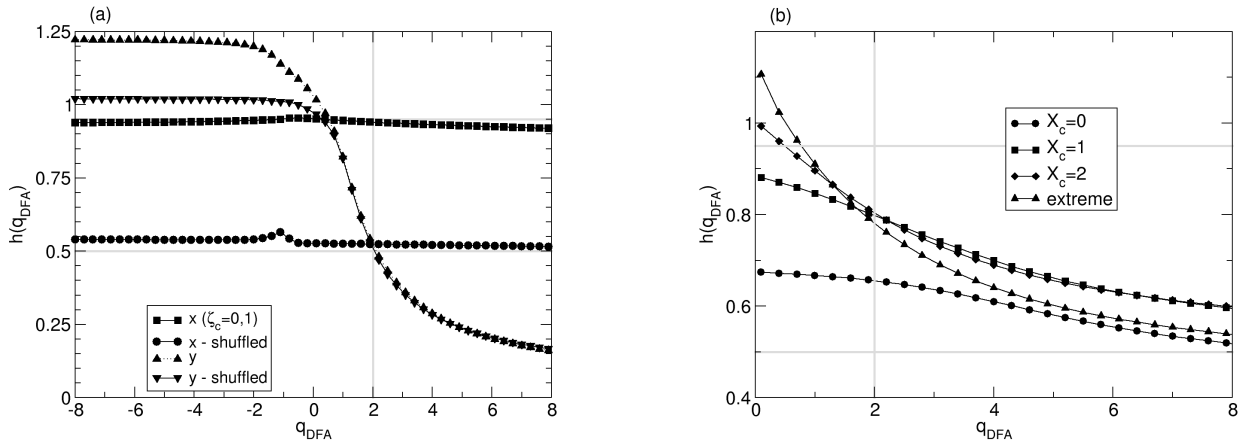

Figure 3.6: (b) Generalized Hurst exponent of the time series of x and y ($M = 2^{20} \approx 10^6$ points) as a function of the scale q_{DFA}. The horizontal gray lines are the non-correlated value ($h = 0.5$) and the expected value for $\zeta_c = 0.1$ ($h = 1 - \zeta_c/2 = 0.95$). The difference between the original and the shuffled time series measures the effect of the correlation at each scale q_{DFA}. (b) The same as in (a) for the series of recurrence times ($\{T_1, T_1, ..., T_{Me}\}$) obtained for intervals with $\mu(I) = 0.01$, and different values of X_c in long-term correlated linear time series with $\zeta_c = 0.1$ ($M_e = 2^{18} \approx 2 \times 10^5$).

Transformation (3.25) provides an example of equivalence between the RTD of different observables obtained using extreme intervals, and the RTD calculated in the same series but using different recurrence intervals. Always when the transformation of observables is invertible, there exist a one-to-one correspondence between the original extreme values and a new interval. This provides another justification to the generalization of the recurrence of extreme events to

general recurrence intervals inspired by the analogy to the Poincaré recurrences.

The series of recurrence times

It is also interesting to apply the distinction between the time properties of the series and its PDF, discussed in Sec. 3.2.2, to the series of recurrence times $\{T_1, T_2, ...T_{Me}\}$ itself [Afr97, AZ97, HLMV02]. In this case this means that the PDF, which is the RTD of the original time series, is independent of its correlation and shows that the results *(ii)* and *(iii)* of [BEHK03] (stated in Sec. 3.2.3) are independent. This is an important remark when prediction algorithms are considered, since in many cases the correlation between the waiting times is more important than their distribution.

The result *(iii)* of Ref. [BEHK03] is verified in Fig. 3.6(b) through the multifractal analysis of the series of recurrence times T. Instead of the same correlation exponent the simulations show a multifractal spectrum. It is necessarily originated by the long-term correlations since the PDF of these series are stretched exponential distributions, as verified in Fig. 3.4, which do not have fat tails.

3.2.4   Discussion of the results

The application of the statistical properties of the RTD, which are well known in the context of Poincaré recurrences, helped to clarify results of time series analysis. In particular, new interpretation of previous simple results in the earthquake analysis were performed and a closed expression for the stretched exponential distribution, uniquely defined by the exponent ζ, was obtained here. As limits $\zeta = 1$ and $\zeta = 0$, respectively, the exponential and the power-law decay are recovered (with the restriction that the power is fixed to $\gamma = 3/2$), suggesting that stretched exponentials describe recurrences in systems that have neither exponential nor power-law RTD but that lie in between these two cases. These results were verified numerically for the class of linear long-term correlated time series, and show reasonable agreement. In order to verify if the fluctuations around the stretched exponential distribution, shown in the figures of Sec. 3.2.3, are a consequence of numerical limitations or real deviations, an analytical deduction of the stretched exponential distribution (3.22) is necessary, what remains an open task (see Ref. [Oll06] for a recent development).

Even if one might argue that these results are established only for the class of linear models (as shown above), the reproduction of these findings for empirical data [BEG$^+$03, SK05, Pen05] suggests some generality of the stretched exponential distribution. Here, the link to Poincaré recurrences shows the opposite: Hamiltonian systems with mixed phase space are long-term correlated and show power-law tails in the Poincaré RTD due to stickiness. In fact, the temporal properties of typical data are *not* fully specified by the autocorrelation function, Eq. (3.19), what explains why there cannot be a unique RTD for long-term correlated data. Connections between the long-term correlation exponent ζ_c and the RTD have to be established independently in every class of long-term correlated dynamical systems, as was done for Hamiltonian systems with mixed phase space (Sec. 3.1.3) and fractal renewal point processes [TLF$^+$97]. From the perspective of Poincaré recurrences, this shows that the power-law tails obtained in the Poincaré RTD are suited to quantify stickiness while the decay of correlation depends on the observable. As mentioned above, the natural choice of correlation function uniform in the phase space around sticky region leads also to power-law decay of the correlation. However, different choices of the observation variables may lead to different decays.

The change of observables were simulated in the linear long-term correlated time series by performing simple reversible transformations [like Eq. (3.25)] on the original series $\{x_n\}$. This shows that the stretched exponential distribution characterizes also the RTD of extreme events

in time series that are not long-term correlated. The presence and absence of long-term correlations in the series of the original observable x and of the transformed observable y, respectively, is similar to the one reported above for climatic records (temperature and precipitation) and stock-market indexes (volatility and fluctuation of price). It is remarkable that this interesting behavior is obtained already through the simplest possible approach, i.e., two different observables that depend directly and exclusively on each other. These considerations emphasize that the temporal characterization of the system through the autocorrelation or RTD depend crucially on the chosen observable. By analyzing both the dependence of the exponent ζ of the stretched exponential distribution with the center of the recurrence interval [relation (3.24)] and the multi-fractal spectrum of the y-series (Fig. 3.6) one concludes that, in long-term correlated linear time series, the correlations are concentrated in the extreme events.

Many interesting questions arise if one supposes that the measurements in a given experiment lead to the time series of the observable y, introduced in Sec. 3.2.3, and that no natural access to the observable x exists. The y-series has a complex multi-fractal spectrum (Fig. 3.6), a strange PDF [Eq. (3.26)] and a non-trivial dependence of the RTD with the recurrence interval. Nevertheless, through a simple transformation [the inverse of relation (3.25)] one arrives at the x-series, that has a mono-fractal spectrum, is Gaussian distributed and has a simple [Eq. (3.24)] dependence of the RTD on the recurrence interval. This suggests the existence, in some situations, of "distinguished observables" where the time series analysis is extremely simplified. It is an interesting open problem to develop a procedure able to determine the transformation (when it exists) that lead to the "distinguished observables".

Chapter 4

Marginally unstable periodic orbits

The existence of one-parameter families of marginally unstable periodic orbits in the phase space of Hamiltonian systems is one of the simplest mechanism of stickiness. Well known systems following this mechanism are chaotic billiards with parallel walls, like the Sinai and Bunimovich Stadium billiards (Sec. 4.1). A general theory for the stickiness to these orbits is developed and the exponent $\gamma = 2$ deduced (Sec. 4.2). It is shown that a broad class of circular-like billiards also contains such orbits, which are investigated in detail in parameter- and phase-space of mushroom and annular billiards (Sec. 4.3). A proof for the existence of an infinite number of different families of MUPOs and an efficient algorithm to find them are given (Sec. 4.4). Finally, the stickiness theory is confirmed numerically (Sec. 4.5).

4.1   Ergodic systems: Sinai and stadium billiards

Which are the simplest Hamiltonian systems where stickiness exists? An answer to this question is searched among area-preserving maps (or time continuous systems with equivalent phase-space dimension) with simple phase space configurations, where the RTS (recurrence time statistics) is calculated. The simplest phase space configurations are those from integrable and fully chaotic-hyperbolic systems. While in the former case the RTS obtained by the procedure described in Sec. 3.1 (fixed recurrence region and a single trajectory) is composed at most by three different non-zero recurrence times T_1^*, T_2^*, and $T_3^* = T_1^* + T_2^*$ [Sla67], in the latter (fully chaotic) case the RTS decays exponentially [HSV99, Hir93, AdSC04]. Therefore, according to the definition of stickiness provided at the end of Sec. 3.1.2, stickiness is not present in these two limiting cases but is a property of chaotic *non-hyperbolic* systems. It may appear even when the non-hyperbolic sets have zero measure, i.e., for ergodic chaotic systems that are not fully hyperbolic. Examples are an area-preserving maps with a single marginal unstable fixed point [AP98] and billiards with one-parameter families of such orbits [AHO04, GD95]. The latter case is investigated in detail in this chapter. It describes a large class of systems and allows an analytical deduction of the asymptotic exponent γ.

A *billiard* is obtained by considering a closed region A with boundary ∂A, where a pointwise particle with mass m is confined. In the simplest case the particle moves in straight lines ($V = 0$) inside the billiard and experience elastic collisions ($V_{\text{boundary}} = \infty$) at its boundaries, defining the Hamiltonian system $H = \boldsymbol{p}^2/2m + V$. Further generalization may change the reflection rules (e.g., soft-walls), the ballistic free flies (e.g., introducing a magnetic field) or the (Euclidean) geometry of the table. Usually two dimensional tables are considered, in which case the dynamics has $N = 2$ degrees of freedom and can be reduced to a discrete time system in two dimensions

taking into account that energy is conserved and performing a suitable Poincaré section: one constructs a map describing the sequence of collisions of the trajectory with the boundary of the billiard taking as coordinates the position x and the angle θ in respect to the normal vector at the collision point (see Fig.4.1a). The outgoing angle is the same as the incident angle in the usual reflection. The induced map preserves area in the Birkhoff coordinates $[x, \sin(\theta)]$. The time between collisions, measured in actual time, is usually restricted between finite minimum and maximum values and has a mean value proportional to the ratio between the area of the billiard and the perimeter of the boundary.

Billiards defined by simple geometric figures, like a circle or a rectangle, are completely integrable since an additional invariant of motion exists (modulus of the horizontal linear momentum and the angular momentum, respectively). Figure 4.1 shows the two most famous chaotic-ergodic billiards: the Sinai billiard [Sin70] and the Bunimovich stadium billiard [Bun79]. The first billiard leads to the Lorentz gas when considered in the plane. The second shows that apart from dispersive components (like the circular scatterer in the Sinai billiard) focusing boundaries may also lead to chaos.
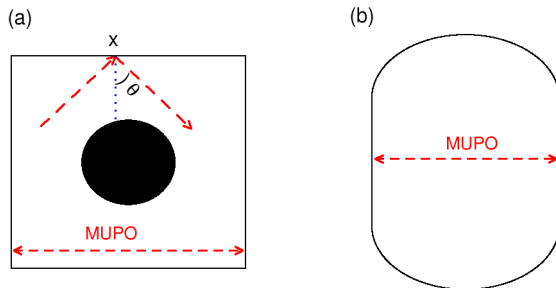

Figure 4.1: (a) Sinai billiard composed by a circular scatterer inside a square and (b) Stadium billiard composed by two semicircles joined by two straight lines. In both cases the MUPOs due to parallel walls are emphasized.

Despite being ergodic (non-existence of KAM-islands), the billiards illustrated in Fig. 4.1 are *not* hyperbolic (in a well defined sense fully chaotic) since, e.g., the orbits bouncing perpendicularly between the two parallel walls (dashed lines with arrows in Fig. 4.1) have marginal stability (see Sec. 2.1.1). The linear stability will be explicitly calculated in the next section where it is shown that perturbations do **not** grow exponentially in time but only linearly. In any case, unless the perturbation is not in the particular direction along the walls (which parameterizes a family of similar orbits), the trajectory eventually leaves the region close to the periodic orbit what motivate us to call such orbits marginally *unstable*. The acronym MUPOs is used to designate the one-parameter family of marginally unstable periodic orbits [GD95] in contact with the chaotic component of the system[1]. The most famous and trivial examples of MUPOs, are the orbits bouncing perpendicularly between parallel walls in the Sinai and Stadium billiards, also known as bouncing ball orbits in the context of quantum chaos [Stö00]. In the next section the scaling exponent $\gamma = 2$ is didactically obtained for the stickiness close to MUPOs.

4.2   Scale exponent $\gamma = 2$ for the stickiness to MUPOs

Consider an area-preserving map $M(x, \theta)$ that contains a one-parameter family of MUPOs of period q. For concreteness, assume that the family of MUPOs is $\{x_i \leq x \leq x_f, \ \theta = \theta_0\}$. The phase space of map $M(x, \theta)$ is sketched in Fig. 4.2(a) and a possible configuration space in

---

[1] The sequence of periodic orbits in an integrable system has the same marginal stability. However, they are not unstable since perturbations generically lead to a close-by quasi-periodic trajectories. The union of such orbits typically builds a torus. In contrast, the MUPOs draw an incomplete segment in the phase space.

Fig. 4.2(b). The following analysis does not depend whether the MUPOs are in the chaotic sea or at the border of a regular island, as it will be discussed in the next Chapter.
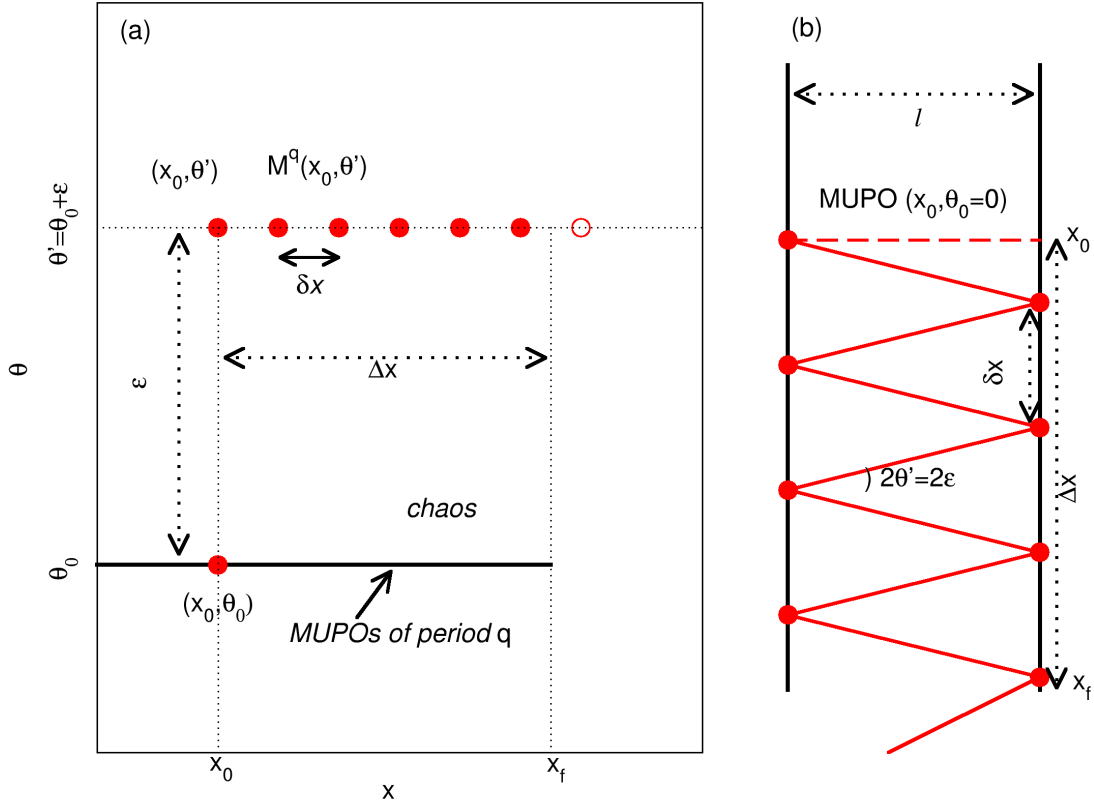

Figure 4.2: (a) Illustration of the dynamics of a perturbed MUPO $(x_0, \theta_0 + \varepsilon)$ in the phase space (see text). (b) The corresponding dynamics in the configuration space of a billiard with parallel walls ($q = 2$).

Consider small perturbations of a MUPO (x_0, θ_0):

(i) If $(x', \theta') = (x_0 + \epsilon_x, \theta_0)$ and $x_i \leq x' \leq x_f$, another periodic orbit of the set of MUPOs is obtained. In this case $M^q(x', \theta_0) = (x', \theta_0)$, what shows that the perturbation neither grows nor shrinks.

(ii) If $(x', \theta') = (x_0, \theta_0 + \varepsilon)$, the perturbation in the θ direction does not grow. On the other hand, in the x direction the trajectory is not strictly periodic anymore and there is a displacement δx every period q: $M^q(x_0, \theta') = (x_0 + \delta x, \theta')$.

Both effects *(i)* and *(ii)* have to be taken into account when a generic perturbation is considered:

$$M^q(x', \theta') \equiv M^q(x_0 + \epsilon_x, \theta_0 + \varepsilon) = (x' + \delta x, \theta'). \tag{4.1}$$

After q iterations, the same arguments used above for (x', θ') apply to $(x' + \delta x, \theta')$. One sees that the perturbed trajectory follows the dynamics (4.1), remaining at a constant distance ε from the *family* of MUPOs, until it travels $\Delta x = x_f - x_0$ reaching the end $x = x_f$ of the family of MUPOs

(see Fig. 4.2)[2]. Note that Eq. (4.1) implies a linear growth of the perturbation in time, what is consistent with the marginal instability, that forbids exponential growth of perturbations.

The displacement δx is related to the difference between the frequency of the perturbed and unperturbed orbits, and can therefore be approximated linearly as

$$\delta x = D\varepsilon, \tag{4.2}$$

in the limit of small ε.[3]

The time a perturbed trajectory takes to reach x_f and escape from the dynamics (4.1) is given by

$$T = \frac{\Delta x}{\delta x} \sim \frac{1}{\varepsilon}, \tag{4.3}$$

for small ε. In what follows, it is argued that this time is equivalent to the recurrence time if the initial conditions are chosen properly. Relation (4.3) shows that the smaller the perturbation the longer the time the trajectory takes to escape. The asymptotic distribution of escape times $P(T)$ as a function of the distribution of perturbations $p(\varepsilon)$ is given by

$$P(T) = \frac{p(\varepsilon)}{|dT/d\varepsilon|} \sim p(\varepsilon)\varepsilon^2, \text{ with } \varepsilon \sim 1/T. \tag{4.4}$$

The distribution $p(\varepsilon)$ depends on the choice of the initial conditions, as discussed in Sec. 3.1.3. For instance, choosing the initial conditions in the neighborhood of the family of MUPOs leads to a rapid convergence of $p(\varepsilon)$ to the invariant measure of the system. In this case, $p(\varepsilon)$ can be asymptotically regarded as a constant. From Eqs. (4.3) and (4.4), one obtain $\gamma'_{tr} = 2$ for the power-law exponent of the distribution of escape times, or $\gamma_{tr} = 1$ for the cumulative distribution. The scaling exponent for the RTS (initial conditions away from the MUPOS) can be obtained applying relation (3.11) and leads to $\gamma = 2$.

Other equivalent deductions of the scaling exponent $\gamma = 2$ have been done previously in systems presenting marginal stability. Apart from the cases of Stadium [AHO04] and Sinai billiards [GD95], also different systems that do not have MUPOs in the sense described above present the same behavior: fixed obstacles in fluid flows [EMZT93], triangular billiards with irrational angles [CP99], escape from an integrable system [HRR+04, BD05]. The rest of this Chapter and the first part of the next Chapter are devoted to expand the class of systems where the stickiness due to MUPOs is valid: circular-like billiards and piecewise-linear maps are considered. From the above derivation it is clear that every family of MUPOs contributes with the same exponent $\gamma = 2$ asymptotically and the exponent does not depend on the possible presence of other families of MUPOs. Indeed, as will be shown in the following sections, an infinite number of other families is observed in mushroom and annular billiards (Sec. 4.4), a small number in the continuous sawtooth map (5.1) and only the border of the regular island in the case of map (5.1)-(5.3). It will be shown that the scaling exponent $\gamma = 2$ is numerically observed in all these cases.

---

[2] If the MUPOs are at the border of a regular island, x_f represents either the vertex of a polygonal island or, as in the case of circular-like billiards, the point of tangency between the first escaping region and the island (see Ref. [AMK05]).

[3] The values of D for the systems used in this and the next Chapters are: $D = 6$ for the continuous sawtooth map with $K = 3/2$; $D = 2l$ in the case of billiards with parallel walls, where l is the distance between the walls; $D = 2qR$ for MUPOs in circular like billiards, such as mushroom and annular billiards, where R is the radius of the circle.

4.3 MUPOS in circular-like billiards

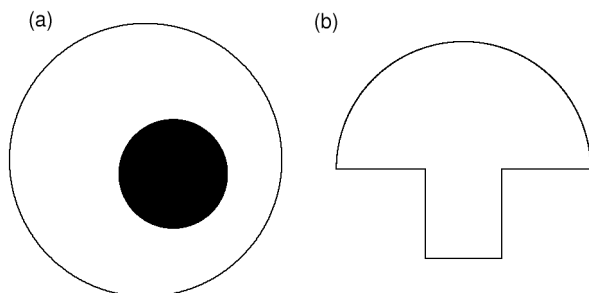### 4.3.1 Analogy with the parallel wall case

Figure 4.3: (a) Annular billiard composed by two eccentric circles and (b) Mushroom billiard composed by a semi-circular "head" with a rectangular "foot".

Billiards are designed using simple geometrical curves, and it is thus no surprise that, apart from straight line segments, circular components appear in many previously studied billiards. Two examples are annular [SHF+82] and mushroom billiards [Bun01] illustrated in Fig. 4.3 and studied in detail below. The surprising observation shown here is that these kind of billiards also have MUPOs. An analogy between the MUPOs in billiards with parallel walls and circular-like billiards is presented in Fig. 4.4. The previous illustrated billiards can be obtained by defining the dynamics in the gray region of the billiards shown in Fig. 4.4: from a rectangular billiard one can obtain the Sinai billiard [Fig. 4.1(a)] inserting an inner circular obstacle or the stadium billiard [Fig. 4.1(b)] introducing a circular concave border. Similarly, one defines the shape in the inner part of the circular billiard (region of radius a, a$<$ $R \equiv 1$), e.g., by placing a circular scatterer to obtain the annular billiard [Fig. 4.3(a)] or "holes" to obtain a mushroom billiard [Fig. 4.3(b), see Sec. 4.3.2 below for the precise analogy]. The value "a" is defined as the distance from the center of the circular billiard to the farthest obstacle (scatterer or hole). It separates the phase space between a possibly chaotic component – composed of the trajectories that repeatedly enter the gray region – and a regular component called whispering gallery [BBdCM93] – build by the trajectories that avoid entering the gray region. This division of the phase space is illustrated in Figs. 4.5 and 4.9 below. The MUPOs are the periodic trajectories inside the chaotic component that exist in the integrable system (rectangular or circular billiard) and that survive the redefinition (in the gray region) of the billiard. It is shown below that many of these orbits exist for different control parameters of the mushroom and annular billiards. These orbits typically exist also for billiards with elliptic components, in higher dimensions, and, more generally, when a chaotic billiard is obtained by **local** modifications of an integrable one. In opposite, global perturbations are described by the KAM-theory discussed in Sec. 2.1.2 and will be illustrated in Sec. (5.2). The rest of this Chapter studies the paradigmatic case of billiards obtained by perturbations of a circular billiard as proposed in Fig. 4.4b (called hereafter circular-like billiards).

A periodic orbit in a circular billiard is defined by two integer numbers: the period q and the rotation number η (the number of laps around the center of the circle), where q/η is an irreducible fraction and $q > 2\eta$. The invariant reflection angle θ_p of this orbit is given by

$$\theta_p(q, \eta) = \pm \pi (q - 2\eta)/2q \Rightarrow \sin(\theta_p) = \cos(\pi \frac{\eta}{q}). \qquad (4.5)$$
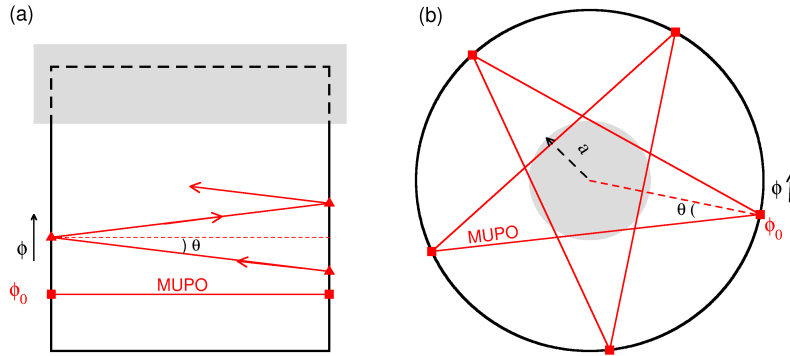
Figure 4.4: Billiards with (a) parallel walls and (b) circular components. Periodic orbits indicated by ■'s have marginal stability. In the gray regions the dynamics is defined in such a way that chaotic motion is possible.

Small perturbations of the collisional angle (in respect to the normal vector) $\theta = \theta_0 + \varepsilon$ lead to a constant increment in time n of the displacement $\Delta\phi$ between the position of collision of the periodic orbit ϕ_0 and of the perturbed one $\Delta\phi_n = v_\varepsilon n$, with $v_\varepsilon \propto \varepsilon$. A perturbation in ϕ, maintaining $\theta = \theta_0$ constant, generically leads to an equivalent periodic orbit, what shows that they have precisely the marginal stability discussed in Sec. 4.2 for the parallel wall case. As discussed above, the MUPOs have to be embedded in the chaotic component of the phase space. In the case of parallel walls they consist of the trajectories colliding exclusively with the outer walls (not touching the inner scatter of the Sinai billiard or the curved boundaries of the Stadium billiard). In the case of circular-like billiards the two necessary conditions (which are sufficient) for a *periodic* orbit (q, η) to be a MUPO of a circular-like billiard are:

Conditions for MUPOs in circular-like billiards

C1: The periodic trajectory must cross the circle of radius a in Fig. 4.4, i.e., the trajectory must be inside the chaotic component of the circular-like billiard.

C2: The trajectory should not hit any of the obstacles introduced in ($r <$a), preserving thus its marginal stability.

These conditions can be thought as the definition of the MUPOs in circular-like billiards studied here. They will be used explicitly in the following sections to obtain geometric relations for the existence of MUPOs in mushroom and annular billiards.

4.3.2   Example 1: mushroom billiards

Recently, Bunimovich [Bun01, Bun03] introduced a new family of Hamiltonian systems, the so called mushroom billiards, which have the remarkable non-generic property of having a phase space with a single island and a single ergodic chaotic region. Figure 4.5 shows an example of mushroom billiard consisting of a semi-circle (*hat*) placed on top of a triangle (*foot*). The precise geometry of the foot (e.g., rectangular in Fig. 4.3b and triangular in Fig. 4.5a) is irrelevant [Bun01]. The important control parameter is the size of the foot given by the ratio r/R. The coordinates used to describe the phase space are the normalized position $x \in [0, 1]$ along the boundary of the billiard and the normalized collision angle $\theta \in [-\pi/2, \pi/2]$. In these coordinates, the border between the regular and the chaotic regions for trajectories in the semi-circular hat

is at $\theta^*(r/R) = \pm \sin^{-1}(r/R)$, as shown in Fig. 4.5b. In the configuration space, the border between the island and the chaotic sea consists of the orbits in the semi-circular hat of the billiard that are tangent to the circle of radius r in Fig. 4.5a. The regular region is composed of the trajectories that do not cross this circle, remaining forever in the semi-circular hat. The chaotic component consists of the complementary set of trajectories, those that cross the dashed circle and may visit the foot of the mushroom. The MUPOs are the trajectories in the chaotic region that do not visit the foot of the mushroom.
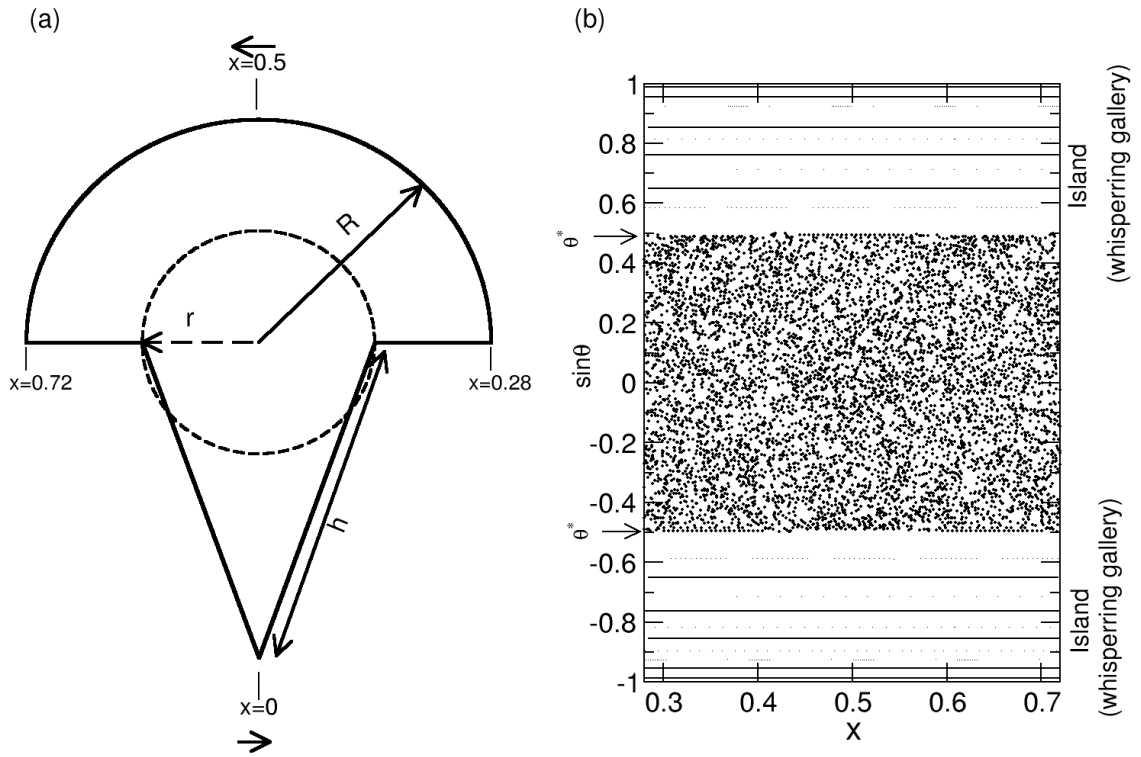

Figure 4.5: A mushroom billiard with triangular foot. (a) Configuration space. (b) Phase-space representation of the semi-circular hat, where x is the normalized position and θ is the normalized reflection angle. The parameters are $r/R = 0.6125$ and $h/R = 1.5$, what implies $\theta^* = \pm 1/6$.

A convenient way to visualize the MUPOs is to consider a circular billiard of radius R, as depicted in Fig. 4.6a, which has the property that trajectories are considered to escape when they hit the horizontal straight-line segment of length $2r$ in the center of the billiard (hereafter referred to as the *hole*). In the notation of the previous section a= r. The equivalence between the two billiards is based on the application of the image construction "trick" to the horizontal segments in the hat of the mushroom billiard and on the independence on the shape of the foot [Bun01]. The coordinates of the circular billiard are the reflection angle $\theta \in [-\pi/2, \pi/2]$ with respect to the normal vector and the position of collision in the circumference, given by the angle $\phi \in [-\pi, \pi]$, as indicated in Fig. 4.6a. The time is again measured as the number of reflections at the border of the billiard. This introduces a minor difference between the two billiards since in the mushroom billiard one counts the reflections at the horizontal segments of

the hat. Nevertheless, the dynamics of the trajectories in the open circular billiard is equivalent to that of trajectories in the semi-circular hat of the mushroom billiard, where stickiness occurs and where the MUPOs are located. Geometrically, the MUPOs are the periodic orbits of the open circular billiard that cross the circle of radius r but that do not hit the hole in the center of this circle. Examples of MUPOs are shown in Figs. 4.6 and 4.14 for the parameter $r/R = 0.6125$.
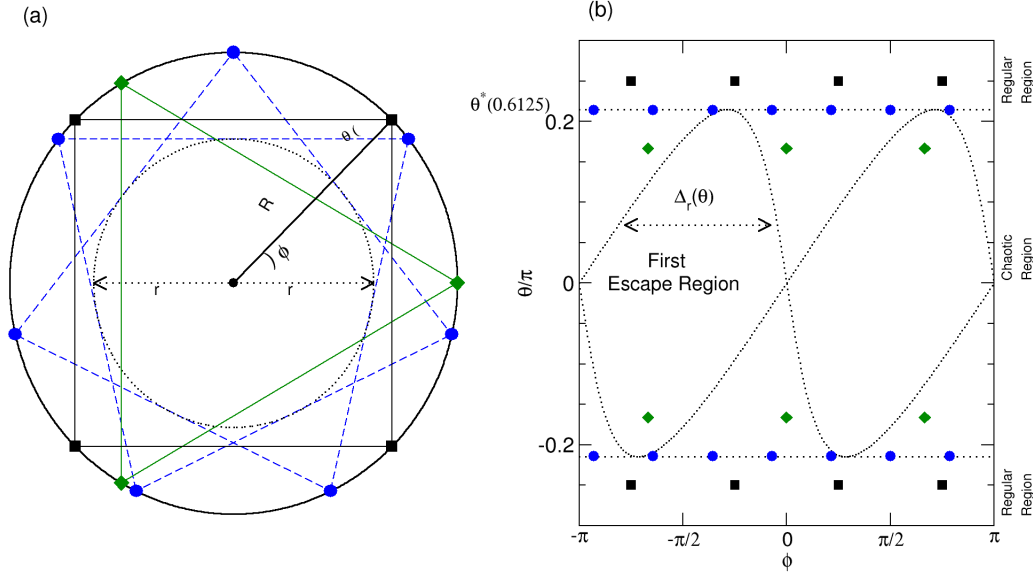

Figure 4.6: (Color online) (a) The open circular billiard for hole length $r/R = 0.6125$. Diamonds ($\blacklozenge$) correspond to an orbit ($q = 3, \eta = 1$) that always hits the hole and squares ($\blacksquare$) to a periodic orbit ($q = 4, \eta = 1$) in the whispering gallery. (b) Phase-space representation of (a). Circles ($\bullet$) correspond to a periodic orbit ($q = 7, \eta = 2$), which is a MUPO and is studied in detail in Fig. 4.14, and the other symbols are the same as in (a). The horizontal lines represent the border θ^* between the chaotic and regular regions. The first escape regions are the areas limited by the dotted curves.

MUPOs in the parameter space

For mushroom the two conditions for existence of MUPOs expressed in Sec. 4.3.1 can be obtained as simple geometrical relations by noting that each MUPO of type (q, η) draws an inner regular polygon with q sides (see Sec. 4.4 for details). For a given orbit (q, η): (C1-mushroom) $r/R > \sin(\theta_p)$ and (C2-mushroom) $r/R < \sin(\theta_p)/\cos(\pi/(jq))$, where θ_p is given by Eq. (4.5) and $j = 1$ if q is even or $j = 2$ if q is odd. Altogether, this determines an interval in the parameter space where a given orbit (q, η) is a MUPO:

$$\cos(\pi\eta/q) < r/R < \frac{\cos[\pi\eta/q]}{\cos[\pi/(jq)]} . \tag{4.6}$$

In Fig. 4.7, the parameters for which the orbits up to period $q = 20$ are MUPOs are shown. An efficient procedure to find higher order MUPOs for a given parameter r/R will be discussed in Sec. 4.4. Briefly, it consists in taking η/q as the convergents of the continued fraction representation of $\frac{1}{\pi}\cos^{-1}(r/R)$ and verify if they fulfill condition (4.6). This procedure revealed the existence of the following MUPOs for $r/R = 0.6125$: $(q, \eta) = (7, 2)$, $(698, 199)$, $(1161, 331)$, $(18341, 5229)$, $(2136146, 609013)$, and $(8526243, 2430823)$.
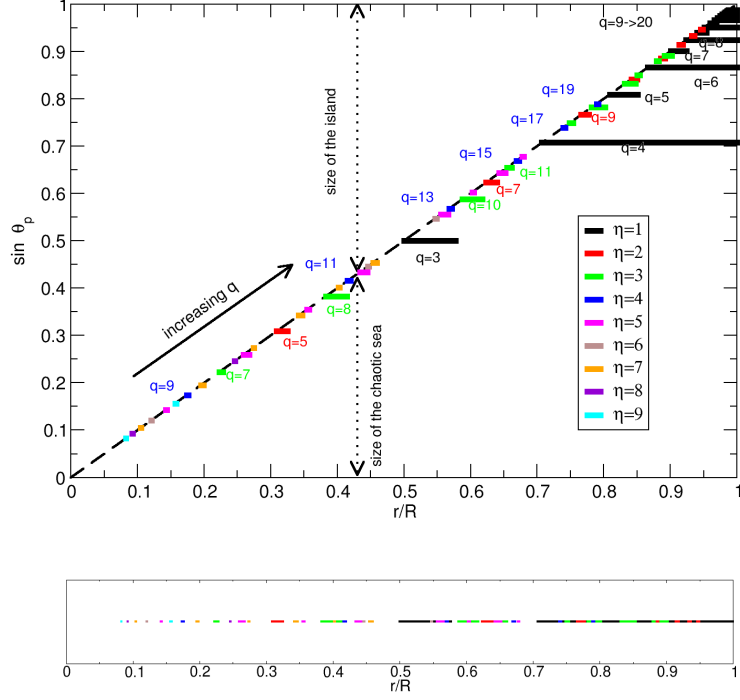
Figure 4.7: (Color) Intervals of the control parameter r/R for which orbits (q, η) are MUPOs. All orbits with $q \leq 20$ are shown.

MUPOs in the phase space

It is also interesting to analyze the implications of the conditions described in Sec. 4.3.1 to the position of such orbits in the phase space. Condition C1 mean simply that the periodic orbit must be inside the chaotic region. C2 states that the trajectory does not hit the hole, what can be satisfied only if it is close to the border. In order to study these conditions in the phase space of the open circular billiard, the points with reflection angle θ that hit the hole in one time step are identified. These points define the *first* escape region, whose width will be denoted by $\Delta_r(\theta)$ (see Fig. 4.6b). The trajectory does not hit the hole if all the q periodic points of the orbit are outside the first escape region. With respect to the coordinate ϕ, the distance between two neighboring periodic points is constant, namely $2\pi/q$. The condition C2 can thus be written as

$$\frac{2\pi}{q} > j\Delta_r(\theta_p), \quad j = \begin{cases} 1 & \text{if } q \text{ is even,} \\ 2 & \text{if } q \text{ is odd.} \end{cases} \tag{4.7}$$

The factor $j = 2$ for the odd-period periodic orbits comes from the 2π periodicity of the points of these orbits in opposition to the π periodicity of the escape region.

To calculate $\Delta_r(\theta)$, the borders of the first escape region (Fig. 4.6b) have to be determined. For a given position ϕ in the circumference of radius R, the angles θ of the trajectories that first hit the hole are limited by the angles $\theta^\pm$ given by

$$\begin{aligned} \theta^+ &= \tfrac{1}{2}[\phi + \tan^{-1}(\tfrac{R\sin(\phi)}{r+R\cos(\phi)})], \\ \theta^- &= \tfrac{1}{2}[\tfrac{\pi}{2} - \phi + \tan^{-1}(\tfrac{R\cos(\phi)-r}{R\sin(\phi)})]. \end{aligned} \tag{4.8}$$

The width of the first escape region is then given by

$$\Delta_r(\theta_p) = \phi_1^{\pm} - \phi_2^{\pm} \;, \tag{4.9}$$

where $\phi_1^{\pm} > \phi_2^{\pm}$ are the two solutions of the equation $\theta^{\pm} = \theta_p$. Observe that, because of the symmetry $\theta \to -\theta$, it follows that $\phi_1^+ - \phi_2^+ = \phi_1^- - \phi_2^-$.

The first escape region is now used to study how the families of MUPOs are distributed inside the chaotic component of the phase space of the mushroom billiard. Figure 4.8 shows the phase space of the open circular billiard for trajectories $|\theta| < |\theta^*|$, associated with the chaotic region of the mushroom billiard, and the Nth escape region, defined by the $(N-1)$th pre-image of the first escape region shown in Fig. 4.6b. The larger the period of the orbit the closer it may be to the border θ^*. For example, for the control parameter $r/R = 0.6125$ considered in Fig. 4.8, the border is at $\theta^*/\pi = 0.2149010...$ and the orbits $(q = 7, \eta = 2)$, $(q = 235, \eta = 67)$ and $(q = 698, \eta = 199)$ highlighted in the figure are at $\theta_p/\pi = 0.2143857...$, $0.2148936...$, and $0.2148997...$, respectively. The widths of the escape regions go to zero when the border is approached. In Fig. 4.8, the MUPOs correspond to the points that do not belong to any of the nth escape regions, for all $n < N$ in the limit of $N \to \infty$. That is, taking the limit $N \to \infty$ in Fig. 4.8, all the points outside the escape regions belong to MUPOs. Note that a complex distribution of families of MUPOs may exist near the border of the island. A deeper understanding of the distribution of such orbits close to the border of the chaotic region is obtained in Sec. 4.4, where it is proven that for almost all control parameters r/R there exist an infinite number of different families of MUPOs and that its distribution depends crucially on the frequency of the critical circle (at the border of the island).
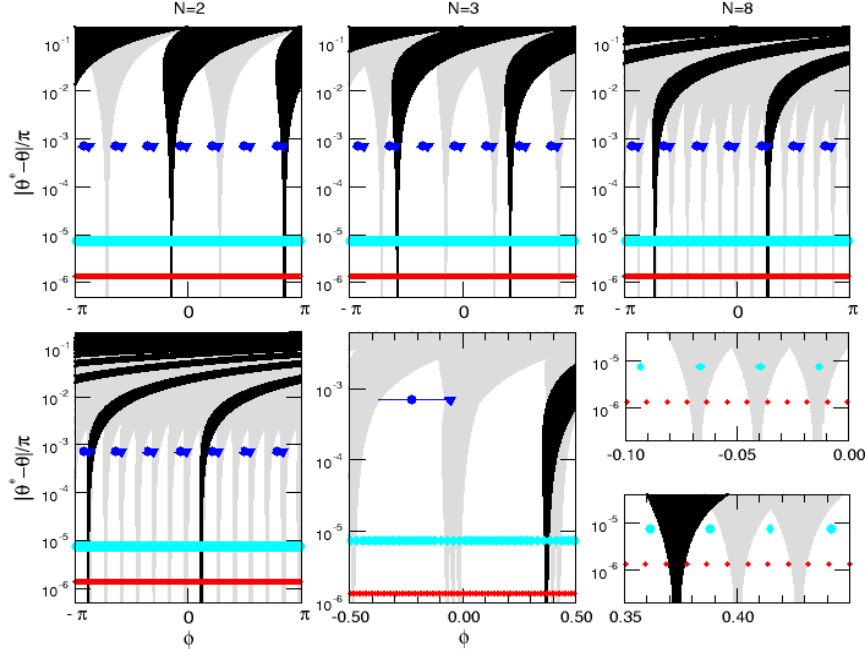

Figure 4.8: (Color online) Escape regions in the the phase space of the open circular billiard for $r/R = 0.6125$. In each panel, the Nth escape region is shown in black and the nth escape regions for all $n < N$ are shown in gray. In the first row, the cases $N = 2, N = 3$, and $N = 8$ are shown, while in the second the case $N = 20$ and successive amplifications for this case are shown. Different symbols correspond to the different orbits $(q = 7, \eta = 2)$, $(q = 235, \eta = 67)$, and $(q = 698, \eta = 199)$, from top to bottom, respectively. The figures at the bottom right show that only the first and the last of these orbits are MUPOs.

4.3.3 Example 2: annular billiards

The annular billiard is composed of two eccentric hard wall circles where a pointwise particle experiences elastic collisions, as drawn in Figs. 4.3(a) and 4.9. The control parameters are the radii R and r of, respectively, the outer and inner circle and the distance δ between the center of the two circles (the inner circle is called the *scatterer*) . Without loss of generality it is assumed that the center of the two circles lye in the x-axis and that $R = 1$. It is remarkable that the existence of MUPOs has not been discussed until now, in spite of many theoretical [SHF+82, BBdCM93, HR02, Rob99, FD98] and experimental [DGH+00, HAD+05] studies of this billiard, including detailed catalogs of periodic orbits [GMGCG01].

As in the case of mushroom billiards, the trajectories were classified in two groups: those that do not cross the inner circle of radius a= $r + \delta$ remaining in an integrable component (this region is sometimes called whispering gallery) and those that collide with the scatterer by eventually satisfying the hitting condition [SHF+82]

$$|\sin(\theta) - \delta \sin(\theta - \phi)| \leq r. \tag{4.10}$$

The hitting condition for the annular billiard plays a similar hole to the escape region in the mushroom billiard given by Eq. (4.9). The MUPOs are the complementary set of trajectories: they cross the circle of radius a, being outside the whispering gallery mode, but do not collide with the scatterer. Two examples are shown in Figs. 4.9 and 4.10, where the phase space is obtained applying the following Poincaré section: position of the collision in the outer circle $\phi \in [0, 2\pi]$ and the sine of the angle $\theta \in [-\pi/2, \pi/2]$ to the normal vector right after the collision.
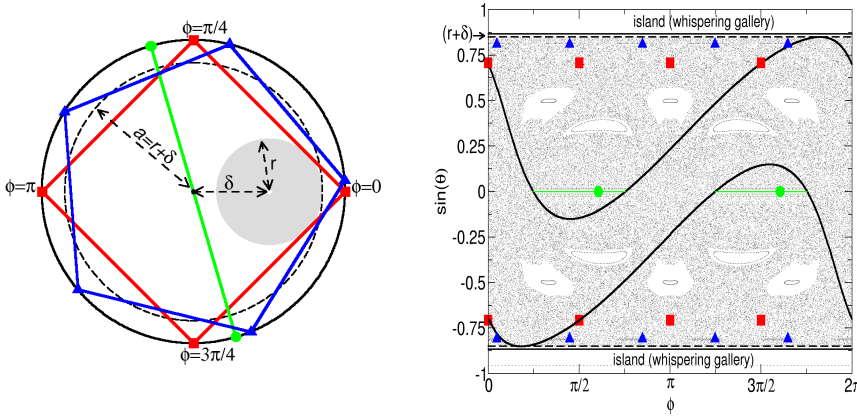

Figure 4.9: (Color online) Configuration and phase spaces of the annular billiard with $r = 0.35, \delta = 0.5$. MUPOs shown: $(5, 1), (4, 1)$, and $(2, 1)$ (inner). The region between the solid lines in the phase space corresponds to the position where relation (4.10) is satisfied.

The two conditions for existence of MUPOs expressed in Sec. 4.3.1 can also be obtained explicitly for annular billiards by noting that each MUPO of type (q, η) draws an inner regular polygon with q sides (see Sec. 4.4 for further details). Simple geometrical arguments show that a periodic orbit of type (q, η) will be an outer MUPO (q, η) if, and only if,

$$\cos(\pi \frac{\eta}{q}) < a = r + \delta < \frac{\cos(\pi \eta/q)}{\cos(\pi/q)} + r(1 - \frac{1}{\cos(\pi/q)}). \tag{4.11}$$

This equation is the equivalent version for the annular billiard from condition (4.6) obtained for the mushroom billiard. The simpler case of *inner* MUPOs also exist [like the MUPO $(2, 1)$ in Fig. 4.9 or the $(3, 1)$ in Fig. 4.10], in which case

$$\delta > \frac{r}{\cos(\pi(1 - \eta)/q)} + \cos(\pi \eta/q) + \sin(\pi \eta/q) \tan(\pi(1 - \eta)/q). \tag{4.12}$$
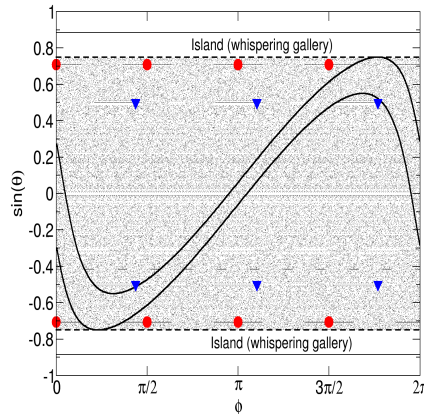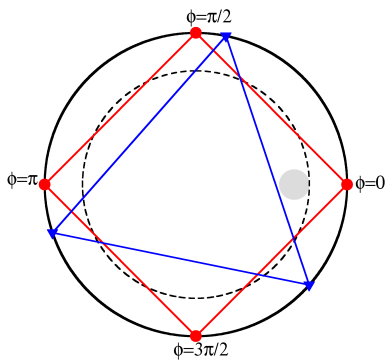
Figure 4.10: (Color online) Configuration and phase spaces of the annular billiard with $r = 0.1, \delta = 0.65$. Shown MUPOs: $(4, 1)$, and $(3, 1)$ (inner). The region between the solid lines in the phase space corresponds to the iterations when (4.10) is satisfied.

Figure 4.11 shows the regions of the parameter space (r, δ) of the annular billiard where the above inequalities are satisfied and a given MUPO (q, η) exists. In a similar way one can also find the parameter for the existence of mixed inner-outer MUPOs, i.e., trajectories that pass alternately inside and outside the scatterer. The number of different families of inner and mixed inner-outer MUPOs is limited, since for increasing period q the distance between two points is $2\pi/q$ while the width in ϕ where condition (4.10) is fulfilled remains bounded (this is better visualized in the phase space). More interesting is the case of outer MUPOs treated in detail here (for simplicity the term outer is omitted hereafter). It is show in the next Section that there are infinitely many different families of MUPOs that accumulate in the border of the whispering gallery for almost all control parameters (r, δ) below the off-diagonal in Fig. 4.11.
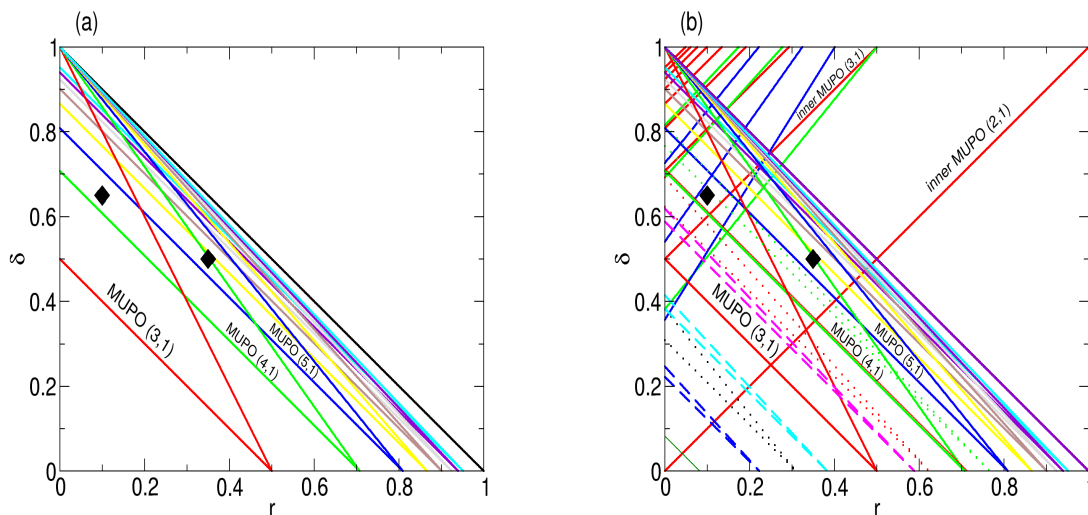

Figure 4.11: (Color) Parameter space of the annular billiard with the regions where a MUPO (q, η) exist. (a) Outer MUPOs with $\eta = 1$ and $q = 3\ldots10$. (b) All MUPOs with $q \leq 10$. The black diamonds represent the parameters used in Figs. 4.9 and 4.10.

4.4 Proof of the existence of infinite families of MUPOs

The existence of MUPOs is better formulated as a purely geometric problem, as stated in Sec. 4.3.1. This approach is adopted in this self-contained Section where a more careful mathematical formulation is needed. The correspondence with the previous notation is in most of the cases evident, e.g., star polygons used below correspond to the periodic orbits mentioned above. The final results can be easily translated to the cases of mushroom, annular, and other circular-like billiards where analogous straightforward calculations lead also to the system specific pre-factors. The main conclusion obtained here is that for a measure one set of control parameters there are an infinite number of different MUPOs. In order to arrive to this result the following simple but nontrivial geometrical problem has to be solved:

STATEMENT OF THE PROBLEM: *How many different* STAR POLYGONS *can be inscribed in a circle with the restriction that the polygon does not intercept a line segment of size r drawn from the center of the circle, but intercepts the inner circle of radius r?*

4.4.1 From geometry to number theory

A *star polygons* of type (q, η) is the figure obtained by connecting by straight lines every η-th point of q equally spaced points on a circumference. The integers q and η are called the order and the density of the star polygon, respectively, are coprime, and satisfy $2\eta < q$. A star polygon of type $(q, 1)$ is commonly known simply as *polygon*. In Fig. 4.12 a star polygon of type $(q = 5, \eta = 2)$ is shown, together with the triangles used to obtain the geometrical relations given below (for simplicity assume that the outer circle has radius $R = 1$). This polygon is a valid solution of our problem for the case $r = 0.35$, as it is illustrated in the figure. Given any parameter r, one would like to obtain the star polygons that satisfy the above mentioned conditions. In particular one wants to know if the number of star polygons of *different* type is finite or infinite. Obviously, given some star polygon, one always may obtain a star polygon of *the same type* by rotating it by a sufficiently small angle.
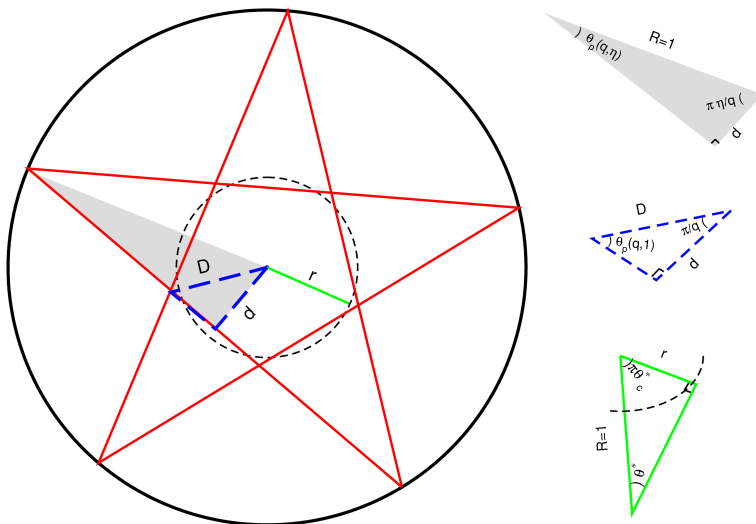

Figure 4.12: (Color online) A star polygon of type $(5, 2)$ which is a solution of the problem for the particular case $r = 0.35$ illustrated here. On the right, three different auxiliary triangles are depicted to help on the geometrical considerations.

The angle at the vertices placed on the outer circumference is given by $\theta_p(q, \eta) = \pi \frac{q - 2\eta}{2q}$, and its complementary angle is $\pi \frac{\eta}{q}$ (gray triangle in Fig. 4.12). Note that every star polygon of type (q, η) defines a central inner polygon $(q, 1)$. The radii of the inscribed and circumscribed

circles of this polygon are, respectively, given by

$$d = \cos(\pi\eta/q) \quad \text{and} \quad D = \frac{d}{\cos(\pi/q)} = \frac{\cos(\pi\eta/q)}{\cos(\pi/q)}. \tag{4.13}$$

In general, a star polygon of type (q, η) is a solution of our problem if, and only if, the circumference of radius r is in between the circumferences that inscribe and that circumscribe the central inner polygon of type $(q, 1)$. Thus, the necessary and sufficient conditions for a star polygon to be satisfied are given by

$$d \; < \; r \; < \; D, \tag{4.14}$$

or, equivalently, using (4.13), by

$$\cos(\pi\frac{\eta}{q}) < \cos(\pi\theta_c^*) \; < \; \frac{\cos(\pi\eta/q)}{\cos(\pi/q)}, \tag{4.15}$$

where $\theta_c^* = \frac{1}{\pi}acos(r)$ (see the lower triangle in Fig. 4.12). Hence, given a star polygon of type (q, η), with (4.15) the interval of parameters r for which it solves the problem is obtained. This relation is analogous to conditions (4.6) and (4.11) for mushroom and annular billiards respectively. A more interesting problem is the inverse one: given $r \in [0, 1]$, determine which polygons satisfy the inequality (4.14).

Clearly, for polygons of high order q the distance $D - d$ tends to zero. Thus, the solutions of our problem must be searched for values of $d \to r_-$ (from below). Let $\eta(q)$ denote the integer η for which $\frac{\eta}{q} - \theta_c^*$ is minimal and non-negative. The solutions of our problem will be searched in the limit

$$q \to \infty \; \Rightarrow \; \frac{\eta(q)}{q} \to (\theta_c^*)_+. \tag{4.16}$$

The error in the above approximation for a given q is defined as $\varepsilon(q) := \frac{\eta(q)}{q} - \theta_c^*$. Note that $\varepsilon(q) \to 0_+$ as $q \to \infty$. The distances $D - d$ and $r - d$, where $D = D(q, \eta)$ and $d = d(q, \eta)$ are given by (4.13), are calculated now in the limit given by (4.16)

$$D - d = \cos\left(\pi(\theta_c^* + \varepsilon(q))\right)\left(\frac{1}{\cos(\frac{\pi}{q})} - 1\right) \approx \frac{r\pi^2}{2}\frac{1}{q^2}, \tag{4.17}$$

and,

$$\begin{aligned} r - d &= \cos(\pi\theta_c^*) - \cos\left(\pi(\theta_c^* + \varepsilon(q)\right) = \cos(\pi\theta_c^*)\left(1 - \cos(\pi\varepsilon(q))\right) + \sin(\pi\theta_c^*)\sin\left(\pi\varepsilon(q)\right) \\ &\approx \sqrt{1 - r^2}\pi\varepsilon(q). \end{aligned} \tag{4.18}$$

Comparing these expressions and the inequality (4.14) one sees that the star polygon of type (q, η) is a solution of our problem if

$$\varepsilon(q) := \frac{\eta(q)}{q} - \theta_c^* < \frac{r\pi}{2\sqrt{1 - r^2}}\frac{1}{q^2}, \tag{4.19}$$

The original problem has been thus reduced to the problem of finding optimal rational approximants η/q of a real number $\theta_c^* = \frac{1}{\pi}a\cos(r)$. This is a classical problem of number theory and some well-known results in this area will be applied in the next section to solve our specific problem.

4.4.2 Approximations using continued fractions

The most efficient approximation of a real number α through rationals is obtained using its continued fraction representation (see Appendix A)

$$\alpha = a_0 + \cfrac{1}{a_1 + \cfrac{1}{a_2 + ...}} = [a_0, a_1, a_2, ...]. \tag{4.20}$$

Irrational numbers have an unique infinite representation while for rationals the representation is finite. Best approximations of α are obtained truncating the sequence of a_i since for any finite approximation (the so-called convergents) η/q there is no other fraction with denominator $q' \leq q$ which is closer to the desired number[4]. Additionally, all best approximators are convergents (or an intermediate fraction) (Theorems 15,16 and 17 of [Khi97]). The following inequality is valid for the convergents of a continued fraction representation (Theorems 9 and 13 of [Khi97])

$$\frac{1}{(a_{n+1}+2)q_n^2} \leq \frac{1}{q_n(q_n+q_{n+1})} < \underbrace{|\frac{\eta_n}{q_n} - \alpha|}_{\varepsilon(q)} < \frac{1}{q_n q_{n+1}} \leq \frac{1}{a_{n+1}q_n^2}. \tag{4.21}$$

Altogether this means that the lower-bounds in relation (4.21) are valid for all possible fractional approximations and that the upper-bounds are valid for all convergents[5]. In terms of the problem described in Sec. 4.4.1, the number α to be expanded is $\theta_c^* \equiv \frac{1}{\pi}\arccos(r)$ and any convergent η/q of the representation of α corresponds to some star polygon of type (q, η). Interestingly, the dependence of the error $\varepsilon(q) \propto 1/q^2$ given in (4.21) is the same as the asymptotic dependence of $D - d$ given by Eq. (4.17) and obtained through a geometrical analysis. In other words, the approximation of a circumference using star polygons is optimal. This shows that the existence of infinitely many star polygons satisfying inequality (4.15) depends on the pre-factors of the lower and upper bounds of (4.19) and (4.21). These pre-factors depend on the "degree of irrationality" (see Appendix B) of the critical angle θ_c^*. The solutions of the proposed problem are obtained below for boundary circles belonging to two important classes of irrational numbers.

The noble numbers

To get some intuition consider initially the class of noble numbers, i.e, those numbers which have continued fraction representation ending in a sequence of 1's:

$$\{[a_1, a_2, ..., a_{n^*}, 1, 1, 1...]\}.$$

This set is dense in $\mathcal{R}$, what means that, given any value of $r > 0$, there is a value r_n arbitrarily close to r so that

$$\theta_c^* \equiv \frac{1}{\pi}\arccos(r_n)\text{belonging to the set of noble numbers.}$$

For large enough q the upper and lower bounds of the error $\varepsilon(q)$ of noble numbers is obtained substituting $a_{n+1} = 1$ in inequality (4.21). Using the extremes (leftmost hand side and rightmost

---

[4]Even-order convergents form an increasing and odd-order convergents a decreasing sequence approaching α (Theorem 4 of [Khi97]). If one takes $''-''$ signs instead of $''+''$ in Eq. (4.20) all convergents form a decreasing sequence, in agreement with the limit proposed in Eq. (4.16).

[5]For rational numbers the continued fraction is finite and the "approximation" is finally exact when the terms q_{n+1}, a_{n+1} are not defined. For irrational numbers, on the other hand, the infinite sequence of terms provide an infinite number of convergents.

hand side) of (4.21) one obtains that $\frac{1}{3} < q^2 \varepsilon(q) < 1$.[6] In Fig. 4.13 a sketch of the comparison between $D - d$ and $r - d$ is presented. The units and the pre-factors are chosen in such a way that the distance $(D - d)$ corresponds to 1. In this case $r - d \propto \frac{\sqrt{1-r^2}}{r}$, which $\to 0, \infty$ when $r \to 1, 0$. This shows that for noble numbers it is always possible to find large enough values of r for which $r - d < D - d$ (infinite polygons exist) and small enough values of r for which $r - d > D - d$ (finite number of polygons).

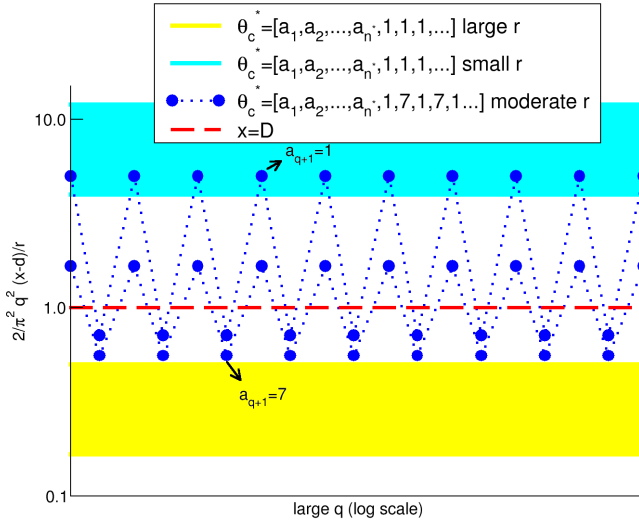**Figure 4.13:** (Color online) Normalized distances as a function of the polygon order $q \in Z^*$. The two horizontal stripes and the zig-zag stripe represent the region where the convergents of the continued fractions approximations of θ_c^* lie (see legend). If they lie below the dashed line, it is a valid polygon, and if they lye above they are not a valid solution.

The set of numbers $\mathcal{F}$

The reasoning above motivates us to introduce the set $\mathcal{F}$ of the numbers that have a continued fraction representation which has only a finite number of terms a_i that appear infinitely often. More formally

Definition:

Given $N \in \mathbb{N}$ let
$$\mathcal{F}_N = \{[a_1, a_2, ...] : \#\{k : a_k = N\} = \infty, \#\{k : a_k > A\} < \infty, \forall A > N\},$$
$$\mathcal{F} = \bigcup_{N \geq 1} \mathcal{F}_N \tag{4.22}$$
$$n^* := \max\{k : [a_1, a_2, ...] \in \mathcal{F}^N \text{ and } a_k > N\}.$$

N is the maximum value of a_i in the representation that appears infinitely often and precisely the maximum whenever $i > n^*$. Noble numbers are equivalent to $\mathcal{F}_\infty$. The following properties of $\mathcal{F}$ hold:

1. $\mathcal{F} \subset \mathbb{R} \backslash \mathbb{Q}$, since any rational has a finite continued fraction representation.

2. All set $\mathcal{F}_N$ are dense in $\mathbb{R}$.

3. $\mathcal{F} = \bigcup_{N \geq 1} \mathcal{F}_N$ is the set of numbers of constant type, i.e., the numbers which have a bounded continued fraction representation. This set has Lebesgue measure zero (see Appendix A and theorem 29 of [Khi97]).

---

[6]A lower upper bound may be obtained for this case considering that $\varepsilon(q) \leq \frac{1}{\sqrt{5}q^2}$ (Theorem 20 of [Khi97]).

4.4.3 Solution of the problem

From the previous results it is possible to divide the interval $r \in [0,1]$ into sets where there are an infinite or a finite number of star polygons that solve our problem. Intervals will be defined in terms of the angle $\theta_c^*(r) \equiv \frac{1}{\pi}\arccos(r)$ and of the number $\rho(b) := \sqrt{\frac{1}{(\frac{b\pi}{2})^2+1}}$, which is the solution for $r > 0$ of the equation $\frac{1}{bq^2} = \frac{\pi}{2}\frac{r}{\sqrt{1-r^2}}\frac{1}{q^2}$ [see inequalities (4.19) and (4.21), $b \in \mathbb{R}$].

Typical real numbers are not of constant type (see Appendix B), meaning that the sequence of a_i in (4.20) is unbounded and arbitrarily small bounds in inequality (4.21) are obtained. This implies that for almost all parameters r (except sets of measure zero) there are infinitely many solutions and the convergents of the continued fractions give an infinite (possibly not all) number of them. For $r > \rho(\sqrt{5}) \approx 0.27382357...$ all values of r, with $\theta_c^*(r)$ irrational, have infinitely many solutions. However, for r_0 small there is an infinite, not countable set $R \subset [0, r_0]$ which is dense in $[0, r_0]$ and for which only a finite number of solutions exists. Note that since $r = \cos(\pi\theta_c^*)$, the results about the measure of sets in θ_c^* can be applied to r. See also Appendix A for further details on how the continued fraction representation can be used to classify the real numbers.

Parameters r with a finite number of solutions

- $\theta_c^*(r) \in \mathbb{Q}, \forall r$, since the rationals have a finite continued fraction representation and there is no other way to approach a rational by rationals that is as fast as $1/q^2$.

- $\theta_c^*(r) \in \mathcal{F}^N$, with $0 < r < \rho(N+2)$.

Parameters r with infinitely many solutions

- $\theta_c^*(r) \in \mathbb{R}\backslash(\mathcal{F} \cup \mathbb{Q}), \forall r$, i.e., all irrational numbers that are not numbers of constant type. This set has full Lebesgue measure meaning that almost all parameter r lead to a $\theta_c^*(r)$ in this set.

- $\theta_c^*(r) \in \mathcal{F}_N$, with $\rho(N) < r \leq 1$. If $N = 1, 2$: $\rho(\sqrt{5}) < r \leq 1$.

The proof sketched above is constructive and provides a method to efficiently obtain the types (q, η) of outer MUPOs for a given billiard. It consists in verifying if the convergents of $\varphi = \arccos(a)/\pi$ satisfy the conditions of existence of MUPOs [condition (4.6) for mushroom and (4.11) for annular billiards]. Apart from the sets of zero measure discussed above, for all billiards configurations an infinite number of MUPOs can be found among the convergents (not necessary *all* outer-MUPOs are convergents). For instance, for the parameters $r = 0.35, \delta = 0.5$ of Fig. 4.9 all odd convergents tested are MUPOs: $(5, 1), (11, 2), (436, 77), (1342, 237), ...$ [the MUPO $(4, 1)$ is not a convergent]. On the other hand, for $r = 0.3, \delta = 0.1$ the first MUPOs found through this method are $(14921, 5506)$ and $(7379467, 2723098)$.

4.5 Numerical results for the stickiness

The existence of infinite families of MUPOs is a generic property of circular-like billiards. These orbits concentrate close to the boundary of the regular island corresponding to the trajectories that avoid collisions with inner obstacles (whispering gallery modes). The existence and characterization of the distribution of such orbits, performed in the two previous sections may have different implications, e.g., the structure of the MUPOs close to the border of the main island may provide a better comprehension for the so-called "beach modes" that were proven to play an important role in experiments of chaos assisted tunneling [FD98, DGH$^+$00, HAD$^+$05].

The stickiness phenomena studied numerically below corresponds to another phenomena where these orbits are relevant. From the stickiness theory developed in Sec. 4.2 an exponent $\gamma = 2$ is expected.
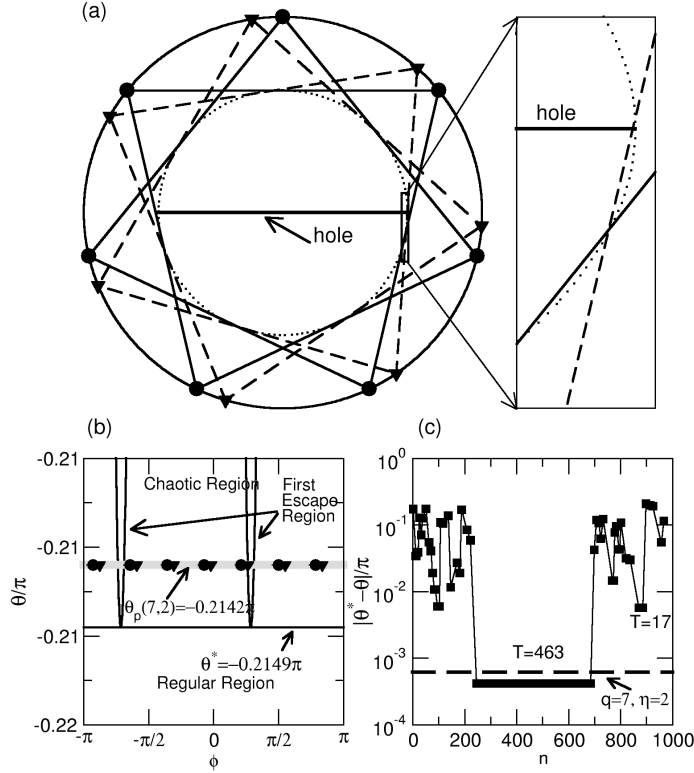

Figure 4.14: Detailed analysis of orbits $(q = 7, \eta = 2)$ for $r/R = 0.6125$. (a) Configuration space, where two orbits $(q = 7, \eta = 2)$ that cross the circle with radius r are shown. The orbit represented by circles (●) does not hit the hole, while the orbit represented by triangles (▼) hits the hole on the right-hand side (see amplification). (b) Phase-space representation of the orbits in (a), where it is shown that they are respectively outside and inside the first escape region. A small perturbation in the reflection angle θ of the first orbit leads to a continuous rotation of the orbit in (a) [horizontal drift in (b)] until the trajectory hits the hole [enters the first escape region in (b)]. (c) Time evolution of the distance from the regular region to a chaotic trajectory that approaches the family of MUPOs $(q = 7, \eta = 2)$ in the original mushroom billiard. Events with recurrence time $T = 463$ and $T = 17$ are highlighted. The events with large recurrence times are associated with approaches to the MUPOs.

Figure 4.14 shows a detailed analysis of the mushroom billiard (introduced in Sec.4.3.2) with parameter $r/R = 0.6125$, where the MUPO $(7, 2)$ play a major role. Such orbits are illustrated in the configuration and phase spaces. In particular, Fig. 4.14(c) shows that long trapping times are obtained when the chaotic trajectory of the mushroom billiards approaches the MUPO $(7, 2)$, not necessarily the border of the islands. In order to compute the RTS the whole foot of the mushroom was taken as the recurrence region meaning that the recurrence time T corresponds to the time the trajectory spends inside the semi-circular hat of the mushroom. Our main observations about the RTS in mushroom billiards are illustrated in Fig. 4.15 and can be summarized as follows:

(*i*) The recurrence times T for which recurrences are observed appear in a very organized way: times without a single recurrence $[P(T) = 0]$ are periodically interrupted by times with a high recurrence time probability. The period t_0 between successive times with positive probability $[P(T) > 0]$ strongly depends on the control parameter r/R and may change over large intervals of time T. In particular, as shown in the inset of Fig. 4.15 for recurrence times in the interval $50 < T < 150$, this period is $t_0 = 5$ for $r/R = 0.5$ and $t_0 = 11$ for $r/R = 0.6125$. For longer recurrence times, higher periods may coexist with short periods.

(*ii*) The overall behavior of the RTS $\rho(\tau)$ presents a clear power-law tail with exponent $\gamma = 2$, independently of the parameter r/R.
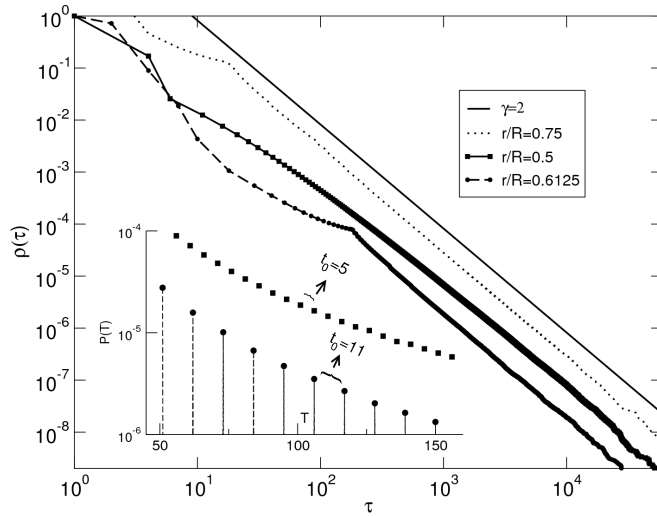
Figure 4.15: RTS of the mushroom billiard for various choices of the control parameter r/R. The results are consistent with a power-law tail with exponent $\gamma = 2$. The distribution for $r/R = 0.75$ was shifted vertically upward by one decade for clarity. Inset: the distribution $P(T)$ in the interval $50 < T < 150$ for $r/R = 0.5$ ($t_0 = 5$) and $r/R = 0.6125$ ($t_0 = 11$).

While observation *(ii)* is explained by the stickiness theory of Sec. 4.2, observation *(i)* can be explained through the approach to the MUPOs by the following analysis. When a chaotic trajectory visits the hat of the billiard, the approach to as well as the escape from the neighborhood of a family of MUPOs takes place in a single time step, as illustrated in Fig. 4.14c by a sharp transition before and after the interval of minimum distance to the island. Due to the injection of trajectories from the foot of the mushroom billiard, the approach to the MUPOs (that requires an angle θ close to θ_p) can only occur close to some of the q periodic points of the MUPO. Actually, it happens always near the same position in the mushrooms hat, right above the intersection point between the boundary of the foot and the bottom part of the hat (i.e., one of the two horizontal lines). Similarly, the escape occurs always when the trajectory is close to the point of the MUPO that lies in the bottom part of the mushrooms hat. Due to these constraints, the intervals of time a chaotic trajectory that approaches a family of MUPOs spends away from the mushrooms foot form a sequence that can be written as $T_i = a - 1 + (q + 2\eta)i$, where $i \in \mathbb{N}$ and a is the time between the first collision in the semi-circular hat and the collision in the bottom part of the hat (close to the hole). The period t_0 between successive recurrence times with positive probability, as point *(i)* above, is thus related to the period q and the rotation number η of the MUPO inside the chaotic region according to

$$t_0 = q + 2\eta . \tag{4.23}$$

The factor 2η comes from the fact that, in contrast with the open circular billiard, in the mushroom billiard one counts the collisions in the bottom of the hat. In Fig. 4.6 it is apparent that for $r/R = 0.5$ the orbit ($q = 3, \eta = 1$) is exactly at the border between the regular island and the chaotic region. Through Eq. (4.23) one obtains $t_0 = 5$, explaining the numerical observation. Analogously for the parameter $r/R = 0.6125$, shown in Fig. 4.14, the MUPO ($q = 7, \eta = 2$) is present and imply $t_0 = 11$, exactly as observed numerically. Higher-order periodicities are associated with the existence of additional families of MUPOs in the chaotic sea.

After the publications of these results in Ref. [AMK05] different publications investigated similar issues in mushroom billiards through different approaches. The Slater theorem [Sla67] was proposed to explain the patterns described above in Ref. [DFMO+06]. The method is based on the quasi-periodic dynamics of the trajectories in the hat of the mushroom and is valid for all recurrence times. For large times only the quasi-periodic trajectories close to the MUPOs survive and the two approaches are expected to be equivalent. Another very recent publication confirm

both results described above through a detailed analysis of the escape regions [Miy06]. Additionally, the escapes from mushroom billiards with parabolic hat was investigated in Ref. [TS06]. See also Refs. [LPB06, LP06] for the classical investigation of many particles in mushroom billiards and Ref. [BB06] for a study in quantum chaos.

In opposite to mushrooms, annular billiards (introduced in Sec. 4.3.3) may have further KAM islands apart from the trajectories that do not collide with the inner scatterer, as shown in Fig. 4.10. The stickiness to these structures obviously violates the theory developed in Sec. 4.2. Therefore, control parameters of the annular billiard where no further islands are apparent are chosen here (see Sec. 5.3 for the other case). One example is the case $r = 0.1, \delta = 0.65$ illustrated in Fig. 4.10. In Ref. [SHF$^+$82] it is argued that this occurs always when $r > 3\delta$. Figure 4.16 shows the RTS for the annular billiard with two such parameters, where the exponent $\gamma = 2$ is apparent. The stickiness in the case of further islands is investigated in Sec. 5.3.

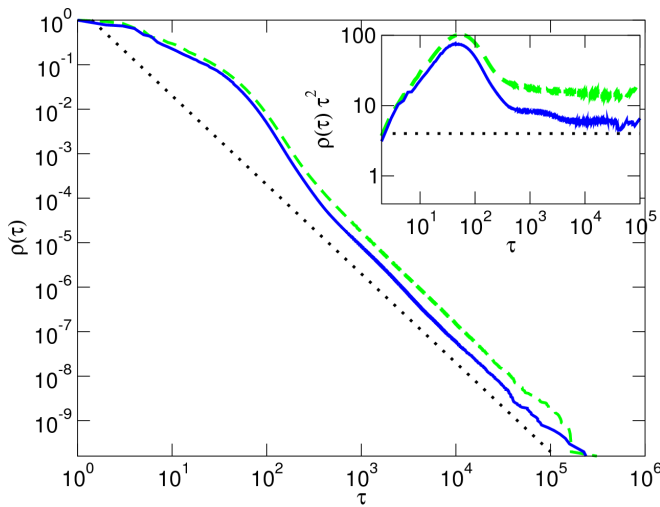

Figure 4.16: RTS for two different configurations of the annular billiard are shown: dashed-line $r = 0.1, \delta = 0.65$ (as in Fig. 4.10) and solid-line $r = 0.25, \delta = 0.5$. In both cases, apart from the whispering gallery, there are no further regular islands observed in the phase space and a decay consistent with $\gamma = 2$ (dotted line) is observed, as emphasized in the inset.

Chapter 5

From sharply-divided to hierarchical phase space

The stickiness theory applied in the previous Chapter for billiards is extended to a larger class of systems having sharply-divided phase space, i.e., non-hierarchical border between regular and chaotic regions (Sec. 5.1). This is done by showing that the exponent $\gamma = 2$ describes also the stickiness in piecewise-linear maps having isolated islands of polygonal shape. These systems, however, are not robust to generic perturbations that lead to a hierarchical phase space. This is illustrated considering mushroom billiards perturbed through a magnetic field (Sec. 5.2). The numerical results for the stickiness in this case, as well as in the annular billiard with the coexistence of sharp and hierarchical borders (Sec. 5.3), indicate a more efficient trapping in the hierarchical than in the sharply-divided phase space ($\gamma < 2$).

5.1 Maps with sharply-divided phase space

5.1.1 Piecewise-linear maps

In the previous Chapter a stickiness theory based on the MUPOs was developed, and confirmed for the mushroom and annular billiards. These billiards have a simple well-defined border between the chaotic component and the island of regular motion (whispering gallery). In this Section area-preserving maps with the same property are studied.

Consider two-dimensional maps of the form

$$\begin{aligned} y_{n+1} &= y_n + K f(x_n) \qquad \text{mod} \ \ 1, \\ x_{n+1} &= x_n + y_{n+1} \qquad \text{mod} \ \ 1, \end{aligned} \qquad (5.1)$$

where $f(x)$ is a non-linear function to be specified and K is a parameter that controls the non-linearity. Note that map (5.1) satisfies the symplectic condition (2.3) being thus area-preserving (Hamiltonian).

For $f(x_n) = \sin(2\pi x_n)$, Eq. (5.1) corresponds to the standard map, introduced in Eq. (2.14) and which has served as a prototype of Hamiltonian system in numerous studies of stickiness [Kar83, Zas02a, WBKZ98, CS99, WHK02a]. As argued in Chap. 2 the *hierarchical phase space* of the standard map, illustrated in Fig. 2.1, is a representative example of a larger class of near-integrable systems. The interpretation of this phase space was intimately connected to the KAM theory.

However, for $f(x_n)$ defined as a piecewise-linear function of the interval $x_n \in [0, 1]$, the map (5.1) show *sharply-divided phase space*, in the sense that regular and chaotic regions are separated

by a simple curve [Woj81]. As shown in Refs. [Woj81, Ash97], the shape and distribution of the regular regions depend on the function f and on the parameter K. Sharply-divided phase space is possible in these systems due to the violation of the hypothesis of the KAM theorem stated in Sec. (2.1.2): two-dimensional maps have to be at least of class C^3 (i.e., three continuous derivatives have to exist) [Mei92, Sev98]. The origin of the sharp border in the circular billiards discussed in Chap. 4 is the singularity created by the difference between trajectories that hit the region where the obstacles exist [Fig. 4.4(b)] and those that do not hit, what introduces some discontinuity in the dynamics[1]. The original motivation to study such maps was that analytical results about the coexistence of regular and chaotic motion obtained in this case [Woj81]. The sharply-divided phase space studied below have always a finite number of regions of regular motion (see Ref. [Ash97] for a different case) in opposite to the generic *hierarchical* KAM phase space.

The following two examples of piecewise linear maps are considered below:
(i) The first example is obtained introducing in map (5.1) the function

$$f(x_n) = 1 - |2x_n - 1|. \tag{5.2}$$

This map was called *continuous sawtooth map* in Ref. [MP02]. where it was argued that for $K = 1.5$ a single regular island exists [Fig. 5.2(a), triangular region].
(ii) A second example of sharply-divided phase space is obtained introducing in map (5.1) the function

$$f(x_n) = \begin{cases} -x_n & \text{if} \quad 0 \leq x_n < 1/4, \\ -1/2 + x_n & \text{if } 1/4 \leq x_n < 3/4, \\ 1 - x_n & \text{if } 3/4 \leq x_n \leq 1, \end{cases} \tag{5.3}$$

as considered in Ref. [Lee98]. The functions (5.2) and (5.3) are illustrated in Fig. 5.1, where one sees that function (5.3) can be thought as a discretization of a sinus, what was the original motivation on Ref. [Lee98].
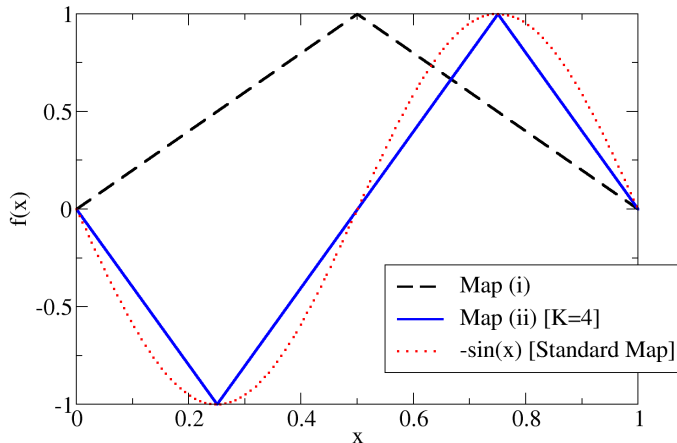

Figure 5.1: Illustration of the piecewise-linear functions (5.2) [map (i)] and (5.3) [map (ii)]. In the last case, the function was multiplied by a factor $K = 4$.

Map *(ii)*, obtain using Eq. (5.3), is equivalent to the map considered in Ref. [Woj81][2], where

---

[1]Rigorously, the KAM theorem does not apply for any kind of billiard since the Hamiltonian is defined by potentials that assume infinite values at the borders.

[2]The equivalence can be obtained taking the inverse of map (5.1) (5.3) and performing a transformation of variable $y \rightarrow -y$

the following interesting picture of the phase space is described: for $K > 4$ a single chaotic component exists, while for $K < 4$ there is an isolated island of regular motion with elliptical shape if

$$\frac{1}{\pi} \arccos(\frac{K}{2} - 1) \in \mathcal{R}/\mathcal{Q} \text{ (,i.e., it is an irrational number)}, \tag{5.4}$$

and a polygonal shape otherwise. In Secs. 5.1.2 and 5.1.3 the stickiness in phase spaces with such polygonal and elliptical islands, respectively, are studied.

5.1.2 Regular islands of polygonal shape

Control parameters K in Eq. (5.1) that lead to sharply-divided phase space with polygonal-shape islands are considered here. According to the discussion in Sec. 5.1.1 this occurs for map *(ii)* when condition 5.4 is violated. Three different example are illustrated in Fig. 5.2. Apart from the islands with polygonal shape, in may cases additional families of MUPOs (marginally unstable periodic orbits), discussed in detail in Chap. 4, are visible, e.g., in Fig. 5.2(a).
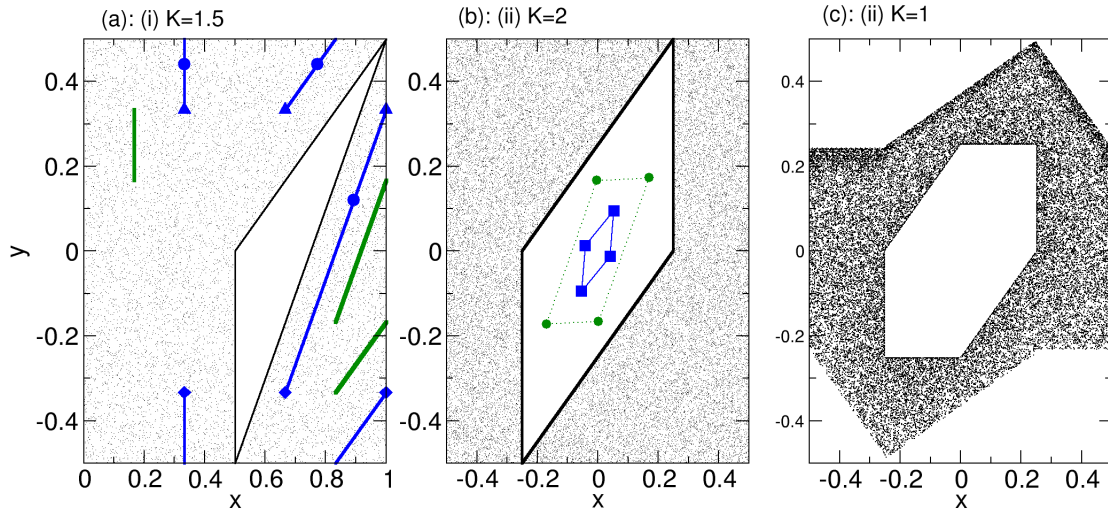

Figure 5.2: (Color online) Phase space of the piecewise-linear maps discussed in Sec. 5.1.1. Black dots correspond to a single chaotic trajectory. Inside the polygonal white regions all trajectories are periodic with the period corresponding to the number of sides of the polygon. (a) Map (i) with $K = 1.5$, and two additional families of MUPOs with period 3 shown by straight lines and symbols; (b) map (ii) with $K = 2$ where two trajectories inside the islands are represented by symbols, and map (ii) with $K = 1$.

Concerning the stickiness close to the regular islands, the relevant component is the border between the chaotic and regular regions. Since the whole regular region is build by periodic orbits with the same period [see Fig. 5.2(b)], the border to the chaotic component is composed by periodic orbit that have marginal stability. The stickiness theory developed in Sec. 4.2 is expected to be valid. Indeed, this is confirmed in Fig. 5.3 where the exponent $\gamma = 2$ is apparent for all the numerically obtained RTS.

The stickiness is investigated further in Fig. 5.4 where the regions of the phase space that survive for long times close to the island are depicted for $n' = 1, 2, 4$ and 1000 iterations of the map (5.1)-(5.2). This figure is analogous to Fig. 4.8 for the mushroom billiard. As expected, the general tendency is that the closer to the island the longer it will take for the trajectory to leave.
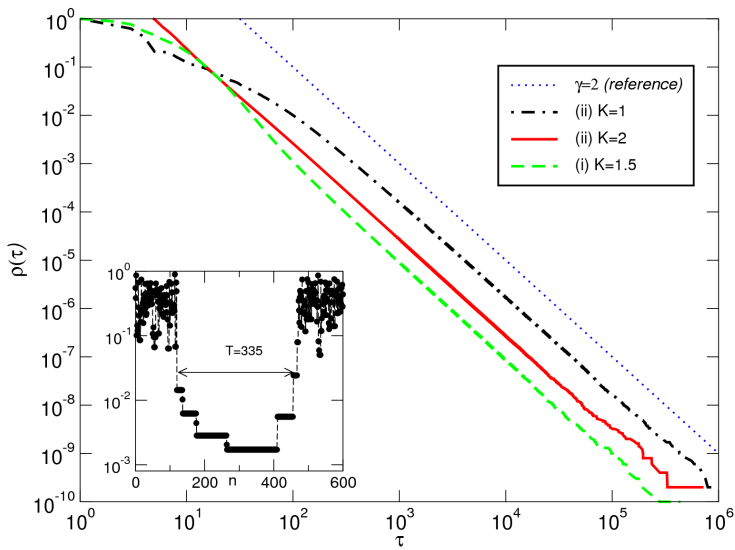
Figure 5.3: (Color online) RTS for the three maps illustrated in Fig. 5.2 (see legend). In all cases the agreement with the exponent $\gamma = 2$ is apparent. The middle curve was multiplied by a factor of 5 for clarity. Inset: distance of a chaotic trajectory to the the border of the island in Fig. 5.2a during an event with recurrence time $T = 335$.
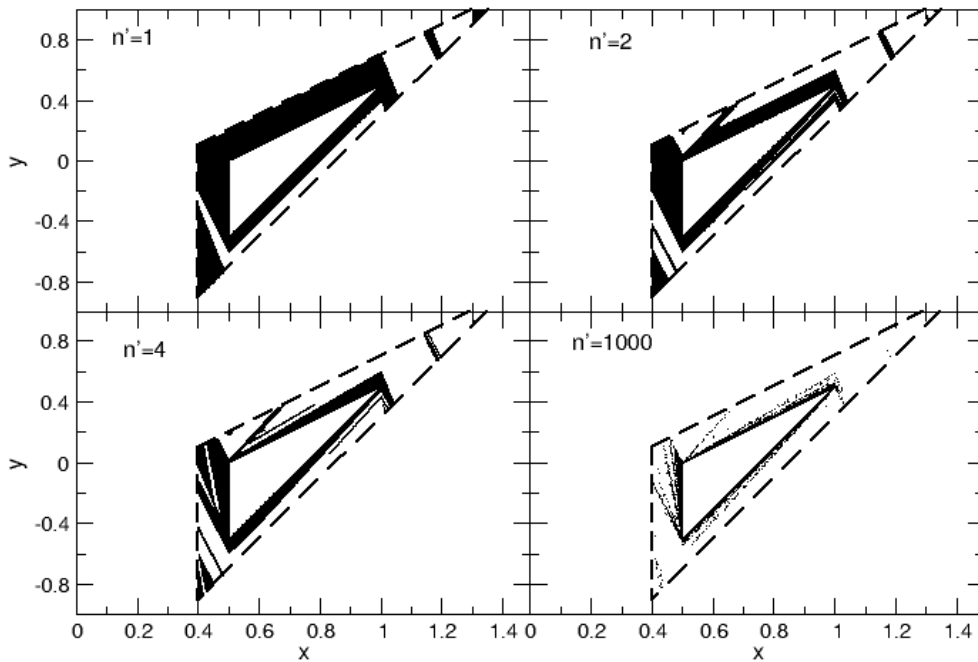
Figure 5.4: Phase-space portrait of map (i) with $K = 3/2$ [as in Fig. 5.2(a)] showing the initial conditions of the trajectories that remain inside the dashed triangle for at least $n' = 1, 2, 4$ and 1000 iterations of the map, respectively. The inner triangle corresponds to the regular island. For visualization convenience the plot is shown between $0 \leq x \leq 1.5$ and $-1 \leq x \leq 1$.

However, while for mushroom the escape regions are tangent to the island and the injection and escape occur in a single iteration, for the case illustrated in Fig. 5.4 the escape/approach of trajectories from/to the island take more iterations. This effect is also illustrated in the inset of

Fig. 5.3, which has to be compared to Fig. 4.14(c) for mushroom billiards.

5.1.3 Regular islands of elliptical shape

Control parameters K in Eq. (5.1) that lead to sharply-divided phase space with elliptical-shape islands are considered here. According to the discussion in Sec. 5.1.1 this occurs for map *(ii)* when condition (5.4) is fulfilled, which is the typical case. Three different example are illustrated in Fig. 5.5. Apart from the elliptical region no further islands are observed.
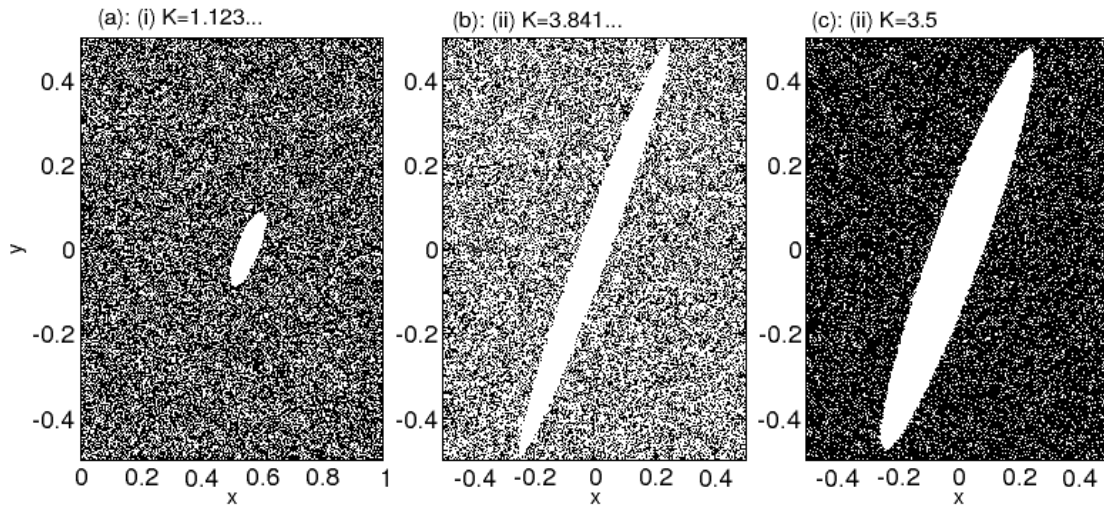
Figure 5.5: (Color online) Phase space of the piecewise-linear maps discussed in Sec. 5.1.1. Black dots correspond to a single chaotic trajectory and white regions to a single regular island with elliptical shape (no further islands are visible). Inside the elliptical white regions all trajectories are quasi-periodic and draw ellipses similar to the border of the island. (a) Map (i) with $K = 1.123...$, (b) map (ii) with $K = 3.841...$, and map (ii) with $K = 3.5$.

Figure 5.6: (Color online) RTS for the three maps illustrated in Fig. 5.5 (see legend). In all cases there are strong oscillations and no agreement with the exponent $\gamma = 2$ is observed for the values of the recurrence time depicted here.

The border between islands with elliptical shape and the chaotic component are no longer built by MUPOs, as was the case in Sec. 5.1.2, but by a quasi-periodic trajectory. It is thus not a surprise that the RTS illustrated in Fig. 5.6, for the three maps illustrated in Fig. 5.5, do not follow the exponent $\gamma = 2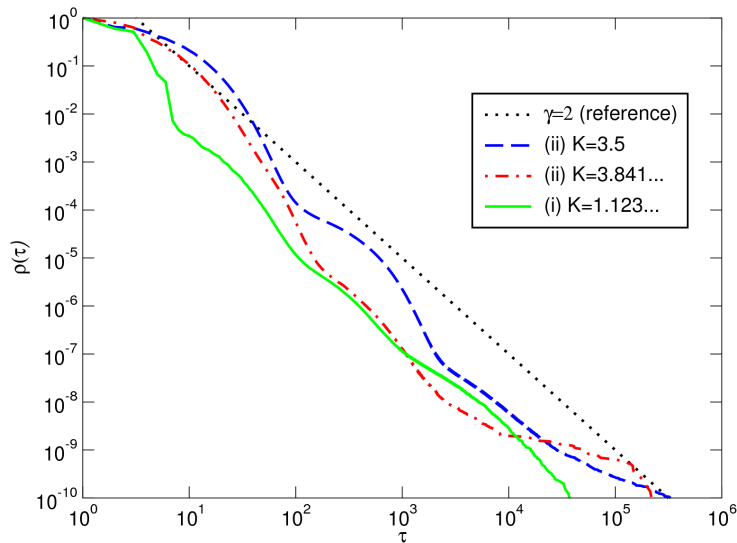$. On the other hand, it is quite surprising that strong oscillations appear already for simple *non-hierarchical* phase-spaces. In general, the estimation $\gamma = 2$ seems not to be so far from an average behavior and one cannot rule out the possibility that a well defined power-law exponent would be obtained for longer times. However, an explanation for the stickiness in sharply-divided phase space with islands with elliptical shape is not provided in this Thesis, and remains as an open question.
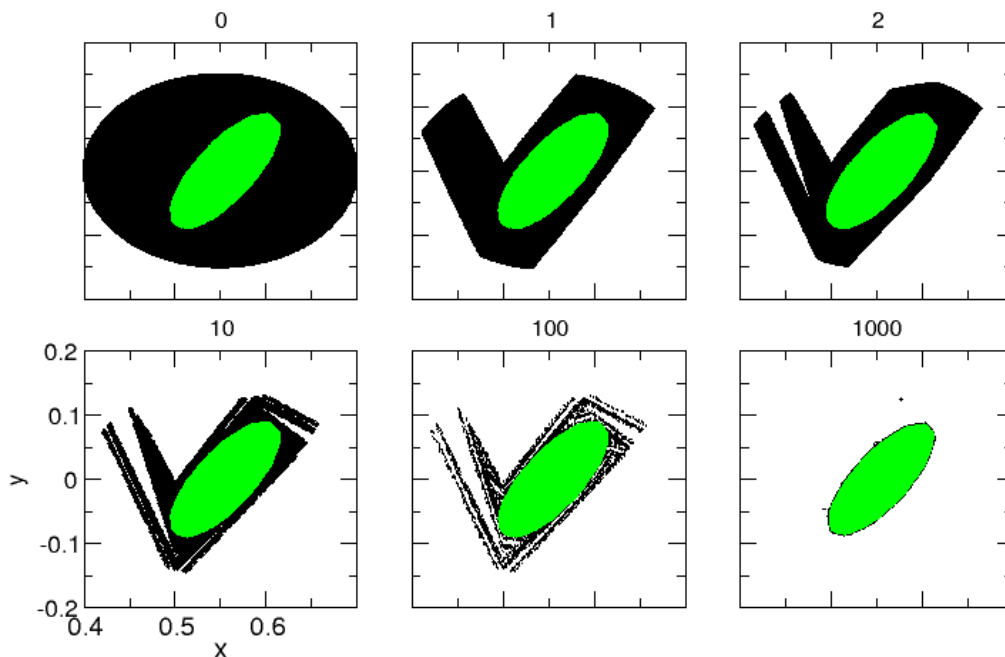
Figure 5.7: (Color online) Phases pace of map (i) with $K = 1.123...$ [as in Fig. 5.5(a)] showing the initial conditions of the trajectories that remain inside the large black ellipses of the upper-left figure at least $n' = 0, 1, 2, 10, 100$ and 1000 iterations of the map, respectively. The inner (green/light gray) ellipse corresponds to the regular island.

A numerical investigation of the escape of trajectories close to the islands with elliptical shape is provided in Fig. 5.7, which has to be compared with Figs. 4.8 for the mushroom billiard and 5.4 for the case of islands of polygonal shape. The general behavior is the same as in the case of polygonal-shape islands: for long times the trajectories concentrate close to the border of the island.

5.2   Perturbed mushroom billiards

Hamiltonian systems with sharply-divided phase space are not generic. This means that they are not robust to small perturbations, as considered in detail below, that lead to the problem of stickiness in Hamiltonian systems with the usual complex hierarchy of infinitely many KAM

islands and cantori described in Chap. 2. As a model system the mushroom billiard introduced in Sec. 4.3.2 is considered and as perturbation a magnetic field is considered. This *magnetic* mushroom billiard allows for a direct comparison between the effects of hierarchical and non-hierarchical borders.

5.2.1 Perturbation of non-hierarchical borders

A common feature of the systems considered in the previous sections is that their dynamics is piecewise smooth and presents abrupt changes. These abrupt changes, generated by non-smooth functions f in map (5.1) and sharp corners in the mushroom billiard, are responsible for the creation of sharply-divided phase spaces. Generic perturbations of these systems are expected to smooth the dynamics and introduce hierarchies of KAM islands and cantori. Examples of such perturbations include to smoothen functions (5.2) or (5.3) in the case of piecewise-linear maps and soften the walls in the case of mushroom billiards. In the case of a billiard with charged particles, a suitable perturbation is performed by introducing a magnetic field, as studied below.

Consider the mushroom billiard, studied in Sec. 4.3.2 subject to uniform transverse magnetic field B and consider the dynamics of charged particles within this billiard. Due to the Lorentz force, the charged particles move on circular orbits. The charge of the particles and orientation of the magnetic field are chosen such that the trajectories are oriented counter-clockwise and have radius

$$L \propto \frac{1}{B} \, , \tag{5.5}$$

which is used as a control parameter. This parameter has to be compared with the geometric scales of the billiard defined in Fig. 4.5(a) (in our simulations we use $R = 2$ and $r = 1$). The unperturbed mushroom billiard corresponds to $L = \infty$.

Previous works on magnetic billiards [RB85] have shown that the curvature of the trajectories often leads to the creation of KAM tori [BKT94, dSdA00] in fully chaotic systems and chaotic regions [MBG93] in integrable systems. Mushroom billiards have both integrable and chaotic regions in the phase space and both effects are expected to take place. More interestingly, mushroom billiards also have MUPOs that are expected to undergo a transformation when the system is perturbed. Indeed, because the eigenvalues associated to these orbits are real and have modulus 1, arbitrarily small perturbations are expected to generate elliptic or saddle points in the neighborhood of the regular island of the unperturbed billiard. Since there are usually an infinite number of families of MUPOs close to the sharp border (as shown in Sec. 4.4), one sees that an infinite hierarchy of islands around islands is created. These effects of the magnetic field in the mushroom billiard are shown in Fig. 5.8, where a representative magnification of the phase space at the border of chaos is shown for different values of L. The hierarchy of KAM islands and cantori are clearly visible, providing evidence that the complete picture of Hamiltonian chaos is obtained in magnetic mushroom billiards.

The emergence of complex structures of KAM islands in the phase space influences the stickiness, as shown in Fig. 5.9 for the RTS of magnetic mushroom billiards with $L = 100$ and $L = 50$. Comparing these distributions with those of the unperturbed system ($L = \infty$), one notes the presence of fluctuations around a slower power-law tendency ($\gamma < 2$). This result indicates that, as intuitively expected, a hierarchical border sticks the trajectories in a more effective way than a non-hierarchical border. This is also in agreement with the results of Ref. [CK], verified in Fig. 2.3, where an universal exponent $\gamma \approx 1.6$ is suggested. One could expect that the outermost torus of a regular island, which is marginally unstable, could play the role of the MUPOs described in Sec. 4.2. However, there is usually an infinite number of cantori that accumulate near the island invalidating relations (4.1) and (4.2) and thus the derivation of the exponent $\gamma = 2$. In the next section a carefully study of the effect of such partial transport
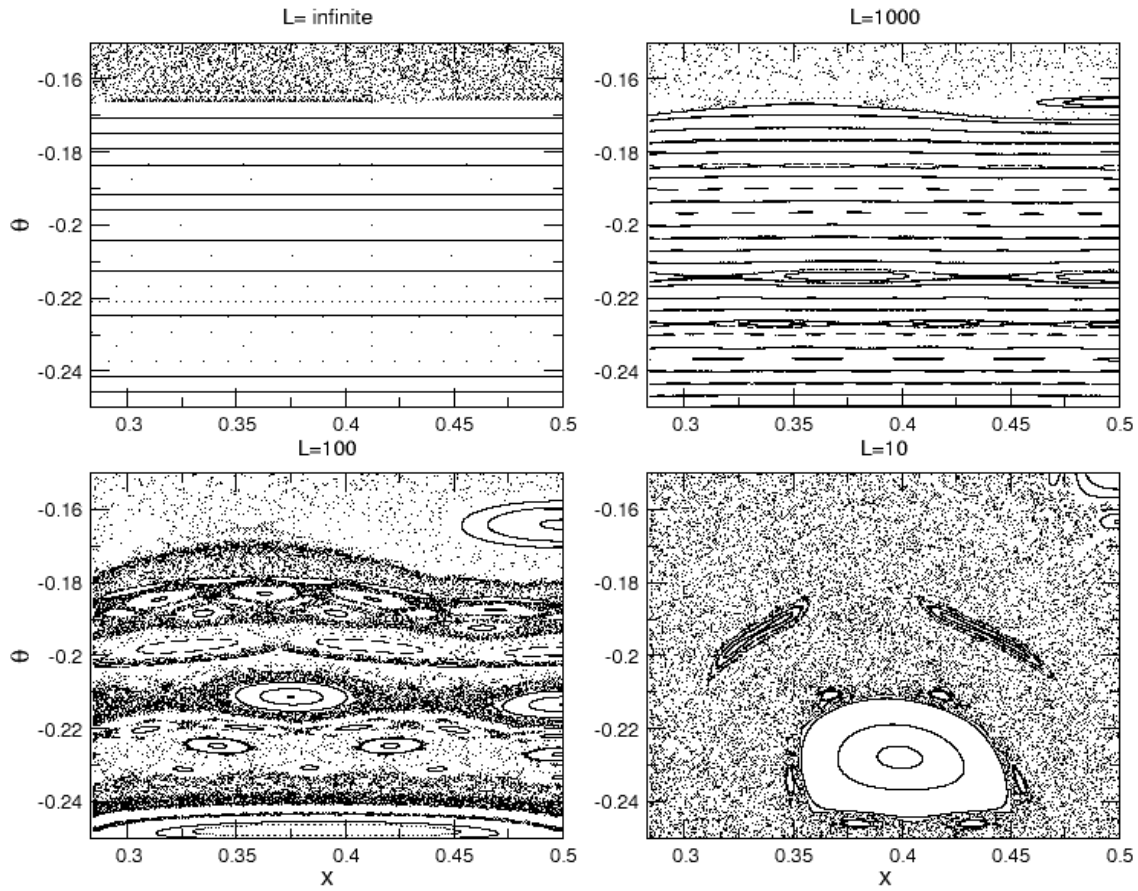
Figure 5.8: Magnification of the phase-space portrait of the magnetic mushroom billiard at the border between the chaotic and regular regions for $r/R = 0.5$ and various values of the magnetic field.
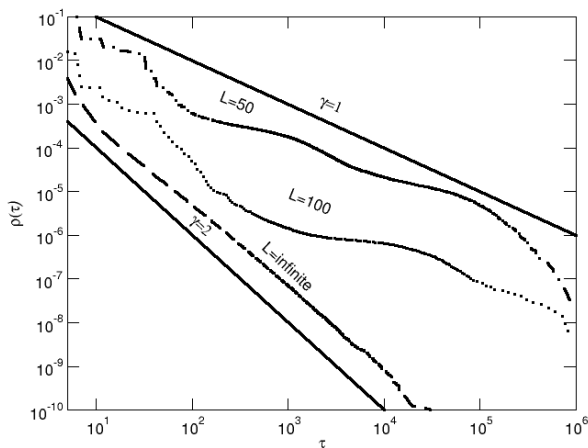
Figure 5.9: RTS for the magnetic mushroom billiard with $r/R = 0.5$ and different values of the magnetic field. From bottom to top the lines represent: a power law with $\gamma = 2$, the numerical results for $L = \infty$ (shifted downward by two decades for clarity), $L = 100$ (shifted downward by one decade) and $L = 50$, and a power law with $\gamma = 1$.

barriers on the stickiness is performed, where the effects of the Markov-tree model mentioned in Sec. 2.2.3 are illustrated.

5.2.2 Hierarchical phase-space scenarios
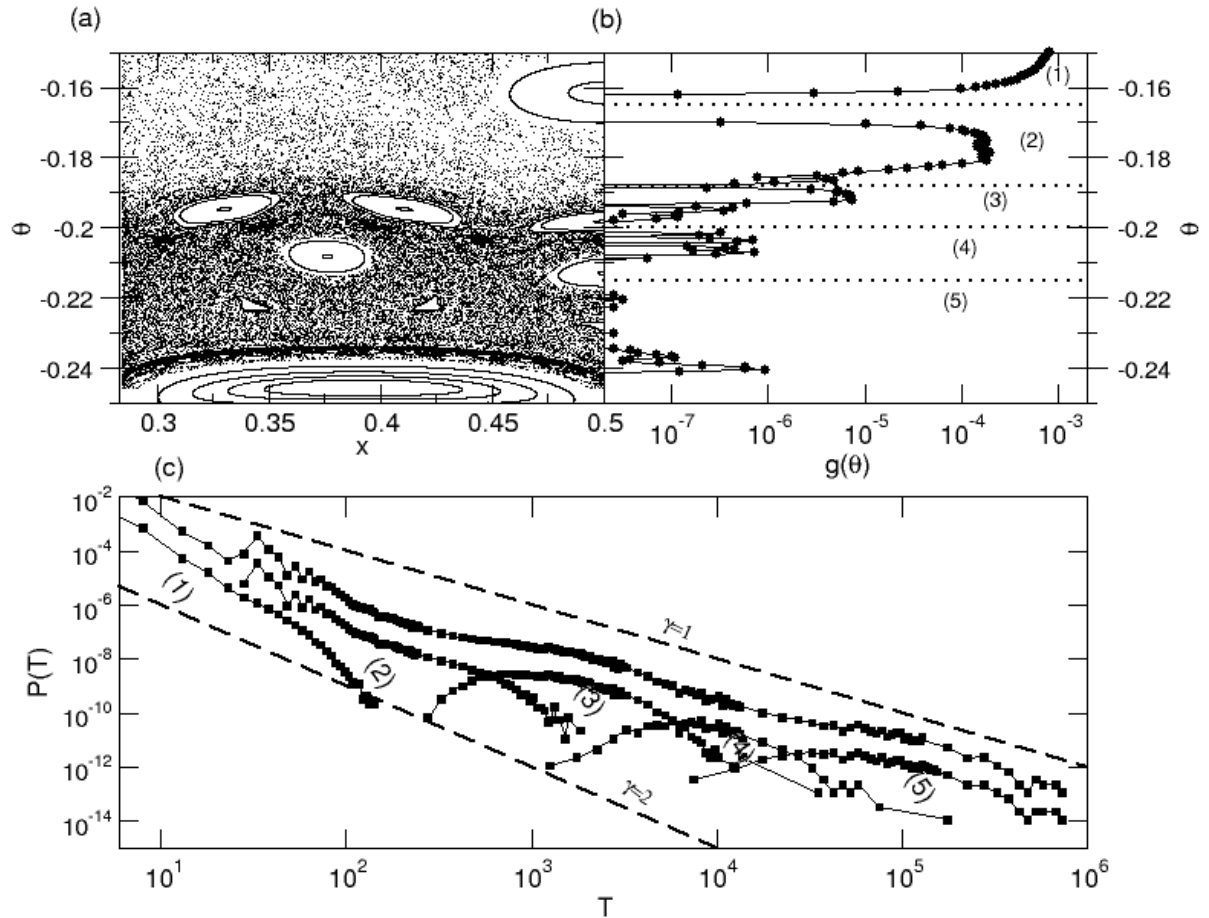
Figure 5.10: Analysis of the magnetic mushroom billiard with $L = 50$: (a) phase-space magnification at the border of chaos; (b) fraction $g(\theta)$ of recurrences that have θ as their minimal angle; (c) the RTD of all trajectories (upper solid curve) and the RTDs of the trajectories in regions (1)-(5) of (b) (lower solid curves). The lower curves in (c) are divided by 10 for clarity.

The investigation concentrates now on the origin of the oscillations and apparently slower decay of the RTS shown in Fig. 5.9. Consider initially the parameter $L = 50$. For this parameter, many KAM tori are destroyed but the chain of islands and cantori are still clearly visible in the phase space, as shown in Fig. 5.10. The different density of points seen in Fig. 5.10(a) is related to the presence of chains of islands and cantori acting as partial barriers [MMP84] to the transport in the θ direction. In order to associate the presence of these barriers to the RTS, consider the minimum distance between the trajectory and the main island before the trajectory leaves the neighborhood of the island and visits the recurrence region (foot of the mushroom). In the simulations the minimum collision angle θ of the trajectory is used as a measure of the distance because the barriers mimic the original tori and have approximately constant θ. The fraction of events that have a minimum angle θ is defined as $g(\theta)d\theta = u_\theta/u$, where u_θ is the number of recurrences that have a minimum angle in the interval $[\theta, \theta + d\theta]$ and u is the total number of recurrences. Numerical results for $g(\theta)$ with $L = 50$ are shown in Fig. 5.10(b). The function $g(\theta)$ goes to zero at the angles that correspond to the position of the barriers because the trajectories that manage to pass a barrier quickly spread throughout the next chaotic layer. From the behavior of $g(\theta)$ in Fig. 5.10(b), 5 different regions limited by these barriers can be

identified. To associate these regions with the RTS, all the recurrence events were labeled from (1) to (5) according to the number of regions the trajectory penetrates before returning to the recurrence region. The RTD (recurrence time distribution) $P(T)$ (i.e., the non-cumulative RTS) of each of these groups of recurrence events are shown in Fig. 5.10(c). The RTD of all the events corresponds to the sum of these partial RTDs and is shown in the same figure (upper solid curve). The partial RTD of each region (1)-(5) presents a relatively peaked maximum followed by an exponential decay. Accordingly, most of the orbits that have the same recurrence time T penetrate the same number of barriers [note the logarithmic scale in Fig. 5.10(c)]. These results indicate that, for $T < 10^6$, the stickiness is dominated by the primary chain of barriers around the main regular island, that is, the contribution of barriers associated to secondary islands is negligible. These results also show that the oscillations observed in the RTD around the power-law behavior are intrinsically associated to the presence of the barriers in the phase space.
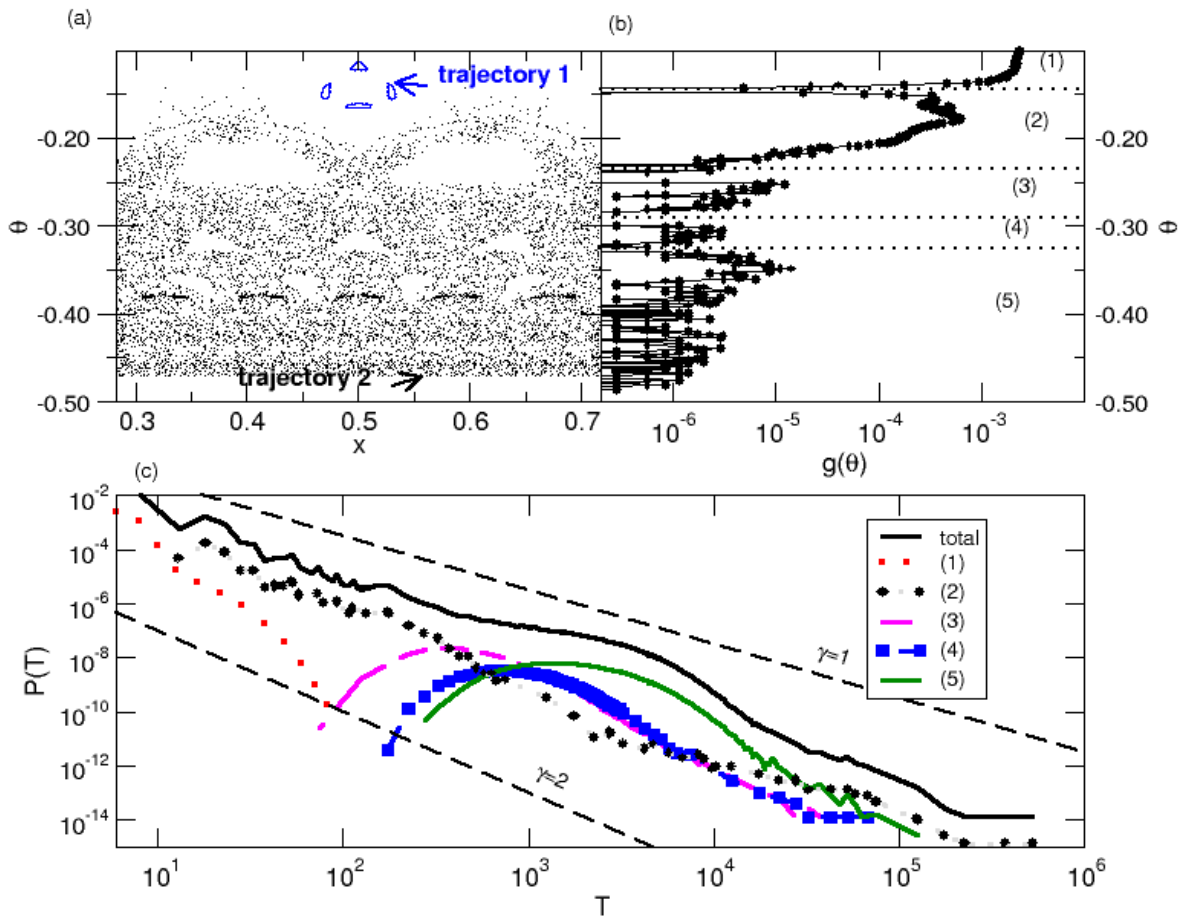
Figure 5.11: (Color online) Analysis of the magnetic mushroom billiard with $L = 10$. (a) Phase-space magnification with two typical sticking trajectories with recurrence time $T \approx 8\,10^4$: trajectory 1 sticks near the upper island and trajectory 2 fills the chaotic region. (b) Fraction $g(\theta)$ of recurrences that have θ as their minimal angle. (c) The RTD of all trajectories (upper solid curve) and the RTDs of the trajectories in regions (1)-(5) of (b) (see legend). The lower curves in (c) are divided by 10 for clarity.

These stickiness properties agree well with the predictions of the model proposed by Motter *et al.* in Ref. [MdMGK05]. In that paper, the hierarchy of cantori is modeled by a chain of coupled hyperbolic systems, where each hyperbolic system models the area of the phase space

limited by successive cantori. One of the strengths of this model is that it predicts not only the asymptotic behavior of the non-hyperbolic dynamics around KAM islands but also the finite-time dynamics assessable in numerical simulations and experiments. The model predicts that the survival probability of particles in the neighborhood of KAM islands fluctuates around a power law and is composed of a sum of exponentials associated to the cantori. Our results in Fig. 5.10 show that this behavior is indeed present in real Hamiltonian systems. As shown below, this picture changes when secondary structures of the hierarchy are relevant. This more general stickiness scenario is observed in the mushroom billiard for larger values of the magnetic field (e.g., $L = 10$).

Figure 5.11 shows the same as Fig. 5.10 for the parameter $L = 10$. The effect of the primary barriers is still important, as shown in Fig. 5.11(b) where these barriers correspond to zeros of $g(\theta)$. However, as shown in Fig. 5.11(c), the partial RTDs corresponding to regions (1)-(5) exhibit a power-law rather than an exponential decay. For instance, the RTD of trajectories belonging to region (2) exhibits an approximate power-law decay that makes these recurrence events dominant not only for small times ($10 < T < 500$) but also for very large times ($T \approx 10^5$). On the other hand, the RTD of events associated to region (4) does not dominate the (total) RTD at any time. The slower decay of the RTD of region (2) is a consequence of the stickiness to the chain of secondary islands shown at the top of Fig. 5.11(a). This figure shows two representative trajectories with recurrence time $T \approx 8 \ 10^4$. The first (trajectory 1) penetrates only two regions and sticks to a secondary island. The second (trajectory 2) penetrates five regions and approaches the main island. The presence of secondary islands at each level, which is expected to be common in typical Hamiltonian systems, shows the limitations of stickiness models based on a single chain of cantori [WHK02a]. In the context of stochastic models [HCM85, WBKZ98], asymptotic effects of secondary islands can be accounted for by the Markov-tree models [MO86].

5.3 Annular billiard with coexistence with islands

In the two previous sections the stickiness to sharply-divided and hierarchical islands were illustrated through representative examples. Islands of both kind may also coexist in the phase space of a given Hamiltonian system, in which case the smaller stickiness exponent prevails (i.e., it is certainly $1 < \gamma \leq 2$). The upper bound $\gamma \leq 2$ is guaranteed by the presence of a single family of MUPOs. However, as argued in Sec. 5.2.1 in an hierarchical phase space generically all the families of MUPOs disappear. The slower decay observed in Fig. 5.9 is thus not guaranteed and shows that the hierarchical scenario sticks in a more efficient way. Recall that for the hierarchical scenario an average exponent $\gamma \approx 1.6$ should be expected (see Ref. [CK] and Fig. 2.3). The coexistence of both scenarios occurs in the annular billiard, e.g., for the parameters used in Fig. 4.9, where apart from the whispering gallery there exist stable periodic orbits that gives rise to an hierarchical KAM island. The stickiness illustrated in Fig. 5.12 for this case shows clearly that the RTS decays slower than the $\gamma = 2$ case, i.e., the exponent is strictly smaller than two ($\gamma < 2$), corroborating the previous observations.
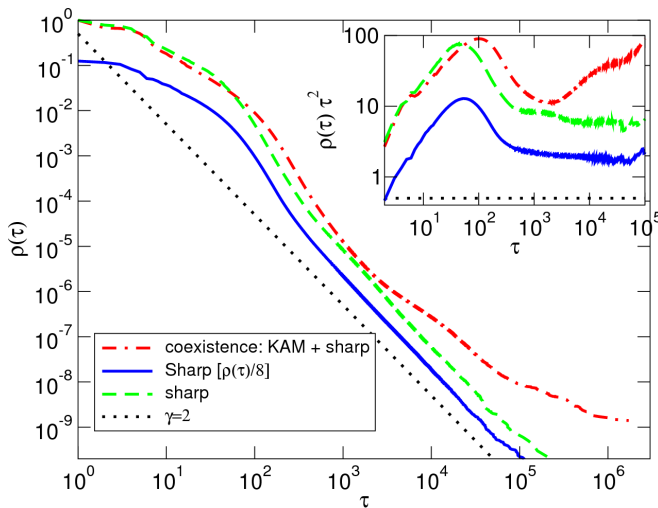
Figure 5.12: (Color online) RTS for the annular billiard with parameters $r = 0.35, \delta = 0.5$ depicted in Fig. 4.9 (solid line) compared to two control parameters ($r = 0.1, \delta = 0.65$ and $r = 0.25, \delta = 0.5$) where the system is sharply divided. It is clear that the RTS in the first case decays slower than $\gamma = 2$.

Chapter 6

Noise-perturbed systems and the effect on the anomalous transport

The effect of additive white noise to the stickiness is considered. An intermediate regime of enhanced trapping is observed in the RTS (recurrence time statistics), due to trajectories performing a random-walk inside the region corresponding to regular islands of the unperturbed system (Sec. 6.1). Asymptotically, the RTS decays exponentially and stickiness is thus suppressed. The effects of the different trapping regimes have a strong impact on the (anomalous) transport of trajectories (Sec. 6.2), what is discussed in the framework of CTRW (continuous time random walks). As a physical example of these results the dispersion of a passive tracer in an incompressible two-dimensional flow subject to molecular diffusion is considered (Sec. 6.3).

6.1 Noise-perturbed system

6.1.1 Recurrence time statistics

The idea of considering an additive noise perturbation to a given deterministic system is quite natural since it corresponds to a test of the robustness of the unperturbed results. From a physical point of view the noise can be thought to incorporate perturbations/interactions that were neglected in the first description of the system. Additionally, there are cases where the presence of noise has a well defined physical origin, such as the molecular diffusion in incompressible two-dimensional flows (see Sec. 6.3.1).

In the case of Hamiltonian systems with mixed phase space, the effect of noise was considered already more than twenty years ago (see Ref. [KRW82] and references therein). Intuitively there are two opposite effects of the noise on the classical chaotic dynamics: (i) it introduces a smaller relevant scale in the hierarchy of islands-around-islands below which structures are not relevant, what typically leads to a cut-off in the power-law decay of the statistical quantity of interest; (ii) chaotic trajectories may enter the deterministically forbidden region of the regular island and hence increase the trapping time. It is shown below how this two effects combine and for which time-scales each of them is more relevant. While many of the individual results of this chapter were already known through different approaches, the novel description in the framework of stickiness, which is presented below, shows an intuitively understandable picture that allow straightforward application of previous theories and helps to clarify previous conflicting results.

Two area-preserving maps are considered in the numerical simulations: a non-generic sharply-divided map as studied in Chap. 5 [composed by Eqs. (5.1) and (5.3) with $K = 2$] and the standard map defined in Eq. (2.14). While the first map was chosen due to its simple phase space

structure – a single polygonal island – the second map is a generic example. Due to numerical reasons that will be mentioned below the following version of the standard map was used

$$
\begin{aligned}
y_{n+1} &= y_n - K \sin(2\pi x_n + 0.25) \quad \mod 1, \\
x_{n+1} &= x_n + y_{n+1} + 0.5 \qquad\qquad \mod 1.
\end{aligned}
\tag{6.1}
$$

The control parameter was usually fixed at $K = 0.52$ where a large (hierarchical) island is observed in the phase space, what emphasizes the effects of the noise discussed here. With the shifts introduced in (6.1), when compared to Eq. (2.14), the center of the island is at $(x, y) = (0.75, 0.5)$, as illustrated in Fig. 6.2b. The recurrence region is defined as the whole region $x < 0.5$, where no island is observed. Typically $2\ 10^{11}$ iterations of this map were performed to obtain the RTS shown in this and in the next Chapter.

The noise is introduced in the above mentioned maps as a kick after each iteration

$$
y_{j+1} = y_j + \xi \delta_G,
\tag{6.2}
$$

where $\xi \in [0, 1]$ is a small control parameter and δ_G is white noise, i.e., Gaussian distributed uncorrelated random variable with zero mean and variance $\sigma = 1$. Different numerical simulations confirm that the result remain unchanged when adding the noise to x, to both variables x, y, or by taking uncorrelated noise with different distributions. The results are also expected to be valid for any generic area-preserving map with mixed phase space[1].

The RTS were computed through the same procedure discussed in Sec. 3.1 (single trajectory started outside the island) and are shown in Fig. 6.1 for both maps mentioned above and different noise strengths $\xi = \{1, 10^{-1}, ..., 10^{-5}\}$. For the sharply-divided map (Fig. 6.1a) it was shown in Sec. 4.2 that the RTS decays as a power-law with $\gamma = 2$ in the unperturbed case ($\xi = 0$). This decay is also observed for small noise ξ and times τ. For large times $\tau \to \infty$, all RTS with $\xi \neq 0$ show a faster than power-law decay of the RTS, which was verified to be exponential in a linear-log graph. Between this two limits an enhanced trapping regime that approaches a power-law with exponent $\gamma \approx 0.5$ is observed. This regime is specially clear for small ξ. For the case of the standard map (Fig. 6.1b) the same regimes are observed. In this case one has to take into account that the unperturbed RTS is not described by a simple power-law anymore but shows intrinsic oscillations, as discussed in Secs. 2.2.2 and 5.2. The explanations of the trapping regimes mentioned above in terms of the trajectories in the phase-space is given in Sec. 6.1.2, while the dependence of the trapping regimes on the noise strength is discussed in Sec. 6.1.3.

6.1.2   Characterization of the trapping regimes

The aim here is to understand the origin of the above mentioned regimes of the RTS by identifying in which region of the phase space were the trajectories corresponding to each of the regimes. For this analysis the standard map (6.1) was chosen due to its generic character. Consider, e.g., the case $\xi = 10^{-3}$ emphasized in Fig. 6.2a, and the four intervals of time IR0-IR3 shown in this figure and specified in the caption. Trajectories that returned with a recurrence time $T \in$ IR are said to *belong* to a given interval IR. The phase-space density of trajectories belonging to all 4 intervals are plotted in Fig. 6.3 and can be interpreted as follows. Trajectories belonging to IR0, an interval of very short times T where the RTS decays exponentially, stay in the chaotic sea without approaching the island of regular motion, as in the unperturbed case. Trajectories belonging to IR1, an interval where the RTS is already non-exponential but similar to the unperturbed case, stick to the border of the island as in the deterministic trajectories.

---

[1]Notice that the special choices of the standard map and its parameter were crucial only for visualization and numerical purposes.
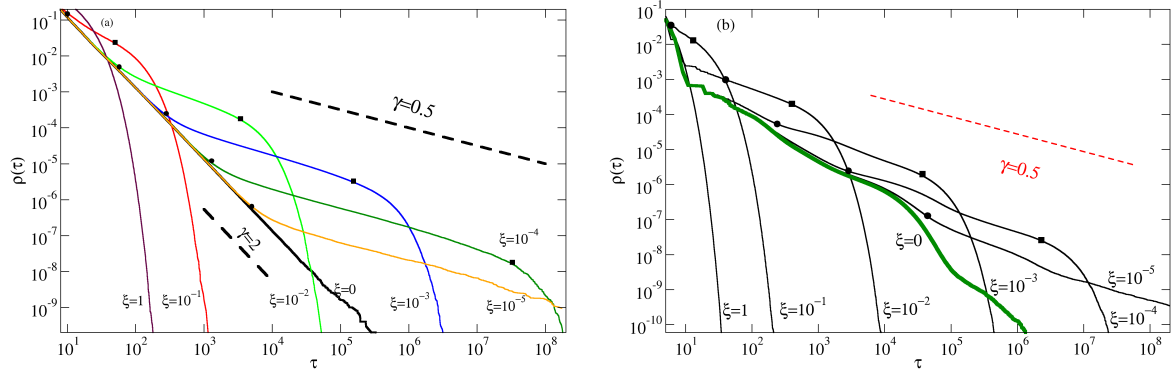
Figure 6.1: (Color online) (a) RTS for the sharply-divided map (5.3) with $K = 2$ (b) RTS for the standard map with $K = 0.52$, , whose phase space is shown in Fig. 6.2b. In both cases the thick solid line corresponds to the unperturbed case ($\xi = 0$) while the thin solid lines correspond to perturbations due to white noise [as in Eq. (6.2)] with $\xi = 10^0, ..., 10^{-5}$ (from left to right). In each curve $\tau_{1,2}$ ($\bullet$) and $\tau_{2,3}$ ($\blacksquare$) are indicated.

Trajectories belonging to IR2, an interval where the RTS shows an enhanced trapping ($\gamma \approx 0.5$) when compared to the unperturbed case, concentrate *inside* the island, i.e., in a region which is forbidden for the deterministic case. Finally, trajectories belonging to IR3, an interval in the exponential tail of the RTS, concentrate in the center of the island.
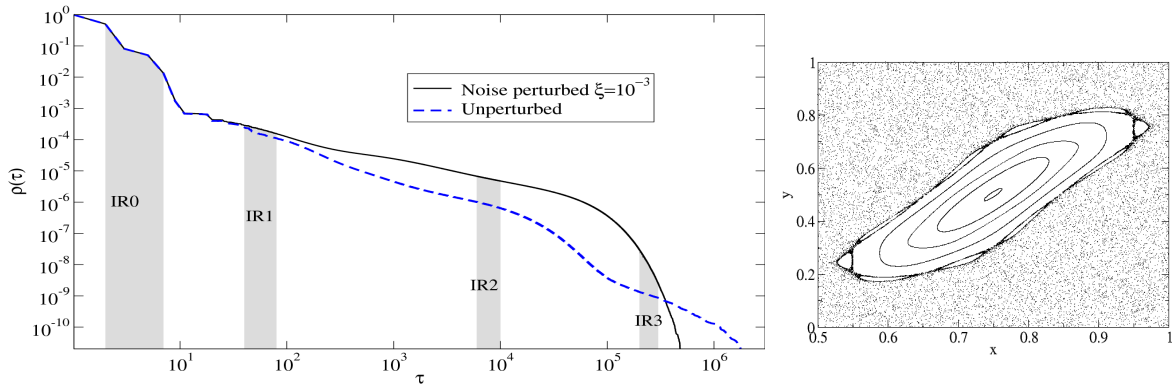
Figure 6.2: (a) RTS as shown in Fig. 6.1 with the indication of the intervals of regions R1-R3: IR0$= [2, 7]$, IR1$=[40, 80]$, IR2$=[6 \ 10^3, 10^4]$, IR3$=[2 \ 10^5, 3 \ 10^6]$, IR3'$=[6 \ 10^5, 10^6]$. (b) Phase space of the standard map with $K = 0.52$ amplified around the island. This figure serves as reference for Figs. 6.3.

The interpretation of the regime of enhanced trapping (trajectories belonging to IR2) is thus quite simple: it is built by trajectories that due to the noise perturbation penetrated the region that corresponds to the island of regular motion in the deterministic case. Once inside the island it circles its center (the elliptic fixed point) and performs an one dimensional random walk in the perpendicular direction. A first quantitative indication that this general picture is correct is that the power-law decay of this regime is close to $\gamma = 0.5$, which is the same obtained for a random-walker in Sec. 3.1.2. Further evidences of this picture are provided in Sec. 6.1.3. This model is specially accurate for the case of sharply-divided phase space, as seen by the nicer power-law decays in this regime of Fig. 6.1a when compared to the standard map case of Fig. 6.1b where further oscillations are observed. Indeed, simulations for other control parameter have shown even greater oscillations around a $\gamma = 0.5$ decay. The reason for this is

the existence of second order resonances and confined chaotic regions inside the main island of the standard map, which are not considered in the simple random walk model mentioned above.
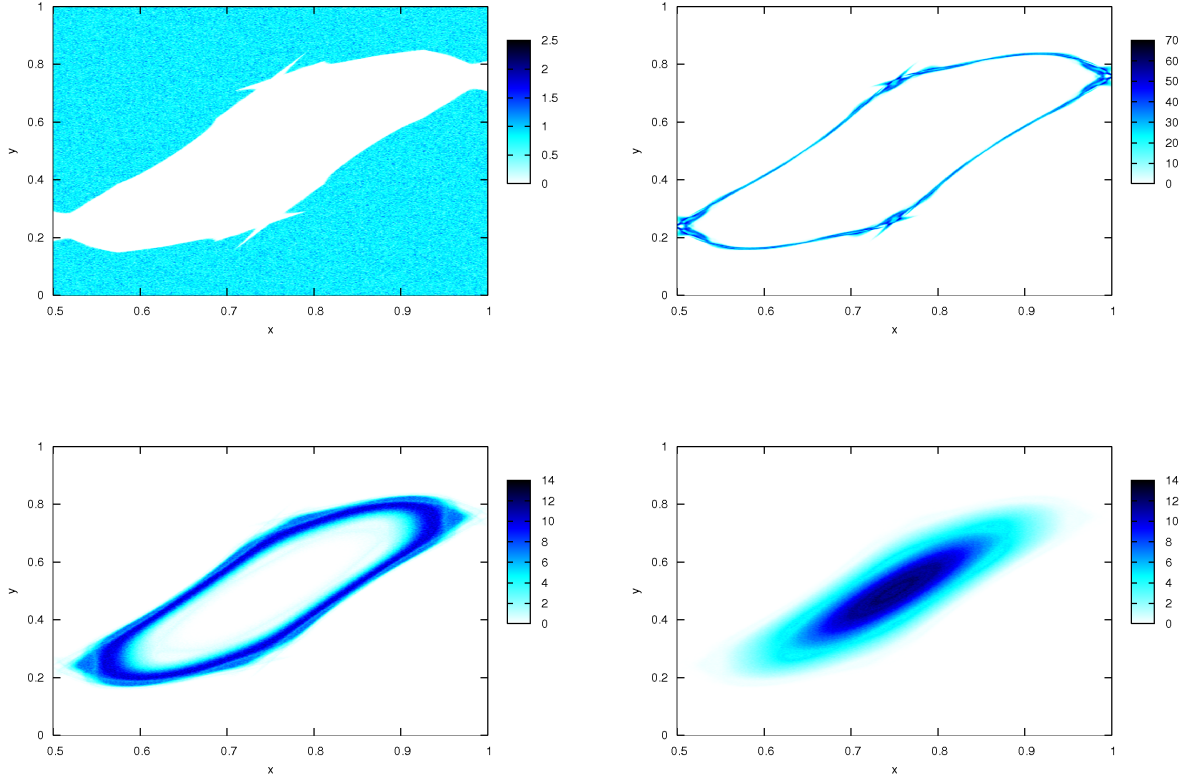
Figure 6.3: (color online) Density of points in the phase space of the standard map $K = 0.52$ with noise perturbation $\xi = 10^{-3}$ for trajectories having recurrence time in the regions assigned in Fig. 6.2(b): IR0 (top left), IR1 (top right), IR2, (bottom left), and IR3 (botom right). Average density corresponds to the color scale 1.

In summary, three different regimes of the RTS in noise perturbed systems can be identified for small enough noise perturbations ξ:

(R1) For short times ($\tau < \tau_{1,2}$) the RTS follows the unperturbed one ($\xi = 0$), i.e., it shows an exponential followed by a power-law decay (with exponent $\gamma_{R1} = \gamma_{\xi=0}$).

(R2) For intermediate times ($\tau_{1,2} < \tau < \tau_{2,3}$) the RTS shows an enhanced trapping due to trajectories that entered the region corresponding to the islands through the action of the noise. Once inside the island the trajectories circle the central elliptic periodic orbit and perform a random walk in the perpendicular direction. The power-law exponent tends to the value of the one of a random walker $\gamma_{R2} \approx \gamma_{RW} = 0.5$ (see Sec. 3.1.2).

(R3) For long times ($\tau > \tau_{2,3}$) the RTS decays exponentially since the regular island has a finite domain and the fine structures of the phase space are irrelevant due to the noise.

6.1.3   Dependence on the noise intensity ξ

The effect of the noise intensity ξ on the trapping regimes described above is evident in Fig. 6.1: the smaller ξ the greater the regimes (R1) and (R2). The dependence on ξ of the starting

and ending time of (R2), defined as $\tau_{1,2}$ and $\tau_{2,3}$, is obtained below. $\tau_{1,2}$ and $\tau_{2,3}$ are obtained numerically as the crossing point between the power-law regime of R2, $\gamma_{R2} \approx 0.5$ with the previous power-law or the next exponential regime, respectively[2]. Theoretically one can estimate this time comparing the displacement in the phase space due to the noise with the distance of the trajectory to the border of the island. A similar reasoning was used in Ref. [FMG95] where, instead, the size of the chaotic layer between two cantori where the trajectory is stuck was considered. When these two quantities are of the same order of magnitude one can estimate that the fine hierarchical structure of the phase space is ignored by the trajectory and the noise dominates. Following these arguments, and using the Markov-tree model for stickiness introduced in ref. [MO85], the authors of ref. [FMG95] obtained

$$\tau_{1,2} \sim \xi^{-c}, \tag{6.3}$$

with $c = 1/(2\gamma_{R1} - 1)$. Since usually $1 < \gamma_{R1} < 2$ one obtains $1/3 < \beta < 1$. Similar arguments can be applied to our case since the distance between cantori in a given level is usually comparable to the distance to the island border. However there are two drawback in the arguments leading to the precise relation in Eq. (6.3): trajectories may approach secondary islands and the coefficient γ is in practice not well defined in the case of stickiness in hierarchical phase space. Therefore, a more realistic approach, also based in the general remarks of Ref. [FMG95], is to say that the time $\tau_{1,2}$ is given by

$$\tau_{1,2} \sim \xi^{-\beta}, \tag{6.4}$$

where $\beta \lessapprox 1$, with no a priori relation between β and γ.
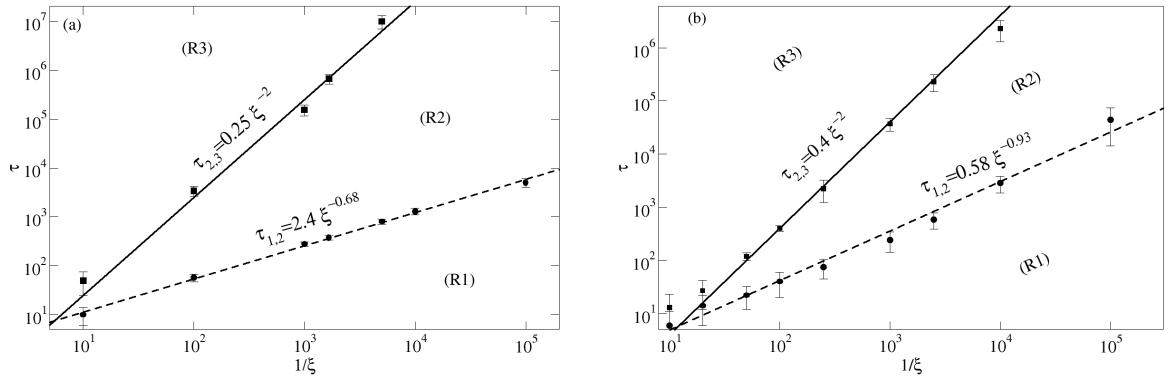
Figure 6.4: Dependence of $\tau_{1,2}$ and $\tau_{2,3}$ on ξ obtained from Fig. 6.1 for (a) the sharply-divided map (5.3); and (b) for the standard map (6.1) with $K = 0.52$. The fitted lines show the agreement with Eqs. (6.4) and (6.5).

It was argued in Ref. [FMG95] that at this time an asymptotic exponential decay should appear, similarly to the case of one dimensional tangent maps. However, as shown above, our simulations indicate that the exponential decay of the RTS occurs at a longer time $\tau_{2,3} > \tau_{1,2}$, since trajectories may enter the island where they performs a random walk. The asymptotic exponential decay of the RTS is due to the finiteness of the random walk domain, i.e., the finiteness of the regular island in the unperturbed case. Considering the measure μ_I of the

---

[2] The power-laws extend over more than two decades only for small ξ but can be extrapolated for higher ξ. As is seen comparing the •'s (indications of $\tau_{1,2}$) in Fig. 6.1a and 6.1b the practical specification of this times are quite arbitrary. However, the same scaling exponent is obtained once it is done consistently for all curves with different ξ.

(largest) island inside which a random walker (with step size proportional to ξ) performs a diffusive motion, the dependence of $\tau_{2,3}$ on ξ can be estimated as

$$\tau_{2,3} \sim \mu_I \xi^{-2}. \tag{6.5}$$

As it will be clear in Sec. 6.3, this scaling is equivalent to the intuitive result that normal diffusion in flows starts for a time $t \sim L^2/D$, where L is a typical length and D is the (molecular) diffusion coefficient [WUS96]. Figure 6.4 verify the agreement of Eqs. (6.4) and (6.5) with the values estimated numerically for both maps studied in Fig. 6.1. Notice that for small enough noise intensity ξ the regime of enhanced trapping becomes increasingly large due to the difference in the exponents in Eqs. (6.4) and (6.5).

In summary, the noise has two qualitatively different effects: while (R3) represents the typical cut-off of the power-law distribution [FMG95], during the novel regime (R2) the noise acts constructively (increasing the regularity of the dynamics) by allowing trajectories to penetrate the regular island. The scale of these regions with the noise is given by Eqs. (6.4) and (6.5).

6.2   Stickiness and anomalous transport

6.2.1   General relations

In this section one of the most important outcomes of stickiness is studied: the possibility of giving rise to anomalous transport of trajectories. Before showing explicitly this connection, some notational remarks about the words transport and diffusion are necessary. In many cases the stickiness phenomena is interpreted more generally as a problem of slow transport in the phase space. In this section the meaning of (anomalous) transport is different. It refers to the global dispersion of *chaotic* trajectories over long periods of times and regions of space and *not* to the transport close to islands or between cantori, as discussed in the previous chapters of this Thesis. The transport will be thus characterized by the algebraic growth in time of the mean square displacement of a given function of phase space variable $r(\vec{p}, \vec{x})$ calculated over an ensemble of trajectories

$$\langle r^2 \rangle = D_\nu t^\nu, \tag{6.6}$$

where $\langle . \rangle$ means ensemble average (i.e., average over many trajectories belonging to the same chaotic ergodic component). If $\nu = 1$ the system has normal or diffusive transport and D_1 is the usual diffusion coefficient. Anomalous transport $\nu \neq 1$ (sometimes called anomalous diffusion) can be subdiffusive $0 < \nu < 1$ or superdiffusive $1 < \nu \leq 2$,. The limiting case $\nu = 2$ is called ballistic and corresponds to particles traveling with constant speed in different directions. The pre-factor D_ν is the generalized diffusion coefficient.

Diffusive transport $\nu = 1$ describes the case of fully chaotic hyperbolic systems, where stickiness does not occur. Contrary to what sometimes seems implicit in other vague uses of the word (anomalous) diffusion/transport, stickiness does *not* lead to subdiffusion in the sense mentioned above. It will be clear below that in deterministic systems stickiness may reduce the value of the diffusion coefficient D_1 but not the value of the exponent $\nu = 1$. On the other hand, stickiness may lead to superdiffusion $\nu > 1$ when the islands or tori to which the chaotic trajectories stick correspond to constant motion in one direction, i.e., ballistic islands ($\nu = 2$). The existence of an asymmetry between sub- and super-diffusion is easily seen already by the calculation of the diffusion coefficient in a simple diffusive process (e.g., normal random walkers)

$$D = \frac{\langle l^2 \rangle - \langle l \rangle}{2\langle t \rangle}, \tag{6.7}$$

where l is the flight (jump) size and $\langle t \rangle$ the typical time between successive jumps. Anomalous diffusion, which corresponds to a vanishing (subdiffusion) or diverging (superdiffusion) diffusion coefficient, arises if one of the terms in Eq. (6.7) diverges. This happens if the waiting-time distribution or the flight distribution have broad tails, as assumed in the model of Sec. 6.2.2. As emphasized below, in Hamiltonian systems the origin of such tails is the stickiness to regular regions. Notice that the numerator of expression (6.7) involves the second moment of the flight distributions while the denominator involves the first moment, what is the origin of the asymmetry between sub- and super-diffusion.

The existence of anomalous transport in Hamiltonian systems due to stickiness was studied in several systems [Kar83, GZR87, GZR88, ZT91, KZ94]. From the considerations above it is clear that one has to distinguish between two kind of sticky domains: localized island corresponding to the regions around some stable fixed point or periodic orbit where stuck trajectories remain localized in space; and ballistic islands or tori corresponding to regions around some stable periodic or quasi-periodic orbit of the closed system (taking modulus 1 or 2π in one periodic coordinate, e.g., one angle) that correspond to constant motion in the expanded space where transport is calculated[3]. In the most general case both kind of islands coexist in the phase space, what motivates the introduction of a continuous time random walk model with periods of spatial localization and of Lévy-walks (constant velocity). This model will be sketched below, based in the work of Klafter and Zumofen in Ref. [KZ94] which is indicated for further details. See also Ref. [GZR88] for a different approach leading to similar results and Ref. [WUS96] for a didactical discussion and for the asymmetric case. The effect of noise perturbations to these models will be discussed in Sec. 6.2.3 through simulations of the standard map. A more didactical and physically motivated illustration of the theory of this section and of the effect of noise is the subject of Sec. 6.3.

6.2.2 Continuous time random walk

Consider particles that move with a constant speed in the direction of negative or positive r. After a given flight time t_f the trajectory remains trapped for a time t_t before choosing at random a new direction with equal probability and a new flight time. An important assumption is that consecutive flights and trappings are completely uncorrelated and thus drawn from invariant probability distribution functions ψ_f and ψ_t, respectively. Anomalous transport may arise in such a model if these probability density functions have long tails. Consider that the probability of flying consecutively to one same direction for a time t or greater is given for long times by

$$\psi_f(t) \sim t^{-\gamma_f}, \gamma_f > 0, \tag{6.8}$$

and, analogously, that the probability of being trapped for a time t or greater is given by

$$\psi_t(t) \sim t^{-\gamma_t}, \gamma_t > 0. \tag{6.9}$$

Additional motivation for such power-law distributions come from the stable Lévy distributions that have asymptotically power-law tails.

In the problem of transport in Hamiltonian systems with mixed phase space, the distributions (6.8) and (6.9) are related to the stickiness to ballistic and localized islands respectively. In case of more that one island of one type those showing a greater stickiness (smaller γ) should be considered. The velocity of flight is given by the length in r of the ballistic island divided by its period. The assumption that consecutive events are uncorrelated is justified by the fact

---

[3] Usually these orbits are periodic in the angular coordinate but sometimes also in the momentum or other spatial coordinate where some symmetry exists.

that between two stickiness events the trajectory spends some (exponentially distributed) time in the chaotic sea, which is enough to destroy the correlations.

From the trapping and flying time distributions one can calculate the propagator $P(r,t)$ of reaching the point r at a time t. Going to the Fourier-Laplace space ($r \to k, t \to u$) the calculation of the mean squared displacement is then given simply by [KZ94]

$$\langle r^2 \rangle = -\frac{\partial}{\partial k} P(k,u)|_{k=0}. \tag{6.10}$$

Depending on the values of γ_f, γ_t of Eqs. (6.8) and (6.9) different values of the transport exponent ν are obtained asymptotically in time. The general relation can be written concisely as

$$[\nu]_2 = 2 + [\gamma_t]_1 - [\gamma_f]_2, \tag{6.11}$$

where the following notation was used

$$[x]_m = \begin{cases} x & \text{if } 0 \le x \le m \\ m & \text{if } x > m \end{cases} \tag{6.12}$$

The different explicit relations between ν and $\gamma_{f,t}$ contained in relation (6.11) are illustrated in Fig. 6.5. When the flight- and trapping-time distribution decay faster than power-law (no stickiness) one considers $\gamma \to \infty$ in (6.11). In the case of non-symmetric flights in positive/negative directions a more rich behavior is obtained [WUS96]. Notice also the asymmetry between flights and traps [$m = 2$ and $m = 1$ in Eq. (6.12), respectively], in agreement with the discussion after Eq. (6.7).
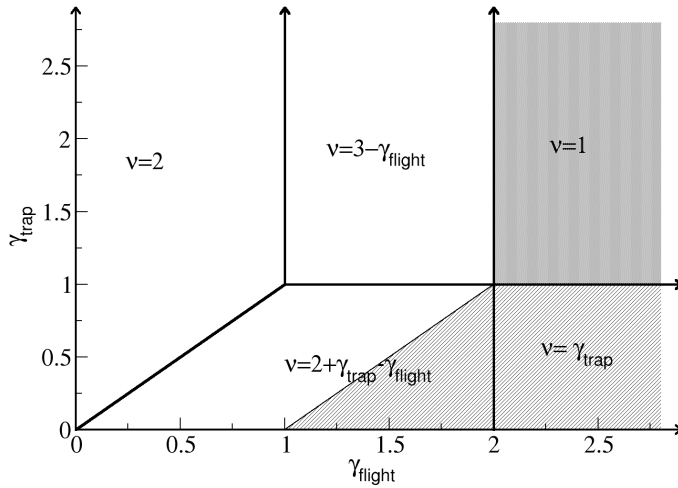
Figure 6.5: Relation between the anomalous transport exponent ν and the exponents of the statistics of flights γ_f and traps γ_t. Regions of sub-diffusion (diagonal lines), normal diffusion (gray), and superdiffusion (white) are indicated [WUS96].

Applying the constrain $\gamma > 1$ (finite mean recurrence time) discussed in Chap. 4 for the values of the stickiness exponent γ in deterministic Hamiltonian system to the values of γ_f, γ_t one sees that actually the distribution of trapping times is irrelevant and Eq. (6.11) reduces to [GZR87]

$$\nu = \begin{cases} 3 - \gamma_f & \text{if } 1 \le \gamma_f \le 2, \\ 1 & \text{if } \gamma_f > 2, \end{cases} \tag{6.13}$$

showing that only superdiffusion is possible. The results of Eqs. (6.11) and (6.13) are valid up to log periodicities, which are specially important in the limiting cases between normal

and anomalous transport. The well-known result of anomalous transport $\langle \Delta r^2 \rangle \sim t \ln(t)$ in the Lorentz gas with infinite horizons (e.g., the open-periodic Sinai billiard of Fig. 4.1) can be interpreted from Eq. (6.13) and the exponent $\gamma = 2$ obtained for the stickiness to MUPOs (e.g., the parallel walls of the Sinai billiard) in Sec. 4.2.

6.2.3 Effect of noise perturbation

Relations (6.11) and (6.13) are obtained asymptotically for long time. As was shown in the previous section, the effect of noise in the stickiness may lead to intermediate but arbitrarily long regimes where $\gamma < 1$ (more precisely $\gamma \approx 0.5$). In this cases one can expect to observe also for intermediate times more complicated regimes of transport described by Eq. (6.11) but absent in Eq. (6.13). This is investigated numerically in this section.

Perhaps the best studied case of anomalous transport in simple Hamiltonian systems corresponds to the dispersion of the momentum y of the standard map (6.1). The transport is anomalous for some special values of the parameter K where, due to particular symmetries of the map, ballistic islands appear (also called accelerator modes). For example, for $1 < K < 1.1854...$ there are two stable periodic orbits of the closed standard map [taking mod (1) in both Eqs.(6.1)] that correspond to a ballistic motion $y \to y \pm 1$ in the open system [taking mod (1) only in the angular component of Eqs.(6.1)], where the transport is computed [i.e., $r(x, y) = y$] [LL83].

For the numerical simulations the case $K = 1.07$ was chosen, since for this parameter there is one big ballistic island that enhance the regime of trapping inside islands discussed in Sec. 6.1. No further chain of islands are visible in the phase space. An ensemble of 10^6 trajectories with initial condition along the $y = 0$ axis was considered **away** from the ballistic islands and the evolution of the mean squared displacement $\langle y^2 \rangle$ was calculated as a function of time. In Fig. 6.6 $\langle y^2 \rangle / t$ is plotted in order to emphasize the existence of anomalous transport (horizontal lines correspond to normal transport). The oscillations observed for the unperturbed case $\xi = 0$ have the same origins of the oscillations in the RTS, discussed in Chaps. 2 and 5. This oscillations are sometimes not seen in other publications because the division of $\langle y^2 \rangle$ by t is not performed.

For nonzero noise intensities Fig. 6.6 shows that different regimes of anomalous transport exist before an asymptotic normal diffusion regime is achieved. Indeed, three regimes of transport are visible in this plot, which can be related to the three regimes of the RTS listed in Sec. 6.1.2 by Eq. (6.13). This leads to the following description of the transport properties of the noise perturbed systems:

(R1) for short times superdiffusion similar to the unperturbed case $1 < \nu < 2$ is observed.

(R2) for intermediate times enhancement of the superdiffusion that tends to ballistic $\nu = 2$ [see Eq. (6.13)] is observed;

(R3) asymptotically the transport is normal $\nu = 1$ with coefficient D_A.

It was verified numerically that the beginning and end of the ballistic regime (R2), denoted as $\tau_{1,2}^\dagger$ and $\tau_{2,3}^\dagger$ respectively, occur at times proportional to, but greater than, those of the RTS (R2). This means that they follow the scaling given by Eqs.(6.4) and (6.5), but have different constants of proportionality. To observe these regimes it is essential that the initial conditions are away from the island, as considered to calculate the stickiness phenomenon. If there are initial trajectories inside the ballistic islands, e.g., starting uniformly in the unit cell of the phase space $0 \leq x, y < 1$, the regime (R1) mentioned above is not observed and a faster convergence to the regime (R3) is achieved with the same D_A. In this case, instead of superdiffusion ballistic motion is obtained for $\xi = 0$.

The asymptotic exponential decay of the RTS in noisy systems leads to an asymptotic normal transport. The asymptotic diffusion coefficient $D_1 = D_A = \lim_{t \to \infty} \langle \Delta y^2(t) \rangle / t$ is determined by the intermediate anomalous regimes. In Fig. 6.6 this is pictorially represented, since the value
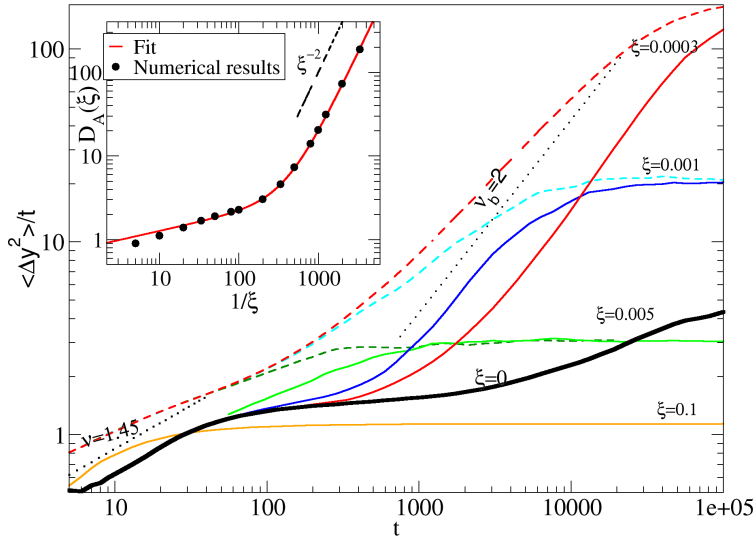
Figure 6.6: (Color online) Transport in the y component of the open standard map (6.1) with $K = 1.07$ (accelerator mode) perturbed by noise (thin solid lines) with intensity ξ. The unperturbed case $\xi = 0$ is depicted as a thick solid line. From top to bottom $\xi = 0.0003, 0.001, 0.005, 0.1$. 10^6 trajectories were used with initial conditions away from islands for the solid lines and uniformly in $0 \leq x, y < 1$ for the dashed lines. When the curves become constant (for $t \to \infty$) transport is normal. Inset: asymptotic diffusion coefficient for different noise intensities. The solid line corresponds to Eq. (6.14) with $a = 0.776, b = 1.7\ 10^{-5}$ and $\nu = 1.45$.

of D_A is given by the height of the horizontal line observed for $t \to \infty$. A simple theory is introduced below to describe the nontrivial dependence of D_A on the noise intensity ξ: for weak noise, Eqs. (6.4) and (6.5) indicate that the dominant contribution comes from the ballistic regime associated to (R2) and thus $D_A \approx [D_{R2}(\tau_{2,3}^\dagger - \tau_{1,2}^\dagger)] \sim \xi^{-2}$. For stronger noise the major contribution is given by a regime of superdiffusion corresponding approximately to (R1), that can be estimated as $D_A \approx (D_{R1}\tau_{1,2}^\dagger)^{\nu-1} \sim \xi^{-\beta(\nu-1)}$, where ν is the unperturbed anomalous transport exponent (for small times) which is related to β and γ through Eqs. (6.3) and (6.11). Considering the composition of this two effects and joining the multiplicative terms in two fitting parameters a, b one obtains

$$D_A(\xi) = a\ \xi^{-\beta(\nu-1)} + b\ \xi^{-2}, \tag{6.14}$$

with $\beta \lessgtr 1$. In the inset of Fig. 6.6 the remarkable agreement of the numerically obtained diffusion coefficient and expression (6.14) is shown. The exponent $\beta(\nu - 1) = 0.2142$ was obtained independently by fitting the anomalous transport of the unperturbed standard map for small times and for the value of β in Eq. (6.4).

While for the theories leading to Eqs. (6.14) it was essential the fact that the ensemble of trajectories was started outside the ballistic islands, the result remains valid for all cases since D_A is independent of this choice. It is clear from the dashed lines of Fig. 6.1 that for short times anomalous superdiffusion slower than ballistic is observed even when initial conditions are chosen inside the ballistic islands. This is the essential element of the most interesting results present in Eq. (6.14): the transition for small ξ from one power-law dependence to an asymptotic ξ^{-2} dependence of D_A. From the perspective of stickiness, this fact is a direct consequence of the nontrivial trapping regime (R2). It is absent in the case of 1-d maps (e.g., Pomeau-Manneville maps) [FMG95, BMW95], and was not previously reported in Refs. [BdCNL$^+$03, FMG95, ISM00]. The asymptotic ξ^{-2} scale was predicted through different arguments in Ref. [Kar83], and it is equivalent to the relation $D_A \sim 1/D_m$ which is well known in fluid mechanics [where D_m is the molecular diffusion coefficient (see Sec. 6.3)] [BCVV95] and can be traced back to the works of Taylor [Tay53].

Finally the possibility of observing intermediate subdiffusion in Hamiltonian systems perturbed by noise is explored, according to the discussions of Sec. 6.2.1. So far, a special parameter

of the standard map where a ballistic KAM island exists in the phase space was considered. This is not the case for $K = 0.52$, extensively studied throughout Sec. 6.1, where only a localized island exists. Numerical results for the transport in the y component of the open standard map (6.1) with this parameter and different noise intensities ξ are shown in Fig. 6.7. It was verified that the results do not change increasing number of trajectories (started away from islands $0 < x < 1, y = 0$). If initial conditions are chosen uniformly between $0 < x, y \leq 1$ a different convergence to the same asymptotic exponent is observed (see the dashed line in Fig. 6.7). As expected from (6.11), normal diffusion is observed for $\xi = 0$ with exponent $D_A^{\xi=0} \approx = 0.081$. For noise perturbation and initial conditions outside the island, one expects that the trajectories will penetrate the island and increase the trapping for intermediate time leading to transient subdiffusion and a consequent reduction of the asymptotic diffusion coefficient. This is indeed observed in the different curves in Fig. 6.7. However, the intensity of the effect is much smaller than predicted by Eq. (6.11) $\gamma_t = 0.5, \gamma_f > 2 \Rightarrow \nu = \gamma_t = 0.5$. The reason for this is quite simple: contrary to the case of superdiffusion, the asymptotic diffusion coefficients in this case are bounded (from below). The minimum diffusion coefficient can be estimated as the value obtained choosing initial conditions uniformly $0 < x, y \leq 1$ in the case $\xi = 0$ (trajectories inside the island remain localized), what is given by $D_A^{min} = D_A^{\xi=0}(1 - \mu_{island})$, where μ_{island} is the measure of the island. Introducing $D_A^{\xi=0} \approx 0.081$ obtained in Fig. 6.7 and $\mu_{island} = 0.1926$ (see Sec. 7.2.2 below) one gets the minimum value of the diffusion coefficient as $D_A^{min} \approx 0.0654$, what is very close to the lower values observed in Fig. 6.7.
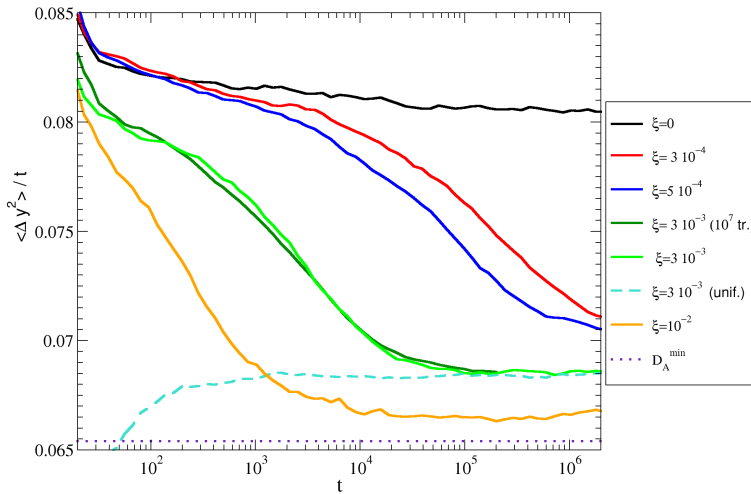
Figure 6.7: (Color online) Transport in the y component of the open standard map (6.1) with $K = 0.52$ (fixed KAM island) perturbed by noise with intensity ξ. From top to bottom $\xi = 0, 0.0003, 0.0005, 0.003, 0.01$. 10^6 trajectories were used with initial conditions away from islands. Two additional simulation for $\xi = 0.003$ are shown: one where 10^7 trajectories are used confirming the convergence of the results and one (dashed line) where trajectories are initiated uniformly between $0 < x, y \leq 1$. When the curves become constant (for $t \to \infty$) transport is normal.

6.3 Example of tracers in a fluid channel

6.3.1 Physical motivation

In this section one concrete example of fluid mechanics is considered, where all the effects discussed above apply and lead to a new interpretation of a known result. The temporal evolution of a passive scalar field $\theta(\vec{x}, t)$ (contaminant), advected by a flow with velocity field given by $\vec{v}(\vec{x}, t)$ is given by [Are84, EMZT93]

$$\frac{\partial \theta}{\partial t} + \nabla.(\vec{v}\theta) = D_m \nabla^2 \theta, \qquad (6.15)$$

where D_m is the molecular diffusion coefficient. The motion of fluid elements (Lagrangian description) is described by

$$\frac{d\vec{x}}{dt} = \vec{v}(\vec{x}, t) + \eta(t), \qquad (6.16)$$

where $\eta(t)$ is a Gaussian stochastic process with zero mean and variance

$$\langle \eta_i(t)\eta_j(t') \rangle = 2D_m \delta_{i,j}\delta(t - t').$$

Assume now that the fluid is two dimensional (negligible vertical velocities) $\vec{x} = (x, y)$ and incompressible

$$\nabla.\vec{v} = 0.$$

These conditions guarantee the preservation of area of the flow, what is equivalent to say that there exist a stream function $\psi(x, y, t)$ such that

$$\frac{dx}{dt} = v_x = -\frac{\partial \psi}{\partial y} \quad \text{and} \quad \frac{dy}{dt} = v_y = \frac{\partial \psi}{\partial x}. \qquad (6.17)$$

Comparing Eqs. (6.17) and (2.1) it is easy to see the analogy to Hamiltonian dynamics, where the stream function $\psi(x, y, t)$ plays the role of the Hamiltonian $H(x, y, t)$. The conjugate position-momentum variables are in this case both spatial coordinates (x, y). This makes the experimental realization and visualization of such systems specially easy since the configuration space is equal to the phase space. One paradigmatic experiment in this field is the rotating annulus experiment, where quasi-geostrophic flows are mimic by a rotating cylindrical container [SWS93]. For certain parameters KAM islands, regions of steady flow, and chaotic regions where observed. In particular, the anomalous transport of the angular position of tracing particles was explored [SWS93, SWS94]. Hamiltonian models of this experiment were proposed, in which case the anomalous transport is generated either by the stickiness into the border of the KAM islands and tori corresponding to steady flow [Kov00] or due to the composition of this effect to some irregular (random) temporal behavior [VJO98].

The effect of molecular diffusion $D_m \neq 0$ on the tracers is usually neglected in these problems. As shown in Eq. (6.16) this corresponds to a noise perturbation of the dynamics in which case the previously described results apply. The estimations of the molecular diffusion made below indicates that, despite being irrelevant for the experimental configurations mentioned above, there are alternative experimentally relevant configurations where it has to be taken into account.

The value of the molecular diffusivity is given by the famous Einstein relation

$$D_m = \frac{RT}{6\pi N_A \eta_k a}, \qquad (6.18)$$

where R is the universal gas constant, N_A the Avogadro number, T the temperature, η_k the kinematic viscosity of the fluid, and a the radius of the Brownian particle considered. From Eq. (6.16) one sees that the effect of molecular diffusion is simulated as a noise perturbation in the system and D_m is proportional to the square of the variance of the noise: $D_m = 4\xi^2$, where ξ is the intensity of the noise perturbation considered in the previous sections. Consider the following estimations of the above parameters: usual temperatures $T = 300K$, viscosity of water/glycerol mixtures $\eta_k \approx 10^{-4}m^2/s$ as used in [SWS94], and radius of the particles $a \approx 1mm$. This leads to $\xi = \sqrt{2D_m} \approx 4 \ 10^{-6}\sqrt{cm^2/s}$. This value is fairly small (see previous simulations) and it is a reasonable approximation to neglect it for the scales of the experiments, as was done in Refs. [SWS93, SWS94]. However, if one considers instead particles of a contaminant or dye, i.e., passive tracers where the value of a are in the scale of molecules $a \approx 1A = 10^{-8}cm$, the estimation leads to $\xi = \sqrt{2D_m} \approx 10^{-2}\sqrt{cm^2/s}$ which is in our range of interest if setups in

the scale of cm and observation times in the scale of hours are considered. Different molecular diffusion coefficients can be easily achieved by changing the type of contaminant. Apart from the molecular diffusion, white noise perturbations may arise from different fluctuations in the experimental configuration as well as from activity (spontaneous motion) of the tracer. The combination of such effects can be modeled by an effective increment of the value of $D_m \sim \xi^2$ what provides additional motivation to the study of the effect of noise in fluid dynamics performed below in a generic model..

The deterministic part of a paradigmatic model is proposed below. It is inspired in the model of Ref. [VJO98] which intended to capture the qualitative elements observed in the rotating annulus experiment. Consider a fluid channel (river) along the x direction with borders at $y = \pm 1$. Basically two flow regimes of this channel will be considered: (i) a regime of shear flow where the fluid is steadily flowing along x with sinusoidal velocity profile

$$\psi_1(x, y) = -v_1 \sin(\pi y), \tag{6.19}$$

illustrated in Fig. (6.8)(a); (ii) a regime of vortex flow where the fluid remains localized in the channel, given by

$$\psi_2(x, y) = v_2 cos(2\pi x)(1 - y^2)^2, \tag{6.20}$$

illustrated in Fig. (6.8)(b). Note that both regimes are periodic in x with period 1 and satisfy the boundary conditions, i.e., $v_x(y = \pm 1) = 0$. The qualitative features of a large class of
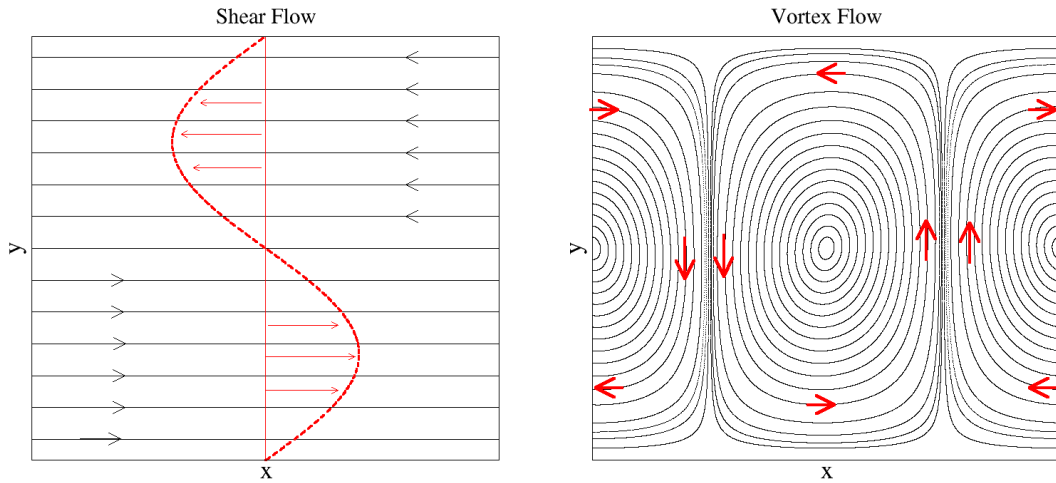
Figure 6.8: Representation of the streamlines of the two fluid regimes discussed in the text and used in order to compose the channel model given by the map (6.22).

time-periodic two-dimensional incompressible flows can be approximated as a superposition of these two regimes. The arguments for this claim are the same used in Sec. 2.1.2 to argue about the generality of the phase space of near-integrable Hamiltonian systems. Additionally, a time discrete system is desired in order to facilitate our numerical simulations. This can be achieved considering that the streamfunctions given by Eqs. (6.19) and (6.20) are alternated periodically in time each one for a fixed time t_0. A discrete system mapping the points (x', y') after one period t_n as a function of the points (x, y) before this period is obtained following Eq. (2.2) by

defining generating functions $F_n(x', y)$ as

$$F_n = x'y + \psi(x', y, nt_0)t_0,$$

The map $T_n(x, y) \rightarrow (x, y)$ is defined implicitly by

$$x = \frac{\partial F_n}{\partial y} \quad \text{and} \quad y' = \frac{\partial F_n}{\partial x'} \tag{6.21}$$

In this way the maps $F^{(1)}$ and $F^{(2)}$ related to ψ_1 and ψ_2 are obtained, and the combination of them is taken as the composition of this two maps [VJO98]. Considering additionally the noise perturbation discussed above, the following implicit map is obtained

$$\begin{aligned}
x_n &= x_{n+1} + \lambda \sin(\pi y_n) - \frac{2\rho}{\pi} y_n (1 - y_n^2) \cos[2\pi(x_{n+1})] + \xi \delta_n, \\
y_{n+1} &= y_n - \rho(1 - y_n^2)^2 \sin[2\pi x_{n+1}] + \xi \delta'_n.
\end{aligned} \tag{6.22}$$

This model is called hereafter *channel*. The control parameters are $\rho = \pi v_2 t_0/2$ – intensity of the vortex regime–, $\lambda = v_1 t_0/2$ – intensity of the laminar flow–, and ξ – intensity of the white noise variable δ ($\xi \sim \sqrt{D_m}$). Fixed $\rho = 0.6$ and two value of $\lambda = 0.25$ and $\lambda = 1$ were used, exploring carefully the dependence on ξ. The phase space for these two parameters are depicted in Fig. 6.9 [4]. Notice that the periodicity of the channel in x is preserved, what was used in the plot of this figure but is not considered in the transport problems in the next section. For both parameters one can identify regimes of steady flow (invariant tori of ballistic motion in x) near the walls $y \approx \pm 1$, which are remnants of the regime illustrated in Fig. 6.8a. In the case $\lambda = 0.25$ there exists additionally localized KAM islands that are not moving in x, which are remnants of the vortex regime illustrated in Fig. 6.8b.
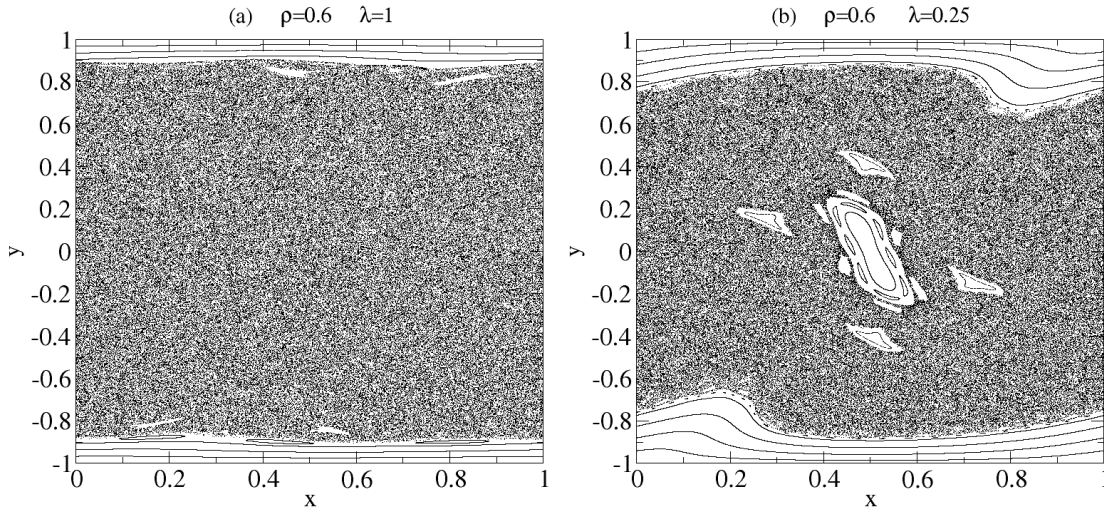
Figure 6.9: Iteration of different initial conditions of the map (6.22), restricted to $0 \leq x < 1$, in the absence of noise $\xi = 0$. The two control parameters studied are: (a) $\rho = 0.6, \lambda = 1$;where only laminar flow tori are visible; and (b) $\rho = 0.6, \lambda = 0.25$ where a localized KAM island is visible.

---

[4] Map (6.22) is iterated numerically using the Newton-Raphson method. Since the map is not defined for $|y| > 1$ reflecting boundaries conditions for the noise were used.

6.3.2   Transport properties of passive tracers

In this section the transport of a passive scalar contaminant in the x direction of the channel model (6.22) is considered (system open in x). The transport results from the combination of the molecular diffusion and of the chaotic advection of particles. It corresponds to a physically relevant and intuitive application of the CTRW theory described in Sec. 6.2.2 and of the theory for the effect of noise perturbations to stickiness developed in Sec. 6.2.3. Precise quantitative comparisons are difficult to perform due to the oscillations in the "power-law" probability density functions and due to finite time simulations. Nevertheless, remarkable qualitative agreement of the different regimes of stickiness described in Sec. 6.1 are obtained.

Figure 6.10: (Color online) Analysis of the temporal evolution of the coordinates x, y of trajectories in the channel (6.22). A single trajectory for each control parameters $\lambda = 0.25$ and $\lambda = 1$, with no molecular diffusivity $\xi = 0$ were considered. Long flights are associated to the stickiness to the running tori at $|y| \approx \pm 1$ and long traps are associated to the stickiness to the central islands (see Fig. 6.9).

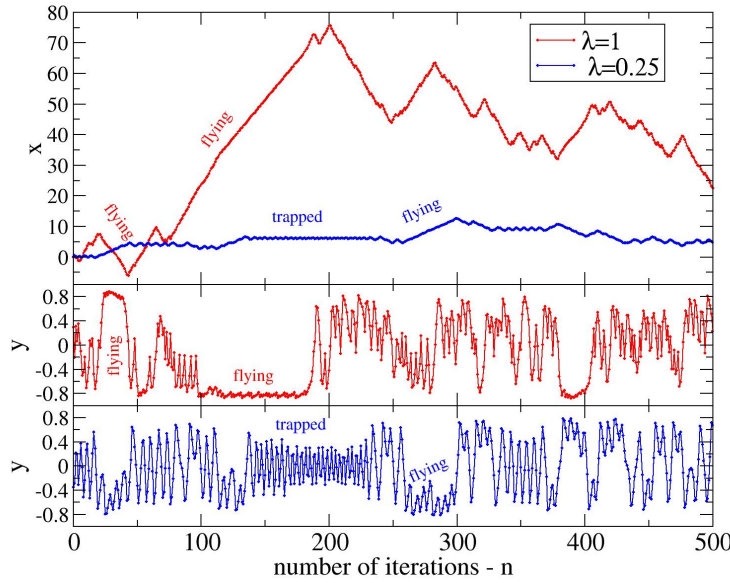Consider initially the movement of individual trajectories in the channel without molecular diffusion, as illustrated in Fig. 6.10. Again, our two representative control parameters $\lambda = 0.25$ and $\lambda = 1$ are chosen. In the latter case one observes in Fig. 6.10 that the dispersion of the trajectory occurs through a sequence of long flights. In the case $\lambda = 0.25$ one additionally sees the existence of long trappings where the position in x hardly changes. Comparing these regimes with the position in y, shown in the two other panels of this figure, one sees that these events coincide with the stickiness to the upper/bottom steady flow regions (left/right flights) and to the central localized islands (traps). Taking into account this relation, the following computational efficient definition of flights and traps were used: if the trajectory crossed th axis $y = 0$ during the last 4 iterations it was considered a trap, otherwise it was considered a flight to the positive/negative direction (for y smaller or greater than 0, respectively)[5] Due to the symmetry of our system there is equal probability of flying to the left and to the right and thus no further distinction will be considered. The numerical results are shown in Fig. 6.11. It is not a surprise that the distribution of flights and traps in the unperturbed case ($\xi = 0$) follow the same kind of power-law like distribution of the stickiness events, justifying thus the power-law assumptions of the continuous time random walk model expressed in Eqs. (6.8) and (6.9). Figure 6.11 shows also that the effect of noise in the statistics of traps and flights is the

---

[5] Notice that the value $y = 0$ separates the regions of flows to the left and right and that the bigger chain of secondary islands has period 4 meaning that a typical trajectory stuck to it crosses the axis $y = 0$ twice in this period.

same as to the stickiness, i.e., an intermediate regime of enhanced probability (tending to a $\gamma_{f,t} = 0.5$ regime) followed by an asymptotic exponential decay.
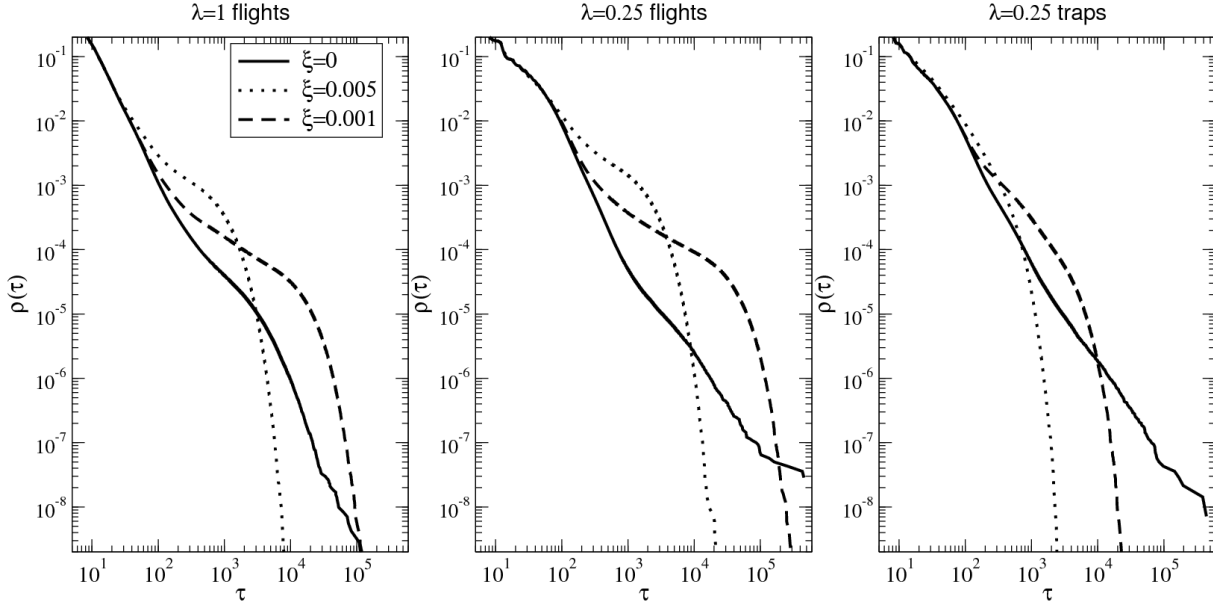

Figure 6.11: Statistical analysis of the flights and traps illustrated in Fig. 6.10 for the two control parameters $\rho = 0.6, \lambda = 1$ and $\rho = 0.5, \lambda = 0.25$, and three different noise intensities $\sqrt{D_m} \sim \xi = 0, 0.005, 0.001$.

So far the statistics of single trajectories was considered. The transport properties of the system, measured by the growth of the mean squared displacement as in Eq. (6.6), is a consequence of the statistical behavior of an ensemble of trajectories. The next numerical experiment performed in the channel model, illustrated in Fig. 6.12, aims to show how this statistical description of the system emerges from the deterministic chaotic dynamics. The temporal evolution of a line of dye (passive tracer) under the channel dynamics (6.22) is shown. For short times the dynamics is controlled by the stable and unstable manifolds of the fixed point $(x, y) = (0, 0)$. The following panels of Fig. (6.12) show the stirring of the dye due to the stretching and folding of phase-space areas, a typical phenomenon of chaotic dynamics. For large times this leads to a seemingly uniform mixing of the contaminant in the chaotic component. Molecular diffusion was not considered in this figure. It would add random fluctuations at each iteration, increasing thus the uniformity of distribution of the contaminant for longer times.

It is clear from Fig. 6.12 that the distribution of dye for long times ($t > 100$) is necessarily described statistically. While anomalous transport is observed for the fully deterministic case $D_m \sim \xi^2 = 0$, by the same arguments presented in Sec. (6.2.3), the transport is normal (diffusive) for any $\xi, D_m \neq 0$ at sufficiently large times ($\tau_{2,3}^{\dagger} \sim 1/D_m$). This is shown for both control parameters in Fig. 6.13, where one sees the same behavior from Fig. 6.6 obtained for the standard map with accelerator modes. In particular, the intermediate regime of enhanced anomalous transport is clearly seen for small molecular diffusivity. In the case $\lambda = 0.25$ regions of regular ballistic flow and of trapped flow exist. Nevertheless, in agreement with the CTRW theory behind Eq. (6.11), and since both regions have similar sizes, superdiffusion dominates the intermediate regimes. All initial conditions were chosen inside the region corresponding to the chaotic sea of the deterministic system, what is essential for the intermediate results.

The asymptotic diffusion coefficient measured as a function of the molecular diffusion intensity for both parameters $\lambda = 0.25$ and $\lambda = 1$ is shown in Fig. 6.14. This is analogous to
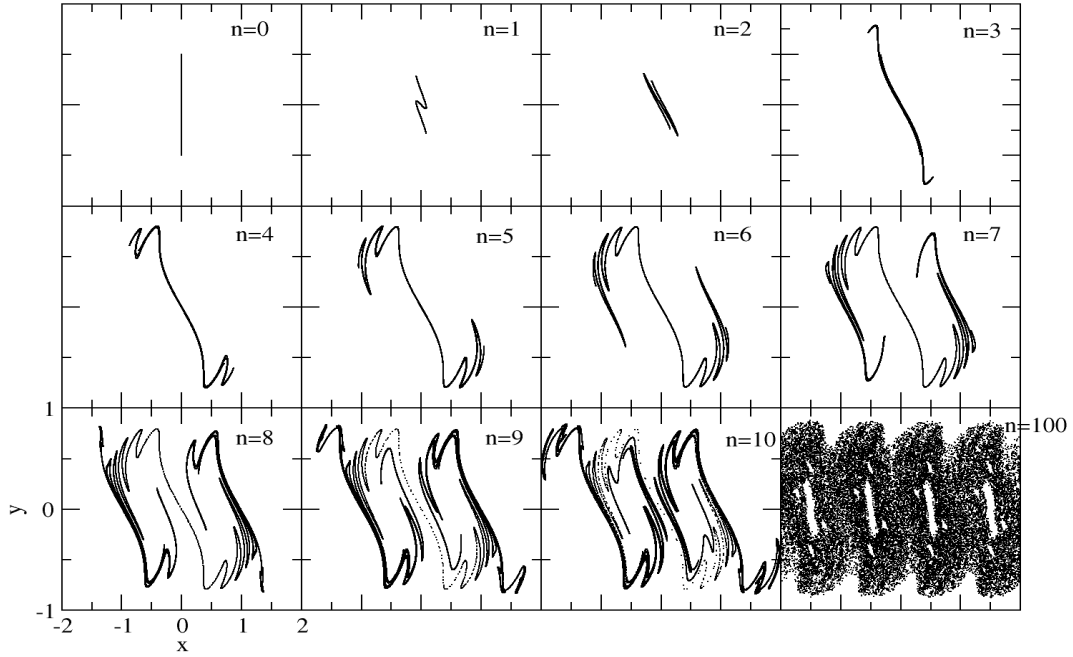
Figure 6.12: Stirring of a line ($x = 0, -0.5 < y < 0.5$) for the channel model (6.22) with $\rho = 0.5, \lambda = 0.25$ and $\xi = 0$ and opened in the x direction. Each panel shows the position of the marked points at a time n.
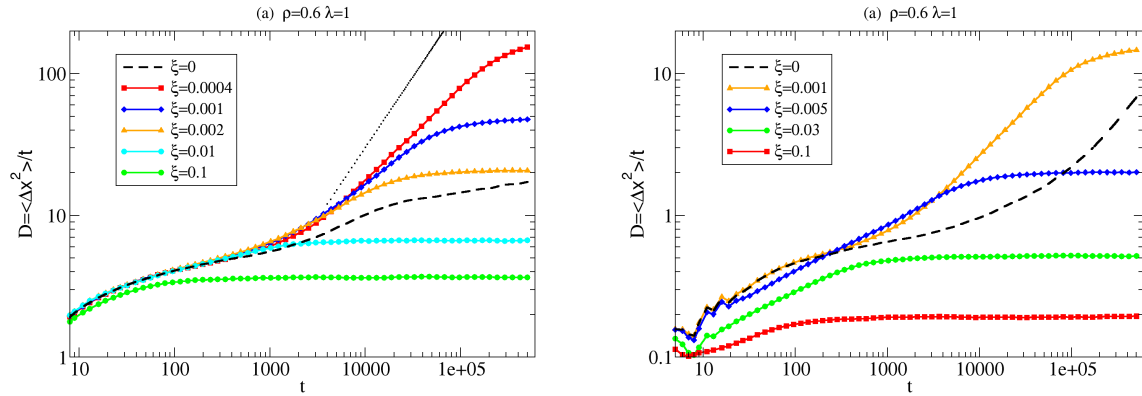
Figure 6.13: (Color Online) Transport of contaminant along the x component of the channel model (6.22) with different noise intensities (molecular diffusivities) $xi \propto \sqrt{D_m}$, reduced from bottom to top (see legends). 10^5 initial conditions were chosen inside the chaotic sea. The thick black curve corresponds to the unperturbed case $\xi = 0$, showing anomalous transport. When the curves become constant (for $t \to \infty$) transport is normal. Control parameters: (a) $\rho = 0.6$ and $\lambda = 1$; (b) $\rho = 0.6$ and $\lambda = 1$.

what is shown in the inset of Fig. 6.6 and consists in a physically and experimentally relevant diagram [BCVV95]. In the academical case of very large molecular diffusion (left of the figure) the trivial relation $D = D_m$ is observed. The opposite limit, of very small molecular diffusion

(right of the figure), is the physically relevant one and shows the asymptotic $D \sim 1/D_m \sim 1/\xi^2$ regime predicted in Eq. (6.14) and already discussed by Taylor [Tay53]. For intermediate values of the molecular diffusion strength another power-law like dependence of D on D_m is observed, similar to what is predicted in Eq. (6.14). While the transport in the case $\lambda = 1$ is completely analogous to the standard map with ballistic islands, discussed in Sec. 6.2.3 and illustrated in Fig. 6.6, the case $\lambda = 0.25$ is more complicated. This is due to the existence, together with the steady flow near the borders (ballistic tori), of localized KAM islands where the trajectories may stick or, through molecular diffusivity, even penetrate. In this case the CTRW models with both algebraic trapping and flight distributions has to be considered, as presented in Sec. 6.2.2. Since, as argued in Sec.6.1.1 the molecular diffusion leads to a large intermediate regime of enhanced stickiness with $\gamma = 0.5$ the stickiness to localized islands might be relevant for intermediate times.

Figure 6.14: (Color online) Asymptotic diffusion coefficient D_A as a function of the noise intensity (molecular diffusivity) $\xi \sim \sqrt{D_m}$ for the two parameters of Fig. 6.13. The asymptotic $D_A = 1/D_m$ is observed for small ξ.

Chapter 7

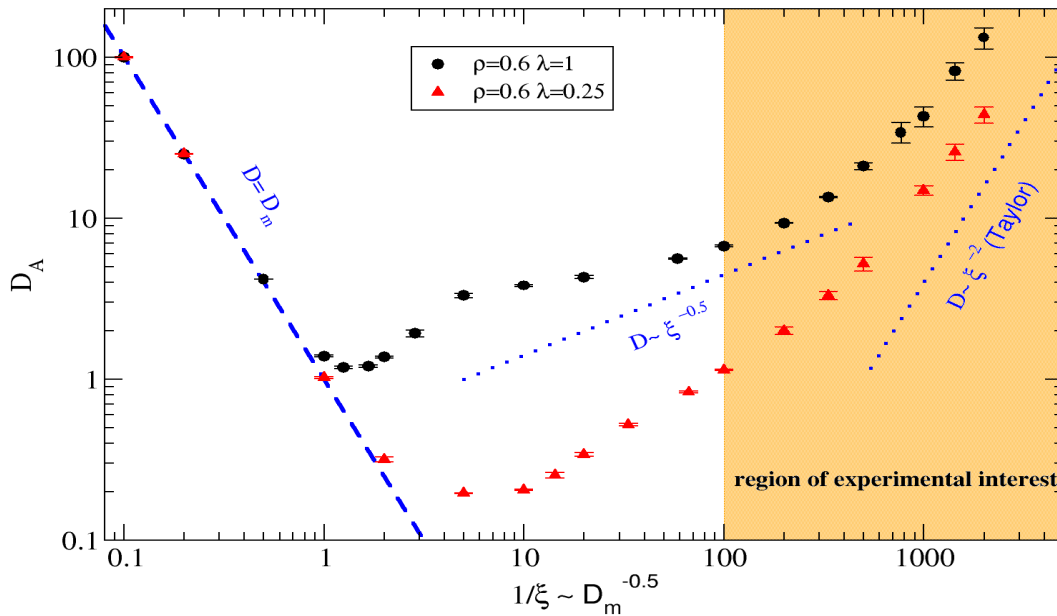# Higher-dimensional Hamiltonian systems

Stickiness in Hamiltonian systems with more than two degrees of freedom is considered. One major motivation for this investigation is the assumptions of strong chaos in high-dimensional Hamiltonian systems (Sec. 7.1). A system composed of N coupled area-preserving maps is considered here (Sec. 7.2). The RTS (recurrence time statistics) is compared to the case of noise-perturbed systems and an asymptotic power-law regime is identified as a pure high-dimensional effect (Sec. 7.3). Numerical results suggest that stickiness is reduced by increasing N, indicating that this paradigmatic class of Hamiltonian systems asymptotically fulfill the requirements of the hypotheses of strong chaos. The consequences to the anomalous transport of trajectories are discussed.

7.1 Stickiness and strong chaos hypotheses

At the end of the XIX century thermodynamical phenomena started to be successfully explained through the statistical properties of a large number of particles (atoms) subject to the laws of mechanics. As mentioned in the beginning of Chap. 3, this exposes some unavoidable contradictions between the time-reversible character of classical mechanics and the irreversibility of thermodynamics, what forced the re-interpretation of thermodynamical laws in a statistical sense. It was clearly from the very beginning that the statistical analysis was justified not only from the astonishing number of particles in a typical thermodynamical system, as indicated by the Avogadro number $N_A = 6 \; 10^{23}$ particles/mol, but also from a hypothesis of "random" motion of the particles. This hypothesis was introduced explicitly in different contexts, like the hypothesis of molecular chaos, Boltzmann's ergodic hypothesis (used in equilibrium), and Gibb's mixing hypothesis (out of equilibrium).

Different computational methods rely in similar assumptions of strong chaotic dynamics. This is the case when kinetic equations of transport are derived for a given system, in linear response theory leading to Green-Kubo formulae, and for the calculation of escape rates [Dor99]. In particular, such hypotheses are essential for the substitution of chaotic variables by a stochastic process leading to an effective Fokker-Planck equation [Bab05, RBG$^+$05]. In these cases the number of particles or degrees of freedom can be much smaller than those of thermodynamical systems mentioned initially.

From a dynamical-systems perspective the different chaotic hypotheses implicitly or explicitly used in the examples above consist essentially of two main assumptions about the

(high-dimensional Hamiltonian) dynamics:

(i) Ergodicity, i.e., the existence of a single chaotic component and negligible measure of the regions of quasi-periodic motion.

(ii) Strong mixing, i.e., exponential decay of correlations.

Low-dimensional Hamiltonian systems, as seen throughout this Thesis, typically violate both hypotheses: the first, due to the existence of islands of regular motion embedded in a chaotic sea, and the second due to the stickiness of chaotic trajectories to the border of such islands. What happens in higher-dimensional systems? As expected, different answers are obtained for different classes of systems. However, for many relevant higher-dimensional systems it is generally expected that hypothesis (i) is effectively valid since the measure of the quasi-periodic trajectories decreases (exponentially) with the number N of degrees of freedom (see, e.g., Sec. 6.5 of Ref. [LL83])[1]. One example where this happens are the N coupled symplectic maps with mixed phase space discussed in detail below. Another indication that ergodicity is approached in higher dimensions comes from the estimation of the KAM perturbation threshold ε^* for the breakdown of the last torus (see Sec. 2.1.2). It is shown that $\varepsilon^* \to 0$ for $N \to \infty$, typically as $\varepsilon^* \sim \exp[-N \ln(N)]$ (see Refs. [PCCS$^+$05, FMV91] and references therein).

However, the vanishing measure of regular regions [hypothesis (i)] does not guarantee the fast decay of correlations [hypothesis (ii)]. The breakdown of hypothesis (ii) occurs, e.g, due to the stickiness of chaotic trajectories around non-hyperbolic structures in the phase-space, and even zero measure sets can be responsible for the anomalous decay of correlations. A class of systems where this happens was exhaustive discussed in Chap. 4 where it was shown that families of MUPOs (marginally unstable periodic orbits) are responsible for stickiness despite having zero measure. This shows clearly the independence of both hypotheses listed above and that even ergodic high-dimensional systems may violate hypothesis (ii) by having slow decay of temporal correlations. A reason for that, as in the low-dimensional case, is the phenomenon of stickiness.

Despite the huge interest on the stickiness phenomenon in Hamiltonian systems with two degrees of freedom and in area-preserving maps, as is hopefully clear from the previous pages of this Thesis, only very few results are known for $N = 2$–5 [DBO90, KG87a, KPS00]. One of the reasons for this is the difficult topological interpretation of the phase space [VCG83, LL83]. KAM tori in high-dimensional systems do not split the phase space and thus do not represent absolute barriers for the chaotic trajectories. The reason is that they have dimension $D_{tori} = N$ in a space of $D_{space} = 2N$ dimensions while absolute barriers occur only if $D_{tori} = D_{space} - 1 \Rightarrow N = 2$. This leads to the phenomenon of Arnold diffusion [Arn64, LL83], i.e., trajectories that in a given Poincaré section are confined between two invariant tori are eventually going to escape this confined region. This effect is however extremely slow, an upper bound being estimated by Nekhoroshevs theorem [Nek71] which states how fast trajectories close to a tori will depart from it. Relations between Nekhoroshev bound and stickiness were proposed in Refs. [Aiz89, PW94]. However, they reflect in some sense the topological structure of the phase space close to typical tori (in a spirit similar to the KAM theorem), but not necessarily the dynamical behavior of typical chaotic trajectories. In any case no convincing derivation of the stickiness exponents were performed so far through this approach.

---

[1] It should be noted that in many cases the ergodicity is not necessary in the full phase-space, but only in projected low-dimensional spaces which take into account all relevant observables.

7.2 Coupled symplectic maps

7.2.1 General coupling procedure

In order to systematically investigate stickiness in higher-dimensional Hamiltonian systems, a computational efficient model with variable dimension is desired. These requisites are fulfilled by a time-discrete $2N$-dimensional Hamiltonian system constructed through the composition $\boldsymbol{T} \circ \boldsymbol{M}$ of the independent one-step iteration of N symplectic two-dimensional maps $\boldsymbol{M} = (M_1, \ldots, M_N)$ and a symplectic coupling $\boldsymbol{T} = (T_1, \ldots, T_N)$. A detailed description of this coupling procedure and a list of references where the dynamics of different coupled maps was studied is found in Appendix B. As a representative example of 2-d maps the standard map is again chosen [LL83]:

$$M_i \begin{pmatrix} p_i \\ q_i \end{pmatrix} = \begin{pmatrix} p_i + K_i \sin(2\pi q_i) & \mathrm{mod}\ 1 \\ q_i + p_i + K_i \sin(2\pi q_i) & \mathrm{mod}\ 1 \end{pmatrix}, \tag{7.1}$$

and a coupling potential between the maps i, j given by $V_{i,j} = \xi_{i,j} \cos[2\pi(q_j - q_i)]$. The action of the coupling on the i-th map is hence given by

$$T_i \begin{pmatrix} p_i \\ q_i \end{pmatrix} = \begin{pmatrix} p_i + \sum_{j=1}^N \xi_{i,j} \sin[2\pi(q_i - q_j)] \\ q_i \end{pmatrix}, \tag{7.2}$$

what corresponds to a perturbation Δp_i. The full coupling $\boldsymbol{T}$ is symplectic, i.e., satisfies Eq. (2.3), if and only if $\xi_{i,j} = \xi_{j,i}$. This guarantees the symplectic character of the full system since Eq. (7.1) is also symplectic and thus their composition [Ott02]. For simplicity all-to-all coupling with $\xi_{i,j} = \frac{\xi}{\sqrt{N-1}}$ was used, in which case a numerically convenient mean-field representation can be written [LRR99]

$$\Delta p_i = \frac{\xi}{\sqrt{N-1}} \sum_{j=1}^N \sin[2\pi(q_i - q_j)] = \xi |\boldsymbol{m}| \sin(2\pi q_i - \phi), \tag{7.3}$$

where $\boldsymbol{m} = (m_x, m_y) = \frac{1}{\sqrt{N-1}} \sum_j [\cos(q_j), \sin(q_j)]$ and $\tan(\phi) = m_y/m_x$. The main results presented below were verified using a different area-preserving map and also linear coupling potential.

When the isolated systems are chaotic and weakly coupled a reasonable assumption is that the autocorrelation of the positions q_j decay fast and that there is no correlation between different q_j's. Each term of the sum in Eq. (7.3) is then given by a random variable $y \in\ ]-1, 1[$ distributed according to the density $P(y) = 1/(2\pi \sqrt{1 - y^2})$, which has variance $\sigma_y = \sqrt{2}/2$. In this case, for large N Eq. (7.3) tends to a normal distribution with $\sigma = \xi \sigma_y$, i.e., a finite perturbation strength. This effect is verified in Fig. 7.1. This indicates that the results for the stickiness of coupled maps have to be compared with the noise perturbed case explored in the previous Chapter, what is done in Sec 7.3. This clarifies the motivation to denote in this Chapter the coupling strength by the same letter ξ used to denote noise intensity in the previous Chapter as well as the motivation to use the normalization factor $1/\sqrt{N}$. This is a major difference from other coupled-oscillator models where a rescale term $1/N$ instead of $1/\sqrt{N-1}$ is used [dCNF02, TMM94, LRR99].

7.2.2 Characterization of the phase space

In this section the phase space structures present in the coupled-map model are investigated. Insights gained in the small coupling limit ($\xi \to 0$) are confirmed numerically (see Refs. [GLS89, ABS06] for more detailed analysis in similar systems). The natural coordinates to describe the full high-dimensional system are the q_i, p_i of the two-dimensional maps. For simplicity, it
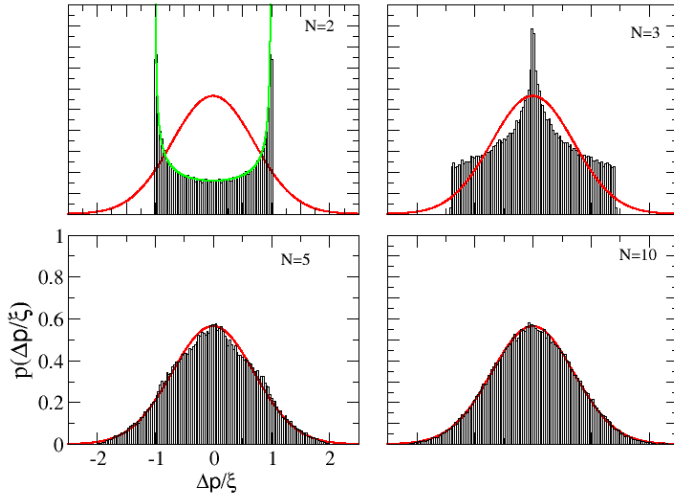
Figure 7.1: (Color online) Distribution of the perturbation (7.3) for $N = 2, 3, 5$, and 10 coupled maps with $K \in [0.51, 0.53]$ and $\xi = 0.1$. The curves are compared to the probability density functions $P(y) = 1/(2\pi\sqrt{1 - y^2})$, expected for $N = 2$ and to a Gaussian distribution with $\sigma = \xi\sigma_y = \xi\sqrt{2}/2$.

will be written that a point is inside the island (or chaotic sea) of the map $N^\dagger$ to refer that the projection of the full phase space (not a Poincaré or quasi-surface section) in the variables $q_{N^\dagger}, p_{N^\dagger}$ lies inside the region corresponding to an island of regular motion (or chaotic sea) of the isolated map $N^\dagger$.

Consider the case $\xi = 0$ (uncoupled maps) and all two-dimensional maps having mixed phase space. Initial conditions corresponding to quasi-periodic trajectories (i.e., inside islands) in all two-dimensional maps correspond to a N-dimensional torus of the high-dimensional system. The question is which of these tori survive for small non-zero coupling ($\xi \gtrsim 0$)? From KAM theory (see Sec. 2.1.2) one gets that almost all of them do. This leads to the natural estimation of the measure of the regular components in the N-dimensional phase space $0 \leq \mu_{total} \leq 1$ as a function of the measure $\mu_i, i = 1...N$ of the islands in lower-dimensional maps by $\mu_{total} = \prod_{i=1}^{N} \mu_i$ for $\xi \to 0$. In the case all maps have similar measure of islands $\mu_i \approx \mu_{island}, \forall i$, this reduces to an exponential decay as discussed in Sec. 7.1

$$\mu_{total} = e^{ln(\mu_{island})N}, \ \xi \to 0. \tag{7.4}$$

Regarding the chaotic trajectories, a great simplification is obtained if the "Froeschlé conjecture" is fulfilled (see p. 380 of Ref. [LL83]): Hamiltonian systems have only global invariant of motions, i.e., all trajectories (apart from zero measure sets) in a system with N degrees of freedom that has P global invariant of motions have additionally either $N - P$ invariant of motions being thus quasi-periodic (regular component) or will have no additional invariant of motion being thus chaotic. This is in agreement with the picture of Arnold diffusion that all chaotic trajectories belong to the same ergodic component. Many publications report possible deviations of this pictures (at least for practical or numerical purposes, i.e., very small values of Arnold diffusion) [GLS89, PV84, LPB06]. However, all our results and numerical simulations are consistent with the validity of such hypothesis, even though no detailed numerical simulation was performed to verify it. In any case, all simulations below consider *typical* trajectories of the main chaotic component without careful choice of initial conditions.

The numerical results obtained are summarized in Fig. 7.2 and described next. In order to avoid artificial symmetries in the coupled map model, different control parameters for each two-dimensional map were chosen $K_i \in [0.51, 0.53], i \in \{2...N\}$, fixing $K_1 = 0.52$. Again, the

numerically convenient standard map (6.1) was used. For the control parameters mentioned above, numerical investigations indicate that approximately $\mu_{island} = 0.1926$ of the phase space of each map ($N = 1$) is built by regular trajectories (the thin chaotic regions inside the island of regular motion were neglected in this estimation). The first simulation considered $N = 2$ and started trajectories close to the center of the island in the first map and in the chaotic sea of the other map. It was verified that all trajectories eventually have escaped the region corresponding to islands ($x_1 < 0.5$). The mean escape time as a function of the coupling strength ξ is shown in Fig. 7.2b and the observed scale $1/\xi^2$ is in agreement with the random-walk theory for the movement inside the island, developed in the previous chapter. This motivates the following condition to determine whether given initial condition belongs to a regular component: trajectories that have not escaped for a time $t_{max} = 5/\xi^2 + 100$, i.e., at least five times greater than the mean escape time[2]. Reducing the value of the coupling strength ξ one observes in Fig. 7.2a that the number of tori abruptly increases from zero for both $N = 2$ and $N = 3$. In the limit of $\xi \to 0$ one observes the tendency of approaching the limit μ^N of Eq. (7.4), indicated by dashed horizontal lines in this figure. A rough numerically estimation of the measure of the regular components as a function of N is given in Fig. 7.2c, in qualitative agreement with Eq. (7.4). The numerical procedure described above was applied also to a system where one of the maps had no islands $\mu_i = 0$, e.g., the standard map with high K value or the cat map. No high-dimensional tori were detected in these cases, in agreement with the previous discussion (see Appendix B for the RTS in such systems).
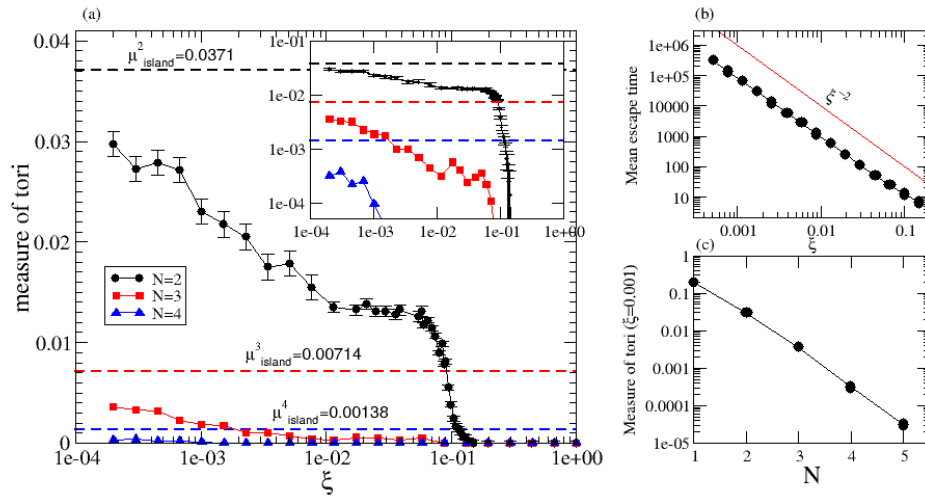
Figure 7.2: (Color online) (a) Numerical estimation of the measure of tori in the coupled-maps model as a function of the coupling strength ξ for $N = 2, 3$, and 4. The straight dashed lines represent the upper limit case (7.4) expected for $\xi \to 0$. Inset: log X log representation. (b) Estimation of the mean escape time of the island in all projections for $N = 2$ and $\xi = 0.002$. Initial conditions: inside the island in x_1, y_1 and in the chaotic sea for x_2, y_2 $\xi = 0.1$. (c) Measure of regular region as a function of N. In all simulations 2000 trajectories were used which were considered to belong to a torus if they remained inside a region containing the islands for a time greater than $t_{max} = 5/\xi^2 + 100$.

---

[2]No verification of the type of movement (quasi-periodic or chaotic) was performed and this condition (for any t_{max}) does not exclude thus chaotic trajectories that belong to a different ergodic component, if such components exist.

In summary, the coupled-map model proposed in Sec. 7.2.1 contains regions of regular motion in the limit of small coupling if, and only if, all two dimensional tori have mixed phase space. These invariant high-dimensional tori are a direct product of the N one-dimensional tori. The number of such tori decreases with increasing dimensionality N, given by Eq. (7.4), and with increasing coupling strength ξ.

7.3 Numerical results for the chaotic dynamics

7.3.1 Stickiness

It is clear from the previous section that a discrete time system with N-dimensional tori was successfully generated. The RTS is calculated next in order to quantify the stickiness close to these generic structures. The construction of the coupled-map model in Sec. 7.2.1 suggests that the results should be compared with the case of noise-perturbed map with noise intensity $\xi' = \sqrt{2}\xi/2$. In order to facilitate such a comparison the RTS is calculated focusing on a single map, i.e., the recurrence region is defined as in the noisy case for one map ($x_1 < 0.5, 0 \leq y_1 \leq 1$) and the full phase-space of the other maps ($0 \leq x_i, y_i < 1, i = 2...N$). It was verified numerically that this choice does not affect the stickiness to higher-dimensional tori since, as discussed in Sec. 7.2.2, all such tori are away from this recurrence region. The numerical RTS obtained for $N > 1$ is shown in Fig. 7.3 and compared to the results for noise-perturbed map. Both curves are almost indistinguishable for recurrence times belonging to the regimes (R1) and (R2) discussed in Sec. 6.1. However, remarkable differences are observed for long times (see also Fig. 7.6a for $\xi = 0.05$). Contrary to the exponential decay of the previously-reported regime (R3) the detailed studies below indicate that the following regime of decay of the RTS exists

(R3') For large times ($\tau > \tau_{2,3}$) the RTS shows an exponential followed by a power-law decay (with exponent γ_{R3}) due to the stickiness to N-dimensional tori.
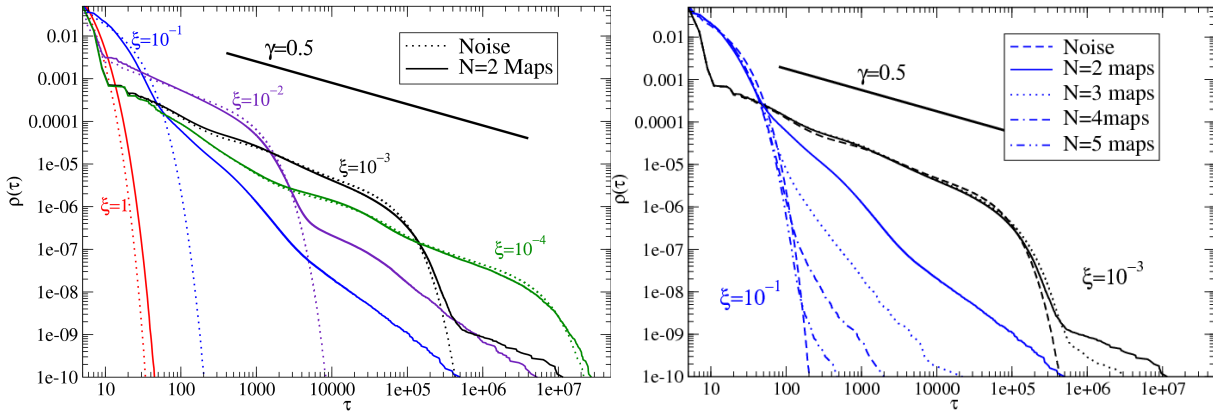
Figure 7.3: (Color online) (a) RTS for two coupled standard maps (6.1) and different coupling strengths ξ (solid lines), compared to the case of a single standard map perturbed by noise with intensity 0.707ξ (dashed lines); (b) RTS for N coupled standard maps for $\xi = 10^{-1}$ and $\xi = 10^{-3}$, compared to the noise perturbed map (dashed line). Parameters $K_1 = 0.52, K_i \in [0.51, 0.53], i = 2...N$ and recurrence region $x_1 < 0.5$.

In order to show that regimes (R1) and (R2) have the same origin from those of noisy system and, specially, that regime (R3') is indeed related to higher-dimensional tori, the question about the position in the phase space of trajectories in these regimes is asked. The procedure used in Sec. 6.1.1 for the noise-perturbed system is repeated here: in Fig. 7.4 intervals of reference for the recurrence times are defined (compare with Fig. 6.2). The density in the phase space
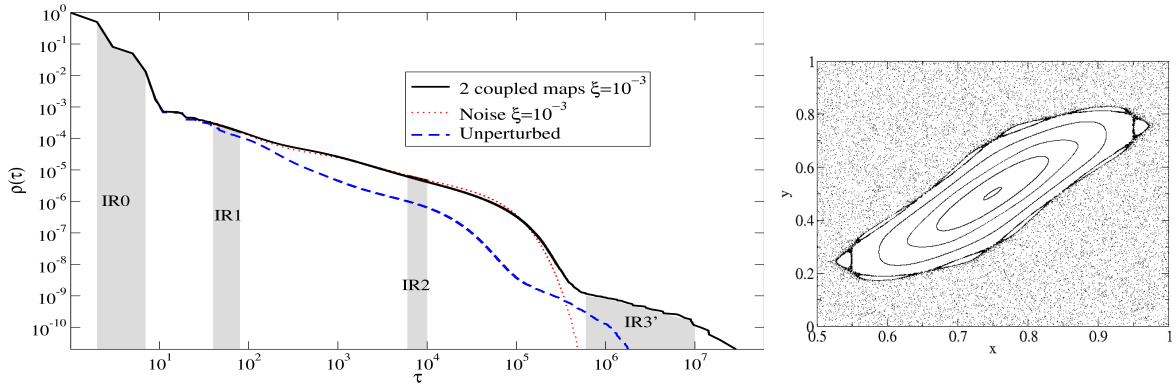
Figure 7.4: (a) RTS for $K = 0.52$, unperturbed, with additive noise, and coupled to another standard map. The intervals R1-R3 are defined as: IR0= $[2, 7]$, IR1=$[40, 80]$, IR2=$[6\ 10^3, 10^4]$, IR3=$[2\ 10^5, 3\ 10^6]$, IR3'=$[6\ 10^5, 10^6]$. (b) Phase space of the standard map with $K = 0.52$ amplified around the main island.

of trajectories that have a recurrence time T belonging to each of these intervals are plotted in Fig. 7.5. The case of $N = 2$ coupled maps is considered and the position in the phase space is projected to the coordinates of each map (left and right columns). It is clear that for the intervals IR0, IR1, and IR2 the same picture as in Fig. 6.3 is observed in the reference map (left) while the trajectories spread almost uniformly in the other map (right). This means that the three regimes are composed, respectively, by trajectories away from the island, stuck to the border of the island, and inside the island (the longer the recurrence time the deeper the trajectories penetrate the island). The term "island" here refers to the area of the phase space of the reference map that in the uncoupled limit corresponds to a KAM island. Remind that the symmetry between the reference map and the additional map is due to the definition of the recurrence region that includes all phase space of the additional map $0 \leq x_2, y_2 < 1$ but only a region of the chaotic component of the reference map[3]. For the interval $IR3'$ Fig. 7.5 shows that trajectories in *both* maps were inside the area corresponding to their islands. As argued above the composition of such trajectories build high-dimensional tori confirming the previous interpretation of this regime as stickiness to high-dimensional tori. This was further verified numerically by noting that the asymptotic power-law behavior is not present whenever one of the N two-dimensional maps is chosen to be fully chaotic (without KAM islands). In this case the RTS is indistinguishable from the noise-perturbed case.

The power-law regime in (R3) is thus a pure high-dimensional effect. The dependence on N of the asymptotic power-law exponent γ_{R3} is investigated next. The term asymptotic here has to be taken with caution since already for $N = 1$ the convergence is very slow [CS99] (as shown in Fig. 2.3). However, for our purposes it is enough to perform a comparative analysis for different N and similar times and initial conditions. Since the following results are exclusively numerical, this does not role out the possibility of the existence of a different behavior for larger times. Initially it is necessary to distinguish between two effects of N on the RTS seen in fig. 7.3a: the later onset of the power-law regime for increasing N, related to the smaller measure of the tori – hypothesis (i) of Sec. 7.1; and the different values of γ_{R3} (slope of the tails), related to the stickiness to higher-dimensional tori – hypothesis (ii) of Sec. 7.1. The latter effect corresponds to the stickiness phenomenon this Thesis studies and which is responsible for the asymptotic decay of correlations as discussed in Chap. 3. Figures 7.3b and 7.6a already suggest that γ_{R3} increases

---

[3]A recurrence region away of islands in both maps was also used without changing the interpretation of the results.
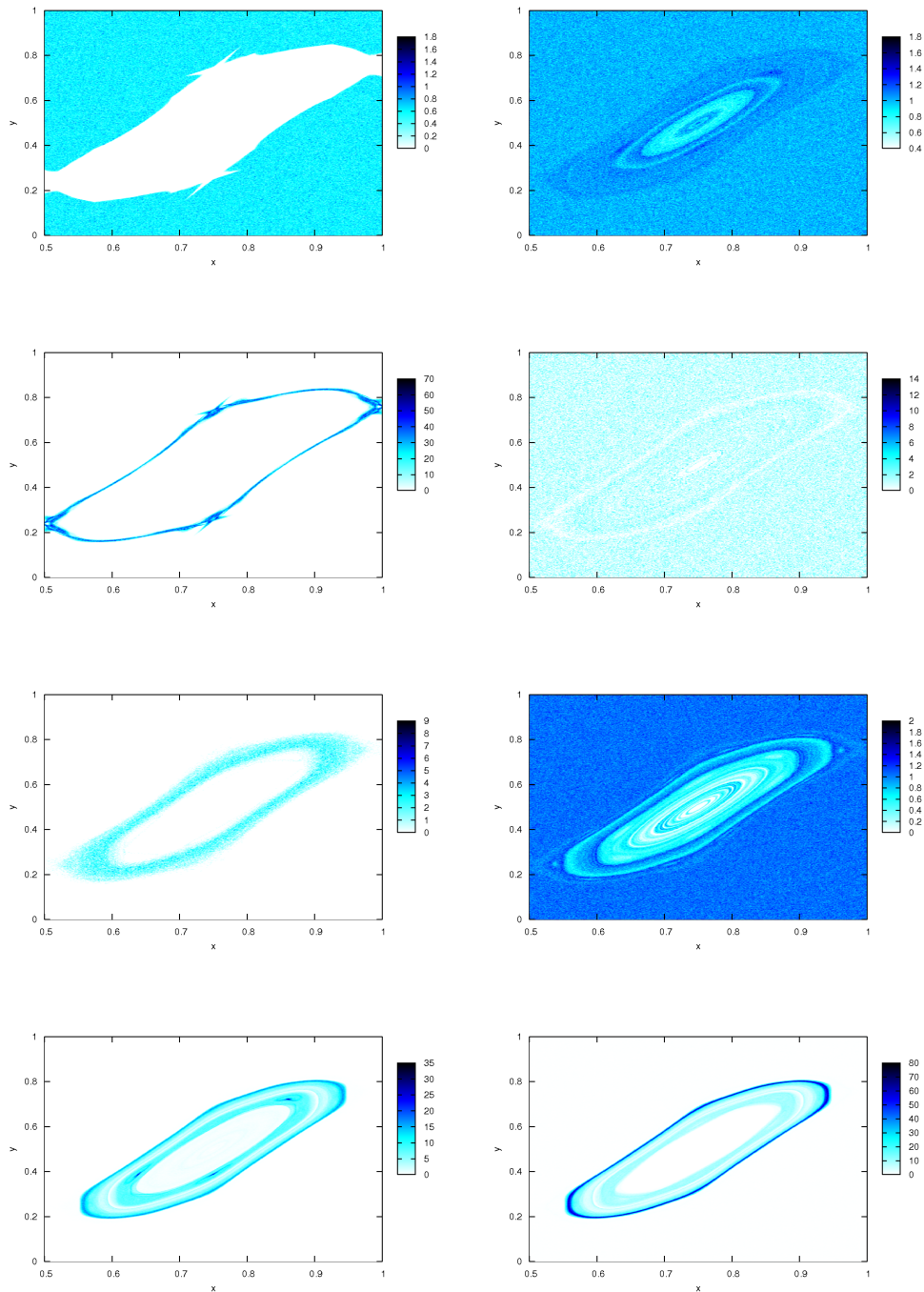
Figure 7.5: (Color online) Density of points in the phase space of two coupled standard maps $K = 0.52$ with $\xi = 10^{-3}$ for trajectories having recurrence time in the regions assigned in Fig. 6.2(b), from top to bottom: IR0, IR1, IR2, and IR3. Left column corresponds to the map of reference, i.e., where the recurrence region was defined (away of the island), and right column to the coupled standard map. A fundamental distinction from the results of Fig. 6.3 is seen only in the case IR3 (last line). Average density corresponds to the color scale 1.

with N. In Ref. [DBO90] similar results were reported for a different system and $N = 2$ and 3. For improved statistics in the tails the survival probability $f(t)$ inside a region containing the N-dimensional tori of 10^{10} trajectories started *close* to them was studied[4]. As discussed in Sec. 3.1 the power-law tails of such distribution is the same of the RTS. $f(t)$ is shown in fig. 7.6b where it is evident that the power-law exponent increases with N. The estimated exponents shown in fig. 7.6c for different moderate values of the coupling ξ suggest a linear dependence $\gamma_{R3} \propto N$.
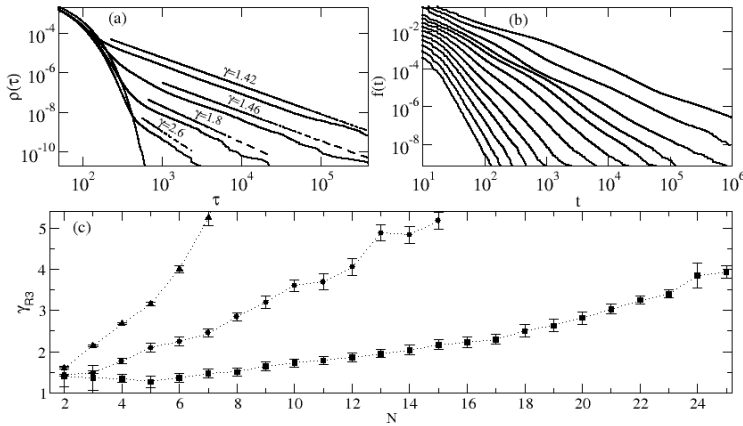
Figure 7.6: (a) RTS for $\xi = 0.05$ and $N = 2, 3, 4, 5$, and noise (from top to bottom). (b) Survival probability $f(t)$ of 10^{10} trajectories near the N-dimensional tori for $\xi = 0.05$ and $N = 2, ..., 15$ (from top to bottom). (c) Exponent γ_{R3} fitted to the power-law regime of $f(t)$ for $\xi = 0.1, 0.05, 0.03$ (from top to bottom). In all cases $K_1 = 0.52$ and $K_i \in [0.51, 0.53], i \in \{2, ..., N\}$ were used in map (6.1).

The numerical results shown in the previous figures refer to the particular case of sinusoidally coupled standard maps. Similar results were obtained also for different control parameters and for a similar area-preserving map with linear coupling. One can expect an even broader generality of this result since the low-dimensional maps chosen are generic themselves. Additionally, as stressed above, the incoherent effects of the coupling maps were fully understood from the comparison with the noisy system and do not affect the result of Fig. 7.6, i.e., that γ_{R3} increases with N. This result is consistent with the effective validity of hypothesis (*ii*) for high-dimensional systems since the sharp tails indicate fast decay of correlations. Usually ergodicity [hypothesis (i)] is assumed to be effective valid even if the measure of quasi-periodic trajectories does not vanish provided it decay fast with N. Similarly, the mixing assumption [hypothesis (ii)] can be considered effective valid even if the correlation does not decay exponentially but power-law provided the exponent is sufficiently high. How large the exponent should be depends on each specific problem, e.g., in the case of anomalous transport it is $\gamma_{R3} \geq 2$ (see next section). The simulations shown in Fig. (7.6)c for $N < 25$ suggest that $\gamma_{R3} = 2$ (or other finite value of γ_{R3}) is achieved for large enough N irrespective of the coupling strength ξ. This interpretation of the validity of hypothesis (ii) that emerges from our numerical simulation in the coupled symplectic maps differs from other explanations based on ergodicity and Arnold diffusion [KK89].

A theory for the stickiness in high-dimensional phase space does not exist so far (besides the general connections to Nekhoroshev theorem [Aiz89, PW94]). Comparing with the case of two-dimensional maps, even if families of high-dimensional cantori exist and can be also well characterized, they do not represent partial barriers to the movement since Arnold diffusion guarantees different paths for the chaotic trajectories to move. Actually due to the dimensionality of space and tori there is no "inside" and "outside", as the construction through turnstiles sketched in Sec. 2.2.3 provide for $N = 1$, and no (Markov) states in the phase space can be defined. A theoretical explanation of the numerical results described above is frustrated due to these major difficulties. A general interpretation of these results is that the topological difference

---

[4]Inside the island $q_i \in [0.7, 0.8], p_i \in [0.4, 0.6]$ for $i \in \{2, ..., N\}$ and close to it $q_1 = 0.9, p_1 \in [0.835, 0.845]$ in the remaining map.

in dimension is responsible for the different stickiness that were observed. This interpretation applies much more generally than to the case of coupled two-dimensional maps and it remains to be verified in other systems.

After these discussions and conjectures about the asymptotic decay of the RTS, one practical remark about the non-asymptotic behavior should be added. In the case of weak-coupled maps the finite time dynamics and asymptotic diffusion coefficients will be dominated by intermediate regimes (R1) and specially (R2) which are exactly equivalent to those originated through noise. These regimes are extremely long for small ξ and may be the most relevant ones for most practical purposes. As will be shown next, the existence of an asymptotic power-law distribution in the RTS *may* lead additionally to asymptotic anomalous transport.

7.3.2 Effect on the anomalous diffusion

So far the study of stickiness in higher-dimensional systems was motivated through fundamental questions and justifications of practical calculation procedures, such as the case of systems with time scale separation which are studied in detail in Appendix B. The calculation of transport properties provides an additional interesting application of the previous results. Transport in higher-dimensional Hamiltonian systems is an important issue in the physics of charged particles accelerators [Viv84a] and in self-consistent transport [TMM94, dCN00]. Recalling the results of CTRW (continuous time random walk) theory of transport summarized in Eq. (6.13) one sees that the transport will be normal (diffusive) whenever the exponent of the RTS is $\gamma \geq 2$. The results for high-dimensional maps of Fig. 7.6c indicates that this happens for all coupling strength ξ for sufficiently large N. In these cases the transport is normal and the theories developed in Sec. (6.2.3) for the effect of noise in the asymptotic diffusion coefficient apply also for these fully deterministic systems.
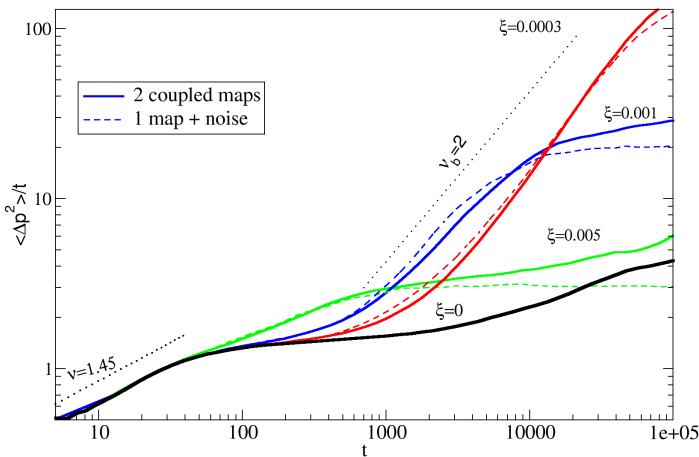
Figure 7.7: (Color online) Transport in the standard map (6.1) with $K = 1.07$ (accelerator mode) perturbed by noise (dashed lines) with intensity $\sqrt{2}\xi/2$ and coupled to another standard map with $K = 0.52$ (solid lines) with intensity ξ. The unperturbed case $\xi = 0$ is depicted as a thick solid line. From top to bottom $\xi = 0.0003, 0.001, 0.005$. 10^6 trajectories were used with initial conditions away from islands $y_i = 0, 0 < x_i \leq 1$. When the curves become constant (for $t \to \infty$) transport is normal. Notice the additional regime of superdiffusion for very long times.

On the other hand, if the asymptotic stickiness exponent is $\gamma_{R3} < 2$ an *additional* regime of anomalous transport is predicted by Eq. (6.11). This is shown in Fig. 7.7, where a similar numerical experiment to the one described in Fig. 6.6 was done. This time the noise perturbation to a standard map in the accelerator mode regime was replaced by a coupling to an additional standard map. The comparison between both results shows that the main difference is that anomalous transport is observed asymptotically in time, in agreement with the qualitative predictions of Eq. (6.13).

Chapter 8

Conclusions

The main results obtained in the previous pages are summarized and discussed in this concluding Chapter. A novel picture of the intermittent-chaotic dynamics in Hamiltonian systems emerges (Sec. 8.1). Additionally, the main specific results are listed (Sec. 8.2). Finally, a non-exhaustive list of possible extensions of the results and of important open problems in the field is presented (Sec. 8.3).

8.1   Summary and outlook

The problem of chaotic dynamics in Hamiltonian systems was studied in this Thesis through a phenomenological and numerical approach. From this perspective, the chaotic dynamics can be described essentially as an intermittent process that alternates between chaotic excursions, that quickly explores different regions of the ergodic component in the phase space, and long periods of almost regular behavior, due to the stickiness close to regions of regular motion. The most important properties of the chaotic dynamics (e.g., the decay of correlations and transport properties) are obtained from the characteristics of this stickiness phenomenom, which was studied in detail in this Thesis.

An elegant way of quantifying stickiness is through the Poincaré recurrences of chaotic trajectories. The RTS (recurrence time statistics) shows asymptotically roughly a power-law decay $\rho(\tau) \sim \tau^{-\gamma}$ where the exponent γ is analogous to the exponent of the distribution of laminar phases in intermittent systems. In Chap. 3 it was shown that long-range linear time series show stretched exponential distribution of recurrence times sensitive to the observable used to quantify the system. This indicates that the connection between power-law RTS and long-range correlation is subtle, and suggests that the power-law observed in Hamiltonian systems is better interpreted as an intermittent phenomena. The dynamical mechanism originating this intermittency is the stickiness phenomenom described above. The manifested aim of many theoretical and numerical works in low-dimensional Hamiltonian systems during the last twenty five years was to obtain the exponent γ of the RTS as a function of the phase-space structures (hierarchies of islands-around-islands and cantori). Different claims of universality failed to find numerical confirmation partially due to the oscillatory behavior of the tails of the RTS (slow convergence) and due to different phase-space configurations. Some very recent promising results indicate that one universal exponent $\gamma \approx 1.6$ indeed exists [CK], what was corroborated by the numerical simulations shown in Fig. 2.3. The variety of different phase-space structures in Hamiltonian systems and the slow convergence to an universal behavior motivates both the study of system-specific stickiness mechanisms and finite time behaviors.

One specific mechanism studied in detail in this Thesis is the stickiness close to MUPOs

(one parameter families of marginally unstable periodic orbits). For this case the exponent $\gamma = 2$ was obtained analytically (Sec. 4.2) and verified numerically. Systems described by this theory include the previously known case of chaotic billiards with parallel walls (e.g., Sinai and Stadium billiards), circular-like billiards (Sec. 4.3) where it was shown that an infinite number of different families of MUPOs typically exist (Sec. 4.4) (e.g., annular and mushroom billiards), and piecewise-linear area-preserving maps (Sec. 5.1). More generally, one expects this exponent to be valid for systems presenting sharply-divided phase space between chaotic regions and regular islands with polygonal shape.

Regarding finite-time stickiness behavior, it was shown in Chap. 6 that they are specially relevant in noise-perturbed Hamiltonian systems. For small noise intensities two important intermediate trapping regimes are observed before the asymptotic exponential decay of the RTS: the first regime is identical to the deterministic case and the second regime, with an exponent $\gamma \approx 0.5$, corresponds to trajectories performing a random walk inside the regular islands. Quantitative scalings of these regimes are carefully discussed in Sec. 6.1. The effect of such regimes to the (anomalous) transport is obtained directly from CTRW models (Sec. 6.2). One intuitive and physically relevant application of the previous results is the transport of passive scalar tracers in two-dimensional incompressible fluids (Sec. 6.3).

All previous examples and results refer to the case of two-dimensional discrete-time systems or, equivalently, Hamiltonian flows with two degrees of freedom. Higher-dimensional systems were usually characterized from other perspectives (e.g., Arnold diffusion and relaxation to equilibrium) and only very little attention was devoted to stickiness in such systems [DBO90, KG87a]. Stickiness was studied in this Thesis for an increasing number of degrees of freedom (Chap. 7). This was possible due to the construction of a suited high-dimensional system through the controlled coupling of different low-dimensional ones. The intermediate regimes of decay of the RTS are similar to those of noise-perturbed system. Additionally, an asymptotic power-law decay was identified as a genuine high-dimensional effect. Numerical simulations up to $N = 25$ indicate that the asymptotic decay of the RTS remains power-law (stickiness exists), but that the power-law exponent γ increases (roughly linearly) with N. This provides a different explanation for the expected validity of hypotheses of strong chaos that usually assume asymptotic exponential decay.

Gathering all these results, a novel picture of stickiness emerges. The previous picture of stickiness, implicitly or explicitly mentioned in different works, associates it to the presence of partial barriers and/or an hierarchical phase space. The power-law decay of the statistics of the relevant quantities is related to the (multi-)fractal properties of chains of islands or cantori. Differently, stickiness is interpreted in this Thesis as a generic phenomenon of Hamiltonian systems that leads to intermittent behavior of chaotic trajectories. The sticky set can be virtually any non-hyperbolic invariant structure. This is actually intuitive since the local Lyapunov exponent or diffusion coefficient is expected to approach continuously zero close to the regions of regular motion. The power-law decay is related in this case to how this approach occurs, i.e., to the stability property close to the regular regions (see Sec. 4.2). The stickiness in the hierarchical phase space, as discussed in Sec. 2.2.3 where the Markov-tree model was introduced, can also be interpreted similarly. The role of the islands-around-islands and cantori is to provide a constructive procedure of defining an infinite number of states accumulating near the border. Stickiness is **not** a direct consequence of the low flux through cantori, but results from the continuous phase-space properties close to the fractal border which are taken into account through the scalings of the states defined by the cantori.

In agreement with this new interpretation of stickiness, this Thesis provides an unified framework for the analysis of further classes of Hamiltonian systems. It describes a set of statistical and numerical tools which were successfully applied to different classes of systems that serve

as comparative examples for further studies. Apart from the usual stickiness in hierarchical phase spaces mentioned above, the following systems were studied: (i) families of MUPOs which have zero measure; (ii) systems presenting sharply-divided phase space; (iii) high-dimensional Hamiltonian systems. Notice that partial barriers to the transport and a hierarchical phase space do not exist or are not necessarily the relevant elements in these systems. Nevertheless, qualitatively the same intermittent dynamics due to stickiness close to the regular regions was observed in all cases. They were quantified through the calculation of the same tool – the RTS – that shows similar power-law decays and that can be related in the same way to the decay of correlations and to the onset of anomalous transport (e.g., through a CTRW model). The influence of noise perturbations to Hamiltonian systems assumes also new contours when studied in this framework since different intermediate trapping regimes are highlighted and naturally interpreted. The stickiness phenomenon in Hamiltonian systems, interpreted through the more general perspective assumed in this Thesis, has a wide range of applicability and deserves a fundamental status among the unconventional effects of nonlinear dynamics.

8.2   List of specific results

The main novel specific results contained in this Thesis can be summarized as:

1. Long-range correlated time series (Sec. 3.2 and Ref. [AK05]):

- Following Ref. [BEHK03], it was verified numerically that the recurrences of linear long-range correlated time series are well described by the closed expression of the stretched exponential distribution introduced in Eq. (3.22).

- This distribution has a single control parameter ζ which tends to the value of the correlation exponent ζ_c for the case of extreme events. For events in the center of the probability density function ζ tends to zero and the stretched exponential distribution tends to a Poisson distribution, indicating that in this sense the long-range correlation concentrates in the extreme events.

- This example shows that there is no unique relation between correlations and RTS (recurrence time statistics). Additionally, the same system may contain different correlation and recurrence properties depending on the observable used to characterize it.

2. MUPOs (marginally unstable periodic orbits) in circular-like billiards (Sec. 4.3 and Ref. [AMK05]):

- It was shown that one parameter families of MUPOs exist inside the chaotic component of circular-like billiards. These orbits are equivalent to the bouncing-ball orbits between parallel walls, which are well known to exist in the stadium and Sinai billiards. The most prominent examples of circular-like billiards are mushroom and annular billiards.

- Based on the properties of continued fraction representation of real numbers it was shown that for almost all control parameters there are an infinite number of different families of MUPOs. This provides additionally an efficient algorithm to obtain the period and winding number of MUPOs of a given system.

3. Stickiness to MUPOs and systems with sharply-divided phase space (Secs. 4.2 and 4.5, Chap. 5, and Ref. [AMK06]):

- A theory for the stickiness close to MUPOs was developed and the power-law exponent $\gamma = 2$ of the RTS deduced. It was well-known that this exponent describes the case of Sinai and stadium billiards and it was shown here that it applies to mushroom and annular billiards.

- Hamiltonian systems presenting **sharply-divided phase space** with polygonal islands also show the scaling $\gamma = 2$ in the RTS. The reason is that the well defined and simple border between the regions of regular and chaotic motion is composed by families of MUPOs. Numerical simulations confirming this result were performed in different piecewise-linear two-dimensional maps.

- Generic perturbations of the systems mentioned above lead to hierarchical phase spaces where it was observed that stickiness was enhanced ($\gamma < 2$).

4. Stickiness in noise perturbed systems (Chap. 6 and Ref. [AK07]):

- The effect of small additive noise to the Hamiltonian chaotic dynamics has two qualitative different effects: (i) it introduces an asymptotic exponential decay of the recurrences (cut-off of the power-law decay); (ii) trajectories may penetrate the regions corresponding to islands and enhance the stickiness for intermediate times. While the first effect is typical for different intermittent systems, the second is specific of Hamiltonian systems with mixed phase space.

- The RTS of Hamiltonian systems perturbed by noise with intensity ξ has essentially three regimes: (R1) for times $0 < \tau < \tau_{1,2} \sim 1/\xi^\beta, \beta \lesssim 1$ the system shows the same behavior as the deterministic one, i.e., exponential followed by a power-law decay; (R2) for times $1/\xi^\beta \sim \tau_{1,2} < \tau < \tau_{2,3} \sim 1/\xi^2$ an enhanced power-law regime with exponent $\gamma_{R2} \approx 0.5$ is observed due to the random walk of the trajectory in the regions corresponding to regular islands; (R3) asymptotically an exponential decay is observed.

- The effect of the previously described regimes to systems showing anomalous transport was studied based on the CTRW (continuous time random walk) model with power-law flying- and trapping-time distributions [Eq. (6.11)]. The asymptotical exponential decay guarantees the onset of normal transport (diffusion) for sufficiently long times. The different intermediate regimes of anomalous transport leave their fingerprints on the asymptotic diffusion coefficient. It shows a crossover between two power-law dependences on ξ: from $D_A \sim \xi^{\beta^\dagger}, \beta^\dagger \lesssim 1$ for intermediate ξ to the case $D_A \sim \xi^{-2}$ for small ξ. The stickiness regimes together with the CTRW model correctly describe this behavior.

- The previous results were applied to the problem of dispersion of contaminants in two-dimensional incompressible flows. The effect of molecular diffusion acts as a noise perturbation. An estimation of the molecular diffusion coefficient D_m shows that the previous results are expected to be relevant in different experimental and practical situations. The results were verified in a channel model containing all typical elements: chaotic trajectories, regions of ballistic flow (leading to super-diffusion), and islands of stagnant motion. In this context the dependence of the asymptotic diffusion coefficient as $D_A \sim 1/D_m \sim 1/\xi^2$ is a well-known result that can be traced back to the work of Taylor [Tay53].

5. High-dimensional systems (Chap. 7 and Ref. [AK07]):

- A high-dimensional system with mixed phase space was constructed by coupling N two-dimensional maps. The RTS shows the same intermediate regimes observed in the noise

perturbed case with an additional asymptotic power-law decay with exponent γ_{R3} due to the stickiness to N-dimensional tori.

- Careful numerical simulations show that γ_{R3} increases with N meaning that the stickiness is reduced with increasing dimensionality. This provides a new explanation for the effective validity of the hypotheses of strong chaos in high-dimensional systems: the system is not fully ergodic but the measure of tori decays exponentially with N becoming negligible; similarly, correlations do not decay exponentially but as a sufficiently fast power-law, since the exponent increases with N.

8.3 Open issues

A list of open questions, possible extensions, and applications of the previous results is provided below:

- An analytical derivation for the RTS of linear long-range correlated time series for both extreme and non-extreme recurrence intervals is desired. This should be compared with the results of Sec. 3.2 that suggest the stretched exponential distribution (3.22) as giving good account of the results for all kinds of recurrence intervals.

- The stickiness to non-polygonal islands in a sharply-divided phase space has to be better understood (see Sec. 5.1.3).

- The existence of an infinite number of one-parameter families of MUPOs inside the chaotic component of circular-like billiards was demonstrated in Chap. 4. Besides their influence to stickiness, discussed in this Thesis, the consequences of such orbits to the problem of quantum (wave) chaos in such billiards remains to be investigated. It is interesting to note that recent numerical and experimental investigations of the phenomenon denoted *chaos assisted tunneling* performed in the annular billiard emphasized the relevance of the region between the whispering gallery and the chaotic component, which was called beach region [FD98, DGH^{+}00, HAD^{+}05]. The families of MUPOs characterized in this Thesis are located precisely in this region and remains to be explored how they may provide a better understanding of the observed phenomena.

- It would be interesting to compare the results obtained here for chaotic Hamiltonian systems to problems of interest in the context of statistical mechanics like the Hamiltonian mean field models [AR95, LRR99]. In these systems, an interesting intermediate regime called "quasi-stationary state" was observed for initial conditions started in non-equilibrium states. The quasi-stationary state is defined by a plateau in an order parameter (magnetization) that diverges with system size and where transient anomalous diffusion was reported. There are remarkable similarities between the results obtained in the Hamiltonian mean field models and the findings for coupled maps reported in Chap. 7. Since both models have also similar interpretations (all-to-all coupled oscillators), the natural questions is whether these phenomena are understandable in the same framework.

- Very recent results indicate the existence of an universal exponent for two-dimensional maps with the generic hierarchical phase space [CK]. The numerical simulations shown in Fig. 2.3 corroborate this results and confirms that the expected exponent is well estimated by $\gamma = 1.60 \pm 0.05$. The obvious question is if one can develop a theory to predict the exact value of the universal exponent γ. According to the ideas of Ref. [CK], this would

be achieved from a better knowledge about the fluctuations around the scalings of the invariant structures of the phase space.

- Stickiness in high-dimensional systems has to be further investigated. Basically no theory exists and very few numerical results are known.

Appendix A

Continued fractions and classification of real numbers

The real numbers can be classified into different sets depending on "how close" they are from the set of rational numbers. The meaning of "close/far" here refers to how the error of an rational approximation $|\alpha - p/q|$ decreases with increasing q. This decay is usually compared to the Diophantine condition

$$|\alpha - p/q| > \frac{C}{q^{\kappa}}. \tag{A.1}$$

Numbers that satisfy this condition for some (C, κ) are called Diophantine numbers and those that do not satisfy this condition for any (C, κ) are called Liouville numbers, a subset of the transcendental numbers mentioned below. It is denoted by Δ_{κ} the set composed by all numbers that satisfy (A.1) for a given κ and sufficiently small C, which defines an *irrationality measure*. It is not difficult to show that the complement of the set $\Delta_{2+\delta}$, for any δ, [i.e., the set of real numbers that violates (A.2) for $\kappa = 2 + \delta$] has zero Lebesgue measure (i.e., the probability of finding such a number decreases to arbitrarily small values by reducing C) [Mei92, dA92]. The argument goes roughly as follows: fix one value q and consider all intervals around rational numbers p/q in the interval $[0, 1]$ where condition (A.1) is violated. The sum of all intervals for a given q scales as $C/q^{1+\delta}$. Summing over all q's this leads to a finite value that can be turned arbitrarily small by reducing C. This shows that the set $\Delta_{2+\delta}$ has measure one. These results can be extended also to higher dimensions, as required by the KAM theory discussed in Sec. 2.1.2. In this case the frequency vector $\boldsymbol{\omega}$ and the sequence of integers $\boldsymbol{q}$ have to satisfy

$$|\boldsymbol{\omega} \cdot \boldsymbol{q}| > \frac{C}{|\boldsymbol{q}|^{\kappa-1}}, \tag{A.2}$$

The measure of the set of numbers in $\mathbb{R}^n$ that satisfy condition (A.2) for some (C, κ) is also one.

An efficient and elegant representation of a real number is obtained using continued fractions

$$\alpha = a_0 + \cfrac{1}{a_1 + \cfrac{1}{a_2 + ...}} = [a_0, a_1, a_2, ...], \tag{A.3}$$

where a_i's are positive integers. Irrational numbers have a unique infinite representation while for rationals the representation is finite. Truncating the sequence of a_i, a rational approximation of the number α is obtained. This approximation is optimal in the sense that there is no other fraction with denominator $q' \leq q$ which is closer to the given number α and that all best approximators are convergents (or an intermediate fraction) (Theorems 15, 16 and 17 of [Khi97]).

From the uniqueness of the continued fraction representation one sees that the values of κ, C in Eq. (A.1) depend exclusively on the values of a_i in (A.3). It is not difficult to see that large values of a_i lead to a particularly good fractional approximation of the number α. This motivates the definition of the "most irrational numbers": α is called a *noble number* if it has a continued fraction representation ending in a sequence of 1's

$$\alpha \in \text{ set of noble numbers } \Leftrightarrow \{[a_1, a_2, ..., a_{n^*}, 1, 1, 1...]\}. \tag{A.4}$$

The most famous noble number is the golden ratio $(\sqrt{5} + 1)/2 = [1, 1, 1...]$. Since an arbitrarily large sequence $a_1, a_2, ...a_{n^*}$ may be chosen, the set of all noble numbers is dense in the set of the real numbers.

Noble numbers are particular examples of the set of *quadratic irrationals*, i.e., the set of numbers written as

$$(P \pm \sqrt{M})/S, \text{ with } P, M, m, S \in \mathbb{Z}, M \neq m^2.$$

Quadratic irrationals have periodic tails in the continued fraction expansions [Khi97]. Quadratic irrationals are specific examples of the *algebraic irrationals*, i.e., the roots of polynomial equations with integer coefficients [1]. Irrational numbers that are not algebraic are called transcendental numbers. More interesting in our context are the *numbers of constant type*, i.e., real numbers for which the sequence a_i is bounded: $a_i < a_{max}, \forall i$. For all numbers of constant type the Diophantine condition (A.1) is satisfied with $\kappa = 1$, for sufficiently small C [see the inequality (4.21)]. The numbers of constant type have Hausdorff dimension 1 [Mar] but zero measure [Khi97]. Note that these numbers belong to Δ_2, while it was proven that algebraic irrationals belong to $\Delta_{2+\delta}$ [Mei92].

From the previous considerations the set of real numbers can be divided as depicted in Fig. A.1. Taking into consideration that the set of Diophantine numbers $\Delta_{2+\delta}$ has measure one, the set of numbers of constant type Δ_2 has measure zero, and that algebraic numbers are countable (by the coefficients of the polynomials), one sees that typical real numbers are neither close to irrationals nor close to noble numbers but lie between both sets.
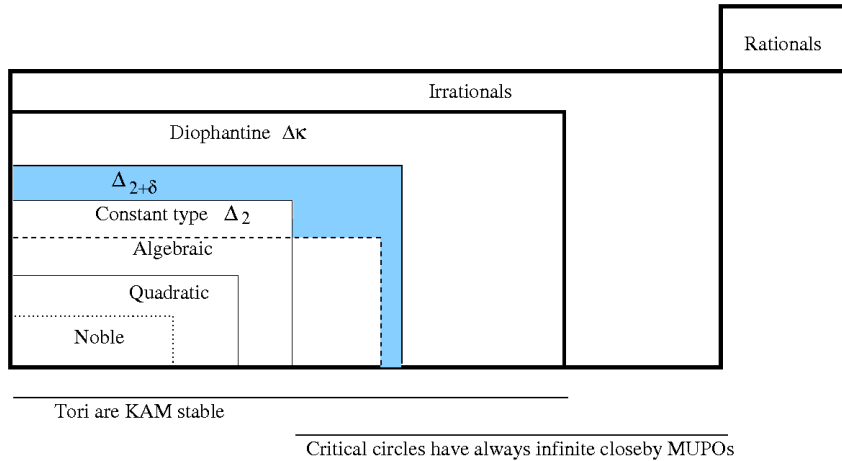
Figure A.1: The division of the real numbers regarding the property of being well approximated by rationals (Venn diagram [Mei92]). The shaded region has Lebesgue measure one. The lines at the bottom indicate the sets where rotation numbers have to belong in order to have: (i) KAM stable tori (as discussed in Sec. 2.1.2); and (ii) always an infinite numbers of MUPOs close to the boundary circle of the whispering gallery modes in circular-like billiards (as discussed in Sec. 4.4).

---

[1]Algebraic numbers are also known as euclidean numbers. Irrational numbers that are not algebraic are called transcendental numbers.

Appendix B

Time-scale separation in symplectic maps

B.1 Hamiltonian flows

The coupling through a small parameter ϵ (see, e.g., Refs. [vK85, Bab05, RBG$^+$05]). The full system is then described by the Hamiltonian

$$H(\boldsymbol{I}, \boldsymbol{J}, \boldsymbol{\theta}, \boldsymbol{\phi}) = \frac{1}{\varepsilon} H_F(\boldsymbol{I}, \boldsymbol{\theta}) + H_S(\boldsymbol{J}, \boldsymbol{\phi}) + \xi H_C(\boldsymbol{\theta}, \boldsymbol{\phi}), \tag{B.1}$$

where ξ is the strength of the coupling and F, S denote the fast and slow variables respectively. The equations of motion (2.1) are

$$\begin{aligned}
\dot{\boldsymbol{I}} &= -\frac{1}{\epsilon}\frac{\partial H_F}{\partial \boldsymbol{\theta}} - \xi\frac{\partial H_C}{\partial \boldsymbol{\theta}}, \\
\dot{\boldsymbol{\theta}} &= \frac{1}{\epsilon}\frac{\partial H_F}{\partial \boldsymbol{I}}, \\
\dot{\boldsymbol{J}} &= -\frac{\partial H_S}{\partial \boldsymbol{\phi}} - \xi\frac{\partial H_C}{\partial \boldsymbol{\phi}}, \\
\dot{\boldsymbol{\phi}} &= \frac{\partial H_S}{\partial \boldsymbol{J}},
\end{aligned}$$

and differ from the uncoupled case by the terms $\boldsymbol{A_F} = \frac{\partial H_C}{\partial \boldsymbol{\theta}}$ and $\boldsymbol{A_S} = \frac{\partial H_C}{\partial \boldsymbol{\phi}}$.

The following coupling were considered previously in systems with two degrees of freedom, not necessarily in the context of time-scale separation:

- Harmonic coupling: The Hamiltonian is defined as $H_C = \frac{1}{2}\xi(\theta - \phi)^2$ and the coupling terms are $A_F = \frac{\partial H_C}{\partial \theta} = \xi(\theta - \phi)$ and $A_S = \frac{\partial H_C}{\partial \phi} = -\xi(\theta - \phi)$. This case was considered in Ref.[Bab05]. The Fermi-Past-Ulam model, which is a high-dimensional system, also considers coupling terms $(\theta - \phi)^p, p = 3, 4, ...$ [PV84, ABS06] .

- Cosine coupling: The Hamiltonian is defined as $H_C = \xi \cos(\theta - \phi)$ and the coupling terms are $A_F = \frac{\partial H_C}{\partial \theta} = \xi \sin(\theta - \phi)$ and $A_S = \frac{\partial H_C}{\partial \phi} = -\xi \sin(\theta - \phi)$. This coupling was used in Refs. [HZ99, Viv84b].

- Linear coupling: The Hamiltonian is defined as $H_C = \xi\theta\phi$ and the coupling terms are $A_F = \frac{\partial H_C}{\partial \theta} = \xi\theta$ and $A_S = \frac{\partial H_C}{\partial \phi} = \xi\phi$. This coupling was used in Ref. [RBG$^+$05].

B.2   Symplectic maps

The coupling between maps is less straight forward than in the continuous time case if one wants to ensure the symplectic (Hamiltonian) character of the whole system. Following Sec. (2.1.1), two methods are possible. The first is to use the generating function $S(\boldsymbol{q}, \boldsymbol{p}')$, which plays the role of a Hamiltonian in the procedure described above. The drawback is that in many cases the higher-dimensional map is given explicitly $(\boldsymbol{p}', \boldsymbol{q}') = \boldsymbol{M}_N(\boldsymbol{p}, \boldsymbol{q})$ and the generating function is difficult to obtain. A more straightforward method consists in verifying if the full coupled-map is symplectic, i.e., satisfies Eq. (2.3) [Ott02]. One important simplification is that the product of symplectic matrices is also symplectic. This can be used to define the coupling between N maps of dimension $2m$ as a symplectic map $\boldsymbol{T}_{Nm}$ of dimension $2Nm$. The coupled map is then given by the composition $\boldsymbol{T} \circ \boldsymbol{M}$ where $\boldsymbol{M} = (M_1, \dots, M_N)$ is the independent iteration of N $2m$-dimensional maps, which is obviously symplectic.

Usually two-dimensional maps ($m = 2$) are coupled through their positions q. The most common coupling $\boldsymbol{T} = \{T_1, ..., T_N\}$ is a sinusoidal coupling defined as [KK94, HZ99]

$$T_i^s \left(\begin{array}{c} \boldsymbol{p} \\ \boldsymbol{q} \end{array} \right) = \left(\begin{array}{c} p_i + \sum_{j=1}^m \xi_{i,j} \sin(2\pi(q_j - q_i)), \\ q_i \end{array} \right), \tag{B.2}$$

where $\xi_{i,j} = \xi_{j,i}$ is needed in order to assure the symplectic character of the coupling.

Example: The map $\boldsymbol{R_2} = \boldsymbol{T_2} \circ \boldsymbol{M}$, with $\boldsymbol{T_2}$ given by Eq. (B.2) and the uncoupled maps $\boldsymbol{M}$ build by two standard maps as in (7.1), is given by [HZ99]

$$\left(\begin{array}{c} p_1' \\ q_1' \\ p_2' \\ q_2' \end{array} \right) = \left(\begin{array}{c} p_1 + K_1 \sin(2\pi q_1) + \xi \sin(2\pi(q_2' - q_1')) \\ q_1 + p_1 + K_1 \sin(2\pi q_1) \\ p_2 + K_2 \sin(2\pi q_2) + \xi \sin(2\pi(q_1' - q_2')) \\ q_2 + p_2 + K_2 \sin(2\pi q_2) \end{array} \right). \tag{B.3}$$

Slightly different maps are obtained when one uses $\boldsymbol{R} = \boldsymbol{M} \circ \boldsymbol{T^s}$ (instead of $\boldsymbol{R} = \boldsymbol{T^s} \circ \boldsymbol{M}$). This system was used in Ref. [KK94] for globally coupled maps. Linear chains of maps (in a lattice) were consider in Refs. [KG87a, KG87b, FMV91, KK89]. A similar coupling (with + signal in the perturbation) was proposed originally by Froeschlé and used also in Ref. [KB85].

Another possible coupling is the linear coupling defined as [Bab05]

$$T_i^l \left(\begin{array}{c} \boldsymbol{p} \\ \boldsymbol{q} \end{array} \right) = \left(\begin{array}{c} p_i + \sum_{j=1}^m \xi_{i,j} q_j, \\ q_i \end{array} \right), \tag{B.4}$$

where again $\xi_{i,j} = \xi_{j,i}$. The drawback is that the coupling is not naturally 2π (or 1) periodic.

Example: Standard map (7.1) coupled to a cat map [Ott02]:

$$\left(\begin{array}{c} p_1' \\ q_1' \\ p_2' \\ q_2' \end{array} \right) = \left(\begin{array}{c} p_1 + K \sin(2\pi q_1) + \xi q_2 \\ q_1 + p_1 + K \sin(2\pi q_1) \\ q_2 + 2p_2 + \xi q_1 \\ q_2 + p_2 \end{array} \right). \tag{B.5}$$

Time-scale separation

An interesting question is how to introduce time-scale separation to coupled symplectic maps [Bab05]. The motivation for this problem is that further analytical methods can be applied to coupled Hamiltonian systems presenting different time scales. For instance, in many situations one is interested in the study of the *slow* system which is coupled with *fast* ones.

In this case one usually tries to eliminate [vK85] the fast variables or to substitute [RBG$^+$05] them by noise. A complementary problem is the study of the fast system, considering the slow one as a perturbation. An additional motivation to study such systems using maps is that in this case more efficient numerical results are obtained. This is needed to verify the long-time decay of correlations, which should be fast in order to formally justify the substitution or elimination procedures mentioned above (see also discussion in Sec. (7.1). The procedure to couple symplectic maps with different time scales used in Ref. [Bab05] is formalized and discussed below[1] and a slightly modified method is proposed.

Assume that the time scale of the slow map is a multiple (say $\Delta \in \mathbb{N}$) of the time scale of the fast map (which is set to 1). The idea used in Ref. [Bab05] is that the fast map is iterated Δ times, independently (*uncoupled*) of the slow map, after what the slow map coupled with the fast map [e.g., Eq. (B.5)] is iterated once. The procedure is then repeated. The iteration of every Δ time steps for two ($N = 2$) coupled area-preserving maps can be represented as

$$\underbrace{\left(\boldsymbol{T} \circ \left| \begin{array}{cc} M_F & \mathbf{0}_2 \\ \mathbf{0}_2 & M_S \end{array} \right| \right)}_{\text{slow (coupled maps)}} \circ \underbrace{\left| \begin{array}{cc} M_F & \mathbf{0}_2 \\ \mathbf{0}_2 & \boldsymbol{I}_2 \end{array} \right|^{\Delta-1}}_{\text{fast dynamics}} \left(\begin{array}{c} p_F \\ q_F \\ p_S \\ q_S \end{array} \right) . \tag{B.6}$$

Notice that, by convention, the "fast dynamics" takes place in a longer time scale (iterated $\Delta - 1$ times) and the "slow dynamics" in a shorter one (iterated once). The symplectic character of this procedure is apparent since both kind of iterations used in Eq. (B.6) are symplectic (and thus their composition).

Example: fast standard map and slow cat map coupled through a linear coupling. The slow dynamics in Eq. (B.6) is given by Eq. (B.5) with the sub-indexes $1, 2$ meaning fast and slow variables respectively. The fast dynamics (the one iterated $\Delta - 1$ times) is given by

$$\left| \begin{array}{cc} M^{sm} & \mathbf{0}_2 \\ \mathbf{0}_2 & \boldsymbol{I}_2 \end{array} \right| \left(\begin{array}{c} p_F \\ q_F \\ p_S \\ q_S \end{array} \right) = \left(\begin{array}{c} p_F + K\sin(2\pi q_F) \\ q_F + p_F + K\sin(2\pi q_F) \\ p_S \\ q_S \end{array} \right) . \tag{B.7}$$

This coupling procedure has the evident drawback that during the faster time scale the fast map remains completely uncoupled from the slow map [see Eq. (B.7)]. Usually one can think that the slow variables remain almost *unchanged* during the fast dynamics but usually the *value* of the unchanged slow variable does matter to the dynamics of the fast one. In the continuous time case this point is naturally implemented, e.g., in the linear coupling described in Sec. B.1 the dynamics of the fast action incorporates the term $+\xi\phi$ for all times (where ϕ is the slow angle variable). The procedure for coupling maps discussed above actually describes a system where the coupling term is turned on and off periodically in the time scale of the slower map. This problem is specially critic when the effect of the slow dynamics on the fast one is studied.

The first idea to solve the above mentioned problem is to keep during the fast dynamics the constant additive term present in the slow dynamics. Since this term is constant during the longer time scale one could naively argue that the fast dynamics remains symplectic. However, since the value of this constant changes every Δ time steps, one realizes that the procedure of adding this constant is equivalent to add to the first equation of (B.7) the term ξq_S while keeping p_s, q_s fixed. However, Eq. (B.7) with the term ξq_S does not satisfy the symplectic condition (2.3). This emphasizes the need of a coupling procedure where the time-scale separation is introduced as the composition of different symplectic maps. This is done next.

---

[1]No further references to this problem were found.

A symplectic map with time-scale separation is obtained through the following permanent coupling procedure that maintain the coupling term during all time steps

$$\underbrace{\left(\boldsymbol{T} \circ \left|\begin{array}{cc} M_F & \boldsymbol{0}_2 \\ \boldsymbol{0}_2 & M_S \end{array}\right|\right)}_{\text{Slow dynamics}} \circ \underbrace{\left(\boldsymbol{T} \circ \left|\begin{array}{cc} M_F & \boldsymbol{0}_2 \\ \boldsymbol{0}_2 & \boldsymbol{I}_2 \end{array}\right|\right)^{\Delta-1}}_{\text{Fast dynamics}} \left(\begin{array}{c} p_F \\ q_F \\ p_S \\ q_S \end{array}\right). \tag{B.8}$$

Since usually the coupling term depends only on the positions q_i and are added to the momentum p_i the coupling term at the fast map remains constant during the fast dynamics. Nevertheless the slower map does not remain unchanged during this time since the term p_S changes due to the coupling to the fast map. This is evident in the example below.

Example: fast standard map and slow cat map coupled with a linear coupling. The slow dynamics in Eq. (B.8) is again given by Eq. (B.5). The fast dynamics is given this time by

$$\left(\boldsymbol{T^l} \circ \left|\begin{array}{cc} M^{sm} & \boldsymbol{0}_2 \\ \boldsymbol{0}_2 & \boldsymbol{I}_2 \end{array}\right|\right) \left(\begin{array}{c} p_F \\ q_F \\ p_S \\ q_S \end{array}\right) = \left(\begin{array}{c} p_F + K\sin(2\pi q_F) + \xi q_S \\ q_F + p_F + K\sin(2\pi q_F) \\ p_S + \xi q_F \\ q_S \end{array}\right), \tag{B.9}$$

which has to be compared with Eq. (B.7) obtained through the previous procedure.

B.3   Stickiness

The question about the decay of correlations in coupled symplectic maps with time-scale separation is investigated now. It was proposed in Ref. [Bab05] and is motivated in Sec. 7.1. The permanent coupling (B.9) will be used below to investigate the decay of the RTS (recurrence time statistics) in a fast map with mixed phase space (taken as the reference map) coupled to two different slow maps: one which is fully chaotic and one which has mixed phase space. The results of Chaps. 6 and 7 are applied to understand the preliminary numerical results shown here.

How can the perturbation generated by the slow map on the fast map be estimated? In the permanent coupling procedure described in Eq. (B.8), and for all couplings mentioned before, the dynamics of the fast map is perturbed simply by an additive constant during the longer time scale ($\Delta - 1$ iterations). In Eq. (B.9) this corresponds to the term ξq_S. Such additive constant slightly changes the phase space of the map, e.g., in the case of the standard map with $K = 0.52$ it was observed that the KAM island is slightly deformed and shifted. Every Δ time steps this constant is changed and a new configuration obtained. When the slower time scale is sufficiently chaotic one can approximate this by random changes[2]. Since q_S is usually related to some angle variable it is taken mod(1) [or mod(2π)] and the random variable is uniformly distributed in the interval. Its strength is given by the coupling term ξ and by the time-scale separation Δ. Since the phase space changes only slightly for sufficiently small ξ, one can also think that the trajectory suffers a random kick every Δ time steps. This provides the link to the results of Chap. 6, obtained for the stickiness in noise-perturbed systems.

In order to make a reasonable comparison a rescaling of the coupling strength is necessary since here a kick of strength ξ occurs every Δ time steps while in the model o f Chap. 6 it occurred every time step. This rescaling has to be done carefully since the obvious rescale $\xi_{effective} = \xi/\Delta$

---

[2]In some cases this is not a bad approximation also for quasi-periodic primary tori since in this case the position q_S also runs through all values $[0, 2\pi]$ independently of the fast time scale.

is not always the correct one. For instance, the end of regime (R2) described in Sec. 6.1.2 is estimated in Eq. (6.5) by the time a random-walker with step size ξ typically takes to explores the area corresponding to the biggest island. The rescale to be used in this equation is thus the step size of the new random walker with the time-scale separation Δ, which is given by $\xi_{effective} = \xi/\sqrt{\Delta}$.

For our numerical experiments the standard map (6.1) with $K = 0.52$ was considered as the fast system. The fast map has mixed phase space and was extensively studied in Sec. 6.1.1. Linearly coupled to it, a slow cat map is considered initially, which is a fully chaotic hyperbolic system [Ott02]. The dynamics is thus given by Eq. (B.8) where the slow dynamics is given by Eq. (B.9) and the fast by Eq. (B.5). Recurrences were calculated through the same procedure described in Sec. 7.3.1 in order to compare the results to those obtained in noise-perturbed systems. In the case of no time-scale separation $\Delta = 1$ it was verified (not shown here) that the RTS is indistinguishable from the noise perturbed map shown in Fig. 6.1. The results for $\Delta = 10$ and $\Delta = 100$ are shown in Fig. B.1. In general, the results discussed in Sec. 6.1.2 apply, i.e., the RTS follows the unperturbed one for short times, shows an enhanced trapping regime for intermediate times, and an exponential decay asymptotically. One can additionally notice for strong couplings (when the asymptotic exponential decay starts at times comparable to Δ) a higher probability for recurrences around multiples of Δ, manifested as oscillations of the RTS (e.g., $\xi = 1$ in Fig. B.1a,b). This is due to the trajectories thrown inside the KAM island that necessarily remain inside it for a multiple of Δ time steps. Additionally, the agreement of the rescale $\xi_{effective} = \xi/\sqrt{\Delta}$ for the time $\tau_{2,3}$, given by Eq. (6.5), is shown for $\xi = 10^{-3}$ and $\Delta = 1$ in panel (b).
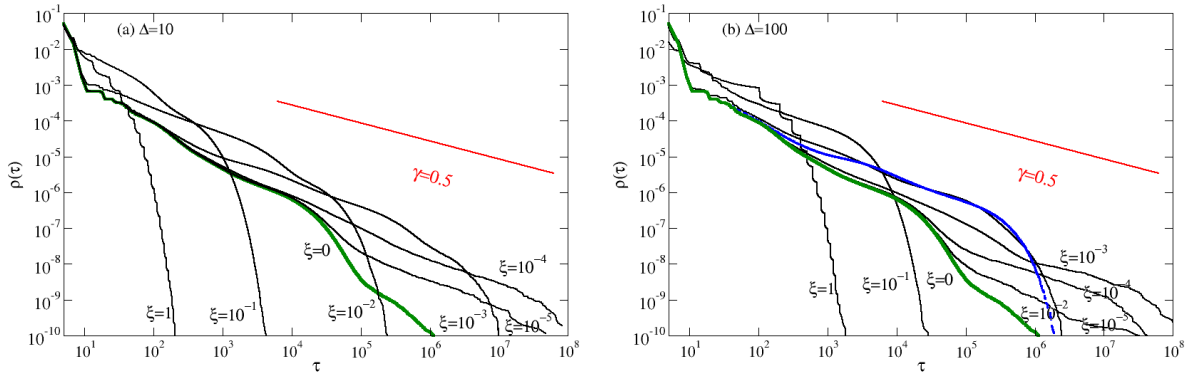

Figure B.1: (Color online) RTS for the standard map (fast system) linearly coupled to a cat map (slow system) as in Eqs. (B.8), (B.5), and (B.9). Different coupling strengths are shown $\xi = 1...10^{-5}$ and two time-scale separations: (a) $\Delta = 10$ and (b) $\Delta = 100$. The thick (green) curve corresponds to the unperturbed case $\xi = 0$. There are remarkable similarities with Fig. (6.1) once the appropriate rescale of ξ is considered: the dashed (blue) curve in panel (b) corresponds to $\Delta = 1$ and $\xi = 10^{-3}$ showing that the exponential decay starts at similar times from the case $\xi = 10^{-2}$ and $\Delta = 100$ (see text).

The previous results are based on the strong chaotic properties of the slow dynamics that resemble a noise perturbation. A more interesting situation is obtained if both slow and fast maps have mixed phase space. In order to explore this case the same procedures described above was repeated replacing the cat map by another standard map with $K = 0.52$. The results are shown in Fig. B.2. It is specially clear from the case $\Delta = 100$ that for small coupling strengths ξ the RTS again follows the unperturbed one for short times and shows an enhanced trapping regime after that. The asymptotic decay is however not exponential and long-time tails are

clearly seen for all ξ when $\Delta = 10$ and also for $\xi = 1$ and $\xi = 0.1$ for $\Delta = 100$. These results are in agreement with those obtained in Sec. 7.3 where the asymptotic tails were identified to stickiness to higher-dimensional tori. In summary, the theories described in Chaps. 6 and 7 provide the correct framework to understand also results obtained for coupled symplectic maps with time-scale separation.
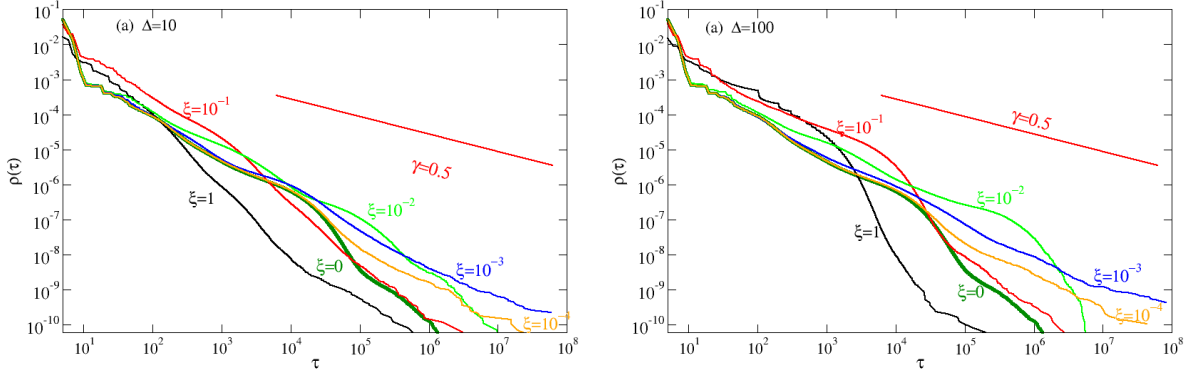
Figure B.2: (Color online) RTS for the standard map with $K = 0.52$ (fast system) linearly coupled to another standard map with $K = 0.52$ (slow system), as in Eqs. (B.8), (B.3, and (B.9). Different coupling strengths are shown $\xi = 1...10^{-4}$ and two time-scale separations: (a) $\Delta = 10$ and (b) $\Delta = 100$. The thick (green) curve corresponds to the unperturbed case $\xi = 0$. Note the slow asymptotic decay for all curves in (a) and for $\xi = 1$ and $\xi = 0.1$ in (b) in agreement with the results of Fig. 7.3a.

Bibliography

[AA89]   V. I. Arnold and A. Avez, *Ergodic problems of classical mechanics*, Addison-Wesley Pub. Co., New York, 1989.

[ABS06]   C. Antonopoulos, T. Bountis, and C. Skokos, *Chaotic dynamics of n-degree of freedom Hamiltonian systems*, Int. J. Bif. Chaos **16** (2006), 1.

[ACP06]   E. G. Altmann, G. Cristadoro, and D. Pazó, *Nontwist non-Hamiltonian systems*, Phys. Rev. E **73** (2006), 056201.

[AdSC04]   E. G. Altmann, E. C. da Silva, and I. L. Caldas, *Recurrence time statistics to finite size intervals*, Chaos **14** (2004), 975.

[Afr97]   V. Afraimovich, *Pésin's dimension for Poincaré recurrences*, Chaos **7** (1997), 12.

[AHK06]   E. G. Altmann, S. Hallerberg, and H. Kantz, *Reactions to extreme events: Moving threshold model*, Physica A **364** (2006), 435.

[AHO04]   D. N. Armstead, B. R. Hunt, and E. Ott, *Power-law decay and self-similar distributions in stadium-type billiards*, Physica D **193** (2004), 96.

[Aiz89]   Y. Aizawa, *Universality of the stagnant motions in Hamiltonian systems*, Prog. Theor. Phys. **81** (1989), 249.

[AK05]   E. G. Altmann and H. Kantz, *Recurrence time analysis, long-term correlations, and extreme events*, Phys. Rev. E **71** (2005), 056106.

[AK07]   _____, *Hypothesis of strong chaos and anomalous diffusion in coupled sympectic maps*, Europhys. Lett. **78** (2007), 10008.

[Alt04]   E. G. Altmann, *Return time in dynamical systems*, Master dissertation in the Physiscs Institute of the Universisty of São Paulo., 2004, in Portuguese.

[AMK05]   E. G. Altmann, A. E. Motter, and H. Kantz, *Stickiness in mushroom billiards*, Chaos **15** (2005), 033105.

[AMK06]   _____, *Stickiness in Hamiltonian systems: from sharply divided to hierarchical phase space*, Phys. Rev. E **73** (2006), 026207.

[AP98]   R. Artuso and A. Prampolini, *Correlation decay for an intermittent area-preserving map*, Phys. Lett. A **246** (1998), 407.

[AR95]   M. Antoni and S. Ruffo, *Clustering and relaxation in Hamiltonian long-range dynamics*, Phys. Rev. E **52** (1995), 2361.

[Are84]   H. Aref, *Stirring by chaotic advection*, J. Fluid Mech. **143** (1984), 1.

[Arn64]   V. I. Arnold, *Instability of dynamical systems with several degrees of freedomm*, Sov. Math.-Dokl. **5** (1964), 581, Reprinted in Ref. [**?**].

[Ash97]   P. Ashwin, *Elliptic behaviour in the sawtooth standard map*, Phys. Lett. A **232** (1997), 409.

[AZ97]   V. Afraimovich and G. M. Zaslavsky, *Fractal and multifractal properties of exit times and Poincaré recurrences*, Phys. Rev. E **55** (1997), 5418.

[Bab05]   N. Baba, *Elimination schneller chaotischer freiheitsgrade in Hamiltonschen systemen*, Ph.D. thesis, Bergische Universität Wuppertal, 2005, in german.

[BB06]   A. H. Barnett and T. Betcke, *Quantum mushroom billiards*, 2006, preprint arXiv: nlin/0611059.

[BBdCM93]   O. Bohigas, D. Boosé, R. Egydio de Carvalho, and V. Marvulle, *Quantum tunneling and chaotic dynamics*, Nucl. Phys. A **560** (1993), 197.

[BCDS02]   P. Bak, K. Christensen, L. Danon, and T. Scanlon, *Unified scaling law for earthquakes*, Phys. Rev. Lett. **88** (2002), 178501.

[BCVV95]   L. Biferale, A. Crisanti, M. Vergassola, and A. Vulpiani, *Eddy diffusivities in scalar transport*, Phys. Fluids **7** (1995), 2725.

[BD05]   L. A. Bunimovich and C. P. Dettmann, *Open circular billiards and the riemann hypothesis*, Phys. Rev. Lett. **94** (2005), 100201.

[BdCNL+03]   G. Boffetta, D. del Castillo-Negrete, C. López, G. Pucacco, and A. Vulpiani, *Diffusive transport and self-consistent dynamics in coupled maps*, Phys. Rev. E **67** (2003), 026224.

[BEG+03]   A. Bunde, J. Eichner, R. Govindan, S. Havlin, E. Koscielny-Bunde, D. Rybski, and D. Vjushin., *Power-law persistence in the atmosphere: analysis and applications*, Nonextensive Entropy-Interdisciplinary Applications, Oxford Univ. Press, New York, 2003, 2003.

[BEHK03]   A. Bunde, J. F. Eichner, S. Havlin, and J. W. Kantelhardt, *The effect of long-term correlations on the return periods of rare events.*, Physica A **330** (2003), 1.

[BEKH05]   A. Bunde, J. F. Eichner, J. W. Kantelhardt, and S. Havlin., *Long-term memory: A natural mechanism for the clustering of extreme events and anomalous residual times in climate records*, Phys. Rev. Lett. **94** (2005), 048701.

[BG96]   J. Barrow-Green, *Poincaré and the three body problem*, American Mathematical Society, 1996.

[BKT94]   W. Breymann, Z. Kovács, and T. Tél, *Chaotic scattering in the presence of an external magnetic field*, Phys. Rev. E **50** (1994), 1994.

[BMW95]   R. Bettin, R. Mannella, and B. J. West, *Influence of the environment on anomalous diffusion*, Phys. Rev. E **51** (1995), 212.

[Bun79]   L. A. Bunimovich, *On the ergodic properties of nowhere dispersing billiards*, Commun. Math. Phys. **65** (1979), 295.

[Bun01]   _____, *Mushrooms and other billiards with divided phase space*, Chaos **11** (2001), 802.

[Bun03]   _____, *Kinematics, equilibrium, and shape in Hamiltonian systems: The "lab" effect*, Chaos **13** (2003), 903.

[CFS82]   I. P. Cornfeld, S. V. Fomin, and Ya. G. Sinai, *Ergodic theory*, Springer-Verlag, Berlin, 1982.

[CGM00]   G. Casati, I. Guarneri, and G. Maspero, *Fractal survival probability fluctuations*, Phys. Rev. Lett. **84** (2000), 63.

[CK]   G. Cristadoro and R. Ketzmerick, Unpublished. Private communication.

[CMS99]   G. Casati, G. Maspero, and D. L. Shepelyansky, *Quantum Poincaré recurrences*, Phys. Rev. Lett. **82** (1999), 524.

[Con71]   G. Contopoulos, *Orbits in highly perturbed systems*, The Astronomical Journal **16** (1971), 147.

[CP99]   G. Casati and T. Prosen, *Mixing property of triangular billiards*, Phys. Rev. Lett. **83** (1999), 4729.

[CS84]   B. V. Chirikov and D. L. Shepelyansky, *Correlation-properties of dynamical chaos in Hamiltonian-systems*, Physica D **13** (1984), 395.

[CS99]   _____, *Asymptotic statistics of Poincaré recurrences in Hamiltonian systems*, Phys. Rev. Lett. **82** (1999), 528.

[dA92]   A. M. Ozorio de Almeida, *Hamiltonian systems: Chaos and quantization*, Cambridge University Press, Cambridge, 1992.

[DBO90]   M. Ding, T. Bountis, and E. Ott, *Algebraic escape in higher dimensional Hamiltonian systems*, Phys. Lett. A **151** (1990), 395.

[dCN00]   D. del Castillo-Negrete, *Self-consistent chaotic transport in fluids and plasmas*, Chaos **10** (2000), 75.

[dCNF02]   D. del Castillo-Negrete and M.-C. Firpo, *Coherent structures and self-consistent transport in a mean field Hamiltonian model*, Chaos **12** (2002), 496.

[dCNGM96]   D. del Castillo-Negrete, J. M. Greene, and P. J. Morrison, *Area preserving nontwist maps: periodic orbits and transition to chaos*, Physica D **91** (1996), 1.

[dCNGM97]   _____, *Renormalization and transition to chaos in area preserving nontwist maps*, Physica D **100** (1997), 311.

[DFMO+06]   B. Dietz, T. Friedrich, M. Miski-Oglu, A. Richter, T. H. Seligman, and K. Zapfe, *Nonperiodic echoes from mushroom billiard hats*, Phys. Rev. E **74** (2006), 056207.

[DG99]   J. Davidsen and C. Goltz, *"power laws in solar flares: self-organized criticality or turbulence?"*, Geophys. Res. Lett. **83** (1999), 4662.

[DGH+00]   C. Dembowski, H.-D. Gräf, A. Heine, R. Hofferbert, H. Rehfeld, and A. Richter, *First experimental evidence for chaos-assisted tunneling in a microwave annular billiard*, Phys. Rev. Lett. **84** (2000), 867.

[Dor99]   J.R. Dorfman, *An introduction to chaos in nonequivlibrium statistical mechanics*, Cambridge Univ. Press, Cambridge, 1999.

[dSdA00]   L. G. G. V. Dias da Silva and M. A. M. de Aguiar, *Periodic orbits in magnetic billiards*, Eur. Phys. J. B. **16** (2000), 719.

[EMZT93]   C. Jung E. M. Ziemniak and T. Tél, *Tracer dynamics in open hydrodynamical flows as chaotic scattering*, Physica D **76** (1993), 123.

[FD98]   S. D. Frischat and E. Doron, *Dynamical tunneling in mixed systems*, Phys. Rev. E **57** (1998), 1421.

[Fel50]   W. Feller, *An introduction to probability theory and its applications*, John Willey & Sons, New York, 1950, Vol. 1, third edition.

[FGK92]   R. Fleischmann, T. Geisel, and R. Ketzmerick, *Magnetoresistance due to chaos and nonlinear resonances in lateral surface superlattices*, Phys. Rev. Lett. **68** (1992), 1367.

[FMG95]   E. Floriani, R. Mannella, and P. Grigolini, *Noise-induced transition from anomalous to ordinary diffusion : the crossover time as a function of noise intensity*, Phys. Rev. E **52** (1995), 5910.

[FMV91]   M. Falcioni, U. Marini Bettolo Marconi, and A. Vulpiani, *Ergodic properties of high-dimensional symplectic maps*, Phys. Rev. A **44** (1991), 2263.

[GD95]   P. Gaspard and J. R. Dorfman, *Chaotic scattering theory, thermodynamic formalism, and transport coefficients*, Phys. Rev. E **52** (1995), 3525.

[GLS89]   G. Györgyi, F. H. Ling, and G. Schmidt, *Torus structure in higher-dimensional Hamiltonian systems*, Phys. Rev. A **40** (1989), 5311.

[GMGCG01]   G. Gouesbet, S. Meunier-Guttin-Cluzel, and G. Grehan, *Periodic orbits in Hamiltonian chaos of the annular billiard*, Phys. Rev. E **65** (2001), 016212, See also Opt. Commun. 201, 223 (2002).

[GZR87]   T. Geisel, A. Zacherl, and G. Radons, *Generic $\frac{1}{f}$ noise in chaotic Hamiltonian dynamics*, Phys. Rev. Lett. **59** (1987), 2503.

[GZR88]   T. Geisel, A. Zacherl, and G. Radons, *Chaotic diffusion and 1/f-noise of particles in two-dimensional solids*, Z. PHys. B **71** (1988), 117.

[HAD$^+$05] R. Hofferbert, H. Alt, C. Dembowski, H.-D. Graf, H. L. Harney, A. Heine, H. Rehfeld, and A. Richter, *Experimental investigations of chaos-assisted tunneling in a microwave annular billiard*, Phys. Rev. E **71** (2005), 046201.

[HAHK07]   S. Hallerberg, E. G. Altmann, D. Holstein, and H. Kantz, *Precursors of extreme increments*, Phys. Rev. E **75** (2007), 016706.

[HCM85]   J. D. Hanson, J. R. Cary, and J. D. Meiss, *Algebraic decay in self-similar markov. chains*, J. Stat. Phys. **39** (1985), 327.

[HH84]   J. E. Howard and S. M. Hohs, *Stochasticity and reconnection in Hamiltonian systems*, Phys. Rev. A **29** (1984), 418.

[Hir93]   M. Hirata, *Poisson law for axiom A diffeomorphisms*, Ergodic Theory Dynamical Systems **13** (1993), 533.

[HKL00]   Bodo Huckestein, Roland Ketzmerick, and Caio H. Lewenkopf, *Quantum transport through ballistic cavities: Soft vs hard quantum chaos*, Phys. Rev. Lett. **84** (2000), 5504.

[HLMV02]   N. Hadyn, J. Luevano, G. Mantica, and S. Vaienti, *Multifractal properties of return time statistics*, Phys. Rev. Lett. **88** (2002), 224502.

[HR02]   M. Hentschel and K. Richter, *Quantum chaos in optical systems: The annular billiard*, Phys. Rev. E **66** (2002), 056207.

[HRR+04]   H. Hu, A. Rampioni, L. Rossi, G. Turchetti, and S. Vaienti, *Statistics of Poincaré recurrences for maps with integrable and ergodic components*, Chaos **14** (2004), 160.

[HSV99]   M. Hirata, B. Saussol, and S. Vaienti, *Statistics of return times: A general framework and new application*, Commun. Math. Phys. **206** (1999), 33–55.

[HZ99]   A. Hampton and D. H. Zanette, *Measure synchronization in coupled Hamiltonian systems*, Phys. Rev. Lett. **83** (1999), 2179.

[ISM00]   R. Ishizaki, H. Shibata, and H. Mori, *Effects of external noise on anomalous diffusion in Hamiltonian dynamical systems*, Prog. Theor. Phys. **103** (2000), 245.

[Kac47]   M. Kac, *On the notion of recurrence in discrete stochastic processes*, Bulletin of the American Mathematical Society **53** (1947), 1002.

[Kac59]   _____, *Probability and related topics in physical sciences*, Interscience, New York, 1959.

[Kar83]   C. F. F. Karney, *Long-time correlations in the stochastic regime*, Physica D **8** (1983), 360.

[KB85]   K. Kaneko and R. J. Bagley, *Arnold diffusion, ergodicity and intermittency in a coupled standard mapping*, Phys. Lett. A **110** (1985), 435.

[Ket96]   R. Ketzmerick, *Fractal conductance fluctuations in generic chaotic cavities*, Phys. Rev. B **54** (1996), 10841.

[KG87a]   H. Kantz and P. Grassberger, *Chaos in low-dimensional Hamiltonian maps*, Phys. Lett. A **123** (1987), 437.

[KG87b]   _____, *Internal Arnold diffusion and chaos thresholds in coupled symplectic maps*, J. Phys. A: Math. Gen **21** (1987), 127.

[Khi97]   A. Ya. Khinchin, *Coninued fractions*, Dover, Mineola, NY, 1997.

[KHSW00]   R. Ketzmerick, L. Hufnagel, F. Steinbach, and M. Weiss, *New class of eigenstates in generic Hamiltonian systems*, Phys. Rev. Lett. **85** (2000), 1214.

[KK89]   K. Kaneko and T. Konishi, *Diffusion in Hamiltonian systems with manyu degrees of freedom*, Phys. Rev. A **40** (1989), 6130.

[KK94]   _____ , *Peeling the onion of order and chaos in a high-dimensional chaos*, Physica D **71** (1994), 146.

[Kov00]   S. Kovalyov, *Phase space structure and anomalous diffusion in a rotational fluid experiment*, Chaos **10** (2000), 153.

[KPS00]   H. E. Kandrup, I. V. Pogorelov, and I. V. Sideris, *Chaotic mixing in noisy Hamiltonian systems*, Mon. Not. R. Astron. Soc. **311** (2000), 719.

[KRW82]   C. F. F. Karney, A. B. Rechester, and R.B. White, *Effect of noise on the standard mapping*, Physica D **4** (1982), 425.

[KSZ96]   J. Klafter, M. F. Schlesinger, and G. Zumofen, *Beyond brownian motion*, Phys. Today **Feb.** (1996), 33.

[KZ94]   J. Klafter and G. Zumofen, *Lévy statistics in a Hamiltonian system*, Phys. Rev. E **49** (1994), 4873.

[KZKB$^+$02]   J. W. Kantelhardt, S. A. Zschiegner, E. Koscielny-Bunde, S. Havlin, A. Bunde, and H. E. Stansley., *Multifractal detrended fluctuation analysis of nostationary time series*, Physica A **316** (2002), 87.

[LBOG92]   Y.-C. Lai, R. Blümel, E. Ott, and C. Grebogi, *Quantum manifestations of chaotic scattering*, Phys. Rev. Lett. **68** (1992), 3491.

[Leb99]   J. L. Lebowitz, *Statistical mechanics: A selective review of two central issues*, Rev. Mod. Phys. **71** (1999), 346.

[Lee98]   K.-C. Lee, *What makes chaos border sticky*, Physica D **35** (1998), 186.

[LL83]   A. L. Lichtenberg and M. A. Lieberman, *Regular and chaotic motion*, Springer-Verlag, New York, 1983.

[LP06]   S. Lansel and M. A. Porter, *Mushroom billiards*, AMS notices **53** (2006), 334.

[LPB06]   S. Lansel, M. A. Porter, and L. A. Bunimovich, *One-particle and few-particle billiards*, Chaos **16** (2006), 013129.

[LRR99]   V. Latora, A. Rapisarda, and S. Ruffo, *Superdiffusion and out-of-equilibrium chaotic dynamics with many degrees of freedoms*, Phys. Rev. Lett. **13** (1999), 2104.

[Mar]   Stefano Marmi, *An introduction to small divisors problems*, citeseer.ist.psu.edu/marmi00introduction.html.

[MBG93]   O. Meplan, F. Brut, and C. Gignoux., *Tangent map for classical billiards in magnetic fields*, J. Phys. A: Math. Gen **26** (1993), 237.

[MdMGK05]   A. E. Motter, A. P. S. de Moura, C. Grebogi, and H. Kantz, *Effective dynamics in Hamiltonian systems with mixed phase space*, Phys. Rev. E **71** (2005), 036215.

[Mei92]   J. D. Meiss, *Symplectic maps, variational principles, and transport*, Rev. Mod. Phys. **64** (1992), 795.

[Mei97]   _____ , *Average exit time for volume preserving maps*, Chaos **7** (1997), 139.

[Miy06]   T. Miyaguchi, *Escape time statistics for mushroom billiards*, arXiv preprint:nlin.CD/0612058.

[MMP84]   R. S. Mackay, J. D. Meiss, and I. C. Percival, *Transport in Hamiltonian systems*, Physica D **13** (1984), 55.

[MO85]   J. D. Meiss and E. Ott, *Markov-tree model of intrinsic transport in Hamiltonian systems*, Phys. Rev. Lett. **55** (1985), 2741.

[MO86]   _____, *Markov-tree model of transport in area-preserving maps*, Physica D **20** (1986), 387.

[MP02]   J. Malovrh and T. Prosen, *Spectral statistics of a system with sharply divided phase space*, J. Phys. A: Math. Gen **35** (2002), 2483.

[Mur91]   N. W. Murray, *Critical function for the standard map*, Physica D **52** (1991), 220.

[Nar96]   O. Narayan, *Self-similar barkhausen noise in magnetic domain wall motion*, Phys. Rev. Lett. **77** (1996), 3855.

[Nek71]   N. N. Nekhoroshev, *Behavior of Hamiltonian systems close to integrable*, Funct. Anal. Appl. **5** (1971), 338, Reprinted in Ref. [**?**].

[Oll06]   Piero Olla, *Return times for gaussian processes with power-law scaling*, 2006, arXiv preprint: cond-mat/0606323.

[Ott02]   E. Ott, *Chaos in dynamical systems*, Cambridge University Press, Cambridge, 2002.

[PCCS+05]   M. Pettini, Lapo Casetti, M. Cerruti-Sola, R. Franzosi, and E. G. D. Cohen, *Weak and strong chaos in fermi-pasta-ulam models and beyond*, Chaos **15** (2005), 015106.

[Pen05]   C. Pennetta, *Distribution of return intervals of extreme events*, 2005, pre-print: physics/0510062.

[PHSS92]   S. Prakash, S. Havlin, M. Schwartz, and H. E. Stanley., *Structural and dynamical properties of long-range correlated percolation*, Phys. Rev. A **46** (1992), R1724.

[Pik92]   A. S. Pikovsky, *Escape exponent for transient chaos and chaotic scattering in nonhyperbolic Hamiltonian systems*, J. Phys. A: Math. Gen. **25** (1992), L477.

[Poi92]   H. Poincaré, *Les méthodes nouvelles de la mécanique céleste*, Gauthier-Villars, Paris, 1892.

[PV84]   M. Pettini and A. Vulpiani, *Possible failure of Arnold diffusion in nonlinear Hamiltonian systems with more than two degrees of freedom*, Phys. Lett. A **106** (1984), 207.

[PW94]   A.D. Perry and S. Wiggins, *KAM tori are very sticky - rigorous lower bounds on the time to move away from an invariant Lagrangian torus with linear flow*, Physica D **71** (1994), 102.

[RB85]   M. Robnik and M. V. Berry, *Classical billiards in magnetic fields*, J. Phys. A-Math. Gen. **18** (1985), 1361.

[RBG$^+$05] A. Riegert, N. Baba, K. Gelfert, W. Just, and H. Kantz, *Hamiltonian chaos acts like a finite energy reservoir: accuracy of the Fokker-Planck approximation*, Phys. Rev. Lett. **94** (2005), 054103.

[RKZ99] V. Rom-Kedar and G. Zaslavsky, *Islands of accelerator modes and homoclinic tangles*, Chaos **9** (1999), 697.

[Rob99] R. W. Robinett, *Periodic orbit theory analysis of the circular disk or annular billiard: non-classical effects and the distribution of energy eigenvalues*, Am. J. Phys. **67** (1999), 67.

[RQ92] J. A. G. Roberts and G. R. W. Quispel, *Chaos and time-reversal symmetry. Order and chaos in reversible dynamical systems*, Phys. Rep. **216** (1992), 63.

[Sev98] M. B. Sevryuk, *The finite-dimensional reversible KAM theory*, Physica D **112** (1998), 132.

[Sev03] _____, *The classical KAM theory at the dawn of the twenty-first century*, Moscow Math. J. **3** (2003), 1113.

[SHF$^+$82] N. Saitô, H. Hirooka, J. Ford, F. Vivaldi, and G. H. Walker, *Numerical study of billiard motion in an annulus bounded by non-concentric circles*, Physica D **5** (1982), 273.

[Sin70] Ya. G. Sinai, *Dynamical systems with elastic reflections. ergodic properties of dispersing billiards.*, Russ. Math. Surv. **25** (1970), 137.

[SK05] M. S. Santhanam and H. Kantz, *Long range correlations and rare events in boundary layer wind fields*, Physica A **345** (2005), 713.

[SKG$^+$98] A. S. Sachrajda, R. Ketzmerick, C. Gould, Y. Feng, P. J. Kelly, A. Delage, and Z. Wasilewski, *Fractal conductance fluctuations in a soft-wall stadium and a sinai billiard*, Phys. Rev. Lett. **80** (1998), 1948.

[Sla67] N. B. Slater, *Gaps and steps for the sequence nθ mod 1*, Proc. Camb. Phil. Soc. **63** (1967), 1115.

[SM70] C. L. Siegel and J. K. Moser, *Lectures on celestial mechanics*, Springer Verlag, Berlin, 1970.

[Sto05] A. Douglas Stone, *Einstein's unknown insight and the problem of quantizing chaos*, Phys. Today **August** (2005), 1.

[Stö00] H. J. Stöckmann, *Quantum chaos*, Cambridge Univ. Press, Cambridge, 2000.

[SWS93] T. H. Solomon, E. R. Weeks, and H. L. Swinney, *Observation of anomalous diffusion and Lévy flights in a two-dimensional rotating flow*, Phys. Rev. Lett. **71** (1993), 3975.

[SWS94] _____, *Chaotic advection in a two-dimensional flow: Lévy flights and anomalous diffusion*, Physica D **76** (1994), 70.

[SZK93] M. F. Shlesinger, G. M. Zaslavsky, and J. Klafter, *Strange kinetics*, Nature **363** (1993), 31.

[Tay53]   G. Taylor, *Dispersion of soluble matter in solvent flowing slowly through a tube*, Proc. R. Soc. London, Ser. A **219** (1953), 186.

[TLF⁺97]   S. Thurner, S. B. Lowen, M. C. Feurstein, C. Heneghan, H. G. Feichtinger, and M. C. Teich", *"analysis, synthesis, and estimation of fractal-rate stochastic point processes"*, Fractals **5** (1997), 565, arXiv preprint: adap-org/9709006.

[TMM94]   J. L. Tennyson, J. D. Meiss, and P. J. Morrison, *Self-consistent chaos in the beam-plasma instability*, Physica D **71** (1994), 1.

[TS06]   Hiroyuki Tanaka and Akira Shudo, *Recurrence time distribution in mushroom billiards with parabolic hat*, Phys. Rev. E **74** (2006), 036211.

[VCG83]   F. Vivaldi, G. Casati, and I. Guarneri, *Origin of long-time tails in strongly chaotic systems*, Phys. Rev. Lett. **51** (1983), 727.

[Viv84a]   F. Vivaldi, *Weak instabilities in many-dimensional hamiltonian systems*, Rev. Mod. Phys. **56** (1984), 737.

[Viv84b]   _____, *Weak instabilities in many-dimensional Hamiltonian systems*, Rev. Mod. Phys. **56** (1984), 737.

[VJO98]   S. C. Venkataramani, T. M. Antonsen Jr, and E. Ott, *Anomalous diffusion in bounded temporally irregular flows*, Physica D **112** (1998), 412–440.

[vK85]   N. G. van Kampen, *Elimination of fast variables*, Phys. Rep. **124** (1985), 69.

[WBKZ98]   R. B. White, S. Benkadda, S. Kassibrakis, and G. M. Zaslavsky, *Near threshold anomalous transport in the standard map*, Chaos **4** (1998), 757.

[WHK02a]   M. Weiss, L. Hufnagel, and R. Ketzmerick, *"can simple renormalization theories describe the trapping of chaotic trajectories in mixed systems?"*, Phys. Rev. E **67** (2002), 046209.

[WHK02b]   M. Weiss, L. Hufnagel, and R. Ketzmerick, *Universal power-law decay in Hamiltonian systems?*, Phys. Rev. Lett. **89** (2002), 239401.

[Wig91]   S. Wiggins, *Chaotic transport in dynamical systems*, Springer-Verlag, Berlin, 1991.

[Woj81]   M. Wojtkowski, *A model problem with the coexistence of stochastic and integrable behaviour*, Commun. Math. Phys. **80** (1981), 453.

[WPM84]   J. Wisdom, S. J. Peale, and F. Mignard, *The chaotic rotation of Hyperion*, Icarus **58** (1984), 137.

[WUS96]   E. R. Weeks, J.S. Urbach, and H. L. Swinney, *Anomalous diffusion in asymmetric random walks with a quasi-geostrophic flow example*, Physica D **91** (1996), 291.

[Zas91]   George M. Zaslavsky, *Weak chaos*, : Cambridge University Press, New York, 1991.

[Zas99]   G. Zaslavsky, *Chaotic dynamics and the origin of statistical laws*, Phys. Today **Aug.** (1999), 39.

[Zas02a]   G. M. Zaslavsky, *Chaos, fractinal kinetics, and anomalous transport*, Phys. Rep. **371** (2002), 461.

[Zas02b] _____ , *Dynamical traps*, Physica D **168-169** (2002), 292.

[Zas05] _____ , *Hamiltonian chaos and fractional dynamics*, Oxford Univ. Press, Oxford, 2005.

[ZK94] G. Zumofen and J. Klafter, *Random walks in the standard map*, Europhys. Lett. **25** (1994), 565.

[ZT91] G. M. Zaslavsky and Michael K. Tippett, *Connection between recurrence-time statistics and anomalous transport*, Phys. Rev. Lett. **67** (1991), 3251.

Acknowledgments

First of all my sincere gratitude to Holger Kantz for his stimulating supervision of this Thesis and for his support and confidence on my autonomous work.

I would like also to emphasize and thank the contribution of my senior colleagues Adilson E. Motter and Giampaolo Cristadoro that played a major role on my investigations.

Many thanks also to all colleagues and staff of the Max Planck Institute for the Physics of Complex Systems, specially those of the research group nonlinear dynamics and time series analysis, for the friendly environment.

I have benefited from inumerous discussions about the contents of this Thesis during the last three years. Therefore I would like to specially thank N. Baba, D. Castillo-Negrete, J. Davidsen, S. Denisov, K. Gelfert, R. D. V. de Oliveira, D. Pazó, S. Ruffo, T. Tél, and A. Vulpiani.

Many valuable corrections and suggestions concerning the text of this Thesis came from B. Lindner and K. Gelfert.

I would also like to thank T. Friedrich, U. Kuhl, O. Merlo, and K. Zapfe, participants of the workshop *Chaotic and Random Wave Scattering in Quantum Mechanics and Acoustics* that took place on October 2005 at the *Centro Internacional de Ciencias* in the beautiful Cuernavaca (Mexico). Special thanks to T. Seligman for inviting me to this meeting and for his interest on my work.

Finally, I would like to thank the Brazilian society for the financial support through a CAPES fellowship (project number BEX1073/03) as part of a cooperation between the financial agencies DAAD (Germany) and CAPES (Brazil). I acknowledge also the *Max Planck Institute for the Physics of Complex Systems* for the financial support that allowed me to participate on different scientific events.

<div align="right">

Eduardo Goldani Altmann
Dresden, January 16, 2007

Defence: March 12, 2007.
Corrected version: March 13, 2007.

</div>